Fakultät für Physik
Technische Universität München

Resummed photon spectra from wino and Higgsino dark matter annihilation at NLL' accuracy

Caspar Hasner

Vollständiger Abdruck der von der Fakultät für Physik der Technischen Universität München zur Erlangung des akademischen Grades eines

Doktor der Naturwissenschaften (Dr. rer. nat.)

genehmigten Dissertation.

Vorsitzender:
Prof. Dr. Lothar Oberauer

Prüfende der Dissertation:
1. Prof. Dr. Martin Beneke
2. Prof. Dr. Björn Garbrecht

Die Dissertation wurde am 26.06.2020 bei der Technischen Universität München eingereicht und durch die Fakultät für Physik am 20.07.2020 angenommen.

Abstract

This thesis investigates the semi-inclusive photon energy spectrum for the dark matter annihilation process $\chi^0\chi^0 \to \gamma + X$, where χ^0 denotes the dark matter particle which is assumed to be non-relativistic and have a mass in the TeV-range. The focus lies on the pure wino and Higgsino DM models. For non-relativistic heavy particles annihilating into light energetic states, the annihilation cross section is affected by large quantum corrections associated with the Sommerfeld effect and electroweak Sudakov logarithms. The Sommerfeld effect is well-understood and will be included at leading-power. This work primarily concentrates on the resummation of electroweak Sudakov logarithms, at NLL' accuracy. This is currently the most accurate prediction for the production of high-energy photons from wino and Higgsino dark matter annihilation.

The calculations are performed assuming narrow $E^\gamma_{\text{res}} \sim m_W^2/m_\chi$ and intermediate $E^\gamma_{\text{res}} \sim m_W$ energy resolutions and will thus be relevant for current and next-generation Imaging Air Cherenkov Telescopes. For both models, we are able to show that the computations of the narrow and intermediate energy resolution cross sections match well, which means that the results shown here provide an accurate representation up to energy resolutions of about 300 GeV. The matching of the cross sections at different resolutions is analysed analytically for wino dark matter. Lastly, we also investigate power corrections in m_W/m_χ for both dark matter models and are able to show why they can safely be neglected.

Zusammenfassung

Diese Dissertation untersucht das semi-inklusive Photon-Energiespektrum für den Streuprozess $\chi^0\chi^0 \to \gamma + X$, wobei χ^0 ein dunkle Materie-Teilchen darstellt welches nicht-relativistisch ist und eine Masse im TeV-Bereich hat. Wir konzentrieren uns auf wino und Higgsino dunkle Materie Modelle. Der Wirkungsquerschnitt für die Annihilation von schweren, nicht-relativistischen Teilchen und die darauffolgende Produktion von leichten, hochenergetischen Teilchen wird beeinträchtigt von grossen Quantuenkorrekturen die mit dem Sommerfeld Effekt und elektroschwachen Sudakov-Logarithmen zusammenhängen. Der Sommerfeld Effekt ist ein wohlverstandener Prozess und ist hier zu führender Ordnung berücksichtigt. Der Fokus dieser Arbeit liegt auf der Resummierung der elektroschwachen Sudakov-Logarithmen, zu NLL'-Genauigkeit. Diese Ergebnisse sind die derzeit genauesten Vorhersagen für die Produktion von hochenergetischen Photonen, von dunkle Materie Stossprozessen für die wino und Higgsino Modelle.

Die Berechnungen wurden gemacht unter der Annahme von schmaler $E^\gamma_{\rm res} \sim m_W^2/m_\chi$ und intermediärer $E^\gamma_{\rm res} \sim m_W$ Energieauflösung und sind daher relevant für Imaging Air Cherenkov Teleskope der gegenwärtigen und der nächsten Generation. Für beide dunkle Materie Modelle können wir zeigen, dass die Ergebnisse der schmalen und intermediären Energieauflösungen gut übereinstimmen für eine grossen $E^\gamma_{\rm res}$-Bereich. Das bedeutet, dass die Resultate dieser Arbeit akkurate Vorhersagen für Energieauflösungen von bis zu 300 GeV ermöglichen. Das genaue Übereinstimmen der Wirkungsquerschnitte für verschiedene Auflösungen wird für das wino Modell analytisch untersucht. Ausserdem prüfen wir die Relevanz von m_W/m_χ-Korrekturen höherer Ordnung für beide dunkle Materie Modelle und können zeigen, dass diese problemlos vernachlässigt werden können.

Contents

List of Figures

List of Tables

1 Introduction

1.1 Evidence for dark matter

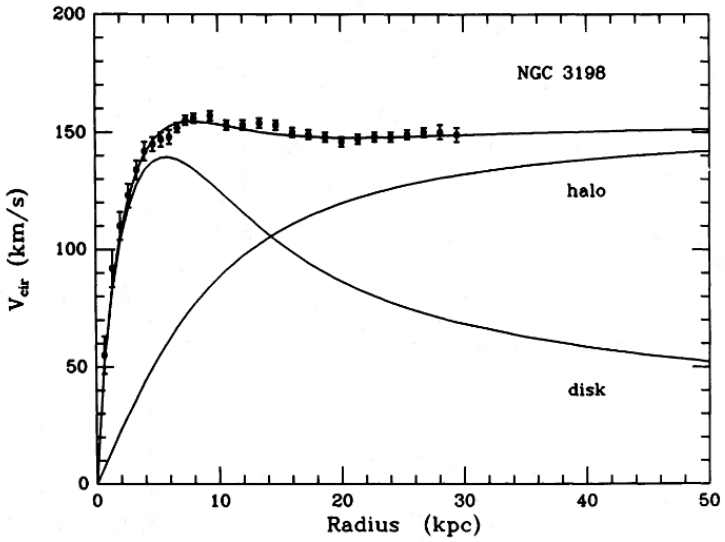

Figure 1.1: Rotation curve of the NGC 3198 galaxy demonstrating that observations cannot be explained by luminous matter (disk) alone, but are well reproduced when taking into account dark matter (halo). Plot was extracted from [1].

One of the biggest mysteries in modern particle physics is the nature of dark matter (DM) in the Universe. Over the past century, an overwhelming amount of evidence has been collected hinting at the existence of a non-luminous matter component in our Universe and today, the existence of DM is generally accepted. In 1933, Fritz Zwicky found that the dispersion velocity of galaxies in the Coma cluster was far too large to be supported by luminous matter [10]. Zwicky referred to the hypothesized non-luminous matter component as *dunkle Materie* (dark matter). In the following decades, more and more evidence was collected hinting towards the existence of DM.

One of the most widely recognized arguments for the existence of DM is based on galaxy rotation curves, i.e. the relation between orbital and radial velocity of visible stars or gas from the center of a galaxy. In the 1970s, Vera Rubin and collaborators [11, 12] measured the rotation curves of individual galaxies and what they found could not be explained by visible matter alone. Figure 1.1 shows the rotation curve of the NGC 3198 galaxy, which demonstrates that the data is not explained by visible matter but is well reproduced by the DM hypothesis [1].

Perhaps the most striking case for the existence of DM in galaxy clusters can be found in the Bullet Cluster. It consists of two clusters of galaxies which have undergone a head-on collision [2]. The hot-gas clouds (observed through X-ray detection) that contain the majority of the baryonic matter in both clusters have been decelerated in the collision, while the movement of the galaxies and the DM halos in the clusters remained almost

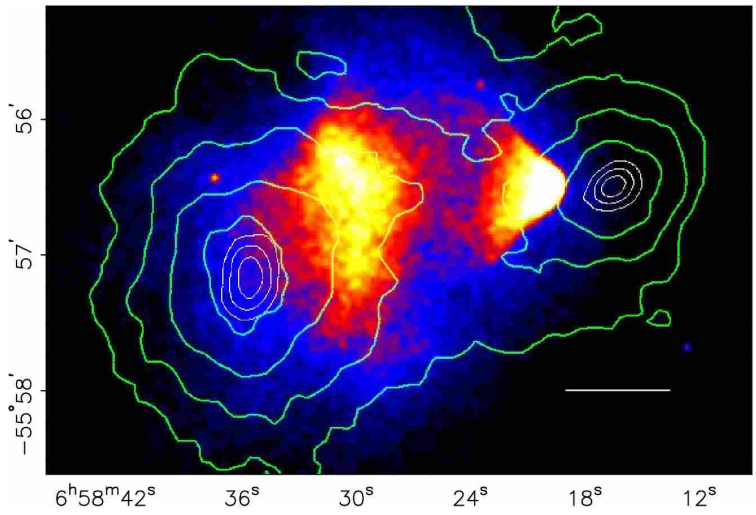

Figure 1.2: Bullet Cluster mass density contours (green) and the distribution of baryonic matter. Plot was taken from [2].

intact. The analysis of the gravitational lensing effects shows that the center of mass for both clusters is clearly separated from the hot-gas clouds, see Figure 1.2. One can thus infer the presence of a large amount of additional mass in both clusters.

Additional data supporting the existence of DM comes from weak [13] and strong [14] gravitational lensing, hot gas clusters [15], further constraints from large scale structures [16], distant supernovae [17, 18] and the cosmic microwave background (CMB) [19].

In total, all this data shows that most of the matter in our Universe is in fact non-luminous and cannot be accounted for by known particles. Current data suggests that DM is approximately five times as frequent as luminous matter, the latter being well explained by the Standard Model (SM) of particle physics. Experimental results can be used to split the energy densities present in our Universe into a luminous baryonic matter component (Ω_{B}), a non-baryonic DM component (Ω_{DM}) and a dark energy component (Ω_{Λ}). These components scale as [19]

$$\begin{aligned} \Omega_{\mathrm{B}} &\simeq 0.0456 \pm 0.0016\,, \\ \Omega_{\mathrm{DM}} &\simeq 0.227 \pm 0.014\,, \\ \Omega_{\Lambda} &\simeq 0.728 \pm 0.015\,. \end{aligned} \tag{1.1}$$

Dark energy is an unknown form of energy which permeates all of space and is hypothesized to accelerate the expansion of the universe, which is indicated by observations since the 1990s. Baryonic matter is well explained by the SM, which has been tested to incredibly high precision by experiments. The nature of DM is completely unexplained but since it might simply be comprised of unknown particles, turning to DM is well motivated when searching for physics beyond the SM. This thesis thus focuses on the computation of DM annihilation cross sections, which will be testable by next-generation telescope experiments.

1.2 Weakly interacting massive particles

Over the years, many DM candidates have been proposed. For an extensive review of DM candidates, we refer to [3]. For this work we are going to focus on so-called *weakly*

interacting massive particles (WIMPs), which provide a DM candidate that is also strongly motivated by particle physics. In this Section we are going to give a short introduction into the general properties and motivation of WIMPs (see [5] for review of WIMPs). Non-WIMP DM candidates have also been explored extensively in the literature. Nevertheless, we focus on WIMP DM since it provides a well motivated DM candidate that naturally arises in many particle physics theories.

1.2.1 Motivation and general properties

One lesson learned from observational evidence is that DM is made up of electrically neutral particles[1] and that it should interact only weakly with ordinary matter. In order to be compatible with constraints from structure formation and observations of galaxy cluster systems, DM self-interactions should not be too strong either. Current limits are of the order of $\sigma/m < 0.7\ \mathrm{cm}^2/\mathrm{g}$ [24]. Moreover, to be in agreement with CMB data, most of the DM should be non-baryonic in nature.

A simple possibility for classifying DM particles is based on how relativistic they were at the time of decoupling from the thermal plasma. Hot DM (HDM) with masses ranging up to a few tens of eV was still relativistic at the time of decoupling. Due to a large mean free path it does not form clumps on the scale of galaxies and numerical simulations of large scale structures (LSS), see for example [25], show that HDM does not reproduce the observed Universe. It is also inconsistent with data from LSS [26–28] and deep-field observations [29, 30], which give an upper limit for the allowed average velocity of DM particles. In conclusion, HDM can at most contribute a small fraction to the total DM density.

In contrast, there might also be cold DM (CDM). Non-baryonic CDM decoupled from the thermal plasma at freeze-out and, starting with the era of matter dominance, its density perturbations started growing linearly. This provided an effective catalyst for density perturbations of baryonic matter, after it decoupled from radiation some time later. This is the main reason why CDM is successful in reproducing observations in numerical simulations of LSS. It should be noted however, that also CDM exhibits some known problems, such as for example predicting too few substructures (missing satellites problem) [31, 32]. CDM as opposed to HDM is also preferred by the properties of the CMB.

The points stated above as well as related arguments have resulted in the establishment of the paradigm that the dominant fraction of DM is probably cold and that it should be both weakly interacting as well as non-relativistic and massive. Since WIMPs have a mass in the $m_{\mathrm{WIMP}} \sim 10\ \mathrm{GeV} - \mathrm{TeV}$ range, they provide an excellent DM candidate compatible with the CDM paradigm. Lastly, DM particles should either be stable or extremely long lived.

Apart from being well motivated by astrophysical obeservations, WIMPs also naturally arise from proposed solutions to particle physics problems. Despite the SM being a very successful theory, it exhibits a number of shortcomings one of which being the gauge hierarchy problem (GHP). The GHP is the question of why the physical Higgs boson mass m_h is so small. Since it is not protected by any symmetry, the natural value of m_h is expected to be of the order of the Planck scale $M_{\mathrm{Pl}} \sim 10^{19}$ GeV. In other words, the GHP is the question of why $m_h = 125.09\ \mathrm{GeV} \ll M_{\mathrm{Pl}}$. The physical mass of the SM Higgs

[1] In principle, the solution to the DM problem could be provided by something else apart from particles, but such approaches suffer from complications. Other options include modifying gravity (MOND) [20] which however still needs to invoke DM to explain all data [21], or cosmic fluids [22] which are also increasingly challenged by observations, see for example [23].

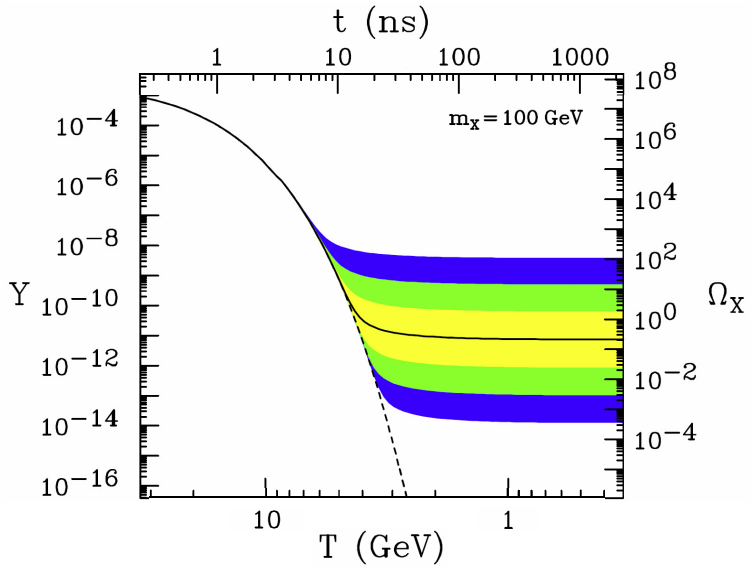

Figure 1.3: The comoving number density Y (left) and the thermal relic density (right) of a 100 GeV, P-wave annihilating DM particle as a function of the time t (top) and the temperature T (bottom). The solid line is for cross section that yields the correct relic density. The shaded regions are for cross sections that by 10, 10^2 and 10^3 from the central value. The dashed line represents the number density for a particle that would remain in thermal equilibrium. The Plot was extracted from [3].

boson is given by $m_h^2 = m_{h,0}^2 + \Delta m_h^2$ where $m_{h,0}$ is the tree-level mass and

$$\Delta m_h^2 \sim \frac{\lambda^2}{16\pi^2} \int^{\Lambda} \frac{d^4p}{p^2} \sim \frac{\lambda^2}{16\pi^2}\Lambda^2 \tag{1.2}$$

is the quantum correction resulting from loop-level contributions. The dimensionless parameter λ is an $\mathcal{O}(1)$ coupling and Λ is the scale at which new physics appears and the SM is no longer a valid description of nature. Since Δm_h is proportional to Λ, the physical Higgs mass is expected to be of the same order of magnitude as the scale at which new physics appears. In the SM it is assumed that $\Lambda \sim M_{\mathrm{Pl}}$, which implies a cancellation of 1 part in 10^{36} between $m_{h,0}$ and Δm_h^2 to yield the correct physical Higgs mass. This appears to be rather arbitrary. The GHP may be eliminated if $\Lambda \lesssim 1$ TeV, implying new physics at the weak scale $m_{\mathrm{weak}} \sim 10$ GeV $-$ TeV. The small mass of the Higgs boson is the leading particle physics motivation for WIMPs as DM candidates.

1.2.2 Production mechanism

If the WIMP paradigm is correct, meaning that WIMPs exist and are stable, they are naturally produced with a relic density consistent with the DM abundance found in our Universe. The fact that WIMPs automatically have the correct relic density is referred to as the *WIMP miracle* and it implies that particles that are motivated by solutions to the GHP, a purely particle physics problem, serve as excellent DM candidates.

The Big Bang may generate DM as a thermal relic in a simple and predictive manner [33–35]. The evolution of the thermal relic's number density, Y, is shown in Figure 1.3 for a 100 GeV, P-wave annihilating DM particle as a function of temperature T (bottom) and time t (top). Note that the behaviour of the number density is similar for S-wave annihilation and larger DM masses. Shortly after the Big Bang all particles are in thermal

equilibrium and the early Universe is in a dense and hot state. As time goes on, the Universe cools to temperatures T below the DM particle's mass m_χ and the number of DM particles becomes Boltzmann suppressed, dropping exponentially as $e^{-m_\chi/T}$. What prevents the number of DM particles from dropping to zero is the fact that the Universe is not only cooling down, but also expanding. At some point, the Universe's expansion has caused the gas of DM particles to become so dilute that DM particle annihilation stops. DM particles are said to *freeze-out* and their number asymptotically approaches a constant - their thermal relic density Ω_χ (depicted as the right y-axis in Figure 1.3). The WIMP miracle implies that many models of particle physics easily provide viable DM candidates and it is at present the strongest reason to expect that central problems in particle physics and astrophysics may in fact be related. Independently of the GHP discussed in the previous Section, the WIMP miracle provides a strong motivation for new particles with masses in the weak scale region.

Although the freeze-out mechanism always contributes to the WIMP DM abundance, the DM annihilation cross section is confined to a fairly specific range at freeze-out, if it is to be the dominant process. However, even if the cross section does not lie within the range prescribed by freeze-out, there exist other WIMP production mechanism that still yield the correct relic density. An analysis of those is however beyond the scope of this thesis and we refer to Section IV and V of [36] for a general and exhaustive discussion.

1.2.3 The neutralino WIMP as DM

As mentioned earlier, a plethora of possible DM particle candidates has been proposed in the past. Even within the class of WIMPs one can distinguish various DM candidates. In this thesis, we focus on DM candidates originating from the idea of supersymmetry (SUSY). In supersymmetric extensions of the SM, every particle has a new, so far undiscovered partner particle which has the same quantum numbers and gauge interactions, but has a spin that differs from the one of its SM partner by 1/2. Introducing supersymmetric partner particles leads to new quantum corrections to the Higgs boson mass. In fact, these corrections contribute with the opposite sign with respect to the quantum corrections originating from SM particles and (1.2) changes as follows

$$\Delta m_h^2 \sim \frac{\lambda^2}{16\pi^2}\int^\Lambda \left(\frac{d^4p}{p^2}\bigg|_{\rm SM} - \frac{d^4p}{p^2}\bigg|_{\rm SUSY}\right) \sim \frac{\lambda^2}{16\pi^2}\left(m_{\rm SUSY}^2 - m_{\rm SM}^2\right)\ln\frac{\Lambda}{m_{\rm SUSY}}\,, \tag{1.3}$$

where $m_{\rm SM}$ and $m_{\rm SUSY}$ are the masses of the SM particles and their superpartners, respectively. If SM particles and their superpartners have masses of comparable size, it would mean that Δm_h is an $\mathcal{O}(1)$ correction even if $\Lambda \sim M_{\rm Pl}$ and there is no longer the problem of fine tuning the cancellation between $m_{h,0}$ and Δm_h.

Apart from solving the GHP, SUSY provides a framework that naturally accommodates at the same time several theoretical expectations and a number of experimental data. Most importantly for this thesis, some superpartners are weakly interacting and, if stable (or at least long lived), provide a natural candidate for a WIMP and thus DM. Among them the most popular one is the lightest neutralino. For technical reasons, supersymmetric models require two Higgs bosons and we thus have the following superpartners of the B, W and Higgs bosons which mix to form four mass eigenstates, the neutralinos

$$\text{Spin 1/2 fermions:}\quad \tilde{B},\,\tilde{W},\,\tilde{H}_u,\,\tilde{H}_d \quad\rightarrow\quad \text{Neutralinos:}\quad \chi_1,\,\chi_2,\,\chi_3,\,\chi_4\,. \tag{1.4}$$

The lightest of the neutralinos, $\chi \equiv \chi_1$, is a WIMP DM candidate. The purpose of the discussion in this Section so far was to motivate why the lightest neutralino is a good DM

candidate, that is worth exploring in more detail. In this thesis we are going to focus on two specific limits of the neutralino, where the mixing of the gauge eigenstates to form the mass eigenstates χ_i is neglected and it is assumed that the mass eigenstates are in one to one correspondence with one of the gauge eigenstates.

Pure wino dark matter The first limit is the so-called pure wino limit, where the neutralinos are solely derived from the gauge eigenstates of the wino $\tilde{W}$. More precisely this means that the SM particle content is extended by a fermionic SU(2) triplet with zero hypercharge, of which the electrically neutral member is the DM particle. In this case, the fermions of the additional multiplet can be of Dirac or Majorana type. The Lagrangian of this model looks as follows

$$\mathcal{L} = \mathcal{L}_{\mathrm{SM}} + \bar{\chi}\left(i\not{D} - m_\chi\right)\chi\,, \tag{1.5}$$

if χ is a Dirac fermion. For the Majorana case, χ is self-conjugate and its Lagrangian is multiplied by $1/2$. In this thesis, we focus on the case where wino DM consists of Majorana fermions. The SU(2) covariant derivative is $D_\mu = \partial_\mu - ig_2 W_\mu^C T^C$ where T^C, $C = 1, 2, 3$, are the SU(2) generators and W_μ^C are the electroweak (EW) gauge bosons. In this model the DM particle contains the correct relic density from thermal freeze-out for m_χ in the $2 - 3$ TeV range [37]. The components of the fermionic SU(2) multiplet before and after EW symmetry breaking (EWSB) are related by the following rotation matrix

$$\begin{pmatrix}\chi_1\\ \chi_2\\ \chi_3\end{pmatrix} = \begin{pmatrix}\frac{1}{\sqrt{2}} & \frac{1}{\sqrt{2}} & 0\\ \frac{i}{\sqrt{2}} & -\frac{i}{\sqrt{2}} & 0\\ 0 & 0 & 1\end{pmatrix}\begin{pmatrix}\chi^+\\ \chi^-\\ \chi^0\end{pmatrix}\,, \tag{1.6}$$

where χ^0 represents the neutral DM candidate.

Pure Higgsino dark matter The second limit we consider is the pure Higgsino limit, where the neutralinos are solely derived from the Higgsino and do not receive contributions from either the wino or the bino. Specifically, the SM is extended by a single fermionic $\mathrm{SU(2)}\otimes\mathrm{U(1)}_Y$ Dirac doublet with hypercharge $Y = 1/2$. The Lagrangian of the model is given by

$$\mathcal{L} = \mathcal{L}_{\mathrm{SM}} + \bar{\chi}\left(i\not{D} - m_\chi\right)\chi + \mathcal{L}_{\mathrm{dim-5}}. \tag{1.7}$$

The $\mathrm{SU(2)}\otimes\mathrm{U(1)}_Y$ covariant derivative is defined as $D_\mu = \partial_\mu - ig_2 W_\mu^C T^C + ig_1 Y B_\mu$, where g_1 is the $\mathrm{U(1)}_Y$ gauge coupling. With the conventions in this thesis, the choice of EW charges is such that the lower component of the multiplet is neutral $\chi = \left(\chi^+, \chi_D^0\right)$, where the superscript denotes the electric charge. The mass eigenstates after EW symmetry breaking (EWSB) are two self-conjugate (Majorana) particles (χ_1^0 and χ_2^0) defined in such a way that $\chi_D^0 = \left(\chi_1^0 + i\chi_2^0\right)/\sqrt{2}$ and an electromagnetically charged Dirac (chargino) particle χ^+. In the pure Higgsino DM model, χ_D^0 represents the DM candidate.

Due to the non-vanishing hypercharge, the naive version of the Higgsino is already ruled out by experiment, since Z-boson mediated tree-level couplings of the Higgsinos to the light quarks would induce a large nucleon-DM cross section. This can be avoided by introducing a higher-dimension effective operator, as shown in (1.7). For example $\mathcal{L}_{\mathrm{dim-5}} = \frac{1}{\Lambda}(\bar{\chi}\Phi)i\gamma_5(\Phi^\dagger\chi)$ where Φ is the standard Higgs doublet, would provide the χ_2^0 particle with a slightly ($\geq \mathcal{O}(100)$ keV) larger mass than the χ_1^0 particle. The precise value chosen for the mass difference between the neutral components χ_1^0 and χ_2^0, denoted

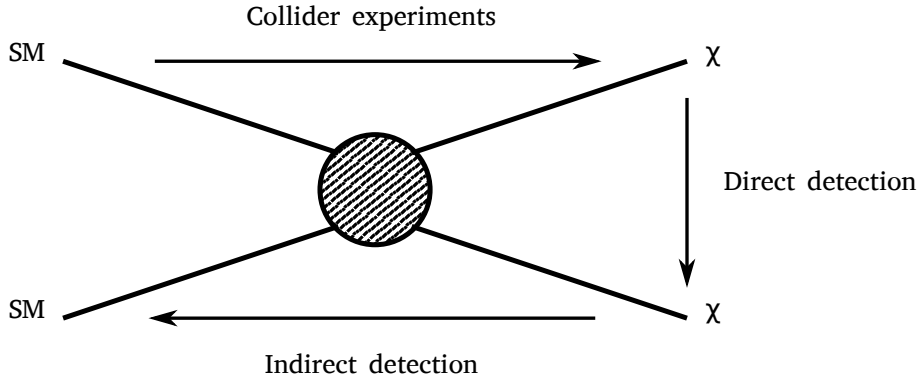

Figure 1.4: DM detection methods, where χ represents a DM particle.

by δm_N, is discussed below in Section 7. Furthermore, the mass splitting between the charged and neutral component of the Higgsino doublet, $\delta m = m_{\chi^-} - m_{\chi_1^0}$, is induced by radiative corrections after EWSB. At the one-loop order [38], this radiative correction takes the numerical value $\delta m = \alpha_{\text{em}}(m_Z/2 + \mathcal{O}(m_Z^2/m_\chi)) \sim 355$ MeV.

Please note that many of the arguments presented throughout this thesis are equivalent for both models. If conceptual or computational differences appear, they will be pointed out explicitly. Otherwise it can be assumed that the arguments hold for both wino and Higgsino DM. Also, in order to make discussions more streamlined, we introduce χ^0 to represent the DM particle for both wino and Higgsino DM. Again, if an argument only applies to one of the two models, it will be stated explicitly.

1.3 Dark matter detection methods

Experiments searching for WIMPs can be classified into three categories: collider experiments, direct detection and indirect detection experiments. The relevant process for each type of detection is visualised in Figure 1.4. In collider experiments, two SM particles collide to potentially produce DM particles, in direct detection experiments, a SM particle collides with a DM particle and in indirect detection experiments, two DM particles annihilate to generate SM particles.

1.3.1 Collider experiments

Particle accelerators have been extremely useful for discovering many types of particles, as well as for establishing and testing the SM. The biggest and most energetic particle accelerator ever built is the currently running Large Hadron Collider (LHC) at the European Organization for Nuclear Research (CERN). At the LHC, high energy proton-proton collisions, with a center-of-mass energy of $\sqrt{s} = 14$ TeV, are used to search for new physics.

In these proton-proton collisions, many different kinds of particles are produced whose characteristics are subsequently measured in a detector. These measurements can then be compared with predictions stemming from theoretical models of new physics. In the specific case of DM, since WIMPs are required to have such a small DM-nucleon scattering cross section, they would simply evade detection. Their non-detection would then show up as missing energy in the experiments, from which conclusions about the nature of the WIMPs can be made. So far, no sign of DM was found using collider experiments, which has in turn led to more stringent bounds for DM-nucleon cross sections.

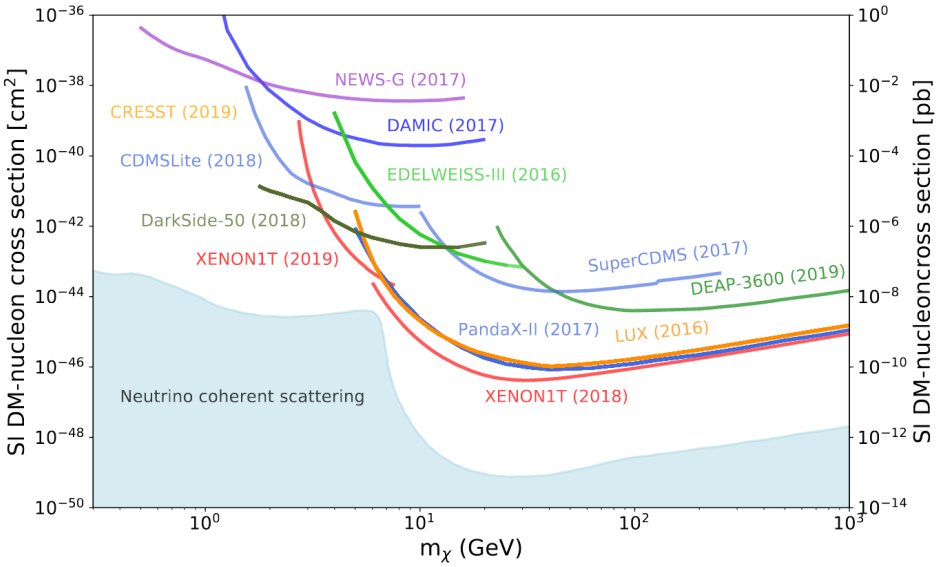

Figure 1.5: Upper limits for spin-independent (SI) DM-nucleon cross section as a function of the DM mass for a number of direct detection experiments. Plot extracted from [4].

1.3.2 Direct detection experiments

In direct detection experiments, DM elastically scatters off an atomic nucleus [39] (for reviews see [40,41]). If the WIMP-baryon interactions are efficient enough, this might lead to an easily identifiable signal in low-background underground experiments. Scatterings of DM particles off nuclei can be detected in three different ways:

1. Scintillating light is produced through excitation and later de-excitation of nuclei. Photons from DM-nucleus scattering can then for example be measured by using scintillating crystals. Experiments measuring scintillating light include DAMA/LIBRA [42], XENON1T [43] and PandaX-II [44].

2. DM-nucleus scattering can lead to an ionization of atoms in the target material. Such a charge (ionization) signal can be efficiently measured for example by low-temperature ultra-low background germanium detectors [45]. Experiments making use of ionized target material include CoGeNT [46], CDEX [47] and MALBEK [48].

3. DM-nucleus scattering can produce heat. Such phonon signals in crystal detectors can provide another important experimental signature in DM direct detection searches. This technique is particularly useful when looking for low mass DM due to a very good energy threshold. Experiments using crystal detectors include CDMS-II [49] and SuperCDMS [50].

Constraints on the DM-nucleon scattering cross section from various direct detection experiments are collected in Figure 1.5. One can see that direct detection experiments have severely constrained the GeV mass regime.

1.3.3 Indirect detection experiments

Indirect detection experiments look for SM particles that are produced in the DM annihilation process $\chi\chi \to$ SM SM. For more detailed reviews than the brief overview given

here on DM indirect detection, we refer to [51–53]. WIMPs are expected to annihilate at present leading to detectable annihilation products. A particularly appealing prospect is the measurement of a spectrum of gamma-rays. Since gamma-rays are not deflected on their journey from the emission point to detection on Earth, the direction of the source can be determined, allowing target regions of DM annihilation to be identified.

The spectrum of gamma-rays expected from DM annihilation depends on the particles produced in the final state. Typically one assumes that DM annihilates to SM particles, which must account for at least some fraction of the annihilations for a WIMP produced through thermal freeze-out. Gamma-ray emissions from DM annihilations can be of two types: a continuous spectrum generated by the decay, hadronization and final state radiation of the SM particles produced, and spectral features in the form a gamma-ray lines and internal bremsstrahlung. Of these possibilities it is especially interesting to investigate gamma-ray lines, which appear from the processes $\chi\chi \to \gamma\gamma$ and $\chi\chi \to \gamma Z$. Since DM has to be electrically neutral, these processes can only arise at the loop level but they are nearly impossible to mimic by astrophysical background [54], which would result in a very clean signal. We will also see later, that in the particular case we are considering one has to take into account certain effects that can alter the DM annihilation cross section by several orders of magnitude thus compensating for the loop level suppression. Lastly, another appealing feature from considering gamma-ray lines is that the measured photons would have an energy approximately equal to the DM particle's mass, $E_\gamma = m_\chi$, thus potentially providing very important information.

In order to detect gamma-rays from DM annihilation, there are two possibilities. Either one seeks to measure the photons directly, which is only possible via space telescopes, or one uses ground based telescopes to observe gamma-rays indirectly via the Cherenkov light produced by the showers of charged particles which are in turn created by the gamma-ray as it hits the atmosphere. Direct observations from space telescopes have been performed by EGRET [55] and by Fermi-LAT [56]. The most promising ground based telescopes are the Imaging Air Cherenkov Telescopes (IACTs). IACT experiments include MAGIC [57], VERITAS [58] and H.E.S.S. [59], while the next-generation telescope is going to be the currently planned CTA [60]. Figure 1.6 shows limits on the DM annihilation cross section from various indirect detection experiments including the projected constraints from the next-generation CTA.

Collider, direct detection and indirect detection searches so far have significantly constrained the WIMP cross section in the mass range up to the EW scale and negative results in this mass region motivate an exploration of the WIMP with multi-TeV masses. Indirect detection experiments are especially well suited for searching for multi-TeV WIMP DM and in particular the next-generation CTA experiment is expected to improve limits in this regime by one order of magnitude (see Figure 1.6). It is thus very important to investigate multi-TeV WIMP DM annihilation into photons and this thesis hence focuses on the computation of the cross section of heavy WIMPs which annihilate into an energetic photon (amongst other particles), that can then in turn be detected by earth based gamma-ray telescopes. A specific focus will lie on the next-generation CTA experiment.

1.4 Process of interest

As explained in Section 1.3, in this work we investigate photons which are produced through heavy WIMP annihilation. Naively this means the computation of the process $\chi^0\chi^0 \to \gamma\gamma$ (or γZ). However, since the annihilation takes place far from earth, gamma-ray telescopes do not measure the two photons (or photon and Z boson) in coincidence. The

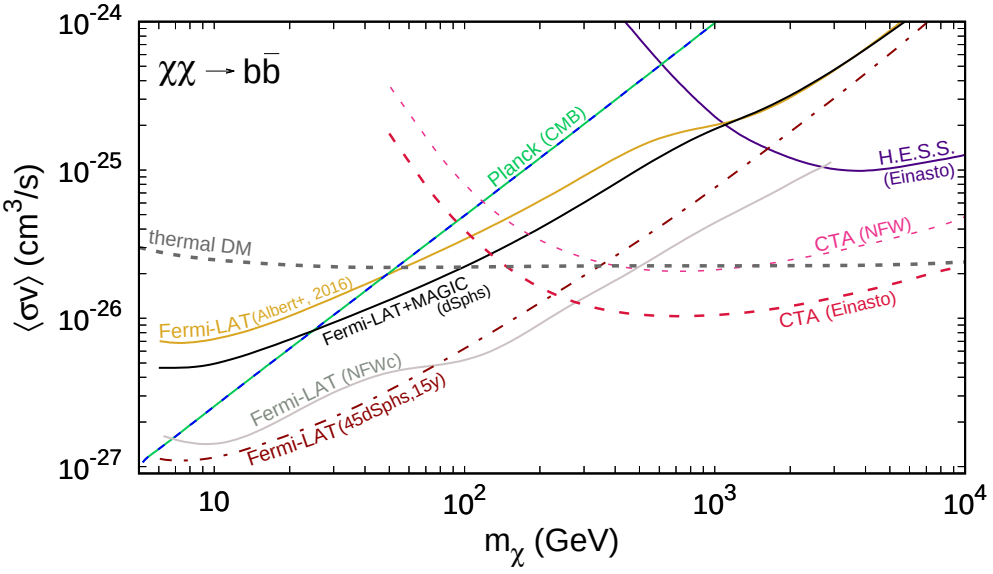

Figure 1.6: Limits on the annihilation cross section for the DM particles annihilating into a $b\bar{b}$ pair, from various indirect detection experiments. Plot extracted from [5].

correct observable is therefore the semi-inclusive single-photon energy spectrum $\gamma + X$, where X denotes the unidentified other final state particles.

The computation of the process $\chi^0\chi^0 \to \gamma + X$, for multi-TeV DM, is complicated by two effects, which, if done naively, would lead to a break down of the perturbative expansion in terms of the electroweak (EW) coupling. Firstly, one has to take into account the Sommerfeld effect, which is generated by the EW Yukawa force acting on the DM particles prior to their annihilation [61–64]. Secondly, for heavy DM annihilation into energetic particles, electroweak Sudakov (double) logarithms $\mathcal{O}((\alpha_2 \ln^2(m_\chi/m_W))^n)$ are large and need to be resummed to all order in the coupling constant [7–9, 65–69]. The treatment of the Sommerfeld effect is well known and in this work we hence mainly focus on the resummation of the large logarithmic corrections. Section 2 will give a more in-depth introduction to these effects and to the effective field theories that will be used for their treatment.

The resummation of the semi-inclusive spectrum is performed for the primary photon energy spectrum $d(\sigma v_{\rm rel})/dE_\gamma$ of the DM pair annihilation cross section multiplied by the relative velocity of the annihilating particles. While in forecasts for the rate observed by a specific telescope, the spectrum will have to be smeared with an instrument-specific resolution function of some width $E^\gamma_{\rm res}$ in energy, the expected impact and accuracy of the theoretical predictions can be equally discussed for the spectrum integrated over the energy interval $E^\gamma_{\rm res}$ from its kinematic endpoint:

$$\langle \sigma v \rangle (E^\gamma_{\rm res}) = \int_{m_\chi - E^\gamma_{\rm res}}^{m_\chi} dE_\gamma \frac{d(\sigma v)}{dE_\gamma} \,. \tag{1.8}$$

The endpoint-integrated spectrum depends on the three scale m_χ, m_W (representative for EW scale masses), and $E^\gamma_{\rm res}$. We consider TeV-scale DM and hence the hierarchy $m_W \ll m_\chi$ is always assumed. The details of the resummation of EW Sudakov logarithms near the endpoint, $E^\gamma_{\rm res} \ll m_\chi$, differ according to the scaling of $E^\gamma_{\rm res}$ and m_W with respect to each other. We distinguish the following three regimes:

$$\text{narrow:} \quad E^\gamma_{\rm res} \sim m_W^2/m_\chi \,,$$

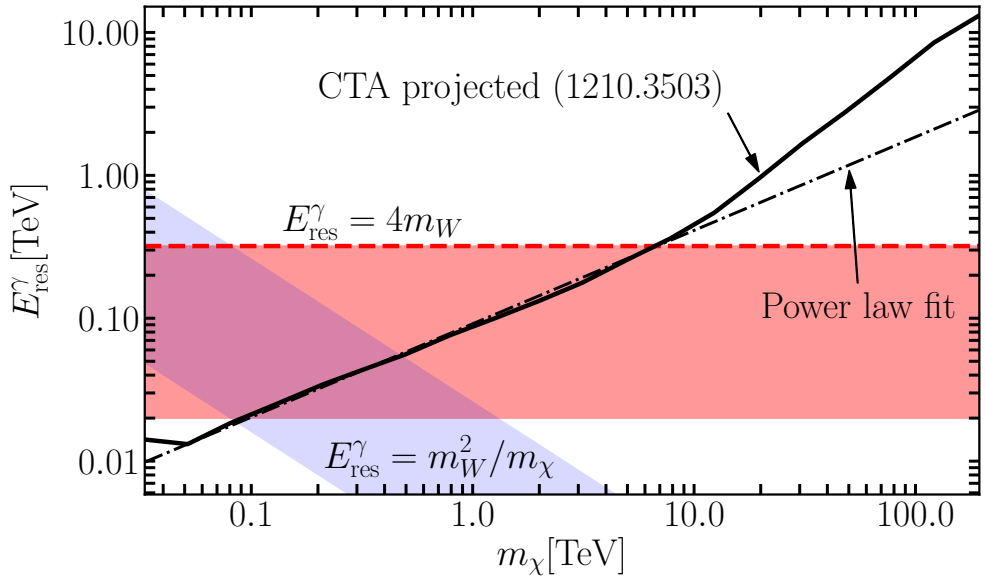

Figure 1.7: Energy resolution of the CTA experiment (solid black line from [6]), and the power-law fit $E^{\gamma}_{\rm res} = 0.0915(E_\gamma/\text{TeV})^{0.653}$ (dash-dotted) with $E_\gamma = m_\chi$. The dark-grey (red) and light-grey (blue) bands show where the intermediate and narrow resolution resummation applies, respectively. The boundaries are define by $m_W[1/4,\, 4]$ (intermediate resolution) and $m_W^2/m_\chi[1/4,\, 4]$ (narrow resolution). This Figure was extracted from [7].

$$\begin{aligned} \text{intermediate:} \quad & E^{\gamma}_{\rm res} \sim m_W\,, \\ \text{wide:} \quad & E^{\gamma}_{\rm res} \gg m_W\,. \end{aligned} \tag{1.9}$$

In Section 1.2, we established that the focus of this thesis lies on the two models of wino and Higgsino DM. In order for wino DM to have the correct relic abundance it is required to have a mass of around $m_\chi \sim 2-3$ TeV. Higgsino DM on the other hand has to have a mass of around $m_\chi \sim 1$ TeV, to give the correct relic density. Figure 1.7 shows the energy resolution of the CTA experiment as a function of the DM mass. One can clearly see that for the next-generation experiment, it will be most appropriate to consider the narrow and intermediate resolution regimes given the relevant masses for the wino and Higgsino DM models. This thesis thus focuses on the computation of the DM annihilation cross section for wino and Higgsino DM, assuming narrow and intermediate energy resolutions.

The outline of this thesis is as follows: in Section 2 we provide an introduction into the theoretical background and effective field theories required for the computation of the process of interest and give the relevant annihilation operators. In Section 3 we derive the factorization theorems for both DM models for both the narrow and intermediate energy resolution. In Section 4 we explain the concept resummation and in Section 5 we discuss the potential relevance of next-to-leading-power mass corrections. In Section 6, we give the results for most of the computations that were done to calculate the cross sections, in Section 7 we show the numerical results and plots of the photon energy spectra, while we conclude in Section 8. In a series of Appendices, we collect more technical details that are necessary for the computation of the cross sections, including the calculation of challenging integrals and explicit expressions of lengthy results. In Appendix A, we analytically expand the resummed wino DM results up to the two-loop order in order to gain a better understanding of the numerical results. This thesis is based on the publi-

cations [7–9], which were done in collaboration with Martin Beneke, Alessandro Broggio, Martin Vollmann and Kai Urban.

2 Effective field theories and annihilation operators

The coherent computation of the annihilation process $\chi^0\chi^0 \to \gamma + X$, requires the combination of several different effective field theories, which will be introduced in this Section. A diagrammatic representation of the annihilation process is shown in Figure 2.2. Prior to their annihilation, the non-relativistic DM particles can exchange EW bosons giving rise to the Sommerfeld effect. In Figure 2.2 this is represented by the dashed-line ladder rungs connecting the incoming WIMPs. The heavy WIMPs then annihilate into an energetic photon and an unobserved state of potentially multiple particles X. The Sommerfeld effect is described by a non-relativistic effective field theory which is introduced in Section 2.3.1, while the rest of the annihilation process is described by soft collinear effective theory (SCET) which is introduced in Section 2.3.2. Before going into the different effective field theories however, we use Section 2.1 to motivate important concepts using a computational example that will also be useful to introduce notation and subtleties that appear when using SCET.

2.1 Strategy of regions

Before going into the details of the effective field theories which are needed to compute the semi-inclusive annihilation process $\chi^0\chi^0 \to \gamma + X$, it is instructive to consider as an example a specific loop integral using the so-called *strategy of regions* [70]. This example will help to demonstrate the necessity of introducing different effective field theories and is going to unveil some technical difficulties which we will face during the computation of the annihilation cross section.

The strategy (or method) of regions is a technique which allows one to carry out asymptotic expansions of loop integrals in dimensional regularization around various limits. The expansion is obtained by splitting the integration into different momentum regions and appropriately expanding the integrand in each case. The general strategy to obtain the expansion of a given Feynman integral in a given kinematic limit is the following [71]:

1. Identify all momentum regions of the integrand which lead to singularities in the limit under consideration

2. Expand the integrand in each region and integrate each expansion over the full phase space

3. Add the result of the integrations over the different regions to obtain the expansion of the original full integral

To illustrate the strategy of regions, we are going to calculate the diagram depicted in Figure 2.1, in dimensional regularization. Incoming DM states have masses m_χ, outgoing gauge bosons are massless and gauge bosons in the loop have a mass of m_W. We thus have $(p_1 + p_2)^2 = (p_3 + p_4)^2 = 4m_\chi^2$. For simplicity, we will neglect the Dirac structure

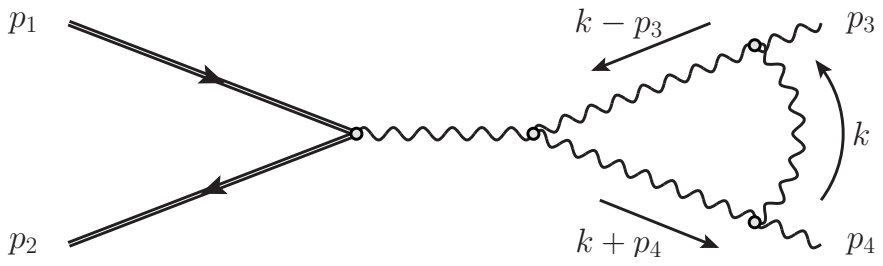

Figure 2.1: One-loop vertex correction. Incoming DM states have masses m_χ, outgoing gauge bosons are massless and gauge bosons in the loop have a mass of m_W.

and focus on the scalar integral, since this does not change the analysis. The full integral in $d = 4 - 2\epsilon$ space-time dimensions is given by

$$\begin{aligned} I_f &= \int [dk] \frac{1}{(k^2 - m_W^2 + i0)((k-p_3)^2 - m_W^2 + i0)((k+p_4)^2 - m_W^2 + i0)} \\ &= \frac{i}{16\pi^2} \frac{1}{8m_\chi^2} \ln^2 \left(\frac{m_W^2 - 2m_\chi^2 + 2m_\chi \sqrt{m_\chi^2 - m_W^2}}{m_W^2} \right) , \end{aligned} \tag{2.1}$$

where

$$[dk] = \tilde{\mu}^{2\epsilon} \frac{d^d k}{(2\pi)^d} = \left(\frac{\mu^2 e^{\gamma_E}}{4\pi} \right)^\epsilon \frac{d^d k}{(2\pi)^d} . \tag{2.2}$$

Before getting into the details of the method of regions analysis, we need to introduce some notation which will also be needed when discussing the effective field theories later on. We choose a reference frame in which the outgoing gauge bosons are moving back-to-back along the z-axis, for which we define two light-like reference vectors

$$n_+^\mu = (1, 0, 0, -1) , \quad n_-^\mu = (1, 0, 0, 1) , \tag{2.3}$$

which means that

$$p_3^\mu = m_\chi n_-^\mu , \quad p_4^\mu = m_\chi n_+^\mu . \tag{2.4}$$

The light-like reference vectors obey $n_+^2 = n_-^2 = 0$ and $n_+ \cdot n_- = 2$. We refer to the direction n_- as "collinear" and to the direction n_+ as "anti-collinear". Any Lorentz vector can now be decomposed into components proportional to n_+, n_- and a remainder perpendicular to both

$$p^\mu = (n_- \cdot p) \frac{n_+^\mu}{2} + (n_+ \cdot p) \frac{n_-^\mu}{2} + p_\perp^\mu \equiv p_+^\mu + p_-^\mu + p_\perp^\mu . \tag{2.5}$$

The expansion of vectors into their light-cone components will prove useful since, in general, different components will scale differently. The precise meaning of this is explained below. Using the properties of the reference vectors n_+ and n_-, it is easy to see that the square of the vector p is given by

$$p^2 = (n_+ \cdot p)(n_- \cdot p) + p_\perp^2 , \tag{2.6}$$

while the scalar product of two Lorentz vectors p and q is

$$p \cdot q = p_+ \cdot q_- + p_- \cdot q_+ + p_\perp \cdot q_\perp . \tag{2.7}$$

For discussing the scaling of the different components of a vector, it will be useful to write it as

$$p^\mu = (p_+, p_-, p_\perp)\,. \tag{2.8}$$

Equipped with the notation we just introduced, we can now separate the diagram in Figure 2.1 into different momentum regions. For this we first introduce the small expansion parameter $\lambda = m_W/m_\chi \ll 1$. The scaling of the different components of a vector will be written as $p^\mu \sim m_\chi(\lambda^a, \lambda^b, \lambda^c)$. The components of p_3 and p_4 for example scale as

$$p_3^\mu \sim m_\chi(1, \lambda^2, \lambda)\,, \quad \text{and} \quad p_4^\mu \sim m_\chi(\lambda^2, 1, \lambda)\,. \tag{2.9}$$

To expand I_f in λ, we need to introduce momentum regions for the loop momentum k^μ with the following scalings

$$\begin{aligned} \text{hard } (h): &\quad k^\mu \sim m_\chi(1,1,1)\,,\\ \text{collinear } (c): &\quad k^\mu \sim m_\chi(1,\lambda^2,\lambda)\,,\\ \text{anti-collinear } (\bar{c}): &\quad k^\mu \sim m_\chi(\lambda^2,1,\lambda)\,,\\ \text{soft } (s): &\quad k^\mu \sim m_\chi(\lambda,\lambda,\lambda)\,. \end{aligned} \tag{2.10}$$

All other possible scalings of the integration momentum $k^\mu \sim m_\chi(\lambda^a, \lambda^b, \lambda^c)$, with a, b, c not matching one of the regions listed above, give rise to scaleless integrals after the expansion in λ and therefore vanish in dimensional regularization. To expand the full integral (2.1) to leading order in λ in each of the regions given in (2.10), we analyse the scaling of each term in each operator and only keep the leading ones.

Before moving on to the computation of the integral in the different momentum regions, we need to comment on a complication which arises when the different momentum regions are not well defined unless one introduces additional regulators on top of dimensional regularization. This problem is referred to as *Collinear Anomaly* in [72] and appears for example in processes with high momentum transfers and small but non negligible masses, such as in the resummation of electroweak Sudakov logarithms [73, 74]. The additional regulator we chose to use is the rapidity regulator introduced in [75, 76]. More details on this regulator are given in Appendix F.

Hard In the hard momentum region, the loop momentum scales as $k^\mu \sim m_\chi(1,1,1)$ and the expansion of the propagators in I_f is given by

$$\begin{aligned} \underbrace{k^2}_{\mathcal{O}(1)} - \underbrace{m_W^2}_{\mathcal{O}(\lambda^2)} =& k^2 + \mathcal{O}(\lambda^2)\\ (k-p_3)^2 - m_W^2 =& \underbrace{k^2}_{\mathcal{O}(1)} - 2(\underbrace{k_+ \cdot p_{3,-}}_{\mathcal{O}(\lambda^2)} + \underbrace{k_- \cdot p_{3,+}}_{\mathcal{O}(1)} + \underbrace{k_\perp \cdot p_{3,\perp}}_{\mathcal{O}(\lambda)}) - \underbrace{m_W^2}_{\mathcal{O}(\lambda^2)}\\ =& k^2 - 2k_- \cdot p_{3,+} + \mathcal{O}(\lambda)\\ (k+p_4)^2 - m_W^2 =& \underbrace{k^2}_{\mathcal{O}(1)} + 2(\underbrace{k_+ \cdot p_{4,-}}_{\mathcal{O}(1)} + \underbrace{k_- \cdot p_{4,+}}_{\mathcal{O}(\lambda^2)} + \underbrace{k_\perp \cdot p_{4,\perp}}_{\mathcal{O}(\lambda)}) - \underbrace{m_W^2}_{\mathcal{O}(\lambda^2)}\\ =& k^2 + 2k_+ \cdot p_{4,-} + \mathcal{O}(\lambda)\,. \end{aligned} \tag{2.11}$$

The hard region integral at leading power in λ is thus given by

$$I_h = \int [dk] \frac{1}{(k^2 + i0)(k^2 - 2k_- \cdot p_{3,+} + i0)(k^2 + 2k_+ \cdot p_{4,-} + i0)}$$

$$=\frac{i}{16\pi^2}\frac{1}{8m_\chi^2}\left[\frac{2}{\epsilon^2}+\frac{1}{\epsilon}\left(2i\pi+4\ln\frac{\mu}{2m_\chi}\right)-\frac{7\pi^2}{6}+4i\pi\ln\frac{\mu}{2m_\chi}+4\ln^2\frac{\mu}{2m_\chi}\right] \tag{2.12}$$

As one can see, there was no need to introduce an additional regulator for the computation of the hard region integral. Since $p_3^2=p_4^2=0$, one can trivially complete the squares in the propagators appearing in (2.12) which turns I_h into a standard Feynman integral.

Collinear The collinear loop momentum scales as $k^\mu\sim m_\chi(1,\lambda^2,\lambda)$. Performing a similar scale analysis as in (2.11), but now with the collinear scaling for the loop momentum, gives the following collinear region integral

$$\begin{aligned}I_c&=\int[dk]\frac{\nu^\eta}{(k^2-m_W^2+i0)(-2k_-\cdot p_{3,+}+i0)((k+p_4)^2-m_W^2+i0)|n_+k|^\eta}\\&=\frac{i}{16\pi^2}\frac{1}{8m_\chi^2}\left[-\frac{2}{\epsilon\eta}-\frac{2}{\epsilon}\ln\frac{\nu}{2m_\chi}+\frac{4}{\eta}\ln\frac{m_W}{\mu}+4\ln\frac{m_W}{\mu}\ln\frac{\nu}{2m_\chi}\right].\end{aligned} \tag{2.13}$$

The term $\nu^\eta/|n_+k|^\eta$ in the first line of (2.13) is introduced by the additional regulator. Specifically, η is the rapidity regulator and ν is the scale associated to the regulator (similar to the scale μ for dimensional regularization). As can be seen from (2.13), I_c has poles from both regulators.

Anti-collinear The anti-collinear loop momentum scales as $k^\mu\sim m_\chi(\lambda^2,1,\lambda)$. It can easily be checked, that the collinear and anti-collinear momentum region give the same contribution, such that

$$\begin{aligned}I_{\bar c}&=\int[dk]\frac{\nu^\eta}{(k^2-m_W^2+i0)((k-p_3)^2-m_W^2+i0)(2k_+\cdot p_{3,-}+i0)|n_-k|^\eta}\\&=\frac{i}{16\pi^2}\frac{1}{8m_\chi^2}\left[-\frac{2}{\epsilon\eta}-\frac{2}{\epsilon}\ln\frac{\nu}{2m_\chi}+\frac{4}{\eta}\ln\frac{m_W}{\mu}+4\ln\frac{m_W}{\mu}\ln\frac{\nu}{2m_\chi}\right].\end{aligned} \tag{2.14}$$

Again, the term $\nu^\eta/|n_-k|^\eta$ in the first line of (2.14) is associated with the rapidity regulator.

Soft The loop momentum scales as $k^\mu\sim m_\chi(\lambda,\lambda,\lambda)$. The soft momentum region integral is given by

$$\begin{aligned}I_s&=\int[dk]\frac{\nu^\eta}{(k^2-m_W^2+i0)(-2k_-\cdot p_{3,+}+i0)((k+p_4)^2-m_W^2+i0)|2k^3|^\eta}\\&=\frac{i}{16\pi^2}\frac{1}{8m_\chi^2}\left[-\frac{2}{\epsilon^2}+\frac{4}{\epsilon\eta}+\frac{1}{\epsilon}\left(-2i\pi+4\ln\frac{m_W}{\mu}-4+4\ln\frac{m_W}{\nu}\right)\right.\\&\quad\left.-\frac{8}{\eta}\ln\frac{m_W}{\mu}+\frac{\pi^2}{6}+4i\pi\ln\frac{m_W}{\mu}+8\ln\frac{m_W}{\mu}\ln\frac{m_W}{\nu}-4\ln^2\frac{m_W}{\mu}\right].\end{aligned} \tag{2.15}$$

Like I_c and $I_{\bar c}$, also the soft integral I_s requires the rapidity regulator for its computation, which introduces $\nu^\eta/|2k^3|^\eta$ in the first line of (2.15). By comparing the rapidity regulator terms in (2.13), (2.14) and (2.15) one can see that the specific form depends on the scaling of the loop momentum. We refer to Appendix F for a more detailed explanation.

Now that we have computed the full integral expanded in the hard, the (anti-) collinear and the soft region, we can to sum over the results from the different momentum regions

to find

$$I_h + I_c + I_{\bar{c}} + I_s = \frac{i}{16\pi^2}\frac{1}{8m_\chi^2}\left[4\ln^2\frac{m_W}{2m_\chi} + 4i\pi\ln\frac{m_W}{2m_\chi} - \pi^2\right]. \tag{2.16}$$

It is straightforward to check that this is indeed equivalent to the original integral I_f, when expanding the second line in (2.1) to leading power in λ. The computation of I_f using the method of regions served the purpose to introduce relevant notation and to exemplify how a computation can be separated according to the momentum scales involved. Looking at (2.16), one notices the appearance of the aforementioned Sudakov (double) logarithms $\alpha_2 \ln^2(m_W/2m_\chi)$. Since we are considering multi-TeV DM, $m_W \ll m_\chi$ and Sudakov logarithms are $\mathcal{O}(1)$ corrections and a naive computation leads to the breakdown of the perturbative expansion in the coupling constant. While the method of regions allows for an expansion at the integrand level, we can use SCET, see Section 2.3.2, to achieve the same separation of momentum modes at the Lagrangian level. This will ultimately result in the resummation of the large Sudakov double logarithms to all orders and will enable us to calculate reliable results. Lastly, we also introduced the concept of rapidity divergences, which will continue to appear throughout this thesis.

2.2 Relevant momentum modes

We are now going to discuss which momentum modes are needed to describe the process $\chi^0\chi^0 \to \gamma + X$. This is similar to (2.10) from the previous Section, only now the modes will be used to factorize the problem at the Lagrangian level. The operators which describe the annihilation process of interest need to have the following properties: the operator contains two incoming DM particles that annihilate at a single point and two outgoing gauge boson fields, which generate final state particles at said annihilation point. The gauge boson fields lie along opposite light-like directions, for which we will use the reference vectors defined in (2.3). This means that one outgoing gauge boson will travel along the collinear direction n_-^μ and which will generate the unobserved jet X, while the other one travels along the anti-collinear direction n_+^μ and will be identified with the observed photon. The observed photon has a momentum of $p_\gamma^\mu = E_\gamma n_+$ and the unobserved state X has a small invariant mass of $m_X = \sqrt{4m_\chi E_{\text{res}}^\gamma}$.

In the previous Section we have seen at the integrand level how a process can be split up according to different momentum modes. To do this at the Lagrangian level, we need to identify all relevant momentum modes that contribute to $\chi^0\chi^0 \to \gamma + X$ for both the narrow and intermediate energy resolution regimes. Note that the modes depend on E_{res}^γ, but are insensitive to the type of particle. Assuming an intermediate energy resolution $E_{\text{res}}^\gamma \sim m_W$ and using the same power counting parameter as in the previous Section $\lambda = m_W/m_\chi$ we find the following momentum modes to be relevant

$$\begin{aligned}
\text{hard}\,(h): &\quad k^\mu \sim m_\chi(1,1,1)\\
\text{hard-collinear}\,(hc): &\quad k^\mu \sim m_\chi(1,\lambda,\sqrt{\lambda})\\
\text{collinear}\,(c): &\quad k^\mu \sim m_\chi(1,\lambda^2,\lambda)\\
\text{anti-collinear}\,(\bar{c}): &\quad k^\mu \sim m_\chi(\lambda^2,1,\lambda)\\
\text{soft}\,(s): &\quad k^\mu \sim m_\chi(\lambda,\lambda,\lambda)\\
\text{potential}\,(p): &\quad k^0 \sim m_W^2/m_\chi,\ \mathbf{k} \sim m_W\\
\text{ultrasoft}\,(us): &\quad k^\mu \sim m_\chi(\lambda^2,\lambda^2,\lambda^2)
\end{aligned} \tag{2.17}$$

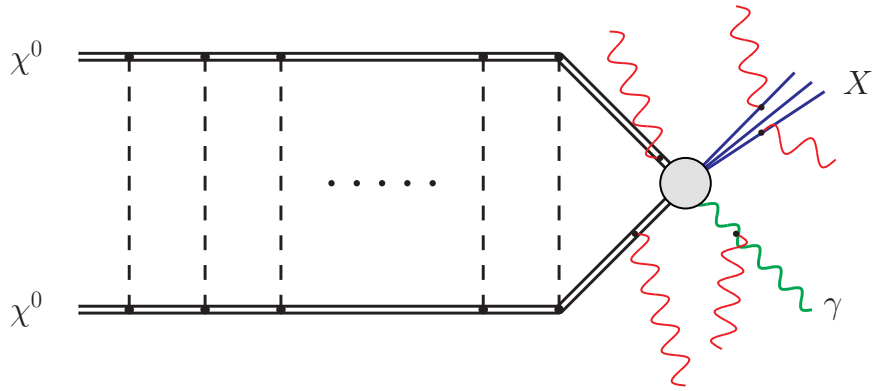

Figure 2.2: Diagrammatic representation of annihilation process of interest.

The hard mode describes the hard annihilation process of the DM particles, the (hard-) collinear modes describe the unobserved final state X, the anti-collinear mode describes the observed photon, the soft mode describes soft radiation coming from initial/final state external particles and the potential and ultrasoft modes describe the exchange of EW bosons between the WIMPs prior to annihilation. The hard modes will be integrated out into matching coefficients (see Section 6.1 for a detailed discussion of the matching procedure). Hard-collinear, (anti-) collinear and soft modes are still dynamical and are described by SCET and potential and ultrasoft modes are described by a non-relativistic effective theory.

In the narrow resolution case, we assume the $E^\gamma_{\text{res}} \sim m_W^2/m_\chi$, which implies $m_X \sim m_W$ and the scale hierarchy $E^\gamma_{\text{res}} \ll m_W, m_X \ll m_\chi$. In the narrow resolution case, there is thus no hard-collinear momentum mode. Also, the narrow energy resolution does not allow for soft EW gauge boson radiation into the final state, which has implications for the structure of the soft function that describes the soft momentum modes. This will be explained in more detail in Section 3. On the other hand, the effective theory for the wide resolution case [69, 77] requires a yet more numerous set of modes to account for the independent scales E^γ_{res} and m_W. This set collapses to (2.17) when E^γ_{res} is set parametrically to m_W.

At leading power in the power counting parameter λ, the DM particles annihilate into two energetic final-state particles since any additional (anti-) collinear field included in the operator would mean a suppression by at least one power in λ. This is caused by the scaling of the gauge fields in the effective Lagrangian (see Section 2.3.2). The aim of this thesis is to sum logarithms of m_W/m_χ to leading order in λ. As was done in all previous works about the resummation of EW Sudakov logarithms in DM annihilation, power-suppressed effects in λ are systematically neglected. In Section 5, we are going to present a quantitative analysis as to why a leading order treatment is justified for both wino and Higgsino DM.

2.3 Effective field theories

We are now in a position to introduce the EFTs that are required for the computation of the annihilation process $\chi^0\chi^0 \to \gamma + X$. If an observable describes a process in a certain energy region, in general one can then integrate out degrees of freedom associated with other energy regions. The result is in an EFT containing only the degrees of freedom relevant for the computation of the observable of interest. This is the basic idea behind

EFTs. An observable can be computed using either the full theory or the EFT, both ways give the same physical results as far as that particular observable or energy region is concerned, but calculations are much simpler with the EFT. This is why we introduce different EFTs for different parts of the annihilation process.

2.3.1 Non-relativistic effective theory

In the present day Universe multi-TeV WIMPs move with non-relativistic velocities $v \sim 10^{-3}$. Prior to their annihilation, they may exchange electroweak bosons depicted diagrammatically by the dashed lines between the incoming DM particles in Figure 2.2. Each exchanged gauge boson contributes a factor of $g^2 m_\chi / m_W$, which means that additional exchanges are not suppressed by the EW coupling if $m_\chi \gg m_W$, which is the case here. This means that we need to resum the ladder rungs to all orders in g^2 to calculate the cross section. These radiative corrections give rise to the Sommerfeld effect, which arises when an attractive interaction between the non-relativistic DM particles significantly distorts their wave function, such that they have a larger probability to undergo annihilation. We will see that the Sommerfeld effect gives rise to corrections that may exceed the lowest-order cross section by orders of magnitude. It is thus vital to correctly account for this effect. Since the Sommerfeld effect is not the main focus of this work however, the introduction into the theoretical background is kept somewhat brief and focuses on points relevant for the remainder of this thesis. For a more in depth introduction into this topic and especially into the technical details, we refer to [78].

The appropriate EFT for describing the Sommerfeld effect and separating it from the remainder of the annihilation process is a non-relativistic DM (NRDM) EFT [78, 79]. Similar to the approach of NRQCD to the annihilation of quarkonium [80], the NRDM EFT is designed to describe the dynamics of two heavy DM particles at energy scales (in the center-of-mass frame) much smaller than their masses. At these energies, further pairs of DM particles cannot be created so it is sufficient to use two-component Pauli spinors for the initial state DM particles. The NRDM EFT is obtained by integrating out the hard modes that scale as m_χ. The leading-order Lagrangian that describes DM interactions at energies below m_χ but above m_W is given by

$$\mathcal{L}_{\text{NRDM}} = \chi_v^\dagger(x) \left(iD^0 + \frac{\mathbf{D}^2}{2m_\chi} \right) \chi_v(x) \,, \tag{2.18}$$

where $D_\mu = \partial_\mu - ig_2 A_\mu^C T^C + ig_1 Y B_\mu$ is the $\mathrm{SU}(2) \otimes \mathrm{U}(1)_Y$ covariant derivative. Remember that $Y = 0$ and $Y = 1/2$ in the cases of wino and Higgsino DM, respectively. In principle, (2.18) can be extended to include power corrections but since we content ourselves with a leading-order treatment of the Sommerfeld effect, this is not necessary. See [81] for the NLO computation of the Sommerfeld effect for wino DM.

After integrating out the hard modes, the remaining dynamical degrees of freedom in the NRDM EFT are soft, potential and ultrasoft. Remember that we only want to keep the degrees of freedom in our EFT which are relevant for the observable we calculate. This means that the soft modes can also be integrated out. Together with the potential modes of the light particles, they generate instantaneous but spatially non-local interactions between the DM fields, i.e. DM potentials. Finally, we are left with a theory that describes the potential modes of the DM fields and the ultrasoft modes of the light fields, which is called potential NRDM (pNRDM) EFT and the corresponding Lagrangian at leading-power is

given by [79]

$$\begin{aligned}\mathcal{L}_{\text{pNRDM}} &= \sum_i \chi_{vi}^\dagger(x)\left(iD^0(t,\mathbf{0}) - \delta m_i + \frac{\boldsymbol{\partial}^2}{2m_\chi}\right)\chi_{vi}(x) \\ &\quad - \sum_{\{i,j\},\{k,l\}} \int d^3\mathbf{r}\, V_{\{ij\}\{kl\}}(r)\, \chi_{vk}^\dagger(t,\mathbf{x})\chi_{vl}^\dagger(t,\mathbf{x}+\mathbf{r})\chi_{vi}(t,\mathbf{x})\chi_{vj}(t,\mathbf{x}+\mathbf{r})\,.\end{aligned} \tag{2.19}$$

The last term in $\mathcal{L}_{\text{pNRDM}}$ summarizes the instantaneous but spatially non-local interactions between the non-relativistic two-particle states that arise through the exchange of SM gauge and Higgs bosons. In order to highlight this non-locality of the potential interaction, we included the space-time arguments in (2.19). Note also that the ultrasoft gauge field in the covariant derivative is multipole-expanded around $\mathbf{x} = 0$. The ultrasoft light fields, which have momentum $k \sim m_\chi\lambda^2 \sim m_W^2/m_\chi$, can only exist for fields with masses much smaller than m_W, the covariant derivative appearing in (2.19) is understood to be the one with respect to the unbroken electromagnetic symmetry. After integrating out soft modes, the EW gauge bosons no longer appear as dynamical fields in pNRDM EFT.

The potential $V_{\{ij\}\{kl\}}$ in (2.19) is the matching coefficient when integrating out soft modes and moving from NRDM to pNRDM EFT. During the matching procedure, the masses of the EW gauge bosons, of the top quark and of the Higgs boson cannot be neglected, since the soft modes of the light particles have a virtuality of order m_W^2. As a result, $V_{\{ij\}\{kl\}}$ will depend on these masses and will feature potentials of the following types: the Yukawa potential from EW gauge bosons and the Higgs boson and the Coulomb potential from photons. After EWSB, the components of the isospin-j DM multiplet acquire slightly different masses. In general, the charged components will be somewhat heavier than the neutral (DM) particle, due to radiative corrections. This can be seen in (2.19) by the term $\delta m_i = m_i - m_{\chi^0} \geq 0$, which gives the mass difference between the lightest neutral particle of the multiplet and the remaining heavier components. Here, m_i is the mass of the eigenstate labeled by i. The heavy fields of the additional multiplet in (2.19) are expressed in terms of mass eigenstate fields χ_{vi} and not in terms of the gauge eigenstate fields χ_{va}, since computations using $\mathcal{L}_{\text{pNRDM}}$ are carried out in EW broken theory. Since the wino and Higgsino DM models have different particle contents, the notation in (2.19) was chosen to allow for a more concise documentation. The explicit form of the terms in (2.19) is generated by replacing the generic fields χ_{vi} with the field symbols ξ, η, ζ which represent the particle species χ^0, χ^+, χ^-, respectively, for wino DM and with the field symbols η^0, ζ^0, η, ζ which represent the particle species χ_1^0, χ_2^0, χ^+, χ^-, respectively, for Higgsino DM.

In Figure 2.3 a representative diagram responsible for the Sommerfeld effect is shown. Additionally, three soft gauge boson emissions are included: one subgraph where the soft momentum does not run through the annihilation vertex (shown in blue), one subgraph with a real soft gauge boson emission (shown in green) and one subgraph where the soft momentum does run through the annihilation vertex (shown in red). The blue emission would constitute a correction to the leading order potential. These types of emissions will thus not be considered here. The wino potential was computed at NLO in [81]. If one of the DM particles would emit a soft gauge boson into the final state (green) it would throw the DM particle off-shell. This would remove the enhancement coming from the ladder rungs after the real soft emission and such emissions can thus only happen between the last gaube boson exchange and the annihilation vertex. If the soft momentum does run through the annihilation vertex however (red line), the propagator of the heavy field between the soft emission and the annihilation vertex is of the eikonal type and comes

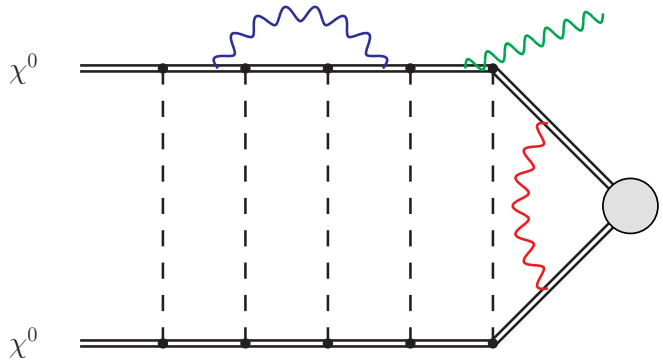

Figure 2.3: Example diagram contributing to the Sommerfeld effect. The blue and the red wavy lines represent soft gauge boson emissions.

from a Wilson line. The heavy field propagators to the left of the (red) soft emission are non-relativistic. In order to remove these soft interactions, we define the field redefinition

$$\chi_{va}(x) = Y_{v,ab}(x_0)\chi^{(0)}_{vb}(x)\,, \tag{2.20}$$

where the soft Wilson line $Y_v(x)$ is defined as the path-ordered exponential

$$Y_v(x) = \mathrm{P}\exp\left[ig_2\int_{-\infty}^{0} dt\, v\cdot A^C_s(x+vt)\,T^C - ig_1 Y\int_{-\infty}^{0} dt\, v\cdot B_s(x+vt)\right]\,, \tag{2.21}$$

with T^C the SU(2) generators in the spin-j representation and $v^\mu = (n_+ + n_-)/2 = (1,\mathbf{0})$. In the case of wino DM, the hypercharge is set to zero $Y = 0$. The Wilson lines $Y_v(x)$ fully capture the coupling of soft EW gauge bosons to the DM field, which means that the soft gauge bosons are decoupled from $\mathcal{L}_{\mathrm{PNRDM}}$ in (2.19).

After having decoupled soft interaction using (2.20), we can now use pNRDM EFT to compute the Sommerfeld effect. To do so, it is convenient to introduce some notation and exchange the indices ij and kl in (2.19), which denote the individual heavy field states, for two-particle state indices $I = \{ij\}$ and $J = \{kl\}$. The heavy field indices take the values 0, +, − for wino DM and 0_1, 0_2, +, − for Higgsino DM. The two-particle indices I and J take on all possible combinations of two heavy field indices. The two-particle states are related to the product of two single heavy fields by

$$\chi^{c\dagger}_{va}\chi_{vb} = K_{ab,I}[\chi^{c\dagger}_v\chi_v]_I\,. \tag{2.22}$$

Since we are only interested in neutral two-particle states, the relevant matrix elements are limited. Specifically, for wino DM, the relevant K-matrix elements are

$$K^{\mathrm{wino}}_{33,(00)} = 1\,, K^{\mathrm{wino}}_{11,(+-)} = \frac{1}{2}\,, K^{\mathrm{wino}}_{12,(+-)} = -\frac{i}{2}\,, K^{\mathrm{wino}}_{21,(+-)} = \frac{i}{2}\,, K^{\mathrm{wino}}_{22,(+-)} = \frac{1}{2} \tag{2.23}$$

while for Higgsino DM, we need

$$K^{\mathrm{Higgs.}}_{11,(11)} = K^{\mathrm{Higgs.}}_{11,(22)} = \frac{1}{2}\,, \quad \text{and} \quad K^{\mathrm{Higgs.}}_{22,(+-)} = 1\,, \tag{2.24}$$

It suffices to focus here on the charge-0 sector of the two-particle states for the calculation of the Sommerfeld factor. The full expressions for the K-matrices for both wino and Higgsino DM have been collected in Appendix C.

In the following, we are going to outline how the Sommerfeld factor is extracted from the squared T-matrix element that appears in the definition of the cross section (see Section 3). The non-relativistic part of the annihilation process is encoded in the expression

$$\chi^{\dagger}_{ve_4}\Gamma\chi^{c}_{ve_3}\,\chi^{c\dagger}_{ve_2}\Gamma\chi_{ve_1}\,. \tag{2.25}$$

The specific shape of the spin matrix Γ, which acts on the spinor indices of χ_v, will be derived in Section 2.4. Since the potential $V_{\{ij\}\{kl\}}(r)$ does not change the total spin of the incoming two-particle state before annihilation, the two Γ-matrices in (2.25) can be assumed to be of the same type. In [78], a detailed derivation of an NRDM EFT matrix element for arbitrary operators is provided. In our case, assuming an incoming DM state $\chi_i\chi_j$ with relative velocity v_{rel} between χ_i and χ_j, orbital quantum number $L = 0$ (S-wave) and total spin S, the matrix element can be written as

$$\begin{aligned}&\langle\chi_i\chi_j|\,\chi^{\dagger}_{ve_4}\Gamma\chi^{c}_{ve_3}\,\chi^{c\dagger}_{ve_2}\Gamma\chi_{ve_1}\,|\chi_i\chi_j\rangle = \langle\chi_i\chi_j|\,\chi^{\dagger}_{ve_4}\Gamma\chi^{c}_{ve_3}|0\rangle\,\langle 0|\chi^{c\dagger}_{ve_2}\Gamma\chi_{ve_1}\,|\chi_i\chi_j\rangle\\ &= \Big[\,\langle\xi^{c\dagger}_j\Gamma\xi_i\rangle\left(\psi^{(0,S)}_{e_4e_3,\,ij} + (-1)^S\psi^{(0,S)}_{e_3e_4,\,ij}\right)\Big]^{*}\langle\xi^{c\dagger}_j\Gamma\xi_i\rangle\left(\psi^{(0,S)}_{e_1e_2,\,ij} + (-1)^S\psi^{(0,S)}_{e_2e_1,\,ij}\right),\end{aligned} \tag{2.26}$$

where $\psi^{(L,S)}_{e_1e_2,\,ij}$ is the $\chi_{e_1}\chi_{e_2}$-component of the scattering wave function for the incoming $\chi_i\chi_j$ state, evaluated for zero relative distance and normalized to the free scattering solution, that is $\psi^{(L,S)}_{e_ae_b,\,ij} \to \delta_{e_ai}\,\delta_{e_bj}$ in the absence of interactions. The symbol $\langle ...\rangle$ denotes the spin sum and ξ_i, ξ_j represent the Pauli spinors of the incoming particles χ_i, χ_j. The multi-component wave function $\psi^{(L,S)}_{e_2e_1,ij}$ accounts for the potential interactions of the incoming $\chi_i\chi_j$-state with all possible intermediate two-body states e_2e_1. Since we only consider leading-order potential interactions, the intermediate e_2e_1-states need to have the same spin and orbital angular momentum as the ij-state, as well as the same charge. For a given operator $\chi^{c\dagger}_{e_2}\chi_{e_1}$ with quantum numbers L and S, we need to take into account both wave-function components e_1e_2 and e_2e_1, where the latter is accompanied by a relative sign $(-1)^{L+S}$. Above, we defined $\psi^{(L,S)}_{e_1e_2,\,ij}$ which we can relate to the coordinate-space scattering wave-function $[\psi_E(\mathbf{r})]_{I,ij}$ at the origin as follows

$$\psi^{(0,S)}_{e_1e_2,\,ij} = [\psi_E(0)]^{*}_{e_1e_2,\,ij}\,. \tag{2.27}$$

This is necessary, since the scattering wave-function in coordinate space can be directly obtained from the Schrödinger equation

$$\left(\left[-\frac{\boldsymbol{\nabla}^2}{2\mu_I} - E\right]\delta_{IK} + V_{IK}(r)\right)[\psi_E(\mathbf{r}\,)]_{K,ij} = 0\,. \tag{2.28}$$

The potential in (2.28) DM model specific and is sensitive to the mass splitting between the neutral and charged particles of the DM multiplet. Specifically, it includes the mass splitting between the mass M_I of the two-particle state I and the mass of the $\chi^0\chi^0$ state via $V_{IK} \to V_{IK} + \delta_{IK}(M_I - 2m_\chi)$. The parameter μ_I refers to the reduced mass of the two-particle state I and since we are only interested in the Sommerfeld effect at leading order, we can set $\mu_I = m_\chi/2$. E denotes the energy and can be fixed using the relative velocity of the initial state. Lastly, the indices ij serve as a reminder to solve (2.28) under the assumption that ij the initial two-particle state. The derivation of the solution to (2.28) is beyond the scope of this thesis and we refer to [78] for further details and the specific methods that are used.

We can now use the coordinate-space scattering wave-functions to define the Sommerfeld factor as follows

$$S_{IJ} = \left[\psi^{(0,S)}_{J,\,00}\right]^{*}\psi^{(0,S)}_{I,\,00}\,. \tag{2.29}$$

For both DM models, the initial state is assumed to be the one consisting of neutral particles $I = 00$. Other two-particle states are only virtual and may appear after an exchange of for example an EW gauge boson. We may focus on the charge-0 sector when solving (2.28), since the potential is block-diagonal, which in turn is caused by electric charge conservation. In the charge-0 sector, the two-particle indices can take the values $I, J = 00, +-, -+$, which however leads to a certain redundancy in the description since the fermion bilinear for the states $+-$ and $-+$ is identical, up to a possible sign. When the number of two-particle states is reduced to non-identical ones, in [78] this is referred to as method-2 while the more redundant one, that includes all two-particle states, is called method-1. Since it is more customary, we will use method-2 in this thesis. This will introduce certain symmetry factors in the potentials (see Appendix B for the Higgsino DM potential and [78] for the wino DM potential) and the cross section (see Section 3).

Up to now the ultrasoft modes, which are also defined in (2.17), have not been taken into consideration. The ultrasoft function is defined in terms of Wilson lines of ultrasoft photons and depends on the electric charges and directions of the particles in the initial and final state. It can be made explicit, via the field redefinition of the DM fermion bilinear

$$[\chi_v^{c\dagger}\chi_v]_I \to S_{vi}S_{vj}[\chi_v^{c\dagger}\chi_v]_I\,, \tag{2.30}$$

where S_{vi} is an electromagnetic time-like Wilson line corresponding to the charge ofthe field χ_{vi} in $I = \{ij\}$. After factoring the Sommerfeld effect, also the $\chi^+\chi^-$ initial state must be considered. But for S-wave annihilation only the total charge of the initial state is relevant, which in our case vanishes. This implies that $S_{vi}S_{vj} = S_{vi}S_{vi}^\dagger = 1$, which means that we can safely ignore ultrasoft momentum modes.

As a last comment, we note that the factorization of non-relativistic dynamics from the soft and collinear dynamics of the final state (see next Section) is independent of $E_{\rm res}^\gamma$ (at least up to leading order). This holds since soft and ultrasoft interactions can be decoupled from the ladder diagrams that are responsible for the Sommerfeld enhancement. The decoupling in turn can be done, because in the intermediate resolution soft gauge bosons would throw potential DM propagators off-shell, while in the narrow resolution real soft gauge boson radiation is forbidden altogether. Ultrasoft photon emission is potentially allowed for both resolutions, but they do not interact with the electrically neutral charge-0 sector.

This concludes the overview of the non-relativistic side of the problem, since the computation of the Sommerfeld factor was not the main focus of this thesis. For a detailed discussion of the Sommerfeld effect for an arbitrary set of heavy fermions nearly degenerate with the DM particle, which was developed for the general minimal supersymmetric SM, we refer to [64, 78, 79, 82].

2.3.2 Soft collinear effective theory

The method of regions introduced in Section 2.1 is a useful tool for calculating loop integrals in a power expansion in a small expansion parameter λ. As we saw in (2.10), different momentum regions scale differently with λ and in general the individual regions can be computed with much less effort than the full integral. While the method of regions can be applied to the computation of individual integrals, a similar expansion can already be performed at the Lagrangian level by making use of a framework called *soft collinear effective theory* (SCET), which was first developed for QCD [83–87]. The hard region will be integrated out into the matching coefficients, while the Feynman rules derived in SCET

replicate the full integral expanded the different momentum regions, which is what we saw in Section 2.1. For a pedagogical introduction, we refer to [88].

It should be noted that SCET is not an effective theory in the classical sense. We saw in the previous Section that an EFT is usually used for a simplified description of the problem, in that irrelevant energy regions are integrated out which allows one to focus on the relevant energy regime only. Neglecting irrelevant scales generally simplifies computations tremendously. Processes computed with SCET on the other hand feature several widely separated scales and only by using SCET one is able to obtain reliable results, since potentially large logarithmic corrections can be resummed. While EFTs in general allow one to compute processes happening at a specific scale in a simplified manner, SCET is necessary to be able to correctly treat processes involving multiple largely separated scales.

Before going into the details of SCET, it will be convenient to introduce some notation. While wino DM has vanishing hypercharge (1.5), Higgsino DM has non-vanishing hypercharge and one thus has to include both SU(2) and $\mathrm{U}(1)_Y$ gauge fields (1.7). For the introduction into SCET and especially the derivation of the factorization theorem later on in Section 3, we are going to collect SU(2) and $\mathrm{U}(1)_Y$ gauge fields into a single multiplet. This will allow us to present a factorization theorem valid for arbitrary hypercharges in a concise form. For the specific case of wino DM one then simply has to set $Y = 0$, see Section 3.2. Hence, we introduce the $\mathrm{SU}(2)\otimes\mathrm{U}(1)_Y$ multiplet

$$\vec{G}_\mu = \left(A^1_\mu, A^2_\mu, A^3_\mu, B_\mu\right)^T \,. \tag{2.31}$$

Generally, the SU(2) fields A^C and the $\mathrm{U}(1)_Y$ field B are accompanied by group structures and coupling constants. We thus define the following generalised group factor

$$\vec{\mathcal{T}} = \left(g_2 T^1, g_2 T^2, g_2 T^3, -g_1 Y\right)^T \,, \tag{2.32}$$

which already includes the coupling constants. The full theory Higgsino DM covariant derivative can then be written very concisely as

$$D_\mu = \partial_\mu - iG^C_\mu \mathcal{T}^C = \partial_\mu - iG_\mu \,, \tag{2.33}$$

and for wino DM, we simply set $Y = 0$, as mentioned earlier. Equipped with the generalised $\mathrm{SU}(2)\otimes\mathrm{U}(1)_Y$ multiplet (2.31) and the group factors (2.32) we are now ready to dive into SCET.

Depending on which momentum modes appear, SCET may appear as two different versions: $\mathrm{SCET_I}$ and $\mathrm{SCET_{II}}$. In the intermediate resolution case the collinear final state is inclusive and features hard-collinear momentum modes, while the anti-collinear direction describes the exclusive photon. Inclusive processes are also called $\mathrm{SCET_I}$ problems, while exclusive processes are called $\mathrm{SCET_{II}}$ problems. As we will see, exclusive $\mathrm{SCET_{II}}$ problems require an additional rapidity regulator. Notice that in the narrow resolution case, the collinear final state also turns into an $\mathrm{SCET_{II}}$ problem and consequently needs additional regularization.

Although at higher orders, all SM fields are present in collinear and soft interactions, we restrict ourselves to the gauge boson Lagrangian, since the gauge boson SCET fields appear directly in the annihilation operators. This will also simplify the introduction of the key concepts. In order to achieve a separation of the Lagrangian into the momentum modes (2.17), one needs to split the fields into a sum of a collinear, an anti-collinear field and a soft field

$$G^\mu(x) \to G^\mu_c(x) + G^\mu_{\bar{c}}(x) + G^\mu_s(x) \,, \tag{2.34}$$

The field $G_c^\mu(x)$ accounts for collinear modes of both, the hard-collinear and collinear type, $G_{\bar{c}}^\mu(x)$ accounts for anti-collinear modes and $G_s^\mu(x)$ accounts for soft modes. It is not necessary to introduce a field for the hard momentum mode, since, as mentioned before, the hard mode is integrated out into the matching coefficients (also called *Wilson* coefficients), which act as the coupling constants of the effective theory. By writing down the most general set of operators and by adjusting their Wilson coefficients, one is able to reproduce the full theory.

In order to write down the Lagrangian for a specific order in λ, we need to determine the power of λ with which the different field components of the SCET fields scale. This information can be obtained by looking at the two-point correlators, which for the gauge fields at hand is given by

$$\langle 0|T\{G^\mu(x)G^\nu(0)\}|0\rangle = \int \frac{d^4p}{(2\pi)^4}\frac{i}{p^2+i0}e^{-ip\cdot x}\left[-g^{\mu\nu}+\xi\frac{p^\mu p^\nu}{p^2}\right]. \tag{2.35}$$

Looking at the second term in the square bracket, we can see that the gauge fields scale like their momentum, i.e. the scaling of the (anti-) collinear and soft fields in (2.34) can be directly read off from (2.17). Having established the power counting, we can now move on to write down the SCET Lagrangian for the gauge fields.

Similarly to splitting the fields according to the momentum modes (2.34), one can split the Lagrangian into contributions with different scalings. In particular, the SCET Lagrangian in our case is given by

$$\mathcal{L}_{\text{SCET-I}} = \mathcal{L}_c + \mathcal{L}_{\bar{c}} + \mathcal{L}_{\text{soft}}\,. \tag{2.36}$$

$\mathcal{L}_{\text{soft}}$ is similar to the SM Lagrangian except that all gauge fields are assumed to be soft

$$\mathcal{L}_{\text{soft}} = -\frac{1}{2}\text{tr}\left(F_{s,\mu\nu}F_s^{\mu\nu}\right), \tag{2.37}$$

with the field strength tensor defined as

$$F_{s,\mu\nu} = i[D_{s,\mu}, D_{s,\nu}]\,, \quad D_{s,\mu} = \partial - iG_{s,\mu} \tag{2.38}$$

On the other hand the collinear Lagrangian $\mathcal{L}_c$ at leading power is

$$\mathcal{L}_c = -\frac{1}{2}\,\text{tr}\left(F_{c,\mu\nu}F_c^{\mu\nu}\right) + (D^\mu\varphi_c)^\dagger D_\mu\varphi_c\,, \tag{2.39}$$

where φ_c is the collinear Higgs doublet and was included for later convenience. The collinear covariant derivative is given by

$$D^\mu = \partial^\mu - iG_c^\mu(x) - in_-G_s(x_- + x_\perp)\frac{n_+^\mu}{2}\,, \tag{2.40}$$

where n_- is the light-like reference vector defined in (2.3) and x_-, $x_\perp$ are the components of the position argument as explained at the beginning of Section 2.1. At leading power, we need to include the projected soft field n_-G_s in the collinear covariant derivative (2.40) since from (2.17) we can see that only the anti-collinear components of G_s are not power-suppressed with respect to the corresponding components of G_c. Moreover, the n_+k soft momentum component can be neglected relative to the large hard-collinear and collinear momentum components. As a consequence, the soft gauge field is evaluated at the position $x_-^\mu + x_\perp^\mu$, where $x_-^\mu = (n_+\cdot x)n_-^\mu/2$. Since the covariant derivatives appearing in the definition of the collinear field strength tensor $F_c^{\mu\nu}$ depend on the soft field G_s, one

might wonder whether $F_c^{\mu\nu}$ give rise to additional kinetic terms for the soft gauge field (additionally to the ones of $\mathcal{L}_{\text{soft}}$). This does not happen since the squared field strength is gauge invariant and one can choose to work in a gauge where $n_- G_s$ vanishes. In such a gauge, the squared collinear field strength tensor is clearly free from terms depending only on the soft gauge boson field. The collinear Lagrangian $\mathcal{L}_c$ describes both hard-collinear and collinear momentum modes. Since the hard-collinear modes have virtuality $m_\chi m_W$, $\mathcal{L}_c$ is written in the unbroken phase of $\mathrm{SU}(2)\otimes\mathrm{U}(1)_Y$ gauge symmetry. The anti-collinear Lagrangian $\mathcal{L}_{\bar{c}}$ is equivalent to its collinear counterpart up to the interchange of $n_+ \leftrightarrow n_-$.

In general, we obtain the matching of a process onto the effective theory by writing down all possible operators with the correct quantum numbers, each with its own Wilson coefficient, that can contribute to said process. This means that in SCET even at leading power in λ, we have to include an infinite number of operators including arbitrarily high derivatives in the direction of the large momentum components. The derivatives

$$n_+\partial G_c(x) \sim \lambda^0 G_c(x) \quad \text{and} \quad n_-\partial G_{\bar{c}}(x) \sim \lambda^0 G_{\bar{c}}(x)\,, \tag{2.41}$$

are not power suppressed, because the (anti-) collinear fields carry large energies in these directions and hence need to be accounted for even at leading order. The expansion of the (anti-) collinear field along the direction associated with the large momentum component can be written in terms of an infinite sum over the non-power suppressed derivatives

$$G_c(x+sn_+) = \sum_{i=0}^{\infty} \frac{s^i}{i!} \left(n_+\partial\right)^i G_c(x)\,, \quad G_{\bar{c}}(x+tn_-) = \sum_{i=0}^{\infty} \frac{t^i}{i!} \left(n_-\partial\right)^i G_{\bar{c}}(x)\,. \tag{2.42}$$

Therefore, to include terms with arbitrarily high derivatives is equivalent to allowing non-locality of the (anti-) collinear fields along the (anti-) collinear directions.

In a gauge theory, a product of fields at different space-time points is only gauge invariant if the fields are connected by Wilson lines, which in our case are defined as

$$\begin{aligned} W_c(x) =& \mathrm{P}\exp\left[i\int_{-\infty}^{0} ds\, n_+\cdot G_c^C(x+sn_+)\mathcal{T}^C\right] \\ W_{\bar{c}}(x) =& \mathrm{P}\exp\left[i\int_{-\infty}^{0} dt\, n_-\cdot G_{\bar{c}}^C(x+tn_-)\mathcal{T}^C\right]\,, \end{aligned} \tag{2.43}$$

for collinear and anti-collinear fields, respectively. Instead of working with the standard fields, it turns out to be convenient to use the Wilson lines (2.43) for constructing gauge invariant building blocks $\mathcal{G}^\mu$ as follows

$$\begin{aligned} \mathcal{G}_c^\mu(x) =& W_c^\dagger[iD^\mu W_c](x) = \int_{-\infty}^{0} ds\, n_{+\nu}[W_c^\dagger F_c^{\nu\mu} W_c](x+sn_+)\,, \\ \mathcal{G}_{\bar{c}}^\mu(x) =& W_{\bar{c}}^\dagger[iD^\mu W_{\bar{c}}](x) = \int_{-\infty}^{0} dt\, n_{-\nu}[W_{\bar{c}}^\dagger F_{\bar{c}}^{\nu\mu} W_{\bar{c}}](x+tn_-)\,. \end{aligned} \tag{2.44}$$

The building blocks $\mathcal{G}_c^\mu(x)$ and $\mathcal{G}_{\bar{c}}^\mu(x)$ are invariant under collinear and anti-collinear gauge transformations, respectively. This can be shown by using the behaviour of the fields G_c and $G_{\bar{c}}$, of the Wilson lines (2.43) and of the covariant derivatives under collinear and anti-collinear gauge transformations.

To rewrite the $\mathcal{L}_c$ in terms of the gauge invariant building blocks (2.44), we define the covariant derivative and the field strength tensor as follows

$$i\mathcal{D}^\mu \equiv W_c^\dagger iD^\mu W_c = i\partial^\mu + \mathcal{G}_c^\mu\,, \quad \mathcal{F}_{c,\mu\nu}^B \mathcal{T}^B = i\left[\mathcal{D}_\mu, \mathcal{D}_\nu\right] \tag{2.45}$$

and write for the collinear Lagrangian

$$\mathcal{L}_c = -\frac{1}{2}\mathrm{tr}\left(\mathcal{F}_c^{\mu\nu}\mathcal{F}_{c,\mu\nu}\right) + \left(\mathcal{D}^\mu\Phi_c\right)^\dagger \mathcal{D}_\mu\Phi_c\,, \tag{2.46}$$

where $\Phi_c = W_c^\dagger(x)\varphi_c(x)$. Using (2.44) we can show that $n_+\mathcal{G}_c = 0$. Furthermore, the gauge field equation of motion can be used to get rid of $n_-\mathcal{G}_c$ (see [89] for operators equation in QCD). This means that the collinear gauge field degrees of freedom are represented by the transverse fields. The same argument holds for the anti-collinear gauge fields. This is why only the transverse components appear in the annihilation operators that will be derived in Section 2.4.

We can see from the SCET Lagrangian (2.36) that at $\mu \ll m_\chi$ there are no interactions between collinear fields of different directions. Also, interactions between collinear and non-relativistic modes would result in hard modes. Remember though that those have already been integrated out into the matching coefficients. Assessing the covariant derivative (2.40) however, it is clear that interactions via soft gauge fields are still possible. As was done for the heavy non-relativistic fields (2.20), we can decouple soft gauge fields from hard-(anti-) collinear fields via the field redefinition

$$\mathcal{G}_c^B(x) = Y_+^{BC}(x_-)\mathcal{G}_c^{C(0)}(x) \qquad \mathcal{G}_{\bar{c}}^B(x) = Y_-^{BC}(x_+)\mathcal{G}_{\bar{c}}^{C(0)}(x)\,, \tag{2.47}$$

with the soft Wilson lines [86]

$$Y_\pm(x) = \mathrm{P}\exp\left[-i\int_0^\infty ds\, n_\mp\cdot G_s^D(x+sn_\mp)\,\mathcal{T}^D\right]. \tag{2.48}$$

It can be checked that after the decoupling transformation, the squared field strength tensor does no longer depend on the soft modes. Using the decoupling transformations defined in (2.20) and (2.47) will allow us to factorize the cross section into contributions from different momentum modes. This will be demonstrated below in Section 3.

We will see later on, that the unobserved jet function in the intermediate resolution case can be computed in the massless limit. On the other hand the narrow resolution unobserved final state, as well as the anti-collinear photon final state for both resolution cases have a virtuality of m_W^2 which means that they have to be computed with massive SM particles. For their computation we thus have to use the SCET Lagrangian for the (anti-) collinear modes of the massive EW gauge bosons and the photon, after EWSB. We can use the Higgs covariant kinetic term in (2.46) to extract the gauge boson mass terms

$$\begin{aligned}\left(\mathcal{D}^\mu\Phi_c\right)^\dagger\mathcal{D}_\mu\Phi_c &= (n_+\partial\Phi_c)^\dagger n_-\mathcal{D}\Phi_c + (n_-\mathcal{D}\Phi_c)^\dagger n_+\partial\Phi_c + (\mathcal{D}_\perp^\mu\Phi_c)^\dagger\mathcal{D}_{\perp,\mu}\Phi_c \\ &\xrightarrow{\Phi_c=(0,v/\sqrt{2})} \frac{g_2^2v^2}{8}\left(\mathcal{A}_{\perp c}^{1,\mu}\mathcal{A}_{\perp c,\mu}^1 + \mathcal{A}_{\perp c}^{2,\mu}\mathcal{A}_{\perp c,\mu}^2\right) + \frac{v^2}{8}\left(g_2\mathcal{A}_{\perp c}^{3,\mu} + g_1\mathcal{B}_{\perp c,\mu}\right)^2\,,\end{aligned} \tag{2.49}$$

from which we can see that the mass term only arises for transverse fields. We can then write the collinear gauge field Lagrangian for virtualities of order m_W^2 (without the Higgs field) as follows

$$\mathcal{L}_c = -\frac{1}{4}\mathcal{F}_c^{B,\mu\nu}\mathcal{F}_{\mu\nu}^{c,B} + \frac{m_W^2}{2}\mathcal{W}_{\perp c}^{+,\mu}\mathcal{W}_{\perp c,\mu}^- + \frac{m_Z^2}{2}\mathcal{Z}_{\perp c,\mu}\,, \tag{2.50}$$

where the gauge eigenstates are now written in terms of mass eigenstates. While the collinear fields can no longer interact soft fields at leading power, interactions with ultrasoft fields are still possible. Ultrasoft fields can only have masses much smaller than m_W. At leading-power, collinear-ultrasoft interactions are included via covariant derivatives acting on electrically charged EW gauge fields. The covariant derivatives given in (2.40) except that the soft field now refers to an ultrasoft photon.

2.4 Annihilation operator basis

After having introduced the theoretical framework in the previous Section, it is now time to discuss the annihilation operator basis. The fact that we are neglecting power-corrections in λ and that we require a photon in the anti-collinear direction has consequences for the type of operators that may appear. First of all, (anti-) collinear fields must preserve their identity while emitting soft radiation. This means that the final state photon in the anti-collinear direction must come from a single SU(2) or $\mathrm{U}(1)_Y$ field, because it cannot be generated from an energetic fermion or Higgs boson. Because the initial state consists of an electrically neutral DM two-particle state, this requires the collinear field in the leading-power operator to also be of SU(2) or $\mathrm{U}(1)_Y$ type, since the anti-collinear SU(2) or $\mathrm{U}(1)_Y$ field cannot combine with any other SM field to form the same quantum numbers as the incoming DM particles. The annihilation process is reproduced by the effective Lagrangian

$$\mathcal{L}_{\text{ann}} = \frac{1}{2m_\chi} \sum_i \int ds dt\, \hat{C}_i(s,t,\mu)\mathcal{O}_i\,, \tag{2.51}$$

where $\mathcal{O}_i$ are the annihilation operators and $\hat{C}_i(s,t,\mu)$ are the matching coefficients containing the integrated-out hard interactions. Fields without position arguments are evaluated at $x=0$. As discussed previously, the operators are non-local since (anti-) collinear field operators are integrated along the light-cone of the respective direction with the coefficient function $\hat{C}_i$.

In this thesis, we restrict our attention to WIMP DM, given by an $\mathrm{SU}(2)\otimes\mathrm{U}(1)_Y$ multiplet of multiplicity $(2j+1)$. We assume the wino DM particles to be of Majorana-type, for which j takes on integer values, while Higgsino DM consists of Dirac fermions with half-integer values for j. For definiteness, $j=1$ for wino DM and $j=1/2$ for Higgsino DM, although many of the results presented here are valid for general multiplicities. The only computation for which a specific j-value has to be assumed, is that of the soft function (see Section 6.4). The operator basis is written in the EW symmetric limit with non-relativistic DM particles. This is done because the Sommerfeld effect is computed using a non-relativistic EFT, while the unbroken notation is used since the Wilson coefficients are calculated in the EW symmetric limit. In order to allow for a concise notation, we denote the DM fields generically by χ_v^a, where a is the group index of the heavy DM field that is neglected in (2.53). For wino DM, the χ_v^a, $a=1,2,3$, represent non-relativistic Majorana fields. For Higgsino DM on the other hand, the fields χ_v^a represent the non-relativistic Dirac fields η_v^a ($Y=-1/2$) and ζ_v^a ($Y=+1/2$), $a=1,2$. Specifically, they are defined as follows

$$\begin{aligned}
\eta_v^1 =& \chi_v^+\,, \qquad \zeta_v^1 = \chi_v^-\,, \\
\eta_v^2 =& \frac{1}{\sqrt{2}}\left(\chi_{v,1}^0 + i\chi_{v,2}^0\right)\,, \qquad \zeta_v^2 = \frac{1}{\sqrt{2}}\left(\chi_{v,1}^0 - i\chi_{v,2}^0\right)\,.
\end{aligned} \tag{2.52}$$

For Higgsino DM we adopt the nomenclature of [79] where the η_v fields represent particles and ζ_v the corresponding anti-particles. The complete basis of operators is given by

$$\begin{aligned}
\mathcal{O}_1 &= \chi_v^{c\dagger}\Gamma^{\mu\nu}\chi_v\, \mathcal{A}^B_{\perp c,\mu}(sn_+)\mathcal{A}^B_{\perp\bar{c},\nu}(tn_-)\,, \\
\mathcal{O}_2 &= \frac{1}{2}\,\chi_v^{c\dagger}\Gamma^{\mu\nu}\{T^B,T^C\}\chi_v\, \mathcal{A}^B_{\perp c,\mu}(sn_+)\mathcal{A}^C_{\perp\bar{c},\nu}(tn_-)\,, \\
\mathcal{O}_3 &= \chi_v^{c\dagger}\sigma^\alpha(n_{-\,\alpha}-n_{+\,\alpha})T^A\chi_v\,\epsilon^{ABC}\mathcal{A}^{\mu\,B}_{\perp c}(sn_+)\mathcal{A}^C_{\perp\bar{c},\mu}(tn_-)\,, \\
\mathcal{O}_4 &= \chi_v^{c\dagger}\Gamma^{\mu\nu}T^C\chi_v\,\left[\mathcal{A}^C_{\perp c,\mu}(sn_+)\mathcal{B}_{\perp\bar{c},\nu}(tn_-) + \mathcal{A}^C_{\perp\bar{c},\mu}(sn_+)\mathcal{B}_{\perp c,\nu}(tn_-)\,\right]\,,
\end{aligned}$$

$$\begin{aligned}\mathcal{O}_5 &= \chi_v^{c\dagger}\sigma^\alpha(n_{-\alpha}-n_{+\alpha})T^C\chi_v\left[\mathcal{A}^{\mu\,C}_{\perp c}(sn_+)\mathcal{B}_{\perp\bar{c},\mu}(tn_-)-\mathcal{A}^{C}_{\perp\bar{c},\mu}(sn_+)\mathcal{B}_{\perp c,\nu}(tn_-)\right],\\ \mathcal{O}_6 &= \chi_v^{c\dagger}\Gamma^{\mu\nu}\chi_v\,\mathcal{B}_{\perp c,\mu}(sn_+)\mathcal{B}_{\perp\bar{c},\nu}(tn_-)\,.\end{aligned} \tag{2.53}$$

Note that for Higgsino DM, one should symmetrize the fermionic part of the operators as follows

$$\chi_v^{c\dagger}\Gamma^{\mu\nu}T_i^{BC}\chi_v \quad\to\quad \zeta_v^{c\dagger}\Gamma^{\mu\nu}T_i^{BC}\eta_v+\eta_v^{c\dagger}\Gamma^{\mu\nu}T_i^{BC}\zeta_v\,. \tag{2.54}$$

This is relevant for the computation of the soft function (that describes soft momentum modes - see Section 6.4), which depends on the two-particle indices I, J. By using a symmetrized operator basis, we ensure that the soft function gives the same result for both index values $I=(+-)$ and $I=(-+)$. The spin matrix $\Gamma^{\mu\nu}$ in d space-time dimensions is given by

$$\Gamma^{\mu\nu}=\frac{i}{4}\left[\sigma^\mu,\sigma^\nu\right]\sigma^\alpha(n_{-\alpha}-n_{+\alpha})=\frac{1}{2i}\left[\sigma^m,\sigma^n\right]\sigma\cdot\mathbf{n}\overset{d=4\,\text{only}}{=}\frac{1}{2}\epsilon^{\mu\nu\alpha\beta}n_{+\alpha}n_{-\beta}\equiv\epsilon_\perp^{\mu\nu}\,, \tag{2.55}$$

with the following conventions $v^\mu=(1,0,0,0)$, $n_\pm^\mu=(1,0,0,\mp1)$, $\mathbf{n}=(0,0,1)$, m, $n=1,2,3$ and $\epsilon^{0123}=-1$.

Since wino DM has vanishing hypercharge only operators $\mathcal{O}_{1-3}$ are relevant for this model at tree level. This arises as a combination of the vanishing hypercharge and the fact that the collinear and anti-collinear field must each consist of a single SU(2) or $\mathrm{U}(1)_Y$ gauge field. Operators $\mathcal{O}_{4-6}$ start to become relevant for wino DM from the two-loop order onwards through closed loops of particles that carry SU(2) and hypercharge, e.g. Higgs boson and SM fermions. Because two-loop functions are beyond the accuracy discussed here, operators $\mathcal{O}_{4-6}$ are not relevant for wino DM. For Higgsino DM on the other hand, all six operators $\mathcal{O}_{1-6}$ need to be taken into account.

The derivation of the operator bases starts from the general expression

$$\mathcal{O}_i=\chi_v^{c\dagger}\Gamma^{\mu\nu}T_i^{BC}\chi_v\,\mathcal{G}^B_{\perp c,\mu}(sn_+)\mathcal{G}^C_{\perp\bar{c},\nu}(tn_-)\,, \tag{2.56}$$

where the indices of the group structure are restricted to the values $B,C=1,2,3$ for the operators $\mathcal{O}_{1-3}$. For the wino model, the two DM fields must couple to an operator with SU(2) isospin 0, 1 or 2 which means that the group index matrix may take on one of the following structures

$$\text{Wino:}\qquad T_1^{BC}=\delta^{BC}\,,\quad T_2^{BC}=\frac{1}{2}\{T^B,T^C\}\,,\quad T_3^{BC}=\epsilon^{BCD}T^D\,, \tag{2.57}$$

where T^B are the SU(2) generators in the isospin-j representation. For Higgsino DM, which has isospin $j=1/2$, operators $\mathcal{O}_1$ and $\mathcal{O}_2$ are not linearly independent. Specifically, they satisfy the relation

$$\mathcal{O}_2^{\text{Higgsino}}=\frac{1}{4}\mathcal{O}_1^{\text{Higgsino}}\,. \tag{2.58}$$

Note that (2.58) does not hold for $j>1/2$ SU(2) multiplets, for which operators $\mathcal{O}_1$ and $\mathcal{O}_2$ are linearly independent. For Higgsino DM, the DM fields must couple to an operator with isospin 0 or 1 and the group structures in (2.56) may thus be of the following type

$$\begin{aligned}\text{Higgsino:}\qquad & T_{1,2}^{BC}=\delta^{BC}\,,\quad T_3^{BC}=\epsilon^{BCD}T^D\,,\quad T_4^{BC}=\delta^{B4}T^C+\delta^{C4}T^B\\ & T_5^{BC}=\delta^{B4}T^C-\delta^{C4}T^B\,,\quad T_6^{BC}=\delta^{B4}\delta^{C4}\,.\end{aligned} \tag{2.59}$$

Moving on to spinor and Lorentz indices (note that spinor indices have been left implicit in (2.56)). For both wino and Higgsino DM, the two spin-1/2 DM fields can either couple to spin-0 or spin-1. If the DM fields couple to spin-0, the spinor indices of the spin matrix $\Gamma^{\mu\nu}$ must be of the form $\delta_{\alpha\beta}$. Since the Lorentz indices μ and ν are of the transverse type, we obtain two possibilities for the spin matrix in the spin-0 case

$$g_\perp^{\mu\nu} = g^{\mu\nu} - \frac{n_+^\mu n_-^\nu + n_-^\mu n_+^\nu}{2} \qquad \text{or} \qquad \epsilon_\perp^{\mu\nu} \,. \tag{2.60}$$

If on the other hand the DM fields couple to spin-1, the structure of the spinor indices is the vector of Pauli matrices $(0, \sigma)$ or $[\sigma^\rho - (v\cdot\sigma)v^\rho]_{\alpha\beta}$. In this case, $\Gamma^{\mu\nu}$ can take one of the following three independent forms

$$(n_{-\rho} - n_{+\rho}) g_\perp^{\mu\nu} \,, \quad (n_{-\rho} - n_{+\rho}) \epsilon_\perp^{\mu\nu} \,, \quad g_{\rho\lambda} v_\kappa \epsilon^{\lambda\kappa\mu\nu} \,. \tag{2.61}$$

Here the equality $v_\rho(\sigma^\rho - (v\cdot\sigma)v^\rho) = 0$ was used to reduce a number of further structures to the ones given. Combining the spin structures (2.60) and (2.61) with the group structures from (2.57) and (2.59) results in 6 spin-0 and 9 spin-1 structures for wino DM, as well as 10 spin-0 and 15 spin-1 structures for Higgsino DM. We will see next how they can be reduced to the operator basis given in (2.53).

As the DM particles annihilate into two gauge bosons, the final state must respect Bose symmetry which constrains the operators to be symmetric under the simultaneous exchange of all labels $c \leftrightarrow \bar{c}$, $n_+ \leftrightarrow n_-$, $B \leftrightarrow C$ and $\mu \leftrightarrow \nu$. For wino DM, the SU(2) structures T_1^{BC} and T_2^{BC} are symmetric, while T_3^{BC} is anti-symmetric and for Higgsino DM, $T_{1,2}^{BC}$, T_4^{BC} and T_6^{BC} are symmetric, while T_3^{BC} and T_5^{BC} are anti-symmetric. All spin-0 structures from (2.60) are symmetric, while the spin-1 structures from (2.61) are anti-symmetric. Combining (anti-) symmetric group and spinor structures thus results in four spin-0 and three spin-1 operators for wino DM, as well as in six spin-0 and six spin-1 operators for Higgsino DM. Lastly, the DM gauge interaction conserves CP symmetry, which excludes $g_\perp^{\mu\nu}$ from (2.60) and all but the first structure from (2.61). In the case of wino DM, we are thus left with the two spin-0 operators $\mathcal{O}_{1,2}$ and the one spin-1 operator $\mathcal{O}_3$. For Higgsino DM on the other hand, there remain three spin-0 operators $\mathcal{O}_{1,4,6}$ (not distinguishing operators one and two due two the linear dependence (2.58)) and two spin-1 operators $\mathcal{O}_{3,5}$.

Before moving on, it is important to note that not all operators in (2.53) are relevant for the $\chi^0\chi^0 \to \gamma + X$ annihilation process. In particular, it turns out that the spin-triplet operators $\mathcal{O}_3$ and $\mathcal{O}_5$ are unable to contribute to the annihilation process and can thus be neglected in the computation of the cross section. This is because there is no spin-triplet initial state for both wino and Higgsino DM and the Sommerfeld-enhanced scattering prior to annihilation does not change the spin. The remaining operators $\mathcal{O}_{1,2,4,6}$ are spin-singlet, so the dominant short-distance annihilation process occurs in the ${}^1S_0$ configuration.

When matching computations are performed using dimensional regularization, one has to take into account the appearance of evanescent operators. Evanescent operators are operators that appear for space-time dimensions $d \neq 4$, which vanish however if $d = 4$. An arbitrary full theory diagram in the calculation of the hard matching coefficients contains a single string of Dirac matrices of the form

$$\bar{v}(m_\chi v)\gamma^{\mu_1}\gamma^{\mu_2}\cdots\gamma^{\mu_N}u(m_\chi v) \,. \tag{2.62}$$

The indices μ_i are contracted with each other, $n_\pm$ from the spin matrix $\Gamma^{\mu\nu}$ or the polarization vectors, $\varepsilon_{c\perp}$, $\varepsilon_{\bar{c}\perp}$, of the outgoing gauge bosons. One can then make use of the

on-shell condition $\not{p}u(p) = 0$ and the relations $n_- = 2v - n_+$ and $n_+ \cdot \varepsilon_{c\perp} = n_+ \cdot \varepsilon_{\bar{c}\perp} = 0$, which imply $\{\not{n}_+, \not{\varepsilon}_{c\perp}\} = \{\not{n}_+, \not{\varepsilon}_{\bar{c}\perp}\} = 0$. Combining these equalities with the fact that the number of Dirac matrices in (2.62), N, has to be odd to obtain an S-wave annihilation operator in the non-relativistic EFT, we are able to reduce the Dirac string (2.62) to

$$\varepsilon_{c\perp} \cdot \varepsilon_{\bar{c}\perp} \bar{v}(m_\chi v) \not{n}_+ u(p)\,, \quad \bar{v}(m_\chi v)\,[\not{\varepsilon}_{c\perp}, \not{\varepsilon}_{\bar{c}\perp}]\,\not{n}_+ u(p)\,. \tag{2.63}$$

Rewriting the spinors $\bar{v}$ and u in terms of non-relativistic two-component objects ζ_v and η_v, the first structure corresponds to the spin matrix of $\mathcal{O}_{3,5}$ and the second one to $\Gamma^{\mu\nu}$. We thus confirm that there are indeed no evanescent operators and that (2.53) provides a complete operator basis in d dimensions.

3 Factorization of the energy spectrum

After having introduced the relevant theoretical framework as well as the annihilation operator basis in the previous Section, we can now move on to derive the factorization theorem for the annihilation cross section. This means that we use the SCET-methods from Section 2.3.2 to split the cross section into contributions describing the different momentum modes. We will see that in the end each momentum mode is described by a dedicated function, which can be computed separately from the rest.

Since the cross section for the intermediate resolution case can be understood as a generalisation of the narrow resolution case, we will present a more detailed discussion for the former case and discuss modifications for the narrow resolution when appropriate. In the following derivation, we will be as general as possible and keep quantum numbers such as hypercharge or isospin multiplicity arbitrary. To allow for the notation to be as clean as possible, we will again use the conventions introduced in (2.31) and (2.32). Only at the end in Section 3.2 are we going to be more explicit and provide the cross sections that are specific to wino and Higgsino DM in the two resolution cases. The logic of the following derivation follows Section 2.2 of [7]. Furthermore, many equations presented here have also either been extracted from Section 2.2 of [7], or represent generalisations of the versions presented there.

To derive the factorization theorem for the intermediate resolution cross section, we start from the general expression

$$\begin{aligned}\frac{d(\sigma v_{\rm rel})}{dE_\gamma} =& \frac{1}{4}\frac{1}{4m_\chi^2}\sum\!\!\!\!\!\!\int_X \frac{d^3\mathbf{p}_\gamma}{(2\pi)^3 2p_\gamma^0}\,(2\pi)^4 \\ &\times \delta^{(4)}(p_{\chi\bar\chi}-p_\gamma-p_X)\delta(E_\gamma-|\mathbf{p}_\gamma|)\left|T_{\chi^0\chi^0\to\gamma X}\right|^2. \end{aligned} \tag{3.1}$$

where it is implied that we sum over all spin configurations. The explicit factor $1/4$ accounts for the initial-state spin average. The sum-integral implies a sum over all kinematically allowed final states X with total momentum p_X and the phase-space integral over the final-state momenta. The momentum of the two fermion initial-state in the center-of-mass frame is $p_{\chi\bar\chi} = (2m_\chi + E_{\chi\bar\chi})v$, where $E_{\chi\bar\chi}$ is the small kinetic energy of the two-particle DM state. The T-matrix element $T_{\chi^0\chi^0\to\gamma X}$ which provides the probability of a neutral two-particle DM state transitioning into a γ and an unobserved final state is non-zero only if it is built with one of the operators established in the previous Section. It is therefore given by

$$T_{\chi^0\chi^0\to\gamma X} = \frac{1}{2m_\chi}\sum_{i=}\int dsdt\,\hat C_i(s,t,\mu)\,2m_\chi\,\langle\gamma(p_\gamma)X_cX_s|\mathcal{O}_i|\,[\chi\chi]_{00}\rangle\,, \tag{3.2}$$

where the sum goes over $i=1,2$ or $i=1,4,6$ for wino or Higgsino DM, respectively (where for Higgsino DM we made use of the linear dependence (2.58) of operators $\mathcal{O}_{1,2}$). Since we want to factorize the cross section into components corresponding to the momentum modes (2.17), we have split the sum over the unobserved final state X into a (hard-) collinear X_c and soft part X_s. We will see below how this matrix element separates into a part containing the DM particles, which will be described by a NRDM EFT as introduced

in Section 2.3.1, and a part containing the gauge bosons, which will be described using SCET as introduced in Section 2.3.2. The factor $2m_\chi$ comes from the non-relativistic normalization of the external DM states.

We now make use of the decoupling transformations (2.20) and (2.47), which are field redefinitions using Wilson lines, that decouple soft gauge bosons from the (hard-) collinear, (hard-) anti-collinear and non-relativistic fields. The operators $\mathcal{O}_i$ then take the form

$$\mathcal{O}_i = \chi_v^{c\dagger}\Gamma_i^{\mu\nu}[Y_v^\dagger T_i^{AB} Y_v]\chi_v\, \mathcal{Y}_+^{AV}\mathcal{Y}_-^{BW}\mathcal{G}^V_{\perp c,\mu}(sn_+)\mathcal{G}^W_{\perp\bar{c},\nu}(tn_-)\,. \tag{3.3}$$

We make use of the symbol $\mathcal{Y}_\pm$ to denote Wilson lines in the adjoint representation. Having decoupled fields with different momentum modes means that those fields no longer interact and that we can hence factorize the matrix element as follows

$$\begin{aligned}\langle\gamma(p_\gamma)X_cX_s|\,\mathcal{O}_i\,|[\chi\chi]_{00}\rangle \;&=\; \langle\gamma(p_\gamma)|\,\mathcal{G}^W_{\perp\bar{c},\nu}(tn_-)\,|0\rangle\langle X_c|\,\mathcal{G}^V_{\perp c,\mu}(sn_+)\,|0\rangle \\ &\quad\times\langle X_s|\,[Y_v^\dagger T_i^{AB}Y_v]_{ab}\,\mathcal{Y}_+^{AV}\mathcal{Y}_-^{BW}\,|0\rangle\,K_{ab,I}\,\langle 0|\,[\chi_v^{c\dagger}\Gamma_i^{\mu\nu}\chi_v]_I\,|[\chi\chi]_{00}\rangle\,.\end{aligned} \tag{3.4}$$

From (3.4) one can already guess which terms will give rise to which (anti-) collinear or soft function. In order to evaluate the s and t integration in (3.2), we make use of translation invariance

$$\begin{aligned}\langle\gamma(p_\gamma)|\,\mathcal{G}^W_{\perp\bar{c},\nu}(tn_-)\,|0\rangle &= e^{itn_-\cdot p_\gamma}\,\langle\gamma(p_\gamma)|\,\mathcal{G}^W_{\perp\bar{c},\nu}(0)\,|0\rangle\,,\\ \langle X_c|\,\mathcal{G}^V_{\perp c,\mu}(sn_+)\,|0\rangle &= e^{isn_+\cdot p_{X_c}}\,\langle X_c|\,\mathcal{G}^V_{\perp c,\mu}(0)\,|0\rangle\,,\end{aligned} \tag{3.5}$$

where p_{X_c} is the total four-momentum of the collinear final state. Using (3.5), we perform the integration

$$C_i(n_+p_X, n_-p_\gamma, \mu) = \int dsdt\, e^{isn_+\cdot p_{X_c}+itn_-\cdot p_\gamma}\,\hat{C}_i(s,t,\mu)\,. \tag{3.6}$$

Making use of the kinematics of the process of interest and of the fact that we are only considering leading order in λ, provides us with the relations $n_-p_\gamma = 2E_\gamma \approx 2m_\chi$ and $n_+\cdot p_X \approx 2m_\chi$ which allow us to define

$$C_i(\mu) = C_i(2m_\chi, 2m_\chi, \mu)\,. \tag{3.7}$$

These are the Wilson coefficients which contain the hard momentum modes and serve as the coupling constants of the EFT. Analytic expressions for the Wilson coefficients of all operators $\mathcal{O}_{1-6}$ are provided below in Section 6.1.

Having factorized the matrix element, we plug (3.4) and (3.7) into (3.2). After then squaring the T-matrix element as well as writing the four-momentum conservation delta-function in (3.1) as the space-time integral of the exponential, we arrive at the following expression for the cross section

$$\begin{aligned}\frac{d(\sigma v_{\rm rel})}{dE_\gamma} \;&=\; \sum_{i.j=1,2} C_i(\mu)C_j^*(\mu)\sum_{I,J}\frac{1}{4}\frac{1}{4m_\chi^2}\int\frac{d^3\mathbf{p}_\gamma}{(2\pi)^3 2p_\gamma^0}\,\delta(E_\gamma-|\mathbf{p}_\gamma|) \\ &\quad\times\int d^4x\, e^{i(p_{\chi\chi}-p_\gamma)\cdot x}\,\langle[\chi\chi]_{00}(p_{\chi\chi})|\,[\chi_v^{c\dagger}\Gamma_j^{\mu'\nu'}\chi_v]_J^\dagger\,|0\rangle\,\langle 0|\,[\chi_v^{c\dagger}\Gamma_i^{\mu\nu}\chi_v]_I\,|[\chi\chi]_{00}(p_{\chi\chi})\rangle \\ &\quad\times\langle 0|\,\mathcal{G}^Y_{\perp\bar{c},\nu'}\,|\gamma(p_\gamma)\rangle\langle\gamma(p_\gamma)|\,\mathcal{G}^W_{\perp\bar{c},\nu}\,|0\rangle\sum\!\!\!\!\!\!\int_{X_c} e^{-ip_{X_c}\cdot x}\,\langle 0|\,\mathcal{G}^X_{\perp c,\mu'}\,|X_c\rangle\langle X_c|\,\mathcal{G}^V_{\perp c,\mu}\,|0\rangle \\ &\quad\times\sum\!\!\!\!\!\!\int_{X_s} e^{-ip_{X_s}\cdot x}\,K_{ab,I}K^\dagger_{a'b',J}\,\langle 0|\,\mathcal{Y}_+^{\dagger A'X}\mathcal{Y}_-^{\dagger B'Y}\,[Y_v^\dagger T_j^{A'B'}Y_v]^\dagger_{a'b'}\,|X_s\rangle\end{aligned}$$

$$\times \quad \langle X_s|\,[Y_v^\dagger T_i^{AB} Y_v]_{ab}\,\mathcal{Y}_+^{AV}\mathcal{Y}_-^{BW}\,|0\rangle\,. \tag{3.8}$$

Now we are almost in a position to read off the individual contributions of the momentum modes to the cross section. The Sommerfeld factor can be extracted from the second line of (3.8) by using (2.26) and (2.29), which results in

$$\begin{aligned}&\langle[\chi\chi]_{00}(p_{\chi\chi})|\,[\chi_v^{c\dagger}\Gamma_j^{\mu'\nu'}\chi_v]_J^\dagger\,|0\rangle\,\langle 0|\,[\chi_v^{c\dagger}\Gamma_i^{\mu\nu}\chi_v]_I\,|[\chi\chi]_{00}(p_{\chi\chi})\rangle\\ &=\,4\,\langle\xi_0^{c\dagger}\Gamma_j^{\mu'\nu'}\xi_0\rangle^*\,\langle\xi_0^{c\dagger}\Gamma_i^{\mu\nu}\xi_0\rangle\,S_{IJ}\,,\end{aligned} \tag{3.9}$$

where ξ_0 is the spinor of an external χ^0 field (with the two spin orientations $\uparrow$, $\downarrow$). The Sommerfeld factor depends on the small kinetic energy $E_{\chi\bar{\chi}}$, which in the present day Universe is much smaller than the electroweak scale and thus smaller than any other scale appearing in the process of interest. After having decoupled the non-relativistic matrix element, the kinetic energy $E_{\chi\bar{\chi}}$ can be neglected in the other terms due to its smallness. For the computation of the (hard-) collinear, anti-collinear and soft functions we can thus set $p_{\chi\bar{\chi}} = 2m_\chi$.

Next, we again use translation invariance to absorb the exponentials $e^{-ip_{X_c}\cdot x}$ and $e^{-ip_{X_s}\cdot x}$, which enables us to perform the sums over the complete sets of collinear and soft intermediate states. For the collinear function this means

$$\begin{aligned}\sum\!\!\!\!\!\!\int_{X_c} e^{-ip_{X_c}\cdot x}\,\langle 0|\,\mathcal{G}^X_{\perp c,\mu'}\,|X_c\rangle\langle X_c|\,\mathcal{G}^V_{\perp c,\mu}\,|0\rangle =&\sum\!\!\!\!\!\!\int_{X_c}\langle 0|\,\mathcal{G}^X_{\perp c,\mu'}(x)\,|X_c\rangle\langle X_c|\,\mathcal{G}^V_{\perp c,\mu}\,|0\rangle\\ =&\langle 0|\,\mathcal{G}^X_{\perp c,\mu'}(x)\,\mathcal{G}^V_{\perp c,\mu}\,|0\rangle\,.\end{aligned} \tag{3.10}$$

It will also prove to be convenient to introduce the soft operators

$$\mathcal{S}^i_{I,VW}(x) = K_{ab,I}\,[Y_v^\dagger T_i^{AB} Y_v]_{ab}(x)\,\mathcal{Y}_+^{AV}(x)\mathcal{Y}_-^{BW}(x)\,, \tag{3.11}$$

which allow for a more concise notation. The soft momentum modes are then described by

$$\begin{aligned}&\sum\!\!\!\!\!\!\int_{X_s} e^{-ip_{X_s}\cdot x}\;\langle 0|\;\Big[\mathcal{S}^\dagger\Big]^j_{J,XY}\;|X_s\rangle\langle X_s|\,\mathcal{S}^i_{I,VW}\,|0\rangle\\ &\quad=\sum\!\!\!\!\!\!\int_{X_s}\langle 0|\;\Big[\mathcal{S}^\dagger\Big]^j_{J,XY}(x)\,|X_s\rangle\langle X_s|\,\mathcal{S}^i_{I,VW}(0)\,|0\rangle\\ &\quad=\langle 0|\,\bar{\mathbf{T}}\Big[\;\Big[\mathcal{S}^\dagger\Big]^j_{J,XY}(x)\Big]\,\mathbf{T}\big[\mathcal{S}^i_{I,VW}(0)\big]\,|0\rangle\,.\end{aligned} \tag{3.12}$$

Before arriving at the final formula for the factorized cross section, we are going to provide the proper definitions of the individual functions appearing therein in the next Section.

3.1 Function definitions

3.1.1 Photon collinear function

The final state photon in the anti-collinear direction is described by the photon jet function, which is defined as the following squared matrix element

$$-\,g^\perp_{\nu\nu'}\,Z_\gamma^{YW} = \sum_\lambda \langle 0|\mathcal{G}^Y_{\perp\bar{c},\nu'}(0)|\gamma(p_\gamma,\lambda)\rangle\langle\gamma(p_\gamma,\lambda)|\mathcal{G}^W_{\perp\bar{c}\nu}(0)|0\rangle\,. \tag{3.13}$$

The sum over λ describes the sum over the different polarizations of the photon. The possible values of the gauge boson indices in (3.13) are limited to $Y, W = \{3, 4\}$, where the value is 3 or 4 if the photon originates from an SU(2) or a $\mathrm{U}(1)_Y$ gauge boson, respectively. This means that in the case of wino DM where only operators $\mathcal{O}_{1,2}$ contribute, the only allowed index combination is Z_γ^{33}. For Higgsino DM on the other hand, we have to take into account the index combinations Z_γ^{33} (from $\mathcal{O}_{1,2}$), Z_γ^{34} and Z_γ^{43} (from $\mathcal{O}_4$), and Z_γ^{44} (from $\mathcal{O}_6$). We will see in Section 6.2 however, that the different index combinations are related in a rather straightforward manner. This means that one only has to compute Z_γ^{YW} for one specific choice of Y and W, from which the other combinations can then be derived.

From 2.17 we can see that the anti-collinear photon jet function has a virtuality of m_W^2, which means that it has to be computed using massive EW gauge bosons. It hence depends on the SM particle masses m_W, m_Z, m_H and m_t. Furthermore, Z_γ^{YW} exhibits the same virtuality as the soft function and the narrow resolution unobserved jet function, but has parametrically different (anti-) collinear momentum components. In these cases, as was already touched upon in Sections 2.1 and 2.3.2, a single regulator does not suffice for the computation. Thus, the photon jet function depends on both the dimensional regularization scale μ and the rapidity scale ν.

3.1.2 Unobserved-jet collinear function

The unobserved final state X is given by the collinear jet function that is defined as

$$\begin{aligned} -g_{\mu\mu'}^{\perp}\, J^{XV}(p^2, m_W) &= \frac{1}{\pi}\,\mathrm{Im}\big[-g_{\mu\mu'}^{\perp}\, i\mathcal{J}^{XV}(p^2, m_W)\big] \\ &\equiv \frac{1}{\pi}\,\mathrm{Im}\big[\, i\int d^4x\, e^{ip\cdot x}\langle 0|\mathbf{T}\big\{\mathcal{G}^X_{\perp c,\mu'}(x)\,\mathcal{G}^V_{\perp c,\mu}(0)\big\}|0\rangle\,\big] \\ &= \frac{1}{2\pi}\int d^4x\, e^{ip\cdot x}\,\langle 0|\,\mathcal{G}^X_{\perp c,\mu'}(x)\,\mathcal{G}^V_{\perp c,\mu}(0)\,|0\rangle\,. \end{aligned} \tag{3.14}$$

The computation of the unobserved jet function changes depending on whether we consider the narrow or intermediate resolution regime. Hence, we will discuss the two cases separately and to avoid confusion, we will write the unobserved jet function in the narrow and intermediate resolution regimes as J_{nrw}^{XV} and J_{int}^{XV}, respectively.

$J_{\mathbf{nrw}}^{XV}$ in the narrow resolution regime

The narrow resolution regime implies the following scaling for the invariant mass squared p^2 of the final state X: $p^2 \sim m_W^2$. Hence the narrow resolution unobserved jet function has the same virtuality as the photon jet function and the soft function. For its computation, which is discussed in detail in Section 6.3.1, we thus also rely on the rapidity regulator and it depends on the regulator scales μ and ν, as well as the EW scale masses m_W, m_Z, m_H and m_t. Similar to the photon jet function the gauge boson indices can take the values $X, V = \{3, 4\}$, where for wino DM we only need J_{nrw}^{33} while for Higgsino DM we need the combinations J_{nrw}^{33}, J_{nrw}^{34}, J_{nrw}^{43} and J_{nrw}^{44}. Similar to the photon jet function, all index combinations are related and once one combination is computed, the others can be derived from it in a rather straightforward manner.

$J_{\mathbf{int}}^{XV}$ in the intermediate resolution regime

The intermediate resolution case unobserved jet function is defined in terms of hard-collinear fields and the invariant mass squared of the final state X scales as $p^2 \sim m_W m_\chi$.

This implies that J_{int}^{XV} is defined in SCET_I (while J_{nrw}^{XV} is defined in SCET_II). J_{int}^{XV} not only depends on the hard-collinear scale through p^2, but also on the EW scale m_W which arises from particles inside the jet. Using the naive definition (3.14), the unobserved jet function is still a two-scale object and in order to obtain a factorization theorem that depends on single-scale objects only, J_{int}^{XV} has to be re-factorized into a hard-collinear and a collinear part [69]. Furthermore, the presence of both SU(2) and $\text{U}(1)_Y$ gauge bosons means that it is convenient to further split J_{int}^{XV} into an SU(2) and a $\text{U}(1)_Y$ part

$$J_{\text{int}}^{XV}(p^2, m_W) = J_{\text{int}}^{\text{SU}(2)}(p^2) J_{m,\text{SU}(2)}^{XV}(m_W) + J_{\text{int}}^{\text{U}(1)}(p^2) J_{m,\text{U}(1)}^{XV}(m_W) + \mathcal{O}\left(\frac{m_W^2}{p^2}\right). \quad (3.15)$$

The hard-collinear parts $J_{\text{int}}^{\text{SU}(2)}$, $J_{\text{int}}^{\text{U}(1)}$ can be seen as a matching coefficients for the collinear mass-jet functions $J_{m,\text{SU}(2)}^{XV}$ and $J_{m,\text{U}(1)}^{XV}$. The coefficients $J_{\text{int}}^{\text{SU}(2)}$ and $J_{\text{int}}^{\text{U}(1)}$ depend on p^2 and the virtuality scale μ and are computed in the EW symmetric, i.e. massless, limit. Since it does not feature the same virtuality as the photon jet function or the soft function, we do not require an additional regulator for its calculation.

The mass-dependent collinear functions $J_{m,\text{SU}(2)}^{XV}$ and $J_{m,\text{U}(1)}^{XV}$ do not depend on p^2 and require a rapidity regulator. In Appendix E we show that if we assume massive gauge boson propagators during the computation, we indeed obtain a result sensitive to m_W. However, as we explain there, this mass dependence should actually be attributed to the soft region and must thus be discarded to avoid double counting, as it is already taken into account by the soft function. We hence find the mass-dependent collinear function to be trivial up to the one-loop order, which allows us to write (3.15) as

$$J_{\text{int}}^{XV} = \left(\delta^{XV} - \delta^{X4}\delta^{V4}\right) J_{\text{int}}^{\text{SU}(2)} + \delta^{X4}\delta^{V4} J_{\text{int}}^{\text{U}(1)}. \quad (3.16)$$

While for wino DM we only require $J_{\text{int}}^{\text{SU}(2)}$, for Higgsino DM we need to compute both $J_{\text{int}}^{\text{SU}(2)}$ and $J_{\text{int}}^{\text{U}(1)}$. The computation of the intermediate resolution unobserved jet function is discussed below in Section 6.3.2.

3.1.3 Soft function - intermediate resolution

The definition for the soft function can be obtained from (3.8) and (3.11). First, we use (3.11) to rewrite the last two lines in (3.8) as follows

$$\begin{aligned}
&\sum\!\!\!\!\!\!\int_{X_s} e^{-ip_{X_s}\cdot x} K_{ab,I} K^\dagger_{a'b',J} \langle 0| \mathcal{Y}_+^{\dagger A'X} \mathcal{Y}_-^{\dagger B'Y} [Y_v^\dagger T_j^{A'B'} Y_v]^\dagger_{a'b'} |X_s\rangle \langle X_s| [Y_v^\dagger T_i^{AB} Y_v]_{ab} \mathcal{Y}_+^{AV} \mathcal{Y}_-^{BW} |0\rangle \\
&= \sum\!\!\!\!\!\!\int_{X_s} e^{-ip_{X_s}\cdot x} \langle 0| \left[\mathcal{S}^\dagger\right]^j_{J,XY}(x) |X_s\rangle\langle X_s| \mathcal{S}^i_{I,VW}(0) |0\rangle . \quad (3.17)
\end{aligned}$$

The sum over X_s in (3.17) is the unit operator, which we can use to define the soft function in momentum space

$$\langle 0| \bar{\mathbf{T}}[[\mathcal{S}^\dagger]^j_{J,XY}(x)] \mathbf{T}[\mathcal{S}^i_{I,VW}(0)] |0\rangle \equiv \int \frac{d^4k}{(2\pi)^4} e^{-ik\cdot x} \boldsymbol{W}^{ij}_{IJ,VWXY}(k). \quad (3.18)$$

We also define the integrated soft function

$$\begin{aligned}
W^{ij}_{IJ,VWXY}(\omega) &= \frac{1}{2}\int \frac{d(n_+k) d^2k_\perp}{(2\pi)^4} \boldsymbol{W}^{ij}_{IJ,VWXY}(k) \\
&= \frac{1}{4\pi}\int d(n_+y)\, e^{i\omega n_+\cdot y/2} \langle 0| \bar{\mathbf{T}}[[\mathcal{S}^\dagger]^j_{J,XY}(y_-)] \mathbf{T}[\mathcal{S}^i_{I,VW}(0)] |0\rangle , \quad (3.19)
\end{aligned}$$

where $\omega = n_- \cdot k$.

Wino DM For wino DM, we can somewhat simplify the general soft function definition (3.19). The gauge boson indices W, Y are contracted with the photon jet function. In the case of wino DM, this means that we can fix $W = Y = 3$ since wino DM has vanishing hypercharge. Furthermore, the soft function indices V, X are contracted with the unobserved jet function (3.16). Since we only need the soft function contraction with $J^{\mathrm{SU}(2)}_{\mathrm{int}}$ for wino DM, in this case we may define

$$W^{\mathrm{SU}(2),\,ij}_{IJ,33}(\omega) = \left(\delta^{XV} - \delta^{X4}\delta^{V4}\right) W^{ij}_{IJ,V3X3}(\omega)\,. \tag{3.20}$$

Higgsino DM For Higgsino DM, the indices W and Y can take the values 3 and 4, which means that a notable simplification is not possible here. We can however use (3.16) to define SU(2) and $\mathrm{U}(1)_Y$ projected soft functions as follows

$$\begin{aligned} W^{\mathrm{SU}(2),\,ij}_{IJ,WY}(\omega) &= (\delta^{XV} - \delta^{X4}\delta^{V4})\, W^{ij}_{IJ,VWXY}(\omega)\,, \\ W^{\mathrm{U}(1),\,ij}_{IJ,WY}(\omega) &= \delta^{X4}\delta^{V4}\, W^{ij}_{IJ,VWXY}(\omega)\,. \end{aligned} \tag{3.21}$$

While (3.21) does not aid in writing the cross section more compactly, it will make the origin of the various terms more transparent and it is thus worthwhile to split the soft function accordingly.

For both wino and Higgsino DM, the soft functions must be calculated in the EW broken theory and consequently depend on the EW masses of the SM particles. Also, they depend on the renormalization scale μ and the rapidity regularization scale ν. Details of the computation are given in Section 6.4.

3.1.4 Soft function - narrow resolution

In the intermediate resolution case, the energy resolution is large enough to allow for soft radiation into the final state. As a consequence, the intermediate resolution soft function is defined at the squared amplitude level, as can be seen from (3.19). In the narrow resolution case we have the scaling $E^{\gamma}_{\mathrm{res}} \sim m_W^2/m_\chi$, which forbids real soft radiation. This can be used to define the narrow resolution soft function at the amplitude level. The sum over X_s in (3.17) is now empty, which allows us to write

$$\begin{aligned} &\sum_{X_s} \langle 0|\, [\mathcal{S}^\dagger]^j_{J,XY}(x)\, |X_s\rangle \, \langle X_s|\, \mathcal{S}^i_{I,VW}(0)\, |0\rangle \\ &\quad\xrightarrow{} \quad \langle 0|\, [\mathcal{S}^\dagger]^j_{J,XY}(x)\, |0\rangle \, \langle 0|\, \mathcal{S}^i_{I,VW}(0)\, |0\rangle \equiv D^i_{I,VW}\, D^{j\,*}_{J,XY} \end{aligned} \tag{3.22}$$

where $D^i_{I,VW}$ is defined as the vacuum matrix element of the soft operator (3.11).

Wino DM We discussed earlier in Sections 3.1.1 and 3.1.2 which index values are relevant for wino DM in the narrow resolution case. The indices W, Y are contracted with the photon jet function, which fixes them to $W = Y = 3$ and the indices V, X are contracted with the unobserved jet function, which means they are also fixed to $V = X = 3$. In summary, for wino DM, only the single SU(2) component $D^i_{I,33}$ of the soft amplitude is needed.

Higgsino DM The presence of a non-vanishing hypercharge makes things a bit more intricate for Higgsino DM. Taking into account the discussion in Sections 3.1.1 and 3.1.2, we can see that the relevant soft function amplitudes which need to be computed are the following $D^i_{I,33}$, $D^i_{I,34}$, $D^i_{I,43}$ and $D^i_{I,44}$.

3.2 Derivation of the final formula

Using the definitions of the individual functions provided in the previous Section, we can now write down the factorization theorem in its final form. In Sections 3.2.1 and 3.2.2 we are first going to give the factorization theorems for the intermediate and narrow resolution cases, respectively, in their most general forms. Then, in the same Sections, we will also provide the factorization theorems specifically for wino and Higgsino DM.

Before arriving at the final factorization theorems however, we need to comment on ultrasoft modes which we have completely ignored so far. Even though soft modes have been decoupled from (anti-) collinear and non-relativistic fields, they can all still interact with ultrasoft modes. An ultrasoft Wilson line field redefinition on the other hand, takes care of decoupling ultrasoft interactions from (anti-) collinear modes at leading power. Implicitly, this has been used to write the different sectors in a factorized form. This decoupling lead to several convolutions of the ultrasoft function with the different sectors. The reason we did not include the ultrasoft function above is as follows: both the initial state as well as the anti-collinear photon final state are electrically neutral, which prohibits ultrasoft interactions. For the narrow resolution case, this is also true for the collinear and soft final states. However the intermediate resolution hard-collinear and soft final states, need not be electrically neutral. Now, one needs to remember, that all momentum components of ultrasoft modes are small compared to the corresponding hard-collinear and soft momentum modes, as can be seen from (2.17). Hence, at leading power, ultrasoft interactions can be neglected, which allows us to ignore the ultrasoft mode.

3.2.1 Intermediate resolution

Using the definitions of the unobserved collinear jet function (3.14) and of the soft function (3.19), allows us to rewrite the corresponding terms in (3.8) as follows

$$\begin{aligned}
&\int d^4x\, e^{i(p_{\chi\chi}-p_\gamma)\cdot x}\, \langle 0|\, \mathcal{G}^X_{\perp c,\mu'}(x)\, \mathcal{G}^V_{\perp c,\mu}\, |0\rangle \times \sum_{X_s} \!\!\!\!\!\!\int \langle 0|\, [\mathcal{S}^\dagger]^j_{J,XY}(x)\, |X_s\rangle\, \langle X_s|\, \mathcal{S}^i_{I,VW}(0)\, |0\rangle \\
&\quad = -2\pi\, g^\perp_{\mu\mu'} \int d^4x \int \frac{d^4p}{(2\pi)^4} \int \frac{d^4k}{(2\pi)^4}\, e^{i(p_{\chi\chi}-p_\gamma-p-k)\cdot x}\, J^{XV}(p^2, m_W)\, \boldsymbol{W}^{ij}_{IJ,VWXY}(k) \\
&\quad = -2\pi\, g^\perp_{\mu\mu'} \int \frac{d^4k}{(2\pi)^4}\, J^{XV}(4m_\chi(m_\chi - E_\gamma - n_-k/2), m_W)\, \boldsymbol{W}^{ij}_{IJ,VWXY}(k) \\
&\quad = -2\pi\, g^\perp_{\mu\mu'} \int d\omega J^{XV}(4m_\chi(m_\chi - E_\gamma - \omega/2), m_W)\, W^{ij}_{IJ,VWXY}(\omega)\,, \qquad (3.23)
\end{aligned}$$

where in passing from the second to the third line we used $p^2 \to (p_{\chi\chi} - p_\gamma - k)^2 \approx 4m_\chi(m_\chi - E_\gamma - n_-k/2)$. The convolution between the intermediate resolution collinear jet function and the soft function accounts for radiation of soft EW gauge bosons and other soft particles into the final state, and virtual corrections. Next, we note that all relevant operators for wino and Higgsino DM involve the same spin matrix (2.55), i.e. $\Gamma^{\mu\nu}_i = \epsilon^{\mu\nu}_\perp$, $i = \{1, 2, 4, 6\}$. Consequently, we can simplify

$$\langle \xi^{c\dagger}_0 \Gamma^{\mu\nu}_j \xi_0\rangle^* \langle \xi^{c\dagger}_0 \Gamma_{i,\mu\nu} \xi_0\rangle = \epsilon^{\mu\nu}_\perp \epsilon_{\perp,\mu\nu} \langle \xi^{c\dagger}_0 \xi_0\rangle^* \langle \xi^{c\dagger}_0 \xi_0\rangle = 4\,. \qquad (3.24)$$

Lastly, we can use the fact that no function in (3.8) depends on the direction of the photon momentum $\mathbf{p}_\gamma$, which allows us to execute the photon phase-space integral as follows

$$\int \frac{d^3\mathbf{p}_\gamma}{(2\pi)^3 2p^0_\gamma}\, \delta(E_\gamma - |\mathbf{p}_\gamma|) = \frac{E_\gamma}{4\pi^2}\,. \qquad (3.25)$$

Collecting all the results from the above discussion, we are able to write down the general formula for the intermediate resolution factorization theorem, assuming an arbitrary $\mathrm{SU}(2)\otimes\mathrm{U}(1)_Y$ DM multiplet

$$\frac{d(\sigma v_{\mathrm{rel}})}{dE_\gamma} = 2\sum_{I,J} S_{IJ}\,\Gamma_{IJ}(E_\gamma)\,, \tag{3.26}$$

where S_{IJ} and Γ_{IJ} represent the Sommerfeld factor and the Sudakov annihilation rate, respectively. The focus of this thesis lies on the calculation of the latter to NLL' accuracy, for the wino and Higgsino DM models. It is explicitly given by

$$\begin{aligned}\Gamma_{IJ}(E_\gamma,\mu) =& \frac{1}{(\sqrt{2})^{n_{id}}}\frac{1}{4}\frac{2}{\pi m_\chi}\sum_{i,j} C_i(\mu)C_j^*(\mu)Z_\gamma^{YW}(\mu,\nu) \\ &\times\int d\omega J_{\mathrm{int}}^{XV}(4m_\chi(m_\chi-E_\gamma-\omega/2),\mu)W_{IJ,VWXY}^{ij}(\omega)\,.\end{aligned} \tag{3.27}$$

In writing down (3.26) and (3.27) we switched from method-1 to method-2 (see Section 2.3.1) and sum over distinguishable two-particle states I, J only. This implies certain replacement rules for the potential used in the computation of the Sommerfeld effect and for the annihilation matrix Γ_{IJ} [78]. For example it introduces the factor $1/(\sqrt{2})^{n_{id}}$ in (3.27). The value of n_{id} depends on how often identical DM particles appear in the index pair I, J. Likewise, the overall factor of 2 in (3.26) is also a remnant of changing to method-2.

Wino DM The general expression for the Sudakov annihilation rate (3.27) can be further simplified if a specific DM model is assumed. For wino DM, only operators $\mathcal{O}_{1,2}$ contribute. Furthermore, we can use (3.16) and (3.20) to simplify the unobserved jet function and soft function, respectively. Lastly, remembering that the gauge indices of the photon jet function are fixed to $W = Y = 3$, we define $Z_\gamma \equiv Z_\gamma^{33}$ and write the soft function as $W_{IJ,33}^{\mathrm{SU}(2),ij} \equiv W_{IJ}^{ij}$. The wino DM Sudakov annihilation rate is then given by

$$\begin{aligned}\Gamma_{IJ}(E_\gamma,\mu)|_{\mathrm{Wino}} =& \frac{1}{(\sqrt{2})^{n_{id}}}\frac{1}{4}\frac{2}{\pi m_\chi}\sum_{i,j=1,2} C_i(\mu)C_j^*(\mu)Z_\gamma(\mu,\nu) \\ &\times\int d\omega J_{\mathrm{int}}^{\mathrm{SU}(2)}(4m_\chi(m_\chi-E_\gamma-\omega/2),\mu)W_{IJ}^{ij}(\omega)\,.\end{aligned} \tag{3.28}$$

For wino DM, the two-particle indices can take the values $I, J = (00), (+-)$.

Higgsino DM In the case of Higgsino DM, the final form Γ_{IJ} will be more involved. First of all, we can use the linear dependence of operators $\mathcal{O}_{1,2}$ (2.58) to introduce new Wilson coefficients

$$\tilde{C}_1 = \left(C_1+\frac{1}{4}C_2\right)\Big|_{j=1/2}, \qquad \tilde{C}_4 = C_4|_{j=1/2}\,, \qquad \tilde{C}_6 = C_6|_{j=1/2}\,. \tag{3.29}$$

Again, using the above discussion, we can write the Higgsino DM Sudakov annihilation rate as follows

$$\Gamma_{IJ}(E_{\mathrm{res}}^\gamma)|_{\mathrm{Higgsino}} = \frac{1}{(\sqrt{2})^{n_{id}}}\frac{1}{4}\frac{2}{\pi m_\chi}\sum_{i,j=1,4,6}\tilde{C}_i(\mu)\tilde{C}_j^*(\mu)Z_\gamma^{WY}(\mu,\nu)$$

$$\times \int d\omega \left(J_{\text{int}}^{\text{SU(2)}}(2m_\chi(2E_{\text{res}}^\gamma - \omega), \mu)\, W_{IJ,WY}^{\text{SU(2)},ij}(\omega, \mu, \nu) \right.$$
$$\left. + \; J_{\text{int}}^{\text{U(1)}}(2m_\chi(2E_{\text{res}}^\gamma - \omega), \mu)\, W_{IJ,WY}^{\text{U(1)},ij}(\omega, \mu, \nu) \right) . \quad (3.30)$$

In the case of Higgsino DM, there are three non-relativistic two-particle indices relevant for the annihilation process. Namely $I, J = (11), (22), (+-)$, where the indices (11) and (22) refer to the neutral two-particle states $\chi_1^0\chi_1^0$ and $\chi_2^0\chi_2^0$, respectively, while $(+-)$ refers to the two-particle state $\chi^+\chi^-$ which is made up of charginos. The initial DM state is made up of two χ_1^0 particles, since χ_1^0 constitutes the lighter neutral particle (see discussion in Section 1.2.3). Note that the state $\chi_1^0\chi_2^0$ is irrelevant, since the Sommerfeld effect does not mix it either of the relevant states $\chi_1^0\chi_1^0$, $\chi_2^0\chi_2^0$ or $\chi^+\chi^-$. It is important to remark that the Higgsino DM Sudakov annihilation rate does not depend on the mass splittings δm and δm_N at the NLL' accuracy level. This implies the following relations between certain index combinations of Γ_{IJ}: $\Gamma_{(11)(11)} = \Gamma_{(11)(22)} = \Gamma_{(22)(11)} = \Gamma_{(22)(22)}$ and $\Gamma_{(11)(+-)} = \Gamma_{(22)(+-)} = \Gamma^*_{(+-)(11)} = \Gamma^*_{(+-)(22)}$.

3.2.2 Narrow resolution

If we assume an energy resolution of $E_{\text{res}}^\gamma \sim m_W^2/m_\chi$, we learned earlier that some functions in the factorization theorem need to be adjusted accordingly. For one, the gauge bosons in the unobserved jet function (3.14) are assumed to have collinear scaling, which means that J_{nrw}^{XV} has to be computed in the EW broken limit with massive SM particles. Furthermore, the narrow energy resolution prohibits real soft radiation of EW gauge bosons into the final state. Consequently, the narrow resolution soft function is defined at the amplitude level (3.22). Note that the soft coefficients $D_{I,VW}^i$ are independent of ω, which means that the convolution with the unobserved jet function disappears for the narrow resolution cross section. The Sommerfeld factor S_{IJ} does not depend on E_{res}^γ and thus remains the same for both resolution cases.

Wino DM For wino DM the Sudakov-resummed annihilation rate for the narrow resolution case is given by

$$\Gamma_{IJ}^{\text{nrw}}(E_{\text{res}}^\gamma)|_{\text{Wino}} = \frac{1}{(\sqrt{2})^{n_{id}}} \frac{1}{4} \frac{2}{\pi m_\chi} \sum_{i,j=1,2} C_i(\mu) C_j^*(\mu) Z_\gamma^{33}(\mu, \nu)$$
$$\times D_{I,33}^{\text{W},i}(\mu, \nu) D_{J,33}^{\text{W},j*}(\mu, \nu) J_{\text{nrw}}^{33}(4m_\chi E_{\text{res}}^\gamma, \mu, \nu) . \quad (3.31)$$

The two-particle indices I and J can take the values $I, J = (00), (+-)$ and the superscript W on the soft coefficients identifies them as the wino DM soft coefficients.

Higgsino DM For Higgsino DM the Sudakov-resummed annihilation rate for the narrow resolution case is given by

$$\Gamma_{IJ}^{\text{nrw}}(E_{\text{res}}^\gamma)|_{\text{Higgsino}} = \frac{1}{(\sqrt{2})^{n_{id}}} \frac{1}{4} \frac{2}{\pi m_\chi} \sum_{i,j=1,4,6} \tilde{C}_i(\mu) \tilde{C}_j^*(\mu) Z_\gamma^{WY}(\mu, \nu)$$
$$\times D_{I,VW}^{\text{H},i}(\mu, \nu) D_{J,XY}^{\text{H},j*}(\mu, \nu) J_{\text{nrw}}^{XV}(4m_\chi E_{\text{res}}^\gamma, \mu, \nu) , \quad (3.32)$$

where the $\text{SU(2)}\otimes\text{U(1)}_Y$ indices are summed over $V, W, X, Y = 3, 4$. The two-particle indices I and J can take the values $I, J = (11), (22), (+-)$ and the superscript H on the soft coefficients identifies them as the Higgsino DM soft coefficients.

4 Resummation

The functions appearing in the annihilation rates derived in the previous Section all "live" different natural scales. The factorization theorems that we derived allow us to compute each function at its natural scale, which means that they will not exhibit any large Sudakov logarithms. In order to arrive at a physical, scale-independent cross-section however, all functions need to be evolved to one common reference scale. To achieve this, one has to solve the renormalization group equations (RGEs), for the scales μ (virtuality) and ν (rapidity), for each function appearing in the Γ_{IJ} which results in evolution factors for each function. Therefore, all functions can be calculated perturbatively at their own characteristic scale and then be evolved to a common reference scale in μ and ν. Since each function is evaluated at its own natural scale, no large logarithms are present in the perturbative calculations. All of the large logarithms are resummed in the evolution factors originating from the solution of the RGEs. How this works in practice will be demonstrated explicitly for each function in Section 6.

The factorization theorems put constraints on the anomalous dimensions governing the RG and RRG equations of the various functions in Γ_{IJ}. The final result must be independent of the virtuality and rapidity scale, which offers a strong check on the correctness of the calculation. After having solved all RG and RRG equations, in Section 6.5 we will confirm explicitly the RG and RRG invariance for both models and both resolutions. Before moving on however, let us discuss which common reference scales were chosen in the narrow and intermediate resolution cases.

Narrow resolution In the case of the narrow resolution, the unobserved jet function, the photon jet function and the soft function all have the natural soft virtual scale $\mu_s \sim m_W$. In this case it is thus easiest to evolve the Wilson coefficients, which naturally reside at the hard scale $\mu_h \sim 2m_\chi$, down to the soft scale. Furthermore, the collinear and anti-collinear jet functions have as natural rapidity scale $\nu_h \sim 2m_\chi$, while the soft scale has as natural rapidity scale $\nu_s \sim m_W$. We choose to evolve the soft function from $\nu_s \to \nu_h$.

Intermediate resolution When computing the intermediate resolution cross sections, one has to choose a specific path to resum all functions to one common scale. Since there are more scales involved, it is not as clear as in the narrow resolution case and two possibilities for the resummation paths are displayed in Figure 4.1.

One possibility, shown in the left plot of Figure 4.1, is to evolve all functions in virtuality μ and rapidity ν to the soft scales μ_s and ν_s. This means that the Wilson coefficients are evolved in μ from the hard scale $\mu_h \sim 2m_\chi$ down to the soft scale $\mu_s \sim m_W$ and the unobserved jet functions are also evolved from the jet scale $\mu_j \sim \sqrt{2m_\chi m_W}$ to the soft scale. The photon jet function does not need to be resummed in virtuality, but the rapidity scale is evolved from $\nu_h \sim 2m_\chi$ to $\nu_s \sim m_W$. The natural virtuality and rapidity scales of the soft functions are the soft scales μ_s and ν_s, so there is no need for resummation here. This resummation scheme is more in line with the narrow resolution case, where there are only two virtuality scales μ_h and μ_s and here it is most convenient to simply evolve the Wilson coefficients to the soft scale.

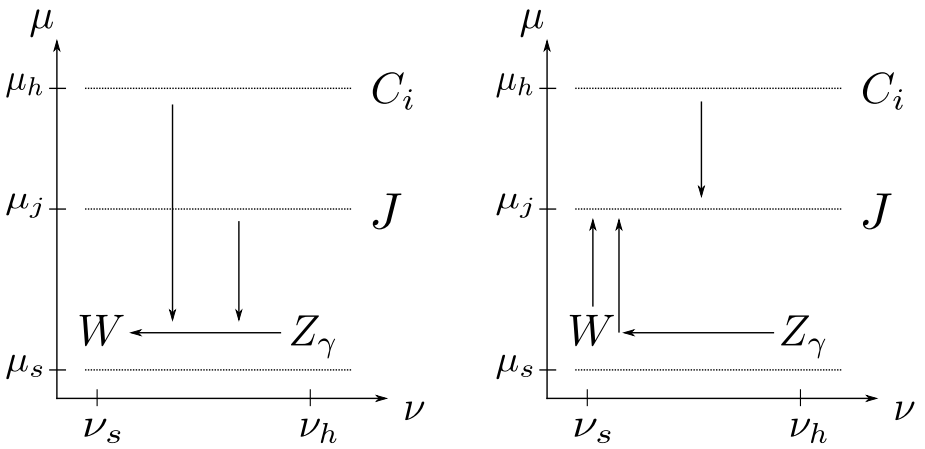

Figure 4.1: Different possibilities for resumming the functions in the factorization theorem. Left: common reference scale is μ_s. Right: common reference scale is μ_j. In both cases, Z_γ is evolved in ν from ν_h to ν_s. This Figure has been extracted from [7].

While the first resummation option allows one to treat the resummation of both resolution cases on a similar footing, there is another option that is more conventional in the presence of an intermediate hard-collinear scale. This resummation scheme is illustrated in the right plot of Figure 4.1. Here, the common virtuality reference scale is chosen to be the jet scale μ_j. As a consequence, the Wilson coefficients are evolved from μ_h to μ_j. The photon jet function is first evolved in ν from ν_h to ν_s and then in μ from μ_s to μ_j. The soft function is also evolved in μ from μ_s to μ_j and the unobserved jet function does not require resummation since with the scale choice $\mu = \mu_j$ all logarithms are small.

Both resummation schemes give the same results up to effects beyond the accuracy of the truncation of the RG equations. This was checked explicitly for the wino DM model by expanding the resummed cross section up to two-loops and the discussion for this analysis is presented in Appendix A.

5 Mass corrections

The factorization formulas derived in Section 3 only take into account leading order power corrections. This means that terms proportional to v^2, $\delta m/m_\chi$ or $\lambda \sim m_W/m_\chi$ and higher powers are neglected. The DM velocity has a value of $v^2 \sim 10^{-6}$ for DM annihilation in Milky Way-sized galaxies and the mass splittings are of the order of $\delta m/m_\chi \sim 10^{-4}$ for wino and Higgsino DM models. Corrections from v^2 and $\delta m/m_\chi$ can thus safely be discarded since they are negligible compared to the percent level accuracy of NLL' resummed annihilation rates. Linear mass corrections on the other hand might give also give percent level corrections since $m_W/m_\chi \sim 0.1 \times (1\text{ TeV}/m_\chi)$. This is especially interesting for Higgsino DM, where the correct relic density is achieved for $m_\chi \sim 1$ TeV. In this Section we investigate whether such linear $\mathcal{O}(\lambda)$, next-to-leading-power mass corrections may be important. The computations presented here have been done independently by CH, Kai Urban and Martin Vollmann, in order to assure their correctness. The arguments given here follow Section 3 of [8].

In order to assess the impact of power corrections on the cross section we compute the amplitude for $\chi^0\chi^0 \to \gamma\gamma$ to $\mathcal{O}(\lambda)$ in the full theory. For Higgsino DM, we find for the amplitude at vanishing relative velocity $v = 0$, expanded in $\lambda = m_W/m_\chi$ up to $\mathcal{O}(\lambda)$ the expression

$$\begin{aligned} i\mathcal{M}^{\chi_1^0\chi_1^0\to\gamma\gamma} &= \frac{ie^4}{16\pi^2 s_W^2 m_\chi^2}\frac{1}{2}\varepsilon_\mu^*(p_3)\varepsilon_\nu^*(p_4)\bar{v}(p_2)\left[\gamma^\mu,\gamma^\nu\right]\not{p}_3 u(p_1) \\ &\quad\times\left[-2\pi\frac{m_\chi}{m_W}\left(1+\frac{1}{24}\frac{m_W^2}{m_\chi^2}\right)-2+\frac{\pi^2}{4}+(-1+i\pi)\ln\frac{4m_\chi^2}{m_W^2}+\mathcal{O}\left(\frac{m_W^2}{m_\chi^2}\right)\right] \end{aligned} \tag{5.1}$$

The amplitude (5.1) was computed assuming Higgsino DM. We note however that this result also holds for wino DM up to an overall constant. More specifically, $i\mathcal{M}^{\chi^0\chi^0\to\gamma\gamma}_{\text{Wino}} = 4i\mathcal{M}^{\chi_1^0\chi_1^0\to\gamma\gamma}_{\text{Higgsino}}$, since the only different relevant couplings are $\frac{1}{2}\bar{\chi}_1^0 \not{W}^+\chi^-$ for the Higgsino and $\bar{\chi}^0\not{W}^+\chi^-$ for the wino. In order to arrive at this result, we used `FeynRules` [90] for the model implementation, `FeynArts` [91] for the Feynman rules and diagram generation, `FormCalc` [92] for amplitude processing and `PackageX` [93] for the evaluation of the loop integrals.

Having computed (5.1) to next-to-leading-power in the mass corrections, we now need to identify the origin of each term. We will see below that the finite and logarithmic pieces are all included in the Sudakov annihilation rate. In particular, by removing the m_χ/m_W and m_W/m_χ terms and squaring the remaining amplitude, we reproduce the result we obtained from performing an NNLO expansion of the Sudakov annihilation rate. The relevant results from this expansion are collected in (A.33). What remains to be checked is whether the terms m_χ/m_W and more interestingly m_W/m_χ are associated with the Sommerfeld effect, or whether they also originate from the Sudakov factor.

To confirm this, we compute the diagram depicted in Figure 5.1 (and the one with the photon lines crossed) in the potential region up to $\mathcal{O}(\lambda)$ using the strategy of regions. The potential region of these diagrams is associated with the Sommerfeld effect and this procedure hence allows us to check if the m_χ/m_W and m_W/m_χ terms in (5.1) should

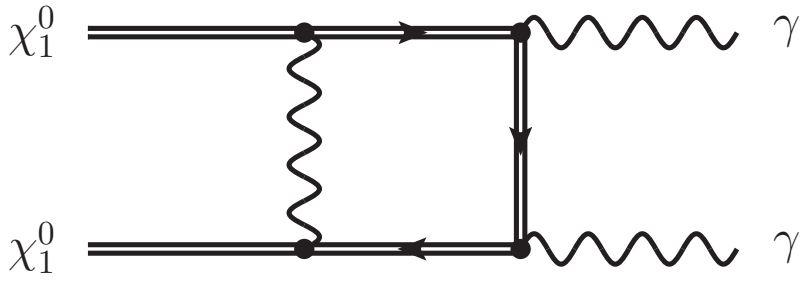

Figure 5.1: Diagram computed in the potential region to subleading power to subtract the Sommerfeld effect from the fixed order result. This Figure has been extracted from [8].

be associated with the Sommerfeld factor. We verify that the mass ratio terms in (5.1) are indeed associated with the non-relativistic dynamics of the problem. In particular, in the context of non-relativistic effective theory, the coefficient 1/24 originates partly from subleading-power potentials (-1/8), which are $\mathcal{O}(v^2)$ and thus not included in [81], and partly from (at the squared amplitude level) the matrix element of the dimension-8 derivative S-wave operator $\mathcal{P}(^1S_0)$ introduced in [78,82] (+1/6). In the non-relativistic effective theory, leading-power contributions are counted as $\mathcal{O}(\lambda^{-1})$ and linear power corrections actually should be treated as quadratic corrections $\mathcal{O}(\lambda^2)$ to the leading Sommerfeld enhancement, as depicted in (5.1). This means that the next-to-leading-power correction, including the factor 1/24, will be responsible for a 3×10^{-4} correction to the cross section. In conclusion, we confirm that for both wino and more importantly also for Higgsino DM it is safe to neglect power corrections in m_W/m_χ, since these do not degrade the percent level accuracy at NLL' in the interesting m_χ regime.

6 NLL' resummation

In this Section, we collect the one-loop results for the hard matching coefficients, the (anti-) collinear and the soft functions which are the required ingredients to compute the cross section at NLL' accuracy. We furthermore solve the renormalization group equations (RGEs) and rapidity renormalization group equations (RRGs) of these functions, which is required for resummation. The results are presented in the most general possible way, i.e. the matching coefficients are computed for general isospin j and hypercharge Y. Also, the (anti-) collinear jet functions are universal. Only the soft functions are model specific and had to be computed separately for wino DM with $j = 1$, $Y = 0$ and Higgsino DM with $j = 1/2$, $Y = 1/2$. Lastly, we confirm the consistencies of the different renormalization groups. This Section follows, collects and extends the results that have already been given in Section 3 and Appendix B.2 of [7] and Appendix C of [8].

6.1 Hard function

This Section discusses the computation of the Wilson coefficients and their resummation. For completeness, we compute all Wilson coefficients C_i, $i = 1{-}6$ with general isospin j and hypercharge Y. Since resummation is model specific, we will discuss wino and Higgsino DM separately in Section 6.1.4 and only for the relevant operators that contribute to $\chi^0\chi^0 \to \gamma + X$. As is common for complex calculations, they are usually done independently by different people. In the case of the hard function the results which are specific to wino DM have been computed by Alessandro Broggio and CH, while the results specific to Higgsino DM have been computed by CH and Kai Urban.

6.1.1 Method of computation and bare amplitudes

The hard matching coefficients are computed by matching the full theory (SM plus an isospin-j DM multiplet) onto the effective theory. This is done via a matching condition, which requires on-shell amplitudes computed in the full and the effective theory for $2 \to 2$ annihilation of two DM fields into two gauge bosons of SU(2) and/or U(1)$_Y$ type to be equal

$$\mathcal{M}^{AB}_{\text{full}}(\{p,s\}) = \frac{1}{2m_\chi} \sum_i C_i^{\text{bare}}(\{p\})\ (2m_\chi)\langle \mathcal{O}_i^{\text{bare}}\rangle^{AB}(\{p,s\})\,, \tag{6.1}$$

where $\mathcal{M}^{AB}_{\text{full}}(\{p,s\})$ is the UV-renormalized amplitude in the full theory and the symbol $\{p,s\}$ represents the momenta and spin/polarization orientations of the four external particles. For the computation, the momenta of the initial-state DM particles are set to $p_\chi^\mu = m_\chi(1,\mathbf{0})$ and the momenta of the final-state gauge bosons are $p_3^\mu = m_\chi n_-^\mu$ and $p_4^\mu = m_\chi n_-^\mu$. This is possible since the operators $\mathcal{O}_i$ in (6.1) are of S-wave type as explained in Section 2.4, which means that we can set the relative momenta of the annihilating particles to zero when computing their coefficients. To extract the individual matching coefficients, we define projectors which project out the specific group and spin structures

of the individual operators

$$\sum_s \mathcal{P}_i^{AB}(\{p,s\})\,\mathcal{M}_{\text{full}}^{AB}(\{p,s\}) = \mathcal{M}_{i,\,\text{full}}(4m_\chi^2)\,, \tag{6.2}$$

where $\mathcal{M}_{i,\,\text{full}}$ are the full theory projected amplitudes, associated with the gauge and spin structures of operators $\mathcal{O}_i$. Since $m_\chi \gg m_W$, the hard matching coefficients are computed in the EW symmetric limit and all SM particles are assumed to be massless. This means that all loop diagrams on the effective theory side of the matching computation are scaleless and vanish in dimensional regularization, since the heavy WIMPs are integrated out. Hence the expressions in (6.2) directly correspond to the bare matching coefficients. The specific form of the projectors is as follows

$$\begin{aligned}
\mathcal{P}_1^{AB}(\{p,s\}) &= \frac{1}{(3-4c_2(j))(2j+1)}\left(\frac{1-2c_2(j)}{2}T_1^{AB}+T_2^{AB}\right)\\
&\quad\times\frac{\bar u(p_\chi,s_1)(\not p_+-\not p_-)[\gamma^\sigma,\gamma^\rho]v(p_\chi,s_2)\varepsilon_\rho(p_3,s_3)\varepsilon_\sigma(p_4,s_4)}{32\,m_\chi\,(1-3\epsilon+2\epsilon^2)}\,,\\
\mathcal{P}_2^{AB}(\{p,s\}) &= \frac{1}{(3-4c_2(j))(2j+1)}\left(T_1^{AB}+\frac{-3}{c_2(j)}\,T_2^{AB}\right)\\
&\quad\times\frac{\bar u(p_\chi,s_1)(\not p_+-\not p_-)[\gamma^\sigma,\gamma^\rho]v(p_\chi,s_2)\varepsilon_\rho(p_3,s_3)\varepsilon_\sigma(p_4,s_4)}{32\,m_\chi\,(1-3\epsilon+2\epsilon^2)}\,,\\
\mathcal{P}_3^{AB}(\{p,s\}) &= \frac{i\varepsilon^{CAB}T^C}{2c_2(j)(2j+1)}\,\frac{\bar u(p_\chi,s_1)(\not p_+-\not p_-)g_\perp^{\sigma\rho}v(p_\chi,s_2)\varepsilon_\rho(p_3,s_3)\varepsilon_\sigma(p_4,s_4)}{32\,m_\chi\,(1-\epsilon)}\,,\\
\mathcal{P}_4^{AB}(\{p,s\}) &= \frac{T^A\delta^{B4}}{c_2(j)(2j+1)}\,\frac{\bar u(p_\chi,s_1)(\not p_+-\not p_-)[\gamma^\sigma,\gamma^\rho]v(p_\chi,s_2)\varepsilon_\rho(p_3,s_3)\varepsilon_\sigma(p_4,s_4)}{32\,m_\chi\,(1-3\epsilon+2\epsilon^2)}\,,\\
\mathcal{P}_5^{AB}(\{p,s\}) &= \frac{T^A\delta^{B4}}{c_2(j)(2j+1)}\,\frac{\bar u(p_\chi,s_1)(\not p_+-\not p_-)g_\perp^{\sigma\rho}v(p_\chi,s_2)\varepsilon_\rho(p_3,s_3)\varepsilon_\sigma(p_4,s_4)}{32\,m_\chi\,(1-\epsilon)}\,,\\
\mathcal{P}_6^{AB}(\{p,s\}) &= \frac{2\delta^{A4}\delta^{B4}}{(2j+1)}\,\frac{\bar u(p_\chi,s_1)(\not p_+-\not p_-)[\gamma^\sigma,\gamma^\rho]v(p_\chi,s_2)\varepsilon_\rho(p_3,s_3)\varepsilon_\sigma(p_4,s_4)}{32\,m_\chi\,(1-3\epsilon+2\epsilon^2)}\,,
\end{aligned} \tag{6.3}$$

where $\epsilon = (4-d)/2$, d is the space-time dimension and $c_2(j) = j(j+1)$ for an isospin-j representation. The projectors $\mathcal{P}_{1,2,4,6}$ and $\mathcal{P}_{3,5}$ respectively have the same Dirac and Lorentz index structure between them, while group index structures are different. This reflects the Dirac, Lorentz and group structures of the operator basis (2.53). Both the operators and amplitudes can be considered as operators in spin space.

For NLL' accuracy, we need to compute the matching coefficients at one-loop order. In Figure 6.1, we show a representative sample of diagrams that appear in the matching calculation. The matching procedure was automatized using a number of software tools. In particular, as for the computation of the fixed order process $\chi^0\chi^0 \to \gamma\gamma$ in Section 5, we used `FeynRules` [90], `FeynArts` [91] and `FormCalc` [92] for model implementation and amplitude generation. Afterwards, a private code written in `FORM` [94] was used to simplify Dirac structures and SU(2) group structures. This works as follows: `FormCalc` is able to output the set of amplitudes describing the annihilation process in a `FORM`-compatible style. These amplitudes are then loaded into the `FORM`-code for further processing. There, after having implemented the projectors (6.3), one multiplies the `FormCalc`-amplitudes with $\mathcal{P}_i$. The next step is to simplify the group structures as much as possible, for which the necessary relations are given in [95]. Then, one can take the trace of the Dirac structure and use the kinematics of the annihilation process to simplify scalar products. Lastly, any

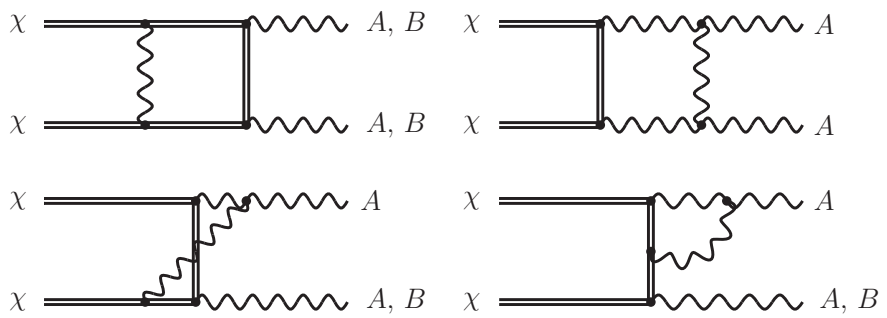

Figure 6.1: Representative sample of one-loop diagrams contributing to the computation of the Wilson coefficients. External A and B represent SU(2) and U(1)$_Y$ gauge bosons, respectively. This Figure has been extracted [7].

scalar products in the numerator involving the loop momentum are removed using the structures of the denominators of the amplitude's propagators. An example for this is

$$\begin{aligned}\frac{k\cdot p_\chi}{(k^2-m_\chi^2)(k-p_\chi)^2} =& \frac{-\frac{1}{2}\left[(k-p_\chi)^2-p_\chi^2\right]}{(k^2-m_\chi^2)(k-p_\chi)^2}\\ =& -\frac{1}{2}\frac{1}{(k^2-m_\chi^2)}+\frac{p_\chi^2}{2}\frac{1}{(k^2-m_\chi^2)(k-p_\chi)^2}\,,\end{aligned} \tag{6.4}$$

where k is the loop momentum. Removing all loop momenta from the numerators like this leaves us with scalar integrals only. Finally, `Reduze` [96] was used to reduce the scalar loop integrals to a set of seven master integrals via integration by parts. These master integrals were then computed by hand and the results are given by

$$\begin{aligned}&\int\frac{d^dk}{(2\pi)^d}\frac{1}{((k+p_\chi)^2-m_\chi^2)((k+p_\chi-p_4)^2-m_\chi^2)((k-p_\chi)^2-m_\chi^2)} =\\ &\qquad i(4m_\chi^2)^{-\epsilon}(e^{-\gamma_E}4\pi)^\epsilon\left(-\frac{\pi^2}{8m_\chi^2}\right)\\ &\int\frac{d^dk}{(2\pi)^d}\frac{1}{k^2((k+p_\chi)^2-m_\chi^2)((k-p_\chi)^2-m_\chi^2)} = i(4m_\chi^2)^{-\epsilon}(e^{-\gamma_E}4\pi)^\epsilon\left(-\frac{\pi^2}{8m_\chi^2}\right)\\ &\int\frac{d^dk}{(2\pi)^d}\frac{1}{k^2((k-p_\chi)^2-m_\chi^2)} = i(4m_\chi^2)^{-\epsilon}(e^{-\gamma_E}4\pi)^\epsilon\left(\frac{1}{\epsilon}+2\right)\\ &\int\frac{d^dk}{(2\pi)^d}\frac{1}{((k+p_\chi)^2-m_\chi^2)} = i(4m_\chi^2)^{-\epsilon}(e^{-\gamma_E}4\pi)^\epsilon m_\chi^2\left(\frac{1}{\epsilon}+1+2\ln 2\right)\\ &\int\frac{d^dk}{(2\pi)^d}\frac{1}{(k^2-m_\chi^2)((k-p_3)^2-m_\chi^2)(k+p_\chi-p_3)^2(k-p_\chi)^2} =\\ &\qquad\frac{i(4m_\chi^2)^{-\epsilon}(e^{-\gamma_E}4\pi)^\epsilon}{m_\chi^4}\left(\frac{1}{4\epsilon^2}-\frac{7}{48}\pi^2\right)\\ &\int\frac{d^dk}{(2\pi)^d}\frac{1}{(k^2-m_\chi^2)(k+p_\chi)^2(k+p_\chi-p_4)^2(k-p_\chi)^2} =\\ &\qquad\frac{i(4m_\chi^2)^{-\epsilon}(e^{-\gamma_E}4\pi)^\epsilon}{m_\chi^4}\left(-\frac{1}{4\epsilon^2}-\frac{i\pi}{8\epsilon}+\frac{\pi^2}{12}\right)\\ &\int\frac{d^dk}{(2\pi)^d}\frac{1}{(k+p_\chi)^2(k+p_\chi-p_4)^2} = i(4m_\chi^2)^{-\epsilon}(e^{-\gamma_E}4\pi)^\epsilon\left(\frac{1}{\epsilon}+2\right)\,,\end{aligned} \tag{6.5}$$

The results of this matching procedure are the following bare projected full theory amplitudes

$$\begin{aligned}
\mathcal{M}^{\text{bare}}_{1\,\text{full}}(4m_\chi^2) &= \frac{g^4_{2\,\text{bare}}}{16\pi^2}(4m_\chi^2)^{-\epsilon}(e^{-\gamma_E}4\pi)^\epsilon\left[\frac{1}{\epsilon}c_2(j)\,(2-2i\pi)-c_2(j)\left(4-\frac{\pi^2}{2}\right)\right]\\
\mathcal{M}^{\text{bare}}_{2\,\text{full}}(4m_\chi^2) &= g^2_{2\,\text{bare}}+\frac{g^2_{2\,\text{bare}}\,g^2_{1\text{bare}}Y^2}{16\pi^2}\left(\frac{\pi^2}{2}-10\right)+\frac{g^4_{2\,\text{bare}}}{16\pi^2}(4m_\chi^2)^{-\epsilon}(e^{-\gamma_E}4\pi)^\epsilon\\
&\quad\times\left[-\frac{4}{\epsilon^2}+\frac{1}{\epsilon}\,(-6+2i\pi)+16-\frac{\pi^2}{6}-c_2(j)\left(10-\frac{\pi^2}{2}\right)\right]\\
\mathcal{M}^{\text{bare}}_{3\,\text{full}}(4m_\chi^2) &= \frac{g^2_{2\,\text{bare}}\,g^2_{1\text{bare}}Y^2}{16\pi^2}(4m_\chi^2)^{-\epsilon}(e^{-\gamma_E}4\pi)^\epsilon\left(-\frac{6}{\epsilon}-12+2\pi^2-28\log 2\right)\\
&\quad+\frac{g^4_{2\,\text{bare}}}{16\pi^2}(4m_\chi^2)^{-\epsilon}(e^{-\gamma_E}4\pi)^\epsilon\left[-\frac{6c_2(j)}{\epsilon}+\frac{20}{3}-2\pi^2+8\log 2\right.\\
&\quad\left.+c_2(j)\left(-12+2\pi^2-28\log 2+(1+2j)\left(\frac{26}{9}-\frac{\pi^2}{3}+\frac{2}{9}n_G\right)\right)\right]\,,\\
\mathcal{M}^{\text{bare}}_{4\,\text{full}}(4m_\chi^2) &= g_{2\,\text{bare}}\,g_{1\text{bare}}Y+\frac{g_{2\,\text{bare}}\,g^3_{1\text{bare}}Y^3}{16\pi^2}\left(\frac{\pi^2}{2}-10\right)+\frac{g^3_{2\,\text{bare}}\,g_{1\text{bare}}Y}{16\pi^2}\\
&\quad\times(4m_\chi^2)^{-\epsilon}(e^{-\gamma_E}4\pi)^\epsilon\left[-\frac{2}{\epsilon^2}-\frac{2}{\epsilon}+\frac{\pi^2}{6}+6+c_2(j)\left(\frac{\pi^2}{2}-10\right)\right]\,,\\
\mathcal{M}^{\text{bare}}_{5\,\text{full}}(4m_\chi^2) &= 0\,,\\
\mathcal{M}^{\text{bare}}_{6\,\text{full}}(4m_\chi^2) &= g^2_{1\text{bare}}Y^2+\frac{g^2_{2\text{bare}}g^2_{1\text{bare}}Y^2}{16\pi^2}\,c_2(j)\,\left(\frac{\pi^2}{2}-10\right)+\frac{g^4_{1\text{bare}}Y^4}{16\pi^2}\,\left(\frac{\pi^2}{2}-10\right)\,,
\end{aligned}\tag{6.6}$$

where

$$g_{2\text{bare}}=Z_{g_2}\tilde{\mu}^\epsilon\hat{g}_2(\mu)\,,\quad g_{1\text{bare}}=Z_{g_1}\tilde{\mu}^\epsilon\hat{g}_1(\mu)\,,\quad \tilde{\mu}^2=\frac{\mu^2e^{\gamma_E}}{4\pi}\,.\tag{6.7}$$

For reasons of brevity, we suppress the μ-dependence of the renormalized SU(2) and $\mathrm{U}(1)_Y$ coupling constants in intermediate results. Having computed the bare amplitudes, we now need to remove the UV divergences, which is done by coupling, field and DM mass renormalization. The coupling constants are renormalized in the $\overline{\text{MS}}$ scheme while the mass and field renormalization is done in the on-shell scheme so that no further residue factor is required to obtain the on-shell amplitude. The SU(2) and $\mathrm{U}(1)_Y$ coupling, DM mass and field renormalization, and the SU(2) and $\mathrm{U}(1)_Y$ gauge boson field renormalization constants are respectively given by

$$Z_{g_2}=1+\frac{\hat{g}_2^2}{16\pi^2}\,\frac{1}{\epsilon}\left[\frac{2}{3}c(j)r-\frac{43}{12}+\frac{2}{3}n_G\right]\,,\tag{6.8}$$

$$Z_{g_1}=1+\frac{\hat{g}_1^2Y^2}{16\pi^2}\,\frac{1}{\epsilon}\left[\frac{2}{3}r+\frac{1}{12}+\frac{10}{9}n_G\right]\,,\tag{6.9}$$

$$Z_{m_\chi}=1-\frac{\left(\hat{g}_2^2c_2(j)+\hat{g}_1^2Y^2\right)}{16\pi^2}e^{\gamma_E\epsilon}\Gamma(1+\epsilon)\Big(\frac{\mu^2}{m_\chi^2}\Big)^\epsilon\,\frac{3-2\epsilon}{\epsilon(1-2\epsilon)}\,,\tag{6.10}$$

$$Z_\chi=1-\frac{\left(\hat{g}_2^2c_2(j)+\hat{g}_1^2Y^2\right)}{16\pi^2}e^{\gamma_E\epsilon}\Gamma(1+\epsilon)\Big(\frac{\mu^2}{m_\chi^2}\Big)^\epsilon\,\frac{3-2\epsilon}{\epsilon(1-2\epsilon)}\,,\tag{6.11}$$

$$Z_A=1+\frac{\hat{g}_2^2}{16\pi^2}\Big(\frac{\mu^2}{m_\chi^2}\Big)^\epsilon\Big[-\frac{4}{3\epsilon}c(j)r+\mathcal{O}(\epsilon)\Big]\,,\tag{6.12}$$

$$Z_B = 1 + \frac{\hat{g}_1^2 Y^2}{16\pi^2}\Big(\frac{\mu^2}{m_\chi^2}\Big)^\epsilon\Big[-\frac{4}{3\epsilon}r + \mathcal{O}(\epsilon)\Big], \tag{6.13}$$

where $c(j) = c_2(j)(2j+1)/3$ and $n_G = 3$ is the number of fermion generations. It is interesting to identify the origin of the terms in the renormalization constants of the coupling constants given in (6.8) and (6.9). The terms $2c(j)r/3$ and $2r/3$ correspond to the heavy DM fermion contributions, $-43/12$ and $1/12$ are gauge boson and Higgs contributions, while $2n_G/3$ and $10n_G/9$ arise from the SM fermion loops. The parameter r takes the values $r = 1$ for Dirac DM and $r = 1/2$ for Majorana DM.

As explained in Section 2, the heavy WIMPs are integrated out from the effective theory which means that they do not contribute to the running of the gauge couplings anymore. This is similar to the case of QCD, when switching between schemes with different massless quark flavors. To decouple the DM contribution from the running of the couplings $\hat{g}_1$ and $\hat{g}_2$, we perform the replacements

$$\begin{aligned}
\hat{g}_1^2 \quad &\longrightarrow \quad \hat{g}_1^2 + \frac{\hat{g}_1^4}{16\pi^2}\left[\frac{4}{3}r\ln\frac{\mu^2}{m_\chi^2}\right], \\
\hat{g}_1^2 \quad &\longrightarrow \quad \hat{g}_2^2 + \frac{\hat{g}_2^4}{16\pi^2}\left[\frac{4}{3}c(j)r\ln\frac{\mu^2}{m_\chi^2}\right],
\end{aligned} \tag{6.14}$$

After decoupling the DM contribution from the running of the gauge couplings and applying the renormalization constants (6.8)– (6.13) to the bare projected full theory amplitudes, we arrive at the UV-renormalized projected full theory amplitudes, which equal the bare Wilson coefficients

$$\begin{aligned}
C_1^{\text{bare}} &= \frac{\hat{g}_2^4}{16\pi^2}\left[\frac{c_2(j)}{\epsilon}(2-2i\pi) - c_2(j)\left(4-\frac{\pi^2}{2}\right) + c_2(j)(2-2i\pi)\ln\frac{\mu^2}{4m_\chi^2}\right], \\
C_2^{\text{bare}} &= \hat{g}_2^2 + \frac{\hat{g}_2^2\,\hat{g}_1^2 Y^2}{16\pi^2}\left(\frac{\pi^2}{2}-10\right) + \frac{\hat{g}_2^4}{16\pi^2}\left[-\frac{4}{\epsilon^2} + \frac{1}{\epsilon}\left(-\frac{79}{6}+\frac{4}{3}n_G + 2i\pi - 4\ln\frac{\mu^2}{4m_\chi^2}\right)\right. \\
&\quad \left. +16 - \frac{\pi^2}{6} - c_2(j)\left(10-\frac{\pi^2}{2}\right) - (6-2i\pi)\ln\frac{\mu^2}{4m_\chi^2} - 2\ln^2\frac{\mu^2}{4m_\chi^2}\right], \\
C_3^{\text{bare}} &= \frac{\hat{g}_2^2\,\hat{g}_1^2 Y^2}{16\pi^2}\left(-4+2\pi^2-16\log 2\right) + \frac{\hat{g}_2^4}{16\pi^2}\left[\frac{20}{3} - 2\pi^2 + 8\log 2 + \right. \\
&\quad \left. c_2(j)\left(-4+2\pi^2-16\log 2 + (1+2j)\left(\frac{26}{9}-\frac{\pi^2}{3}+\frac{2}{9}n_G\right)\right)\right], \\
C_4^{\text{bare}} &= \hat{g}_2\hat{g}_1 Y + \frac{\hat{g}_2\hat{g}_1^3 Y^3}{16\pi^2}\left[\frac{1}{\epsilon}\left(\frac{1}{12}+\frac{10}{9}n_G\right) + \frac{\pi^2}{2} - 10\right] \\
&\quad + \frac{\hat{g}_2^3\hat{g}_1 Y}{16\pi^2}\left[-\frac{2}{\epsilon^2} + \frac{1}{\epsilon}\left(-\frac{67}{12}+\frac{2}{3}n_G - 2\ln\frac{\mu^2}{4m_\chi^2}\right)\right. \\
&\quad \left. +6 + \frac{\pi^2}{6} + c_2(j)\left(\frac{\pi^2}{2}-10\right) - 2\ln\frac{\mu^2}{4m_\chi^2} - \ln^2\frac{\mu^2}{4m_\chi^2}\right], \\
C_5^{\text{bare}} &= 0\,, \\
C_6^{\text{bare}} &= \hat{g}_1^2 Y^2 + \frac{\hat{g}_2^2\hat{g}_1^2 Y^2}{16\pi^2}\,c_2(j)\left(\frac{\pi^2}{2}-10\right) + \frac{\hat{g}_1^4 Y^4}{16\pi^2}\left[\frac{1}{\epsilon}\left(\frac{1}{6}+\frac{20}{9}n_G\right) + \frac{\pi^2}{2} - 10\right].
\end{aligned} \tag{6.15}$$

Before moving on to discussing the cancellation of the remaining IR divergences, we should comment on some subtleties concerning the calculation of C_3^{bare} and C_5^{bare}. We will also highlight some differences between the two DM models and mention alternative methods

of computations. Since C_3^{bare} has no tree level contribution one would naively suspect that it should be finite at one loop. However, as can be seen from (6.6) this is not the case. To understand this, we note that the vanishing tree level comes from a cancellation between the s-channel diagram and the t/u-channel diagrams. This is similar to what has been observed for the corresponding quarkonium calculation in QCD [97]. On the other hand, DM mass counterterm insertions exist only for t- and u-channel diagrams but not for the s-channel diagram. This means that the mass renormalization contribution survives, resulting in a finite C_3^{bare} Wilson coefficient (6.15).

How can the same result be recuperated in bare perturbation theory, since there is apparently no bare mass to substitute the renormalized one as there is no tree-level? When performing on-shell matching, the masses of the external particles take the renormalized on-shell values at the corresponding loop order. At tree level, this means that we have bare masses from the explicit mass terms in the propagators and renormalized masses when applying on-shell kinematics to the momenta of the external particles. The cancellation between the s-channel and t/u-channel diagrams then has a one-loop difference remaining between the bare and the renormalized mass in the t- and u-channel diagrams. In this way, we also arrive at the finite result (6.15) using bare perturbation theory.

Operator $\mathcal{O}_5$ only appears in the Higgsino DM model, but even there it is irrelevant for the process of interest as already explained in Section 2.4. We also find that the corresponding Wilson coefficient vanishes at the one-loop order, which is a consequence on the Landau-Yang theorem. The theorem does not apply to non-abelian gauge theories [97,98], since the final state bosons carry an internal quantum number and structures can be form involving the group structure constant. While it is possible that these structures form for the matching coefficient of $\mathcal{O}_5$, this is not possible at the one-loop level since one of the final state gauge bosons is abelian.

To obtain the bare Wilson coefficients specific to wino and Higgsino DM from the generic expressions in (6.15), one has to set $j = 1$ and $Y = 0$ for wino DM and $j = 1/2$ and $Y = 1/2$ for Higgsino DM. It is interesting to note that for the matching procedure for Higgsino DM, one has to take into account more diagrams. This is on the one hand due to the larger operator basis which now also contains the $\mathrm{U}(1)_Y$ gauge boson and on the other hand due to the fact that Higgsino DM consists of Dirac fermions, which means that one has to take into account multiple charge flows for closed DM particle loops. Despite the differences in diagrams, it turns out that the relevant Wilson coefficients are equivalent for both Dirac and Majorana DM particles. The reason for this is explained below (6.27).

The Wilson coefficients here are computed by applying the projectors (6.3) to the full theory amplitude according to (6.2). The advantage of this method is that it allows us to use the trace properties of the γ-matrices, which greatly simplify expressions. This can be done particularly efficiently in `FORM`. Also, since the are no open Lorentz indices, one only has to deal with scalar integrals which can be reduced to a set of master integrals more easily. While this method allows for an arguably easier computation, a possible disadvantage is that one might miss evanescent operators, although these do not appear in our case as explained at the end of Section 2.4. Alternatively, one can obtain the Wilson coefficients by removing spinors and polarization vectors from the amplitudes and then use commutation relations for γ-matrices and group generators to simplify their structures as much as possible. The integrals are written in terms of Passarino-Veltman inegrals, which can be reduced and solved using for example `PackageX`. In the end, the group and Dirac structures should resemble those from the operator basis and the Wilson coefficients can be readily read off. Using this alternative method, one does not miss evanescent operators, but the calculation might be more cumbersome (although given the advent of more and

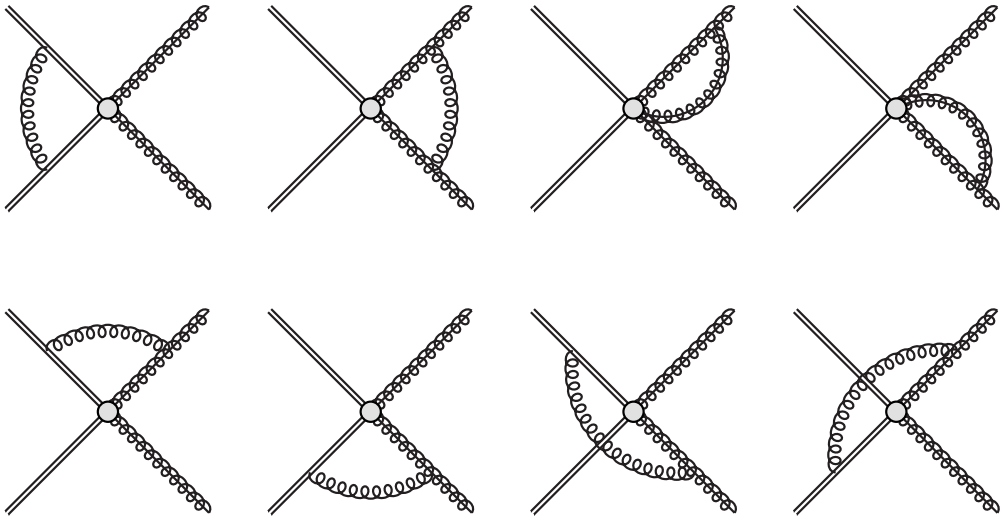

Figure 6.2: One-loop diagrams contributing to the effective theory matrix elements. Double lines represent the heavy fermions, curly lines represent soft gauge bosons while curly lines with a solid line inside represent collinear and anti-collinear gauge fields.

more reliable software for manipulating analytic expressions of Feynman diagrams, this point is not quite true anymore).

6.1.2 Operator renormalization in the effective theory

To cancel the remaining IR divergences in the bare Wilson coefficients (6.15), we need to compute the annihilation process in the effective theory. Making use of the matching condition (6.1) will then allow us to remove the IR divergences from the C_i^{bare}. However, effective theory diagrams are scaleless and therefore vanish in dimensional regularization. To regulate the IR divergences, we put the momenta for the incoming heavy DM particles and outgoing gauge bosons slightly off-shell. The relevant effective theory diagrams are depicted in Figure 6.2 and for their calculation we make use of the Feynman rules which are provided in Appendix D, as well as of the integrals

$$
\begin{aligned}
&\int [dk]\, \frac{1}{k^2(k\cdot p_3)(-k\cdot p_4)} = \frac{i}{(4\pi)^2 m_\chi^2}\left[\frac{1}{\epsilon^2}+\frac{1}{\epsilon}\left(\ln\frac{4m_\chi^2}{\mu}-\ln\left(-\frac{p_3^2}{\mu^2}\right)-\ln\left(-\frac{p_4^2}{\mu^2}\right)-i\pi\right)\right]\\
&\int [dk]\, \frac{1}{k^2(-k\cdot p_\chi)(-k\cdot p_{3,4})} = -\frac{i}{(4\pi)^2 m_\chi^2}\left[\frac{1}{\epsilon^2}+\frac{1}{\epsilon}\left(\ln\frac{4m_\chi^2}{\mu^2}-2\ln\left(-\frac{p_{3,4}^2}{\mu^2}\right)\right)\right]\\
&\int [dk]\, \frac{1}{k^2(k\cdot p_{4,3})(k-p_{3,4})^2} = \frac{1}{p_{4,3}\cdot p_{3,4}}\frac{i}{(4\pi)^2}\left(-\frac{1}{\epsilon^2}+\frac{1}{\epsilon}\ln\left(-\frac{p_{3,4}^2}{\mu^2}\right)\right)\\
&\int [dk]\, \frac{1}{k^2(-k\cdot +p_{3,4})\cdot p_{4,3}(k-p_{3,4})^2} = \frac{1}{p_{4,3}\cdot p_{3,4}}\frac{i}{(4\pi)^2}\left(-\frac{1}{\epsilon^2}+\frac{1}{\epsilon}\ln\left(-\frac{p_{3,4}^2}{\mu^2}\right)\right)\\
&\int [dk]\, \frac{1}{k^2(k-p_{3,4})^2} = \frac{i}{(4\pi)^2}\frac{1}{\epsilon}\\
&\int [dk]\, \frac{1}{k^2(k\cdot p_\chi)(-k\cdot p_\chi)} = \frac{i}{(4\pi)^2 m_\chi^2}\frac{2}{\epsilon}\,,
\end{aligned}
\tag{6.16}
$$

where the integration measure $[dk]$ is defined in (2.2). For computing these integrals, it is useful to remember the definitions $p_\chi^\mu = m_\chi v^\mu$. $p_3^\mu = m_\chi n_-^\mu$ and $p_4^\mu = m_\chi n_+^\mu$. This allows us to obtain the following UV poles in the $\overline{\text{MS}}$ scheme

$$
\begin{aligned}
\langle \mathcal{O}_1^{\text{bare}} \rangle &= \langle \mathcal{O}_1 \rangle^{\text{tree}} \left\{ 1 + \frac{\hat{g}_1^2 Y^2}{16\pi^2} \frac{1}{\epsilon} (-2) + \frac{\hat{g}_2^2}{16\pi^2} \left[\frac{4}{\epsilon^2} + \frac{1}{\epsilon} \Big(4 - 2c_2(j) + 4i\pi + 4 \ln \frac{\mu^2}{4m_\chi^2} \Big) \right] \right\}, \\
\langle \mathcal{O}_2^{\text{bare}} \rangle &= \langle \mathcal{O}_1 \rangle^{\text{tree}} \frac{\hat{g}_2^2}{16\pi^2} \frac{1}{\epsilon} \Big[- c_2(j)(2 - 2i\pi) \Big] \\
&\quad + \langle \mathcal{O}_2 \rangle^{\text{tree}} \left\{ 1 + \frac{\hat{g}_1^2 Y^2}{16\pi^2} \frac{1}{\epsilon} (-2) + \frac{\hat{g}_2^2}{16\pi^2} \left[\frac{4}{\epsilon^2} + \frac{1}{\epsilon} \Big(10 - 2c_2(j) - 2i\pi + 4 \ln \frac{\mu^2}{4m_\chi^2} \Big) \right] \right\}, \\
\langle \mathcal{O}_3^{\text{bare}} \rangle &= \langle \mathcal{O}_3 \rangle^{\text{tree}} \left\{ 1 + \frac{\hat{g}_1^2 Y^2}{16\pi^2} \frac{1}{\epsilon} (-2) + \frac{\hat{g}_2^2}{16\pi^2} \left[\frac{4}{\epsilon^2} + \frac{1}{\epsilon} \Big(6 - 2c_2(j) + 2i\pi + 4 \ln \frac{\mu^2}{4m_\chi^2} \Big) \right] \right\}, \\
\langle \mathcal{O}_4^{\text{bare}} \rangle &= \langle \mathcal{O}_4 \rangle^{\text{tree}} \left\{ 1 + \frac{\hat{g}_1^2 Y^2}{16\pi^2} \frac{1}{\epsilon} (-2) + \frac{\hat{g}_2^2}{16\pi^2} \left[\frac{2}{\epsilon^2} + \frac{1}{\epsilon} \Big(4 - 2c_2(j) + 2 \ln \frac{\mu^2}{4m_\chi^2} \Big) \right] \right\}, \\
\langle \mathcal{O}_5^{\text{bare}} \rangle &= \langle \mathcal{O}_5 \rangle^{\text{tree}} \left\{ 1 + \frac{\hat{g}_1^2 Y^2}{16\pi^2} \frac{1}{\epsilon} (-2) + \frac{\hat{g}_2^2}{16\pi^2} \left[\frac{2}{\epsilon^2} + \frac{1}{\epsilon} \Big(4 - 2c_2(j) + 2 \ln \frac{\mu^2}{4m_\chi^2} \Big) \right] \right\}, \\
\langle \mathcal{O}_6^{\text{bare}} \rangle &= \langle \mathcal{O}_6 \rangle^{\text{tree}} \left\{ 1 + \frac{\hat{g}_1^2 Y^2}{16\pi^2} \frac{1}{\epsilon} (-2) + \frac{\hat{g}_2^2}{16\pi^2} \frac{1}{\epsilon} (-2c_2(j)) \right\},
\end{aligned}
\tag{6.17}
$$

where $\langle \mathcal{O}_i \rangle$ corresponds to the tree-level matrix element of operator $\mathcal{O}_i$. It is important to notice that these expressions do not depend on the infrared regulator and that they only depend on the hard scale $2m_\chi$. We still need to add to the expressions in (6.17) the effective theory wavefunction renormalization factors, which read as follows

$$
\begin{aligned}
Z_{\chi_v} &= 1 + \frac{\hat{g}_1^2 Y^2}{16\pi^2} \frac{2}{\epsilon} + \frac{\hat{g}_2^2}{16\pi^2} \frac{2c_2(j)}{\epsilon}, \\
Z_A &= 1 + \frac{\hat{g}_2^2}{16\pi^2} \frac{1}{\epsilon} \Big[\frac{19}{6} - \frac{4}{3} n_G \Big], \\
Z_B &= 1 + \frac{\hat{g}_1^2 Y^2}{16\pi^2} \frac{1}{\epsilon} \Big[- \frac{1}{6} - \frac{20}{9} n_G \Big].
\end{aligned}
\tag{6.18}
$$

By combining everything we arrive at

$$
\begin{aligned}
Z_{\chi_v} Z_A \langle \mathcal{O}_1^{\text{bare}} \rangle &= \langle \mathcal{O}_1 \rangle^{\text{tree}} \left\{ 1 + \frac{\hat{g}_2^2}{16\pi^2} \left[\frac{4}{\epsilon^2} + \frac{1}{\epsilon} \left(\frac{43}{6} - \frac{4}{3} n_G + 4i\pi + 4 \ln \frac{\mu^2}{4m_\chi^2} \right) \right] \right\}, \\
Z_{\chi_v} Z_A \langle \mathcal{O}_2^{\text{bare}} \rangle &= \langle \mathcal{O}_1 \rangle^{\text{tree}} \frac{\hat{g}_2^2}{16\pi^2} \frac{1}{\epsilon} \Big[- c_2(j)(2 - 2i\pi) \Big] \\
&\quad + \langle \mathcal{O}_2 \rangle^{\text{tree}} \left\{ 1 + \frac{\hat{g}_2^2}{16\pi^2} \left[\frac{4}{\epsilon^2} + \frac{1}{\epsilon} \left(\frac{79}{6} - \frac{4}{3} n_G - 2i\pi + 4 \ln \frac{\mu^2}{4m_\chi^2} \right) \right] \right\}, \\
Z_{\chi_v} Z_A \langle \mathcal{O}_3^{\text{bare}} \rangle &= \langle \mathcal{O}_3 \rangle^{\text{tree}} \left\{ 1 + \frac{\hat{g}_2^2}{16\pi^2} \left[\frac{4}{\epsilon^2} + \frac{1}{\epsilon} \left(\frac{55}{6} - \frac{4}{3} n_G + 2i\pi + 4 \ln \frac{\mu^2}{4m_\chi^2} \right) \right] \right\}, \\
Z_{\chi_v} Z_A^{1/2} Z_B^{1/2} \langle \mathcal{O}_4^{\text{bare}} \rangle &= \langle \mathcal{O}_4 \rangle^{\text{tree}} \left\{ 1 + \frac{\hat{g}_1^2 Y^2}{16\pi^2} \frac{1}{\epsilon} \left(- \frac{1}{12} - \frac{10}{9} n_G \right) \right. \\
&\quad \left. + \frac{\hat{g}_2^2}{16\pi^2} \left[\frac{2}{\epsilon^2} + \frac{1}{\epsilon} \left(\frac{67}{12} - \frac{2}{3} n_G + 2 \ln \frac{\mu^2}{4m_\chi^2} \right) \right] \right\},
\end{aligned}
$$

$$
\begin{aligned}
Z_{\chi_v} Z_A^{1/2} Z_B^{1/2} \langle \mathcal{O}_5^{\rm bare} \rangle =& \langle \mathcal{O}_5 \rangle^{\rm tree} \left\{ 1 + \frac{\hat{g}_1^2 Y^2}{16\pi^2} \frac{1}{\epsilon} \left(-\frac{1}{12} - \frac{10}{9} n_G \right) \right. \\
& \left. + \frac{\hat{g}_2^2}{16\pi^2} \left[\frac{2}{\epsilon^2} + \frac{1}{\epsilon} \left(\frac{67}{12} - \frac{2}{3} n_G + 2 \ln \frac{\mu^2}{4 m_\chi^2} \right) \right] \right\} , \\
Z_{\chi_v} Z_B \langle \mathcal{O}_6^{\rm bare} \rangle =& \langle \mathcal{O}_6 \rangle^{\rm tree} \left\{ 1 + \frac{\hat{g}_2^1 Y^2}{16\pi^2} \frac{1}{\epsilon} \Big[-\frac{1}{6} - \frac{20}{9} n_G \Big] \right\} .
\end{aligned} \tag{6.19}
$$

The $\overline{\rm MS}$ operator renormalization constants Z_{ij} are a matrix in operator space such that $\hat{\mathcal{O}}_i^{\rm bare} = Z_{ij} \hat{\mathcal{O}}_j^{\rm ren}(\mu)$, $i,j = 1,2,3,4$. The explicit expressions for the Z_{ij} are given by

$$
\begin{aligned}
Z_{11} =& 1 + \frac{\hat{g}_2^2}{16\pi^2} \left[\frac{4}{\epsilon^2} + \frac{1}{\epsilon} \left(\frac{43}{6} - \frac{4}{3} n_G + 4 i\pi + 4 \ln \frac{\mu^2}{4 m_\chi^2} \right) \right] , \\
Z_{12} =& 0 , \\
Z_{21} =& \frac{\hat{g}_2^2}{16\pi^2} \frac{1}{\epsilon} \left[-c_2(j)(2 - 2 i\pi) \right] , \\
Z_{22} =& 1 + \frac{\hat{g}_2^2}{16\pi^2} \left[\frac{4}{\epsilon^2} + \frac{1}{\epsilon} \left(\frac{79}{6} - \frac{4}{3} n_G - 2 i\pi + 4 \ln \frac{\mu^2}{4 m_\chi^2} \right) \right] , \\
Z_{33} =& 1 + \frac{\hat{g}_2^2}{16\pi^2} \left[\frac{4}{\epsilon^2} + \frac{1}{\epsilon} \left(\frac{55}{6} - \frac{4}{3} n_G + 2 i\pi + 4 \ln \frac{\mu^2}{4 m_\chi^2} \right) \right] , \\
Z_{44} =& 1 + \frac{\hat{g}_1^2 Y^2}{16\pi^2} \frac{1}{\epsilon} \left(-\frac{1}{12} - \frac{10}{9} n_G \right) + \frac{\hat{g}_2^2}{16\pi^2} \left[\frac{2}{\epsilon^2} + \frac{1}{\epsilon} \left(\frac{67}{12} - \frac{2}{3} n_G + 2 \ln \frac{\mu^2}{4 m_\chi^2} \right) \right] , \\
Z_{55} =& 1 + \frac{\hat{g}_1^2 Y^2}{16\pi^2} \frac{1}{\epsilon} \left(-\frac{1}{12} - \frac{10}{9} n_G \right) + \frac{\hat{g}_2^2}{16\pi^2} \left[\frac{2}{\epsilon^2} + \frac{1}{\epsilon} \left(\frac{67}{12} - \frac{2}{3} n_G + 2 \ln \frac{\mu^2}{4 m_\chi^2} \right) \right] , \\
Z_{66} =& 1 + \frac{\hat{g}_1^2 Y^2}{16\pi^2} \frac{1}{\epsilon} \Big[-\frac{1}{6} - \frac{20}{9} n_G \Big] .
\end{aligned} \tag{6.20}
$$

By applying the operator renormalization constants to the UV renormalized Wilson coefficients $C_i^{\rm bare}$ as follows

$$
C_i(\mu) = Z_{ji} C_j^{\rm bare} , \tag{6.21}
$$

we find that all $1/\epsilon$ poles cancel and we obtain the explicit results for the hard matching coefficients $C_i(\mu)$, which are given below in Section 6.1.4.

6.1.3 Operator Z-factors from the anomalous dimension

Above we computed the operator renormalization factors by using the effective theory amplitudes. Another possibility to obtain Z_{ij} is by adapting the anomalous dimension knows for QCD processes [99, 100] to the SU(2) and $\mathrm{U}(1)_Y$ gauge groups. We switch to the operator basis where the DM bilinear is in a definite isospin representation

$$
\mathcal{O}' = \hat{V}^T \mathcal{O} , \quad \hat{V} = \begin{pmatrix} 1 & -\frac{c_2(j)}{3} & 0 & 0 & 0 & 0 \\ 0 & 1 & 0 & 0 & 0 & 0 \\ 0 & 0 & 1 & 0 & 0 & 0 \\ 0 & 0 & 0 & 1 & 0 & 0 \\ 0 & 0 & 0 & 0 & 1 & 0 \\ 0 & 0 & 0 & 0 & 0 & 1 \end{pmatrix} . \tag{6.22}
$$

The advantage of this representation is that the anomalous dimension at threshold is diagonal. For the case of Higgsino DM, the anomalous dimension has to account for the appearance of SU(2) and $\mathrm{U}(1)_Y$ gauge bosons, in different operators. Hence, the anomalous dimension given in (A.21) of [7] has to be augmented by terms associated to the $\mathrm{U}(1)_Y$ gauge boson. Then, to write the anomalous dimensions in a compact form and to make obvious which parts contribute to which operator, it is convenient to split the anomalous dimension into an SU(2) and a $\mathrm{U}(1)_Y$ part

$$\begin{aligned}\Gamma^{(J)}_{\mathrm{SU}(2),i} &= \frac{1}{2}\gamma_{\mathrm{cusp}}\left[c_2(\mathrm{ad})\, n_{i,\mathrm{SU}(2)}\left(\ln\frac{4m_\chi^2}{\mu^2} - i\pi\right) + i\pi c_2(J)\right] + \gamma_{\mathrm{ad}}\, n_{i,\mathrm{SU}(2)} + \gamma^J_{H,s}\,,\\ \Gamma_{\mathrm{U}(1),i} &= \gamma_{\mathrm{U}(1)}\, n_{i,\mathrm{U}(1)}\,,\end{aligned} \tag{6.23}$$

where $n_{i,\mathrm{SU}(2)}$ and $n_{i,\mathrm{U}(1)}$ give the number of SU(2) and $\mathrm{U}(1)_Y$ gauge fields in operator $\mathcal{O}_i$, J is the representation of the DM fermion pair, $c_2(\mathrm{ad})$ is the Casimir value of the SU(2) gauge boson in the adjoint representation and $c_2(J)$ the one for the DM fermion pair. The quantities γ_{ad} and $\gamma_{\mathrm{U}(1)}$ are the SU(2) and U(1) gauge boson anomalous dimensions, respectively, and $\gamma^J_{H,s}$ is the anomalous dimension of the heavy fermion pair. The anomalous dimensions have perturbative expansions in terms of $\hat\alpha_1$ and $\hat\alpha_2$

$$\begin{aligned}\gamma_{\mathrm{cusp}}(\hat\alpha_2) =& \gamma^{(0)}_{\mathrm{cusp}}\frac{\hat\alpha_2}{4\pi} + \gamma^{(1)}_{\mathrm{cusp}}\left(\frac{\hat\alpha_2}{4\pi}\right)^2 + \mathcal{O}\left(\hat\alpha_2^3\right)\,,\\ \gamma^{(0)}_{\mathrm{cusp}} =& 4\,,\quad \gamma^{(1)}_{\mathrm{cusp}} = \left(\frac{268}{9} - \frac{4\pi^2}{3}\right)c_2(\mathrm{ad}) - \frac{80}{9}n_G - \frac{16}{9}\,,\\ \gamma_{\mathrm{ad}}(\hat\alpha_2) =& \gamma^{(0)}_{\mathrm{ad}}\frac{\hat\alpha_2}{4\pi} + \mathcal{O}\left(\hat\alpha_2^2\right)\,,\\ \gamma^{(0)}_{\mathrm{ad}} =& -\beta_{0,\mathrm{SU}(2)} = -\left(\frac{43}{6} - \frac{4}{3}n_G\right)\,,\\ \gamma_{\mathrm{U}(1)}(\hat\alpha_2) =& \gamma^{(0)}_{\mathrm{U}(1)}\frac{\hat\alpha_1}{4\pi} + \mathcal{O}\left(\hat\alpha_1^2\right)\,,\\ \gamma^{(0)}_{\mathrm{U}(1)} =& -\beta_{0,\mathrm{U}(1)} = -\left(-\frac{1}{6} - \frac{20}{9}n_G\right)\,,\\ \gamma^J_{H,s} =& \gamma^{(0)}_{H,s}c_2(J)\frac{\hat\alpha_2}{4\pi} + \mathcal{O}\left(\hat\alpha_2^2\right)\,,\\ \gamma^{(0)}_{H,s} =& -2\,.\end{aligned} \tag{6.24}$$

The operator Z-factor in the $\overline{\mathrm{MS}}$ scheme can be obtained from the anomalous dimension and up to order $\hat g_1^2$, $\hat g_2^2$ it reads

$$Z_i = 1 - \frac{\hat g_2^2}{16\pi^2}\left(\frac{\Gamma'^{(0)}_{\mathrm{SU}(2),\,i}}{4\epsilon^2} + \frac{\Gamma^{(0)}_{\mathrm{SU}(2),\,i}}{2\epsilon}\right) - \frac{\hat g_1^2}{16\pi^2}\frac{\Gamma^{(0)}_{\mathrm{U}(1),\,i}}{2\epsilon} + \mathcal{O}(\hat g_2^4,\,\hat g_1^4)\,. \tag{6.25}$$

In the diagonal basis defined in (6.22) we find

$$\begin{aligned}Z_{11} =& 1 + \frac{\hat g_2^2}{16\pi^2}\left[\frac{4}{\epsilon^2} + \frac{1}{\epsilon}\left(\frac{43}{6} - \frac{4}{3}n_G + 4\ln\frac{\mu^2}{4m_\chi^2} + 4i\pi\right)\right]\,,\\ Z_{22} =& 1 + \frac{\hat g_2^2}{16\pi^2}\left[\frac{4}{\epsilon^2} + \frac{1}{\epsilon}\left(\frac{79}{6} - \frac{4}{3}n_G + 4\ln\frac{\mu^2}{4m_\chi^2} - 2i\pi\right)\right]\,,\\ Z_{33} =& 1 + \frac{\hat g_2^2}{16\pi^2}\left[\frac{4}{\epsilon^2} + \frac{1}{\epsilon}\left(\frac{55}{6} - \frac{4}{3}n_G + 4\ln\frac{\mu^2}{4m_\chi^2} + 2i\pi\right)\right]\,,\end{aligned}$$

$$
\begin{aligned}
Z_{44} =& 1 + \frac{\hat{g}_1^2}{16\pi^2}\frac{1}{\epsilon}\left(-\frac{1}{12} - \frac{10}{9}n_G\right) + \frac{\hat{g}_2^2}{16\pi^2}\left[\frac{2}{\epsilon^2} + \frac{1}{\epsilon}\left(\frac{67}{12} - \frac{2}{3}n_G + 2\ln\frac{\mu^2}{4m_\chi^2}\right)\right], \\
Z_{55} =& Z_{44}\,, \\
Z_{66} =& 1 + \frac{\hat{g}_1^2}{16\pi^2}\frac{1}{\epsilon}\left(-\frac{1}{6} - \frac{20}{9}n_G\right). \qquad (6.26)
\end{aligned}
$$

Transforming back to the non-diagonal basis, we find agreement with (6.20).

6.1.4 Wilson coefficients and resummation

Using the the operator renormalization factors Z_{ij} that were derive in the previous two Sections, we can now remove the remaining IR poles of the bare Wilson coefficients (6.15) via the relation (6.21). This results in the following expressions for the Wilson coefficients for general j and Y

$$
\begin{aligned}
C_1(\mu) =& \frac{\hat{g}_2^4}{16\pi^2}\,c_2(j)\left[(2-2i\pi)\ln\frac{\mu^2}{4m_\chi^2} - \left(4 - \frac{\pi^2}{2}\right)\right], \\
C_2(\mu) =& \hat{g}_2^2 + \frac{\hat{g}_2^2\,\hat{g}_1^2 Y^2}{16\pi^2}\left(\frac{\pi^2}{2} - 10\right) \\
&+ \frac{\hat{g}_2^4}{16\pi^2}\left[16 - \frac{\pi^2}{6} - c_2(j)\left(10 - \frac{\pi^2}{2}\right) - 6\ln\frac{\mu^2}{4m_\chi^2} + 2i\pi\ln\frac{\mu^2}{4m_\chi^2} - 2\ln^2\frac{\mu^2}{4m_\chi^2}\right], \\
C_3(\mu)|_{\text{Dirac}} =& \frac{\hat{g}_2^2\,\hat{g}_1^2 Y^2}{16\pi^2}\left(-4 + 2\pi^2 - 16\log 2\right) + \frac{\hat{g}_2^4}{16\pi^2}\left[\frac{20}{3} - 2\pi^2 + 8\log 2\right. \\
&\left. + c_2(j)\left(-4 + 2\pi^2 - 16\log 2 + (1+2j)\left(\frac{26}{9} - \frac{\pi^2}{3} + \frac{2}{9}n_G\right)\right)\right], \\
C_4(\mu) =& -\hat{g}_2\hat{g}_1 Y - \frac{\hat{g}_2\,\hat{g}_1^3 Y^3}{16\pi^2}\left(\frac{\pi^2}{2} - 10\right) \\
&- \frac{\hat{g}_2^4}{16\pi^2}\left[\frac{\pi^2}{6} + 6 + c_2(j)\left(\frac{\pi^2}{2} - 10\right) - 2\ln\frac{\mu^2}{4m_\chi^2} - \ln^2\frac{\mu^2}{4m_\chi^2}\right], \\
C_5(\mu) =& 0\,, \\
C_6(\mu) =& \hat{g}_1^2 Y^2 + \frac{\hat{g}_2^2\hat{g}_1^2 Y^2}{16\pi^2}\,c_2(j)\left(\frac{\pi^2}{2} - 10\right) + \frac{\hat{g}_1^4 Y^4}{16\pi^2}\left(\frac{\pi^2}{2} - 10\right). \qquad (6.27)
\end{aligned}
$$

We find that operators $\mathcal{O}_{1,2}$ have the same Wilson coefficients at one-loop order for both Dirac and Majorana DM. This is no surprise since a possible difference could only arise from s-channel diagrams with a fermion-fermion-gauge boson vertex. At threshold these diagrams do not contribute to the amplitude. The Wilson coefficient $C_3(\mu)$ on the other hand does depend on which type of fermion the DM is made up of. In (6.27) it is assumed that the DM consists of Dirac particles. If on the other hand we consider Majorana DM, we find

$$
\begin{aligned}
C_3(\mu)|_{\text{Majorana}} =& \frac{\hat{g}_2^4}{16\pi^2}\left[\frac{20}{3} - 2\pi^2 + 8\log 2\right. \\
&\left. + c_2(j)\left(-4 + 2\pi^2 - 16\log 2 + (1+2j)\left(\frac{4}{3} - \frac{\pi^2}{6} + \frac{2}{9}n_G\right)\right)\right]. \qquad (6.28)
\end{aligned}
$$

The Wilson coefficients C_{1-3} were computed before in [68] for $j = 1$ and $Y = 0$, i.e. the pure wino DM case, in the context of resumming the annihilation rate to the exclusive

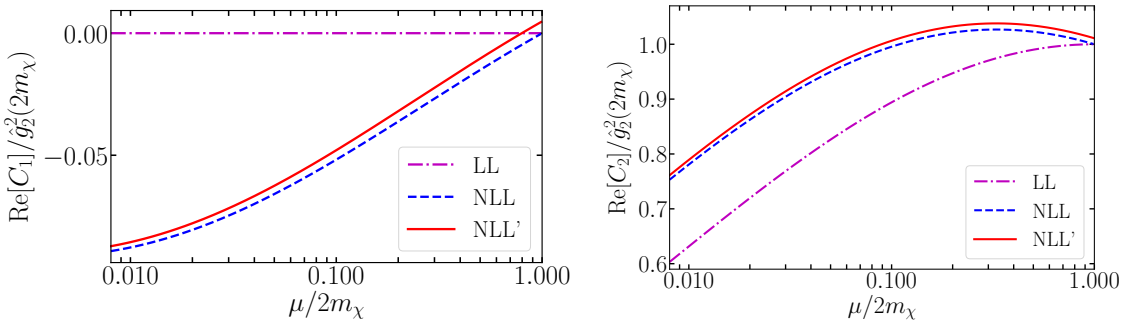

Figure 6.3: Evolution of the real part of the wino DM matching coefficients in various approximations for $m_\chi = 5$ TeV, $\mu_h = 2m_\chi$. This Figure has been extracted from [9].

$\gamma\gamma$, γZ final state. The results given there for C_3 differ from ours. We attribute this difference to an opposite sign in one of the diagrams in [68], namely T_{5b}, and missing mass renormalization (counterterm) diagrams. The subtlety related to the mass renormalization of C_3 was discussed above, in the paragraph below (6.15). On the other hand, we note again that $\mathcal{O}_3$ is not relevant for $\chi^0\chi^0 \to \gamma + X$ and this discrepancy will thus not affect the numerical values of the annihilation rate.

If we assume that the scale μ in (6.27) is of the order of the hard scale $\mu \sim \mu_h \sim 2m_\chi$, it is apparent that no large logarithms appear in the Wilson coefficients. As discussed in Section 4, all functions in the factorization theorem must be evolved to the same reference scale, which is achieved by solving the corresponding RGEs. By doing so one resums any potential large Sudakov logarithms and ends up with a reliable result. Since it is more convenient and will help to avoid confusion, we will discuss the resummation procedure separately for wino and Higgsino DM. Also, because operators $\mathcal{O}_3$ and $\mathcal{O}_5$ are irrelevant, we will disregard C_3 and C_5 from now on.

Resummation wino DM To solve the RGE, it is convenient to first rotate to a basis $\mathcal{O}'_{1,2}$ of definite isospin $J = 0$ and $J = 2$, where the DM bilinear transforms in an irreducible SU(2) representation given by

$$\mathcal{O}'_{\text{wino}} = \hat{V}^T_{\text{wino}} \mathcal{O}_{\text{wino}}, \qquad \hat{V}_{\text{wino}} = \begin{pmatrix} 1 & -\frac{c_2(j)}{3} \\ 0 & 1 \end{pmatrix}, \tag{6.29}$$

such that

$$C(\mu) = \hat{V} \begin{pmatrix} U_1^{(0)}(\mu_h, \mu) & 0 \\ 0 & U_2^{(2)}(\mu_h, \mu) \end{pmatrix} \hat{V}^{-1} C(\mu_h)\,, \tag{6.30}$$

where $C(\mu) = (C_1(\mu), C_2(\mu))^T$. The RG equation of the evolution factor in the irreducible isospin-J representation is given by

$$\frac{d}{d\ln\mu} U_i^{(J)}(\mu_h, \mu) \;=\; \Gamma^{(J)}_{\text{SU(2),i}} U_i^{(J)}(\mu_h, \mu)\,, \tag{6.31}$$

where $\Gamma^{(J)}_{\text{SU(2),i}}$ is defined in (6.23). Eq. (6.31) has to be computed numerically, since at NLL' accuracy we need to include the cusp anomalous dimension at two-loop accuracy and beyond one-loop, other SM couplings appear in the β-function. This is also true for the virtuality evolution factors of the other functions in the factorization theorems for both wino and Higgsino DM. The evolution of the Wilson coefficients $C_{1,2}$ as functions of m_χ

is shown in Figure 6.3. We refer to Section 7 for a discussion of the numerical parameter values that were used for generating Figure 6.3.

Below in Section 6.5 we will demonstrate the scale invariance of the annihilation rate, for which it will be convenient to define the hard function vector

$$\vec{H}_{\text{wino}} = \left(C_1^* C_1, C_2^* C_1, C_1^* C_2, C_2^* C_2\right)^T . \tag{6.32}$$

The RGE for $\vec{H}_{\text{wino}}$ reads

$$\frac{d}{d\ln\mu}\vec{H}_{\text{wino}}(\mu) = \mathbf{\Gamma}_H^{\text{wino},T}(\mu)\,\vec{H}_{\text{wino}}(\mu)\,, \tag{6.33}$$

with

$$\mathbf{\Gamma}_H^{\text{wino}} = \begin{pmatrix} 2\,\text{Re}\,\Gamma_{11} & 0 & 0 & 0 \\ \Gamma_{21}^* & \Gamma_{11}+\Gamma_{22}^* & 0 & 0 \\ \Gamma_{21} & 0 & \Gamma_{11}^*+\Gamma_{22} & 0 \\ 0 & \Gamma_{21} & \Gamma_{21}^* & 2\,\text{Re}\,\Gamma_{22} \end{pmatrix}, \tag{6.34}$$

where the individual terms Γ_{ij} in (6.34) are given by

$$\begin{aligned} \Gamma_{11} &= \frac{\hat{\alpha}_2}{4\pi}\left(8\ln\frac{4m_\chi^2}{\mu^2} - 8i\pi - \frac{43}{3} + \frac{8}{3}n_G\right), \\ \Gamma_{21} &= \frac{\hat{\alpha}_2}{4\pi}(4-4i\pi)c_2(j)\,, \\ \Gamma_{22} &= \frac{\hat{\alpha}_2}{4\pi}\left(8\ln\frac{4m_\chi^2}{\mu^2} + 4i\pi - \frac{79}{3} + \frac{8}{3}n_G\right), \end{aligned} \tag{6.35}$$

which can in turn be derived from the RGE

$$\frac{d}{d\ln\mu}C_i(\mu) = (\Gamma^T)_{ij}(\mu)\,C_j(\mu)\,. \tag{6.36}$$

Resummation Higgsino DM For the resummation of the Wilson coefficients in the Higgsino DM case, it is important to remember the dependence between $\mathcal{O}_1$ and $\mathcal{O}_2$ for $j = 1/2$. Using the notation $\tilde{C}_i$, defined in (3.29), we write the evolution of the vector $\tilde{C} = (\tilde{C}_1, \tilde{C}_4, \tilde{C}_6)^T$ as follows

$$\tilde{C}(\mu) = \begin{pmatrix} \tilde{U}_1^{(0)}(\mu_h,\mu) & 0 & 0 \\ 0 & \tilde{U}_4^{(1)}(\mu_h,\mu) & 0 \\ 0 & 0 & \tilde{U}_6^{(0)}(\mu_h,\mu) \end{pmatrix} \tilde{C}(\mu_h)\,. \tag{6.37}$$

The evolution factors satisfy the RG equation

$$\frac{d}{d\ln\mu}\tilde{U}_i^{(J)}(\mu_h,\mu) = \left(\Gamma_{\text{SU(2)},i}^{(J)} + \Gamma_{\text{U(1)},i}\right)\tilde{U}_i^{(J)}(\mu_h,\mu)\,, \tag{6.38}$$

where $\Gamma_{\text{U(1),i}}$ is defined in (6.23). Like in the wino DM case, the Higgsino DM RG equation (6.38) is solve numerically due to the appearance of the cusp anomalous dimension at two-loops. In Figure 6.4, we plot the evolution of the Wilson coefficients $\tilde{C}_i$ as a function of m_χ.

To demonstrate the scale invariance of the Higgsino DM annihilation rate, we again introduce hard function vectors. Now however, it proves to be convenient to introduce

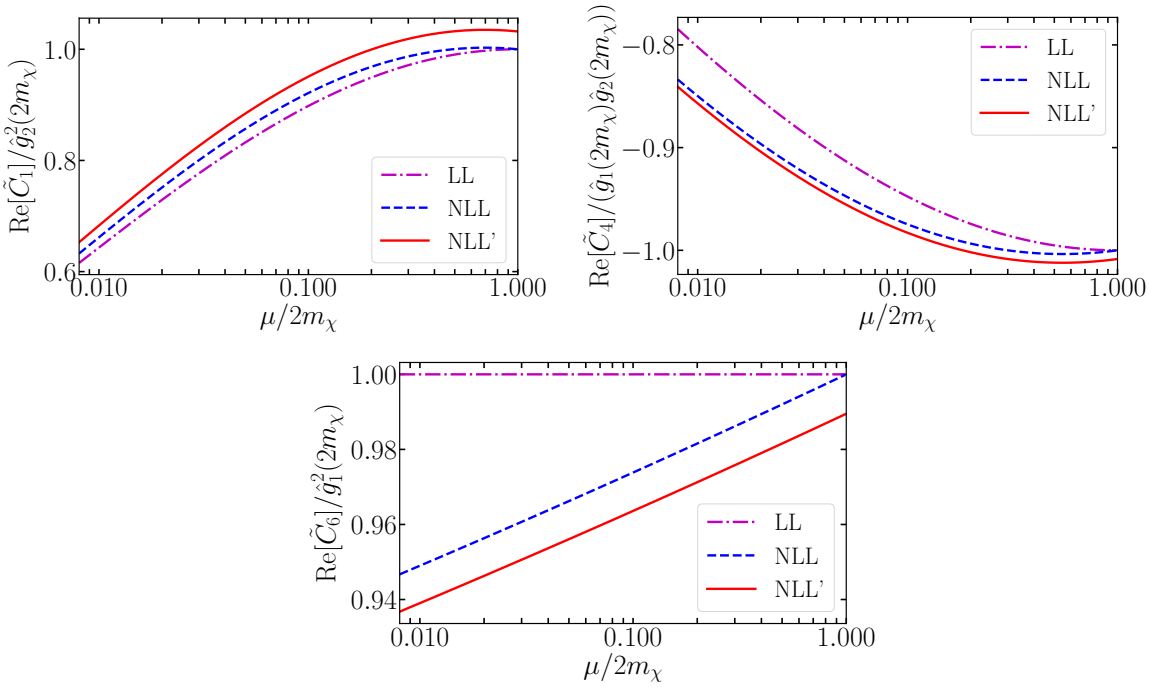

Figure 6.4: Evolution of the real part of the Higgsino DM matching coefficients in various approximations for $m_\chi = 5$ TeV, $\mu_h = 2m_\chi$.

two vectors, where one associated with the SU(2) part of the unobserved jet and soft functions and one is associated with the $\mathrm{U}(1)_Y$ part of these functions. This makes sense, since the SU(2) and $\mathrm{U}(1)_Y$ parts originate from different operators. We define the Higgsino DM hard function vectors as

$$\begin{aligned}\vec{H}_{\mathrm{SU}(2)} &= \left(\tilde{C}_1^*\tilde{C}_1, \tilde{C}_4^*\tilde{C}_1, \tilde{C}_1^*\tilde{C}_4, \tilde{C}_4^*\tilde{C}_4\right)^T, \\ \vec{H}_{\mathrm{U}(1)} &= \left(\tilde{C}_4^*\tilde{C}_4, \tilde{C}_6^*\tilde{C}_4, \tilde{C}_4^*\tilde{C}_6, \tilde{C}_6^*\tilde{C}_6\right)^T. \end{aligned} \tag{6.39}$$

The RGE takes a similar form as the one in (6.33) and the anomalous dimensions are now diagonal

$$\boldsymbol{\Gamma}_H^{\mathrm{SU}(2)} = \mathrm{diag}\left[2\,\mathrm{Re}\,\tilde{\Gamma}_{11}, \tilde{\Gamma}_{11} + \tilde{\Gamma}_{44}^*, \tilde{\Gamma}_{11}^* + \tilde{\Gamma}_{44}, 2\,\mathrm{Re}\,\tilde{\Gamma}_{44}\right], \tag{6.40}$$

$$\boldsymbol{\Gamma}_H^{\mathrm{U}(1)} = \mathrm{diag}\left[2\,\mathrm{Re}\,\tilde{\Gamma}_{44}, \tilde{\Gamma}_{44} + \tilde{\Gamma}_{66}^*, \tilde{\Gamma}_{44}^* + \tilde{\Gamma}_{66}, 2\,\mathrm{Re}\,\tilde{\Gamma}_{66}\right]. \tag{6.41}$$

The individual elements of (6.40) and (6.41) are given by

$$\begin{aligned}\tilde{\Gamma}_{11} &= \frac{\hat{\alpha}_2}{4\pi}\left(8\ln\frac{4m_\chi^2}{\mu^2} - 8i\pi - \frac{43}{3} + \frac{8}{3}n_G\right), \\ \tilde{\Gamma}_{44} &= \frac{\hat{\alpha}_1}{4\pi}\left(\frac{1}{6} + \frac{20}{9}n_G\right) + \frac{\hat{\alpha}_2}{4\pi}\left(4\ln\frac{4m_\chi^2}{\mu^2} - \frac{67}{6} + \frac{4}{3}n_G\right), \\ \tilde{\Gamma}_{66} &= \frac{\hat{\alpha}_1}{4\pi}\left(\frac{1}{3} + \frac{40}{9}n_G\right). \end{aligned} \tag{6.42}$$

They can be determined from (6.36) by exchanging the Wilson coefficients C_i with the Higgsino DM specific Wilson coefficients $\tilde{C}_i$.

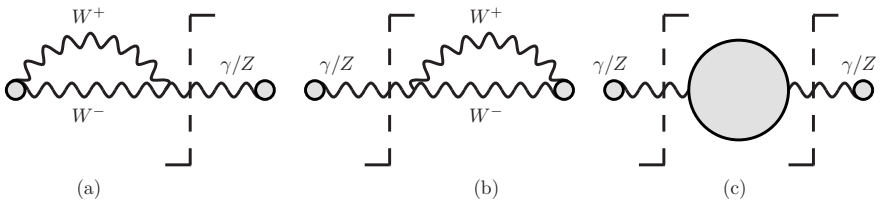

Figure 6.5: Diagrams contributing to the photon jet function.

6.2 Photon jet function

The anti-collinear photon jet function describes the gamma-ray emitted from the DM annihilation which can potentially be detected by a telescope. Figure 6.5 depicts all diagrams relevant for its computation. Diagrams (a) and (b) give identical contributions and originate from Wilson lines, while the self-energy diagram (c) includes the contributions from all SM particles in the loop. Since the photon jet function and the soft function (as well as the unobserved jet function in the narrow resolution case) have the same invariant mass squared of order m_W^2, they are defined in SCET_{II} and require an additional rapidity regulator. This is the same problem that we encountered in the strategy of regions example in Section 2.1. The regulator that we chose is the rapidity regulator that was first introduced in [75, 76]. The use of a rapidity regulator introduces another scale, the rapidity scale ν. Like the virtuality scale μ associated to dimensional regularization, the rapidity scale will also need to be evolved using the rapidity renormalization group (RRG).

The definition of the photon jet function $Z_\gamma^{YW}(\mu,\nu)$ was given in Section 3.1.1. For the case of wino DM, we only need to consider the index combination $Z_\gamma^{33}(\mu,\nu)$, since wino DM has vanishing hypercharge. For Higgsino DM on the other hand, one also requires the index combinations $Z_\gamma^{34}(\mu,\nu)$, $Z_\gamma^{43}(\mu,\nu)$ and $Z_\gamma^{44}(\mu)$, where the index value 4 indicates that the photon originates from the $\text{U}(1)_Y$ gauge boson. Once $Z_\gamma^{33}(\mu,\nu)$ is computed, the derivation of the other functions is fairly straightforward and can be achieved by adapting $Z_\gamma^{33}(\mu,\nu)$ accordingly. To do so, it is helpful to remark that only diagrams (a + c) ((b + c)) contribute to $Z_\gamma^{34}(\mu,\nu)$ ($Z_\gamma^{43}(\mu,\nu)$), while $Z_\gamma^{44}(\mu,\nu)$ is solely determined by diagram (c). Hence, the Wilson line parts of $Z_\gamma^{34}(\mu,\nu)$ and $Z_\gamma^{43}(\mu,\nu)$ are multiplied with a factor of 1/2 with respect to the one of $Z_\gamma^{33}(\mu,\nu)$ (because diagrams (a) and (b) give the same result) and $Z_\gamma^{44}(\mu,\nu)$ does not receive a Wilson line contribution at all. To make the adaption more transparent, it is convenient to write down the rotation from the weak basis to the mass basis of the gauge fields

$$\begin{pmatrix} W^1 \\ W^2 \\ W^3 \\ B \end{pmatrix} = \begin{pmatrix} \frac{1}{\sqrt{2}} & \frac{1}{\sqrt{2}} & 0 & 0 \\ \frac{i}{\sqrt{2}} & \frac{-i}{\sqrt{2}} & 0 & 0 \\ 0 & 0 & \hat{s}_W(\mu) & \hat{c}_W(\mu) \\ 0 & 0 & -\hat{c}_W(\mu) & \hat{s}_W(\mu) \end{pmatrix} \begin{pmatrix} W^+ \\ W^- \\ \gamma \\ Z \end{pmatrix} . \tag{6.43}$$

One can then use (6.43) to compute the index combinations $Z_\gamma^{34}(\mu,\nu)$, $Z_\gamma^{43}(\mu,\nu)$ and $Z_\gamma^{44}(\mu)$ by carefully analyzing the position of the cut in diagrams (a), (b) and (c) and by keeping track of whether the γ or the Z boson originated from a W^3 or a B boson in the unbroken theory. The results given here have been computed by Alessandro Broggio, CH and Martin Vollmann for $Y = W = 3$ and by CH and Martin Vollmann for the remaining index combinations.

6.2.1 $\mathbf{Z_\gamma^{33}}(\mu,\nu)$

The explicit result for $Z_\gamma^{33}(\mu,\nu)$ is given by

$$\begin{aligned} Z_\gamma(\mu,\nu) &= \hat{s}_W^2(\mu)\Bigg\{1-\frac{\hat{\alpha}_2(\mu)}{4\pi}\Bigg[-16\ln\frac{m_W}{\mu}\ln\frac{2m_\chi}{\nu}+8\ln\frac{m_W}{\mu} \\ &\quad -\hat{s}_W^2(\mu)\frac{80}{9}\left(\ln\frac{m_Z^2}{\mu^2}-\frac{5}{3}\right)-\hat{s}_W^2(\mu)\frac{16}{9}\ln\frac{m_t^2}{\mu^2} \\ &\quad +\hat{s}_W^2(\mu)\left(3\ln\frac{m_W^2}{\mu^2}-\frac{2}{3}\right)-4\frac{m_W^2}{m_Z^2}\ln\frac{m_W^2}{\mu^2}\Bigg]-\Delta\alpha\Bigg\}, \end{aligned} \tag{6.44}$$

where $\Delta\alpha$ is the difference between the fine structure constant $\alpha = 1/137.036$ and $\alpha_{\rm OS} = \alpha/(1-\Delta\alpha)$. As mentioned earlier, ν is the scale associated to the rapidity regulator and $\hat{s}_W$ is the sine of the weak mixing angle in the $\overline{\rm MS}$ scheme.

We will first discuss the resummation of the virtuality scale μ, before moving on to the resummation of the rapidity scale ν. The RG equation is

$$\frac{d}{d\ln\mu}Z_\gamma^{33}(\mu,\nu)=\gamma^\mu_{Z_\gamma^{33}}Z_\gamma^{33}(\mu,\nu)\,, \tag{6.45}$$

with anomalous dimension

$$\gamma^\mu_{Z_\gamma^{33}}=4\gamma_{\rm cusp}\ln\frac{\nu}{2m_\chi}+2\gamma^{\rm SU(2)}_{Z_\gamma}\,. \tag{6.46}$$

Generally, from the two-loop order onwards, there may appear terms with multiple SM couplings in the anomalous dimensions. In our case however, the only anomalous dimension which is needed at two-loops for NNL' accuracy is $\gamma_{\rm cusp}$, which does not exhibit this feature of multiple different coupling constants. The cusp anomalous dimension up to two loops has been given in (6.24). The one-loop coefficient $\gamma^{{\rm SU(2)},(0)}_{Z_\gamma}$ can be obtained from its definition (6.45). Calculating the derivative in μ of (6.44), we find that

$$\gamma^{{\rm SU(2)},(0)}_{Z_\gamma}=\beta_{0,{\rm SU(2)}}=\left(\frac{43}{6}-\frac{4}{3}n_G\right)\,. \tag{6.47}$$

A comment that will also be relevant for the computation of the anomalous dimensions of the remaining functions in the factorization theorem: when determining (6.46), we made use of the fact that the cusp anomalous dimension appears in the same way to all orders in perturbation theory [101]. This means that only a one-loop calculation is necessary to compute the prefactor of $\gamma_{\rm cusp}$. Solving the RG equation (6.45) is trivial and we find the following expression for the virtuality resummed photon jet function

$$\begin{aligned} Z_\gamma^{33}(\mu_f,\nu) &= U(\mu_i,\mu_f,\nu)Z_\gamma^{33}(\mu_i,\nu) \\ &= \exp\left[\int_{\ln\mu_i}^{\ln\mu_f}d\ln\mu\left(4\gamma_{\rm cusp}\ln\frac{\nu}{2m_\chi}+2\,\gamma^{\rm SU(2)}_{Z_\gamma}\right)\right]Z_\gamma^{33}(\mu_i,\nu)\,, \end{aligned} \tag{6.48}$$

where μ_i and μ_f denote the initial and final virtuality scales before and after evolution, respectively. We remark that (6.48) is a general solution to the RG equation (6.45) and thus valid to all orders.

The resummation of the rapidity scale is more subtle and greater care needs to be taken when resumming in ν. The rapidity renormalization group (RRG) equation is

$$\frac{d}{d\ln\nu}Z_\gamma(\mu,\nu)=\gamma^\nu_{Z_\gamma^{33}}Z_\gamma(\mu,\nu)\,, \tag{6.49}$$

where the fixed-order one-loop anomalous dimension is given by

$$\gamma^{\nu}_{Z^{33}_{\gamma}} = \frac{\hat{\alpha}_2}{4\pi}\, 4\gamma^{(0)}_{\text{cusp}}\, \ln\frac{\mu}{m_W}\,. \tag{6.50}$$

We now need to discuss a subtlety concerning the order of virtuality and rapidity resummation. In principle, (6.50) can be used to solve the RRG (6.49). Doing so requires one to first resum in ν and then in μ. This is because higher orders in $\gamma^{\nu}_{Z^{33}_{\gamma}}$ contain logarithms of the form $\alpha_2^n \ln^m(\mu/m_W)$ with $m \leq n$. Resummation in virtuality first implies that $\mu \gg m_W$ and thus these logarithms become large and require resummation themselves. This issue can be avoided by making the following observation: any physical observable is independent of the scales μ and ν, which implies the condition

$$\left[\frac{d}{d\ln\mu}, \frac{d}{d\ln\nu}\right] = 0\,. \tag{6.51}$$

Now, we can use the RG equation (6.45), the RRG equation (6.49) and the commutation relation (6.51) to derive the constraint

$$\frac{d}{d\ln\mu}\gamma^{\nu}_{Z^{33}_{\gamma}} = \frac{d}{d\ln\nu}\gamma^{\mu}_{Z^{33}_{\gamma}} = 4\gamma_{\text{cusp}}\,. \tag{6.52}$$

By solving (6.52), we find the integral version of the rapidity anomalous dimension

$$\gamma^{\nu}_{Z^{33}_{\gamma}}(\mu) = \int^{\ln\mu} d\ln\mu' \frac{d}{d\ln\nu}\gamma^{\mu}_{Z^{33}_{\gamma}}(\mu') + \text{const.}\,. \tag{6.53}$$

The constant in (6.53) is needed to reproduce the fixed-order non-cusp piece of the rapidity anomalous dimension. Comparing with (6.50), we see that we can set the constant term to zero. The advantage of (6.53) is that this version of the rapidity anomalous dimension resums the logarithms $\ln(\mu/m_W)$ to all orders in perturbation theory. Using (6.53), we solve the RRG (6.49) and obtain the resummed rapidity evolution factor

$$Z^{33}_{\gamma}(\mu,\nu_f) = V(\mu,\nu_i,\nu_f) Z^{33}_{\gamma}(\mu,\nu_i) = \exp\left[\gamma^{\nu}_{Z^{33}_{\gamma}}(\mu)\, \ln\frac{\nu_f}{\nu_i}\right] Z^{33}_{\gamma}(\mu,\nu_i)\,, \tag{6.54}$$

where ν_i and ν_f denote the initial and final scales of the rapidity evolution, respectively. It is easy to confirm that by expanding the exponent in $V(\mu,\nu_i,\nu_f)$ up to order $\mathcal{O}(\hat{\alpha_2})$, one recovers the rapidity evolution factor that can be computed by using the fixed-order one-loop anomalous dimension (6.50). More details on the rapidity evolution factors can be found in [76].

We now have computed the virtuality and rapidity evolution factors. Due to the logarithms appearing in the exponentials in (6.48) and (6.54), the cusp anomalous dimension is required at different orders in each exponential, depending on the order of resummation. If we first evolve in rapidity, the logarithm $\ln(\mu/m_W)$ in (6.54) is never large and γ_{cusp} in $V(\mu,\nu_i,\nu_f)$ only has to be included up to one-loop. The logarithm $\ln(\nu/2m_\chi)$ in (6.48) however will be large and γ_{cusp} in $U(\mu_i,\mu_f,\nu)$ has to be included up to the two-loop order to achieve NLL' resumation. If on the other hand we first resum in virtuality, the order is reversed. The cusp anomalous dimension has to be included at two-loops in $V(\mu,\nu_i,\nu_f)$ and only at one-loop in $U(\mu_i,\mu_f,\nu)$.

Taking all of this into consideration, i.e. using the resummed expression for the rapidity evolution factor (6.54) and including the cusp anomalous dimension at the appropriate order, ensures resummation path independence

$$V(\mu_f,\nu_i,\nu_f)U(\mu_i,\mu_f,\nu_i) = U(\mu_i,\mu_f,\nu_f)V(\mu_i,\nu_i,\nu_f)\,. \tag{6.55}$$

To resum the photon jet function we decided to first resum in rapidity and then in virtuality. As was just discussed, this requires us to only include γ_{cusp} at one-loop in $V(\mu, \nu_i, \nu_f)$, which allows us to write (6.54) in its LL approximation

$$Z_\gamma(\mu, \nu_f) = \exp\left[\frac{\gamma^{(0)}_{\text{cusp}}}{\beta_{0,\text{SU(2)}}} \ln\left(\frac{\hat{\alpha}_2(\mu)}{\hat{\alpha}_2(m_W)}\right) \ln\frac{\nu_f^2}{\nu_i^2}\right] Z_\gamma(\mu, \nu_i)\,. \tag{6.56}$$

The virtuality evolution factor $U(\mu_i, \mu_f, \nu)$, on the other hand, is computed numerically using the two-loop expression for γ_{cusp} and the one-loop expression for the non-cusp anomalous dimensions $\gamma^{\text{SU(2)}}_{Z_\gamma}$. The final expression for the resummed photon jet function Z_γ^{33} is then given by

$$Z_\gamma^{33}(\mu_f, \nu_f) = U(\mu_i, \mu_f, \nu_f)\, V(\mu_i, \nu_i, \nu_f)\, Z_\gamma^{33}(\mu_i, \nu_i)\,. \tag{6.57}$$

From the arguments of $U(\mu_i, \mu_f, \nu_f)$ in (6.57), it should be clear that the rapidity scale appearing in $\ln(\nu/2m_\chi)$ in the virtuality evolution factor is to be evaluated at its final value, i.e. the value to which $V(\mu_i, \nu_i, \nu_f)$ evolved the scale.

6.2.2 $\mathbf{Z_\gamma^{34}(\mu,\nu)}$, $\mathbf{Z_\gamma^{43}(\mu,\nu)}$ and $\mathbf{Z_\gamma^{44}(\mu,\nu)}$

We now discuss the remaining index combinations of the photon jet function $Z_\gamma^{34}(\mu, \nu)$, $Z_\gamma^{43}(\mu, \nu)$ and $Z_\gamma^{44}(\mu)$. To compute them, we need to remember which diagrams contribute to which index combination and how to change $\hat{s}_W$- and $\hat{c}_W$-terms according to our conventions (6.43). The fact that contributions from diagrams (a) and (b) in Figure 6.5 are identical implies the equality $Z_\gamma^{34}(\mu, \nu) = Z_\gamma^{43}(\mu, \nu)$. We will thus only discuss the results and the resummation for $Z_\gamma^{34}(\mu, \nu)$ and $Z_\gamma^{44}(\mu, \nu)$. We find the following expressions for the jet functions

$$\begin{aligned} Z_\gamma^{34}(\mu, \nu) = -\hat{s}_W(\mu)\hat{c}_W(\mu)\Bigg[1 - \frac{\hat{g}_2^2(\mu)}{(4\pi)^2}\Bigg\{ &- 8\ln\frac{m_W}{\mu}\ln\frac{2m_\chi}{\nu} + 4\ln\frac{m_W}{\mu}\Bigg\} \\ &+ \frac{1}{2}\left(\frac{\hat{g}_1^2(\mu)\hat{c}_W^2(\mu)}{(4\pi)^2} + \frac{\hat{g}_2^2(\mu)\hat{s}_W^2(\mu)}{(4\pi)^2}\right) \\ &\times\left\{\frac{80}{9}\left(2\ln\frac{m_Z}{\mu} - \frac{5}{3}\right) + \frac{32}{9}\ln\frac{m_t}{\mu} + \frac{2}{3} - 6\ln\frac{m_W}{\mu}\right\} \\ &- \left(\frac{\hat{g}_2^2(\mu)}{(4\pi)^2} - \frac{\hat{g}_1^2(\mu)}{(4\pi)^2}\right)\frac{m_W^2}{m_Z^2}\left(-4\ln\frac{m_W}{\mu}\right) - \Delta\alpha\Bigg], \end{aligned} \tag{6.58}$$

$$\begin{aligned} Z_\gamma^{44}(\mu) = \hat{c}_W^2(\mu)\Bigg[1 + \frac{\hat{g}_1^2(\mu)\hat{c}_W^2(\mu)}{(4\pi)^2}\Bigg\{&\frac{80}{9}\left(2\ln\frac{m_Z}{\mu} - \frac{5}{3}\right) + \frac{32}{9}\ln\frac{m_t}{\mu} \\ &+ \frac{2}{3} - 6\ln\frac{m_W}{\mu}\Bigg\} - \frac{\hat{g}_1^2(\mu)}{(4\pi)^2}\, 8\frac{m_W^2}{m_Z^2}\ln\frac{m_W}{\mu} - \Delta\alpha\Bigg]. \end{aligned} \tag{6.59}$$

The discussion presented in Section 6.2.1 on the order of the resummation applies independently of the values of the gauge indices and will thus not be repeated. The RG equations are

$$\begin{aligned} \frac{d}{d\ln\mu} Z_\gamma^{34}(\mu, \nu) &= \gamma^\mu_{Z_\gamma^{34}} Z_\gamma^{34}(\mu, \nu)\,, \\ \frac{d}{d\ln\mu} Z_\gamma^{44}(\mu) &= \gamma_{Z_\gamma^{44}} Z_\gamma^{44}(\mu)\,, \end{aligned} \tag{6.60}$$

with the anomalous dimensions

$$\begin{aligned}\gamma^{\mu}_{Z^{34}_{\gamma}} &= 2\gamma_{\text{cusp}} \ln \frac{\nu}{2m_{\chi}} + \gamma^{\text{SU(2)}}_{Z_{\gamma}} + \gamma^{\text{U(1)}}_{Z_{\gamma}}\,, \\ \gamma_{Z^{44}_{\gamma}} &= 2\gamma^{\text{U(1)}}_{Z_{\gamma}}\,. \end{aligned} \tag{6.61}$$

The anomalous dimension $\gamma^{\text{SU(2)}}_{Z_{\gamma}}$ was already given in (6.47) and $\gamma^{\text{U(1)}}_{Z_{\gamma}}$ is given by

$$\gamma^{\text{U(1)}}_{Z_{\gamma}} = \beta_{0,\text{U(1)}} \frac{\hat{\alpha}_1(\mu)}{4\pi} + \dots\,. \tag{6.62}$$

As can be seen from (6.59), the photon jet function $Z^{44}_{\gamma}(\mu)$ is independent of the rapidity scale ν, since it does not receive contributions from Wilson line diagrams (a) and (b) in Figure 6.5. The RRG of $Z^{34}_{\gamma}(\mu,\nu)$ is given by

$$\frac{d}{d\ln\nu} Z^{34}_{\gamma}(\mu,\nu) = \gamma^{\nu}_{Z^{34}_{\gamma}} Z^{34}_{\gamma}(\mu,\nu)\,, \tag{6.63}$$

where the rapidity anomalous dimension $\gamma^{\nu}_{Z^{34}_{\gamma}}$ has the value

$$\gamma^{\nu}_{Z^{34}_{\gamma}} = \frac{1}{2}\gamma^{\nu}_{Z^{33}_{\gamma}} = \frac{\hat{\alpha}_2(\mu)}{4\pi} 2\gamma^{(0)}_{\text{cusp}} \ln\frac{\mu}{m_W}\,. \tag{6.64}$$

Solving the RGEs (6.60) and the RRG (6.63), we arrive at the expressions for the resummed photon jet functions $Z^{34}_{\gamma}(\mu,\nu)$ and $Z^{44}_{\gamma}(\mu,\nu)$

$$\begin{aligned} Z^{34}_{\gamma}(\mu_f,\nu_f) = &\exp\left[\int_{\ln\mu_i}^{\ln\mu_f} d\ln\mu \left(2\gamma_{\text{cusp}}\ln\frac{\nu_f}{2m_{\chi}} + \gamma^{\text{SU(2)}}_{Z_{\gamma}} + \gamma^{\text{U(1)}}_{Z_{\gamma}}\right)\right] \\ &\times \exp\left[\frac{\gamma^{(0)}_{\text{cusp}}}{2\beta_{0,\text{SU(2)}}} \ln\frac{\hat{\alpha}_2(\mu_i)}{\hat{\alpha}_2(m_W)} \ln\frac{\nu_f^2}{\nu_i^2}\right] Z^{34}_{\gamma}(\mu_i,\nu_i)\,, \\ Z^{44}_{\gamma}(\mu_f) = &\exp\left[\int_{\ln\mu_i}^{\ln\mu_f} d\ln\mu\, \gamma_{Z^{44}_{\gamma}}\right] Z^{44}_{\gamma}(\mu_i)\,. \end{aligned} \tag{6.65}$$

The resummed expression for $Z^{43}_{\gamma}(\mu_f,\nu_f)$ is identical to the expression of $Z^{34}_{\gamma}(\mu_f,\nu_f)$ in (6.65).

6.3 Unobserved jet function

While the hard matching coefficients and the photon jet function in anti-collinear direction, discussed in Sections 6.1 and 6.2, respectively, take the same form for both narrow and intermediate energy resolution, the unobserved jet function in collinear direction needs to be adjusted depending on which value of E^{γ}_{res} is assumed. If $E^{\gamma}_{\text{res}} \sim m_W^2/m_{\chi}$, the invariant mass squared of the unobserved final state is $p^2 \sim m_W^2$ and the external momentum has a collinear scaling $p \sim m_{\chi}(\lambda^2, 1, \lambda)$. This implies that EW scale masses cannot be neglected and the unobserved jet function in the narrow resolution case has to be computed with massive SM particles. If on the other hand $E^{\gamma}_{\text{res}} \sim m_W$, the invariant mass squared is $p^2 \sim m_W m_{\chi}$ and the external momentum has hard-collinear scaling $p \sim m_{\chi}(\lambda, 1, \sqrt{\lambda})$. In this case, SM particle masses can be neglected and the intermediate resolution jet functions are computed in the EW symmetric limit.

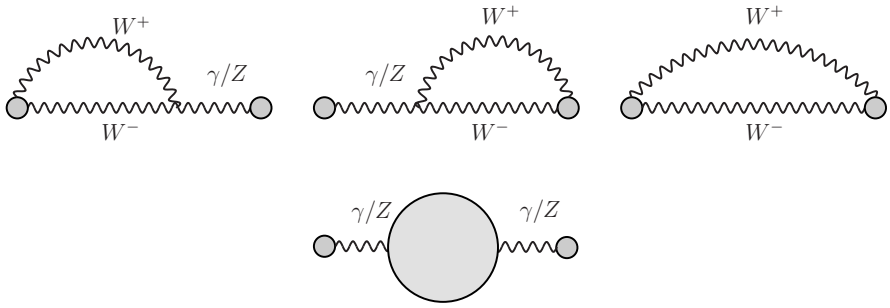

Figure 6.6: Wilson line and self-energy type Feynman diagrams contributing to the narrow resolution jet function. This Figure has been extracted from [9].

6.3.1 Unobserved jet function - narrow resolution case

Assuming $E^\gamma_{\text{res}} \sim m_W^2/m_\chi$ means that $J^{XV}_{\text{nrw}}(p^2)$ has to be computed using SCET_{II}. Since it exhibits the same virtuality as the photon jet function and the soft function, we again need to deal with rapidity divergences. In this Section, we provide explicit expressions for J^{33}_{nrw}, J^{34}_{nrw}, J^{43}_{nrw} and J^{44}_{nrw}, which are complicated functions of the masses of the SM particles, the invariant mass of the jet, the virtuality scale μ and the rapidity scale ν. While here we content ourselves with providing explicit results, we refer the reader to Appendix F for details on the computation of the relevant integrals and explicit expressions concerning the massive SM self-energy functions. Diagrams contributing to the unobserved jet function are depicted in Figure 6.6. The calculations for the narrow resolution unobserved jet function have been done by Alessandro Broggio, CH and Martin Vollmann for $X = V$ and by CH and Martin Vollmann for the remaining index combinations.

Unobserved jet function $\mathbf{J^{33}_{\text{nrw}}}$ As for the photon jet function, let us start with the gauge index combination $X = V = 3$. The computation is done in Feynman gauge to one-loop order, for which we split the unobserved jet function into two contributions

$$\begin{aligned} J^{33}_{\text{nrw}}(p^2,\mu,\nu) =& \hat{s}^2_W(\mu)\delta(p^2) + \hat{c}^2_W(\mu)\delta(p^2 - m_Z^2) \\ &+ J^{33}_{\text{nrw, Wilson}}(p^2,\mu,\nu) + J^{33}_{\text{nrw, se}}(p^2,\mu)\,, \end{aligned} \tag{6.66}$$

a Wilson line type $J^{33}_{\text{nrw, Wilson}}$ and a self-energy type $J^{33}_{\text{nrw, se}}$. Diagrammatically, the Wilson line and self-energy contributions arise from the first line and second line of Figure 6.6, respectively. Different from the computation of the photon jet function where the condition of a final state photon puts constraints on the possible positions of the cut, for the unobserved jet function the cut can be placed anywhere. Taking into account all possible cuts can be achieved by computing the total discontinuity, which is obtained when taking the imaginary part of the gauge boson two-point function (3.14). Furthermore, the fact that we have a neutral two-particle initial state and a photon emitted in the anti-collinear direction imposes the constraint that the unobserved final state also has to be neutral. This implies that we only need to consider the gauge boson index combinations $XV = 33$, $XV = 34$, $XV = 43$ and $XV = 44$.

The result for the virtual diagrams in the first row of Figure 6.6 is given by

$$\begin{aligned} \mathcal{J}^{33}_{\text{nrw, Wilson}}(p^2,\mu,\nu) =& \, i\theta(p^2 - 4m_W^2)\left[\frac{\hat{s}^2_W}{p^2 + i\epsilon} + \frac{\hat{c}^2_W}{p^2 - m_Z^2 + i\epsilon}\right] \\ &\times \left\{1 - \frac{\hat{g}_2^2}{16\pi^2}\left[- 16\ln\left(\frac{m_W}{\mu}\right)\ln\left(\frac{2m_\chi}{\nu}\right) + 8\ln\left(\frac{m_W}{\mu}\right) - 8 + 4\pi^2\right.\right. \end{aligned}$$

$$
\begin{aligned}
&- 4\ln(x)\beta - 4\ln^2(x) - \left[4i\beta\pi + 8i\pi\ln(x)\right]\Bigg]\Bigg\} \\
&+ i\theta(4m_W^2 - p^2)\left[\frac{\hat{s}_W^2}{p^2 + i\epsilon} + \frac{\hat{c}_W^2}{p^2 - m_Z^2 + i\epsilon}\right] \\
&\times \left\{1 - \frac{\hat{g}_2^2}{16\pi^2}\left[- 16\ln\left(\frac{m_W}{\mu}\right)\ln\left(\frac{2m_\chi}{\nu}\right) + 8\ln\left(\frac{m_W}{\mu}\right) - 8 + 4\pi^2\right.\right. \\
&\left.\left. + 4\bar{\beta}\pi - 16\arctan(\bar{\beta})\pi - 8\arctan(\bar{\beta})\bar{\beta} + 16\arctan^2(\bar{\beta})\right]\right\}, \qquad (6.67)
\end{aligned}
$$

where

$$
x \equiv \frac{1-\beta}{1+\beta}\,, \quad \beta = \sqrt{1 - \frac{4m_W^2}{p^2}}\,, \quad \bar{\beta} = \sqrt{\frac{4m_W^2}{p^2} - 1}\,. \qquad (6.68)
$$

From the defintion (3.14) we can see that we still need to extract the imaginary part from the propagators, for which we use the relation

$$
\frac{1}{a + i\epsilon} = \left[\frac{1}{a}\right]_* - i\pi\delta(a)\,, \qquad (6.69)
$$

where the subscript $*$ denotes the Cauchy principle value. In practice, we don't need a particular prescription for the principal value in this case, since it will be multiplied by a theta function and thus cannot be divergent. After extracting the imaginary part we obtain the following result for the Wilson line contribution to the $J^{33}_{\text{nrw}}(p^2,\mu,\nu)$ jet function

$$
\begin{aligned}
J^{33}_{\text{nrw, Wilson}}(p^2,\mu,\nu) = &-\frac{\hat{s}_W^2(\mu)\hat{g}_2^2(\mu)}{16\pi^2}\Bigg\{\delta(p^2)\left[- 16\ln\frac{m_W}{\mu}\ln\frac{2m_\chi}{\nu} + 8\ln\frac{m_W}{\mu}\right] \\
&+ \frac{1}{p^2}\theta(p^2 - 4m_W^2)\left[4\beta + 8\ln\frac{1-\beta}{1+\beta}\right]\Bigg\} \\
&- \frac{\hat{c}_W^2(\mu)\hat{g}_2^2(\mu)}{16\pi^2}\Bigg\{\delta(p^2 - m_Z^2)\Bigg[- 16\ln\frac{m_W}{\mu}\ln\frac{2m_\chi}{\nu} + 8\ln\frac{m_W}{\mu} - 8 + 4\pi^2 \\
&+ 4\pi\bar{\beta}_Z - (16\pi + 8\bar{\beta}_Z)\arctan(\bar{\beta}_Z) + 16\arctan^2(\bar{\beta}_Z)\Bigg] \\
&+ \frac{1}{p^2 - m_Z^2}\,\theta(p^2 - 4m_W^2)\left[4\beta + 8\ln\frac{1-\beta}{1+\beta}\right]\Bigg\}, \qquad (6.70)
\end{aligned}
$$

where

$$
\bar{\beta}_Z = \sqrt{\frac{4\,m_W^2}{m_Z^2} - 1}\,. \qquad (6.71)
$$

The self-energy part of the unobserved jet function, $J^{33}_{\text{nrw, se}}(p^2,\mu)$, does not suffer from rapidity divergences but needs to include all possible SM particles and originates from the second row of Figure 6.6. The expressions for the self-energies are known and can be extracted for example in Feynman gauge from [102]. In general the structure in the 't Hooft-Feynman gauge is given by

$$
-i\left(g_{\mu\nu} - \frac{p_\mu p_\nu}{p^2}\right)\Sigma_T^{ab}(p^2) - i\frac{p_\mu p_\nu}{p^2}\Sigma_L^{ab}(p^2)\,, \qquad (6.72)
$$

where the indexes $a, b = \gamma, Z$. This structure has then to be inserted between gauge collinear building blocks, which will project onto the transverse part of the self energies. The virtual contribution from the self-energies has the following structure

$$\begin{aligned}\mathcal{J}^{33}_{\text{nrw, se}}(p^2) = \hat{s}_W^2 \frac{-i}{p^2+i\epsilon}\big(i\Sigma_T^{\gamma\gamma}(p^2)\big)\frac{-i}{p^2+i\epsilon} + \hat{s}_W\hat{c}_W\frac{-i}{p^2+i\epsilon}\big(i\Sigma_T^{\gamma Z}(p^2)\big)\frac{-i}{p^2-m_Z^2+i\epsilon} \\ +\hat{s}_W\hat{c}_W\frac{-i}{p^2-m_Z^2+i\epsilon}\big(i\Sigma_T^{\gamma Z}(p^2)\big)\frac{-i}{p^2+i\epsilon} + \hat{c}_W^2\frac{-i}{p^2-m_Z^2+i\epsilon}\big(i\Sigma_T^{ZZ}(p^2)\big)\frac{-i}{p^2-m_Z^2+i\epsilon}\,,\end{aligned} \tag{6.73}$$

where we assume that all of the fermions are massless except the top quark

$$m_b = m_c = m_\tau = m_s = m_d = m_u = m_\mu = m_e = 0 \text{ GeV}\,. \tag{6.74}$$

We need a prescription to separate the real and the imaginary parts of the double propagators, i.e. we need to derive the equivalent of (6.69) for the cases appearing in (6.73). Starting with the mixed contribution, which is easier, one can see that a simple partial fractioning is sufficient

$$\begin{aligned}\frac{1}{p^2+i\epsilon}\frac{1}{p^2-m_Z^2+i\epsilon} &= -\frac{1}{m_Z^2}\frac{1}{p^2+i\epsilon} + \frac{1}{m_Z^2}\frac{1}{p^2-m_Z^2+i\epsilon} \\ &= -\frac{1}{m_Z^2}\left[\frac{1}{p^2}\right]_*^{[\mu^2]} + \frac{1}{m_Z^2}\left[\frac{1}{p^2-m_Z^2}\right]_*^{[\mu^2]} + i\pi\frac{\delta(p^2)}{m_Z^2} - i\pi\frac{\delta(p^2-m_Z^2)}{m_Z^2}\,.\end{aligned} \tag{6.75}$$

The star distributions are defined as

$$\begin{aligned}\int_0^{p^2_{\max}} dp^2 \left[\frac{\ln^n \frac{p^2}{\mu^2}}{p^2}\right]_*^{[\mu^2]} f(p^2) = \\ \int_0^{p^2_{\max}} dp^2\, \frac{f(p^2)-f(0)}{p^2}\ln^n\frac{p^2}{\mu^2} + \frac{f(0)}{n+1}\,\ln^{n+1}\frac{p^2_{\max}}{\mu^2}\,,\end{aligned} \tag{6.76}$$

$$\begin{aligned}\int_0^{p^2_{\max}} dp^2 \left[\frac{1}{p^2-m_Z^2}\right]_* f(p^2) = \\ \int_0^{p^2_{\max}} dp^2\, \frac{f(p^2)-f(m_Z^2)}{p^2-m_Z^2} + f(m_Z^2)\ln\left(\frac{p^2_{\max}-m_Z^2}{m_Z^2}\right),\end{aligned} \tag{6.77}$$

where $f(p)^2$ is a test function and $p^2_{\max} > m_Z^2$ in the last equation. For $p^2_{\max} < m_Z^2$ the introduction of star distributions for the Z-boson propagators would not be necessary.

The case where a squared propagator appears is more involved and it needs more care. We analyze the following type of integral

$$\int_c^d da \frac{f(a)}{(a+i\epsilon)^2}\,, \tag{6.78}$$

where $c < 0 < d$. It can be shown by shifting the integration contour by an infinitesimal amount and by making a variable transformation that our initial integral is equivalent to

$$\int_c^d da\,\frac{f(a)}{(a+i\epsilon)^2} \to \int_C da\,\frac{f(a)}{a^2}\,, \tag{6.79}$$

where the contour C starts in c and ends in d along the real axis and performs a semicircular path (we call it γ_C) around the origin with an infinitesimal radius ϵ. It is important for the small radius γ_C-path to avoid the singularity that is present in the upper half-plane as prescribed by $+i\epsilon$. This is relevant to obtain the correct imaginary part. We then perform the a-integration in the complex plane along the C path. From this we obtain

$$\left[\int_c^{-\epsilon} da \frac{f(a)}{a^2} + \int_\epsilon^d da \frac{f(a)}{a^2}\right] + \int_{\gamma_C} da \frac{f(a)}{a^2} \tag{6.80}$$

where the limit $\epsilon \to 0$ is understood. Notice that, contrary to the case where there is only one power of a at the denominator, the expression in between squared brackets is divergent in the limit $\epsilon \to 0$. The divergent part, which amounts to $2f(0)/\epsilon$ can be extracted by integrating by parts. The semicircular path γ_C can be parametrized in the following way

$$a = \epsilon e^{i\theta}, \quad da = i\epsilon e^{i\theta} d\theta, \quad \text{with} \quad \theta \in [\pi, 0]\,. \tag{6.81}$$

We then express the rightmost integral of (6.80) as

$$\begin{aligned}\int_{\gamma_C} da \frac{f(a)}{a^2} &= \int_\pi^0 d\theta \, \frac{i\epsilon e^{i\theta} f(\epsilon e^{i\theta})}{\epsilon^2 e^{2i\theta}} = \int_\pi^0 d\theta \, \frac{i\epsilon e^{i\theta}\left[f(0) + \epsilon e^{i\theta} f'(0) + \dots\right]}{\epsilon^2 e^{2i\theta}}\,, \\ &= -\frac{2f(0)}{\epsilon} - i\pi f'(0) + \dots\,,\end{aligned} \tag{6.82}$$

where in the second equality we Taylor expand the function f around the origin. In total the integral (6.78) is finite and the two divergent parts cancel each other in the limit $\epsilon \to 0$. One can generalize the concept of the Cauchy principal value in the following way (and in principle extend this procedure to arbitrary powers of the denominator)

$$\int_c^d da \left[\frac{1}{a^2}\right]_{**} f(a) \equiv \left[\int_c^{-\epsilon} da \frac{f(a)}{a^2} + \int_\epsilon^d da \frac{f(a)}{a^2}\right] - \frac{2f(0)}{\epsilon}\,, \tag{6.83}$$

where the $**$ symbol generalizes the Cauchy principal value. In conclusion we can use the following equality in a distributional sense

$$\frac{1}{(a+i\varepsilon)^2} = \left[\frac{1}{a}\right]_{**} + i\pi\delta'(a)\,, \tag{6.84}$$

where the symbol δ' refers to the derivative of the Dirac δ distribution. In our particular case it happens that a θ function will force our integral to be in an integration region where it is not divergent, but it is still interesting to derive such an equation in a mathematical sense. From this derivation, it follows that

$$\frac{1}{p^2+i\varepsilon}\frac{1}{p^2+i\varepsilon} = \left[\frac{1}{(p^2)^2}\right]_{**} + i\pi\delta'(p^2)\,, \tag{6.85}$$

$$\frac{1}{p^2-m_Z^2+i\varepsilon}\frac{1}{p^2-m_Z^2+i\varepsilon} = \left[\frac{1}{(p^2-m_Z^2)^2}\right]_{**} + i\pi\delta'(p^2-m_Z^2)\,. \tag{6.86}$$

Notice that the second terms in (6.85) and (6.86) will effectively generate the wave function renormalization factors $\delta Z_{\gamma\gamma}$ and δ_{ZZ} that are needed for the correct UV renormalization of the virtual part of the computation. Everything is now in place to compute the self-energy part of the unobserved jet function $J^{33}_{\text{nrw}}(p^2, \mu, \nu)$, by taking the imaginary part of (6.73).

Since the natural scale of the unobserved jet function lies around the EW scale, it is reasonable to neglect the masses of the light fermions (6.74). We thus assume all fermions except for the top quark to be massless, which allows us to further split the self-energy part into a massive and a massless contribution

$$J^{33}_{\text{nrw, se}}(p^2,\mu) = J^{33}_{\text{nrw, se, } f\neq t\text{ only}}(p^2,\mu) + J^{33}_{\text{nrw, se, } f\neq t\text{ excluded}}(p^2,\mu)\,, \tag{6.87}$$

where the second term includes the W^+W^-, ZH and $t\bar{t}$ loops. For the massless fermion contribution we obtain

$$\begin{aligned}
J^{33}_{\text{nrw, se, } f\neq t\text{ only}}(p^2,\mu) = \frac{\hat{s}^2_W(\mu)\hat{g}_2^2(\mu)}{16\pi^2}\Bigg\{ & \hat{s}^2_W(\mu)\frac{80}{9}\bigg[-\delta(p^2)\frac{5}{3} + \bigg[\frac{1}{p^2}\bigg]^{[\mu^2]}_{*}\bigg] \\
& + 2\left(\frac{10}{3} - \frac{80}{9}\hat{s}^2_W(\mu)\right) \times \bigg[\bigg[\frac{1}{p^2-m_Z^2}\bigg]_{*} - \delta(p^2-m_Z^2)\left(\frac{5}{3} - \ln\frac{m_Z^2}{\mu^2}\right)\bigg] \\
& + \left(-\frac{20}{3} + \frac{7}{2}\frac{1}{\hat{s}^2_W(\mu)} + \frac{80}{9}\hat{s}^2_W(\mu)\right) \\
& \times \bigg[\bigg[\frac{1}{(p^2-m_Z^2)^2}\bigg]_{**} p^2 - \left(\frac{2}{3} - \ln\frac{m_Z^2}{\mu^2}\right)\delta(p^2-m_Z^2)\bigg]\Bigg\}\,.
\end{aligned} \tag{6.88}$$

The massive self-energy contribution reads

$$\begin{aligned}
&J^{33}_{\text{nrw, se, } f\neq t\text{ excluded}}(p^2,\mu) = \\
&\quad 2\hat{s}_W(\mu)\hat{c}_W(\mu)\bigg[\frac{\text{Re}\big[\Sigma_T^{\gamma Z}(0)\big]_{t,W}}{m_Z^2}\delta(p^2) - \frac{\text{Re}\big[\Sigma_T^{\gamma Z}(m_Z^2)\big]_{t,W}}{m_Z^2}\delta(p^2-m_Z^2)\bigg] \\
&-\hat{s}^2_W(\mu)\text{Re}\frac{\partial\Sigma_T^{\gamma\gamma}(p^2)_{t,W}}{\partial p^2}\bigg|_{p^2=0}\delta(p^2) - \hat{c}^2_W(\mu)\text{Re}\frac{\partial\Sigma_T^{ZZ}(p^2)_{t,W,Z,H}}{\partial p^2}\bigg|_{p^2=m_Z^2}\delta(p^2-m_Z^2) \\
&+2\hat{s}_W(\mu)\hat{c}_W(\mu)\bigg[-\frac{1}{m_Z^2}\frac{1}{p^2}\frac{\text{Im}\big[\Sigma_T^{\gamma Z}(p^2)\big]_{t,W}}{\pi} + \frac{1}{m_Z^2}\frac{1}{p^2-m_Z^2}\frac{\text{Im}\big[\Sigma_T^{\gamma Z}(p^2)\big]_{t,W}}{\pi}\bigg] \\
&\quad + \hat{s}^2_W(\mu)\frac{1}{\big(p^2\big)^2}\frac{\text{Im}\big[\Sigma_T^{\gamma\gamma}(p^2)\big]_{t,W}}{\pi} + \hat{c}^2_W(\mu)\frac{1}{\big(p^2-m_Z^2\big)^2}\frac{\text{Im}\big[\Sigma_T^{ZZ}(p^2)\big]_{t,W,Z,H}}{\pi}\,.
\end{aligned} \tag{6.89}$$

Note that for the massive self-energy contribution (6.89) there is no need to introduce star distributions. This is because below the massive thresholds indicated by the subscripts the imaginary parts vanish. Hence, there are no singularities at 0 and m_Z^2.

Plugging (6.70), (6.88) and (6.89) into (6.66) gives us the result for the unobserved jet function $J^{33}_{\text{nrw}}(p^2,\mu,\nu)$. The derivation of the remaining index combinations J^{34}_{nrw}, J^{43}_{nrw} and J^{44}_{nrw} is similar to the case of the photon jet function and can be achieved by using (6.43).

Unobserved jet functions $\mathbf{J^{34}}$, $\mathbf{J^{43}}$ and $\mathbf{J^{44}}$ The lengthy derivation of the result for J^{33}_{nrw}, including the introduction of the star distributions applies independently of the index values of the unobserved jet function. This paragraph will thus be kept rather brief and we focus on the presentation of the results. Also, since $J^{34}_{\text{nrw}} = J^{43}_{\text{nrw}}$ we will content ourselves with presenting the results for J^{34}_{nrw} and J^{44}_{nrw} only. They read

$$\begin{aligned}
J^{34}(p^2,\mu,\nu) = & -\hat{s}_W(\mu)\hat{c}_W(\mu)\delta(p^2) + \hat{s}_W(\mu)\hat{c}_W(\mu)\delta(p^2-m_Z^2) \\
& + J^{34}_{\text{Wilson}}(p^2,\mu,\nu) + J^{34}_{\text{se, } f\neq t\text{ only}}(p^2,\mu) + J^{34}_{\text{se, } f\neq t\text{ excluded}}(p^2,\mu)\,.
\end{aligned} \tag{6.90}$$

$$
\begin{aligned}
J^{34}_{\text{Wilson}}(p^2,\mu,\nu) = \frac{\hat{s}_W(\mu)\hat{c}_W(\mu)\hat{g}_2^2(\mu)}{16\pi^2}\Bigg\{&\delta(p^2)\bigg[-8\ln\frac{m_W}{\mu}\ln\frac{2m_\chi}{\nu}+4\ln\frac{m_W}{\mu}\bigg]\\
&+\frac{1}{p^2}\,\theta(p^2-4m_W^2)\bigg[2\beta+4\ln\frac{1-\beta}{1+\beta}\bigg]\Bigg\}\\
-\frac{\hat{s}_W(\mu)\hat{c}_W(\mu)\hat{g}_2^2(\mu)}{16\pi^2}\Bigg\{&\delta(p^2-m_Z^2)\bigg[-8\ln\frac{m_W}{\mu}\ln\frac{2m_\chi}{\nu}+4\ln\frac{m_W}{\mu}-4+2\pi^2\\
&+2\pi\bar{\beta}_Z-(8\pi+4\bar{\beta}_Z)\arctan(\bar{\beta}_Z)+8\arctan^2(\bar{\beta}_Z)\bigg]\\
&+\frac{1}{p^2-m_Z^2}\,\theta(p^2-4m_W^2)\bigg[2\beta+4\ln\frac{1-\beta}{1+\beta}\bigg]\Bigg\}\,,
\end{aligned}
\tag{6.91}
$$

$$
\begin{aligned}
J^{34}_{\text{se},\,f\neq t\,\text{only}}(p^2,\mu) = \frac{\hat{s}_W^2(\mu)\hat{g}_2^2(\mu)}{16\pi^2}\Bigg\{&-\hat{s}_W(\mu)\hat{c}_W(\mu)\frac{80}{9}\bigg[-\delta(p^2)\frac{5}{3}+\bigg[\frac{1}{p^2}\bigg]_*^{[\mu^2]}\bigg]\\
&+(\hat{s}_W^2(\mu)-\hat{c}_W^2(\mu))\left(\frac{10}{3}\frac{1}{\hat{s}_W(\mu)\hat{c}_W(\mu)}-\frac{80}{9}\frac{\hat{s}_W(\mu)}{\hat{c}_W(\mu)}\right)\\
&\times\bigg[\bigg[\frac{1}{p^2-m_Z^2}\bigg]_*-\delta(p^2-m_Z^2)\left(\frac{5}{3}-\ln\frac{m_Z^2}{\mu^2}\right)\bigg]\\
&+\hat{s}_W(\mu)\hat{c}_W(\mu)\bigg(-\frac{20}{3}\frac{1}{\hat{c}_W^2(\mu)}+\frac{7}{2}\frac{1}{\hat{s}_W^2(\mu)\hat{c}_W^2(\mu)}+\frac{80}{9}\frac{\hat{s}_W^2(\mu)}{\hat{c}_W^2(\mu)}\bigg)\\
&\times\bigg[\bigg[\frac{1}{(p^2-m_Z^2)^2}\bigg]_{**}p^2-\delta(p^2-m_Z^2)\left(\frac{2}{3}-\ln\frac{m_Z^2}{\mu^2}\right)\bigg]\Bigg\}\,.
\end{aligned}
\tag{6.92}
$$

$$
\begin{aligned}
&J^{34}_{\text{se},\,f\neq t\,\text{excluded}}(p^2,\mu) =\\
&\quad\big(\hat{s}_W^2(\mu)-\hat{c}_W^2(\mu)\big)\left[\frac{\text{Re}\big[\Sigma_T^{\gamma Z}(0)\big]_{t,W}}{m_Z^2}\delta(p^2)-\frac{\text{Re}\big[\Sigma_T^{\gamma Z}(m_Z^2)\big]_{t,W}}{m_Z^2}\delta(p^2-m_Z^2)\right]\\
&+\hat{s}_W(\mu)\hat{c}_W(\mu)\,\text{Re}\frac{\partial\Sigma_T^{\gamma\gamma}(p^2)_{t,W}}{\partial p^2}\bigg|_{p^2=0}\delta(p^2)\\
&-\hat{s}_W(\mu)\hat{c}_W(\mu)\,\text{Re}\frac{\partial\Sigma_T^{ZZ}(p^2)_{t,W,Z,H}}{\partial p^2}\bigg|_{p^2=m_Z^2}\delta(p^2-m_Z^2)\\
&+\big(\hat{s}_W^2(\mu)-\hat{c}_W^2(\mu)\big)\left[-\frac{1}{m_Z^2}\frac{1}{p^2}\frac{\text{Im}\big[\Sigma_T^{\gamma Z}(p^2)\big]_{t,W}}{\pi}+\frac{1}{m_Z^2}\frac{1}{p^2-m_Z^2}\frac{\text{Im}\big[\Sigma_T^{\gamma Z}(p^2)\big]_{t,W}}{\pi}\right]\\
&-\hat{s}_W(\mu)\hat{c}_W(\mu)\frac{1}{\big(p^2\big)^2}\frac{\text{Im}\big[\Sigma_T^{\gamma\gamma}(p^2)\big]_{t,W}}{\pi}+\hat{s}_W(\mu)\hat{c}_W(\mu)\frac{1}{\big(p^2-m_Z^2\big)^2}\frac{\text{Im}\big[\Sigma_T^{ZZ}(p^2)\big]_{t,W,Z,H}}{\pi}
\end{aligned}
\tag{6.93}
$$

for $J^{34}(p^2)$ and

$$
J^{44} = \hat{c}_W^2\delta(p^2)+\hat{s}_W^2\delta(p^2-m_Z^2)+J^{44}_{\text{se},\,f\neq t\,\text{only}}(p^2,\mu)+J^{44}_{\text{se},\,f\neq t\,\text{excluded}}(p^2,\mu)\,,
\tag{6.94}
$$

$$
\begin{aligned}
J^{44}_{\text{se},\,f\neq t\,\text{only}}(p^2,\mu) = \frac{\hat{c}_W^2(\mu)\hat{g}_1^2(\mu)}{16\pi^2}\Bigg\{&\hat{c}_W^2(\mu)\frac{80}{9}\bigg[-\delta(p^2)\frac{5}{3}+\bigg[\frac{1}{p^2}\bigg]_*^{[\mu^2]}\bigg]\\
&-2\left(\frac{10}{3}-\frac{80}{9}\hat{s}_W^2(\mu)\right)\bigg[\bigg[\frac{1}{p^2-m_Z^2}\bigg]_*-\delta(p^2-m_Z^2)\left(\frac{5}{3}-\ln\frac{m_Z^2}{\mu^2}\right)\bigg]
\end{aligned}
$$

$$+\frac{\hat{s}_W^2(\mu)}{\hat{c}_W^2(\mu)}\bigg(-\frac{20}{3}+\frac{7}{2}\frac{1}{\hat{s}_W^2(\mu)}+\frac{80}{9}\hat{s}_W^2(\mu)\bigg)$$
$$\times\bigg[\bigg[\frac{1}{(p^2-m_Z^2)^2}\bigg]_{**}p^2-\delta(p^2-m_Z^2)\bigg(\frac{2}{3}-\ln\frac{m_Z^2}{\mu^2}\bigg)\bigg]\bigg\}. \tag{6.95}$$

$$\begin{aligned}
&J^{44}_{\text{se, }f\neq t\text{ excluded}}(p^2,\mu)=\\
&\quad-2\hat{s}_W(\mu)\hat{c}_W(\mu)\bigg[\frac{\text{Re}\big[\Sigma_T^{\gamma Z}(0)\big]_{t,W}}{m_Z^2}\delta(p^2)-\frac{\text{Re}\big[\Sigma_T^{\gamma Z}(m_Z^2)\big]_{t,W}}{m_Z^2}\delta(p^2-m_Z^2)\bigg]\\
&-\hat{c}_W^2(\mu)\text{Re}\frac{\partial\Sigma_T^{\gamma\gamma}(p^2)_{t,W}}{\partial p^2}\bigg|_{p^2=0}\delta(p^2)-\hat{s}_W^2(\mu)\text{Re}\frac{\partial\Sigma_T^{ZZ}(p^2)_{t,W,Z,H}}{\partial p^2}\bigg|_{p^2=m_Z^2}\delta(p^2-m_Z^2)\\
&-2\hat{s}_W(\mu)\hat{c}_W(\mu)\bigg[-\frac{1}{m_Z^2}\frac{1}{p^2}\frac{\text{Im}\big[\Sigma_T^{\gamma Z}(p^2)\big]_{t,W}}{\pi}+\frac{1}{m_Z^2}\frac{1}{p^2-m_Z^2}\frac{\text{Im}\big[\Sigma_T^{\gamma Z}(p^2)\big]_{t,W}}{\pi}\bigg]\\
&\quad+\hat{c}_W^2(\mu)\frac{1}{\big(p^2\big)^2}\frac{\text{Im}\big[\Sigma_T^{\gamma\gamma}(p^2)\big]_{t,W}}{\pi}+\hat{s}_W^2(\mu)\frac{1}{\big(p^2-m_Z^2\big)^2}\frac{\text{Im}\big[\Sigma_T^{ZZ}(p^2)\big]_{t,W,Z,H}}{\pi}
\end{aligned} \tag{6.96}$$

for $J^{44}(p^2)$.

Note that since in the narrow resolution case, the (anti-) collinear jet and soft functions all have the same virtuality, it is more convenient in this case to only resum the Wilson coefficient down to the soft scale. Hence, we are not going to discuss the resummation for the narrow resolution unobserved jet function.

6.3.2 Unobserved jet function - intermediate resolution case

The intermediate resolution jet function describes the unobserved hard-collinear final state. As mentioned before, the invariant mass squared is $p^2\sim m_W m_\chi\gg m_W^2$, which means that in the intermediate resolution case the unobserved jet function is computed using SCET_I and does not suffer from rapidity divergences. The intermediate resolution unobserved jet function is calculated in the massless EW symmetric limit, which will result in much simpler expressions compared to the narrow resolution case. The results shown in the following have been computed by CH, Kai Urban and Martin Vollmann. Different from the narrow resolution, the intermediate resolution unobserved jet function is diagonal which means that the gauge indices of J^{XV}_int can only take the values $XV=33$ or $XV=44$. In (3.16) we introduced the following notation $J^{33}_\text{int}=J^{\text{SU}(2)}_\text{int}$ and $J^{44}_\text{int}=J^{\text{U}(1)}_\text{int}$, making obvious which gauge boson is associated with which jet function. To make the origin of the different terms even more transparent, we again split the jet function into a Wilson line and a self-energy contribution

$$\begin{aligned}
i\mathcal{J}^{\text{SU}(2)}_\text{int}(p^2,\mu)=&i\mathcal{J}^{\text{SU}(2)}_{\text{int, Wilson}}(p^2,\mu)+i\mathcal{J}^{\text{SU}(2)}_{\text{int, se}}(p^2,\mu)\,,\\
i\mathcal{J}^{\text{U}(1)}_\text{int}(p^2,\mu)=&i\mathcal{J}^{\text{U}(1)}_{\text{int, se}}(p^2,\mu)\,.
\end{aligned} \tag{6.97}$$

The results for the SU(2) part of the jet function are as follows

$$i\mathcal{J}^{XV}_\text{Wilson}(p^2,\mu) = \frac{\delta^{XV}}{-p^2-i\epsilon}\bigg\{1+\bigg(\frac{\mu^2}{-p^2-i\epsilon}\bigg)^\epsilon\frac{\hat{g}_2^2(\mu)}{16\pi^2}c_2(\text{ad})\bigg(\frac{4}{\epsilon^2}+\frac{2}{\epsilon}+4-\frac{\pi^2}{3}\bigg)\bigg\} \tag{6.98}$$

$$i\mathcal{J}^{XV}_\text{se}(p^2,\mu) = \frac{\delta^{XV}}{-p^2-i\epsilon}\bigg(\frac{\mu^2}{-p^2-i\epsilon}\bigg)^\epsilon\frac{\hat{g}_2^2(\mu)}{16\pi^2}$$

$$\times \left\{ \frac{1}{\epsilon} \left(\frac{5}{3} c_2(\mathrm{ad}) - \frac{8}{3} T_F n_G - \frac{1}{3} T_s n_s \right) + \frac{31}{9} c_2(\mathrm{ad}) - \frac{40}{9} T_F n_G - \frac{8}{9} T_s n_s \right\}, \tag{6.99}$$

where $T_F = T_s = 1/2$ and $n_s = 1$. For the $\mathrm{U}(1)_Y$ part, the result reads

$$i\mathcal{J}^{\mathrm{U}(1)}(p^2) = \frac{1}{-p^2 - i\varepsilon} \left(\frac{\mu^2}{-p^2 - i\varepsilon} \right)^{\epsilon} \frac{\hat{g}_1^2 Y^2}{16\pi^2} \left[\frac{1}{\epsilon} \left(-\frac{1}{6} - \frac{20}{9} n_G \right) - \frac{104}{9} \right]. \tag{6.100}$$

In order to derive the final form of the jet functions we need to take the imaginary part and expand the result in terms of star distributions as follows [103]

$$\begin{aligned} \frac{1}{\pi} \mathrm{Im} \left[(-p^2 - i\varepsilon)^c \right] =& -\theta(p^2) \frac{\sin(\pi c)}{\pi} (p^2)^c, \\ \frac{1}{p^2} \left(\frac{p^2}{\mu^2} \right)^{-\epsilon} =& -\frac{1}{\epsilon} \delta(p^2) + \sum_{n=0}^{\infty} \frac{(-\epsilon)^n}{n!} \left[\frac{\ln^n \left(\frac{p^2}{\mu^2} \right)}{p^2} \right]_*^{[\mu^2]}. \end{aligned} \tag{6.101}$$

Using (6.101) we obtain for the SU(2) and $\mathrm{U}(1)_Y$ unobserved jet functions in the intermediate resolution case

$$\begin{aligned} J_{\mathrm{int}}^{\mathrm{SU}(2)}(p^2, \mu) &= \delta(p^2) + \frac{\hat{\alpha}_2(\mu)}{4\pi} \left\{ \delta(p^2) \left(\frac{70}{9} - 2\pi^2 \right) - \frac{19}{6} \left[\frac{1}{p^2} \right]_*^{[\mu^2]} + 8 \left[\frac{\ln \frac{p^2}{\mu^2}}{p^2} \right]_*^{[\mu^2]} \right\}, \\ J_{\mathrm{int}}^{\mathrm{U}(1)}(p^2, \mu) &= \delta(p^2) + \frac{\hat{g}_1^2(\mu)}{16\pi^2} \left\{ \delta(p^2) \left(-\frac{104}{9} \right) + \frac{41}{6} \left[\frac{1}{p^2} \right]_*^{[\mu^2]} \right\}. \end{aligned} \tag{6.102}$$

The procedure to solve the RG equations for (6.102) is analogous to the treatment of the QCD gluon jet function [103]. The appearance of star distributions in $J_{\mathrm{int}}^{\mathrm{SU}(2)}$ and $J_{\mathrm{int}}^{\mathrm{U}(1)}$ complicates the resummation and it will be convenient to solve the RGE in Laplace space. In general, the Laplace transform is defined as

$$j_{\mathrm{int}}^{\mathrm{G}} \left(\ln \frac{\tau^2}{\mu^2}, \mu \right) = \int_0^{\infty} dp^2 e^{-lp^2} J_{\mathrm{int}}^{\mathrm{G}}(p^2, \mu), \tag{6.103}$$

where the superscript G is a placeholder for either SU(2) or U(1) and $l = 1/(e^{\gamma_E} \tau^2)$. The explicit results after renormalization read

$$\begin{aligned} j_{\mathrm{int}}^{\mathrm{SU}(2)} \left(\ln \frac{\tau^2}{\mu^2}, \mu \right) =& 1 + \frac{\hat{\alpha}_2(\mu)}{4\pi} \left(4 \ln^2 \frac{\tau^2}{\mu^2} - \frac{19}{6} \ln \frac{\tau^2}{\mu^2} + \frac{70}{9} - \frac{4\pi^2}{3} \right), \\ j_{\mathrm{int}}^{\mathrm{U}(1)} \left(\ln \frac{\tau^2}{\mu^2}, \mu \right) =& 1 + \frac{\hat{\alpha}_1(\mu)}{4\pi} \left[\frac{41}{6} \ln \frac{\tau^2}{\mu^2} - \frac{104}{9} \right]. \end{aligned} \tag{6.104}$$

In Laplace space, the RG equations are now the ordinary differential equations

$$\begin{aligned} \frac{d}{d \ln \mu} j_{\mathrm{int}}^{\mathrm{SU}(2)} \left(\ln \frac{\tau^2}{\mu^2}, \mu \right) =& \gamma_{J^{SU(2)}}^{\mu} j_{\mathrm{int}}^{\mathrm{SU}(2)} \left(\ln \frac{\tau^2}{\mu^2}, \mu \right), \\ \frac{d}{d \ln \mu} j_{\mathrm{int}}^{\mathrm{U}(1)} \left(\ln \frac{\tau^2}{\mu^2}, \mu \right) =& \gamma_{J^{\mathrm{U}(1)}}^{\mu} j_{\mathrm{int}}^{\mathrm{U}(1)} \left(\ln \frac{\tau^2}{\mu^2}, \mu \right), \end{aligned} \tag{6.105}$$

with the Laplace space anomalous dimensions

$$\gamma_{J^{\mathrm{SU}(2)}}^{\mu} = -4\gamma_{\mathrm{cusp}} \ln \frac{\tau^2}{\mu^2} - 2\gamma_{J^{\mathrm{SU}(2)}},$$

$$\gamma^{\mu}_{J^{\mathrm{U}(1)}} = -2\gamma_{J^{\mathrm{U}(1)}} \,. \tag{6.106}$$

The non-cusp anomalous dimensions $\gamma_{J^{\mathrm{SU}(2)}}$ and $\gamma_{J^{\mathrm{U}(1)}}$ are both needed at the one-loop order for NLL' resummation

$$\gamma^{(0)}_{J^{\mathrm{SU}(2)}} = -\beta_{0,\mathrm{SU}(2)}\frac{\hat{\alpha}_2(\mu)}{4\pi} + \cdots \,, \quad \gamma^{(0)}_{J^{\mathrm{U}(1)}} = -\beta_{0,\mathrm{U}(1)}\frac{\hat{\alpha}_1(\mu)}{4\pi} + \cdots \,. \tag{6.107}$$

The RG equations (6.105) are solved by

$$j^{\mathrm{SU}(2)}_{\mathrm{int}}\left(\ln\frac{\tau^2}{\mu^2},\mu\right) = \exp\left[4\,S(\mu_j,\mu) + 2\,A_{\gamma_{J^{\mathrm{SU}(2)}}}(\mu_j,\mu)\right] j^{\mathrm{SU}(2)}_{\mathrm{int}}\left(\partial_\eta,\mu_j\right)\left(\frac{\tau^2}{\mu_j^2}\right)^{\eta} \,, \tag{6.108}$$

$$j^{\mathrm{U}(1)}_{\mathrm{int}}\left(\ln\frac{\tau^2}{\mu^2},\mu\right) = \exp\left[2\,A_{\gamma_{J^{\mathrm{U}(1)}}}(\mu_j,\mu)\right] j^{\mathrm{U}(1)}_{\mathrm{int}}\left(\ln\frac{\tau^2}{\mu^2},\mu_j\right) \,, \tag{6.109}$$

where $\mu_j \sim \sqrt{2m_\chi m_W}$ is the natural scale of the hard-collinear jet function and the integrals $S(\mu_j,\nu)$ and $A_{\gamma_{J^{\mathrm{G}}}}(\mu_j,\mu)$ are defined as

$$S(\mu_j,\mu) = -\int_{\ln\mu_j}^{\ln\mu} d\ln\mu'\,\gamma_{\mathrm{cusp}}(\mu')\ln\frac{\mu_j^2}{\mu'^2} \,, \tag{6.110}$$

$$A_{\gamma_{J^{\mathrm{G}}}}(\mu_j,\mu) = -\int_{\ln\mu_j}^{\ln\mu} d\ln\mu'\,\gamma_{J^{\mathrm{G}}}(\mu') \,. \tag{6.111}$$

Furthermore, the variable η in (6.108) is defined as

$$\eta = 4A_{\gamma_{\mathrm{cusp}}}(\mu_j,\mu) \,. \tag{6.112}$$

As before, the integrals $S(\mu_j,\nu)$ and $A_{\gamma_{J^{\mathrm{G}}}}(\mu_j,\mu)$ in the exponents of (6.108) and (6.109) are solved numerically. Note that in (6.108) the logarithm in the argument of the Laplace-transformed SU(2) jet function has been traded for a derivative with respect to η, which means that the entire τ-dependence of $j^{\mathrm{SU}(2)}_{\mathrm{int}}$ is contained in the ratio $\left(\tau^2/\mu_j^2\right)^{\eta}$ and the inverse Laplace transform becomes simple. Introducing the partial derivatives with respect to η for the $\mathrm{U}(1)_Y$ jet function was not necessary, since the anomalous dimension of $j^{\mathrm{U}(1)}_{\mathrm{int}}$ does not have a cusp term and thus there is no τ-dependence in the exponent of the evolution factor in (6.109). Lastly, we need to return to momentum space. For the $\mathrm{U}(1)_Y$ jet function, this is done via the standard inverse Laplace transform (remembering that $\tau^2 = 1/(e^{\gamma_R}l)$), while for the SU(2) jet function we make use of the relation

$$\int_0^\infty dp^2 e^{-p^2/(\tau^2 e^{\gamma_E})}\left(p^2\right)^{\eta-1} = \Gamma(\eta)e^{\gamma_E\eta}\left(\tau^2\right)^{\eta} \,. \tag{6.113}$$

We then arrive at the expressions for the resummed jet functions of the unobserved final state in momentum space

$$\begin{aligned} J^{\mathrm{SU}(2)}_{\mathrm{int}}(p^2,\mu) &= \exp\left[4\,S(\mu_j,\mu) + 2\,A_{\gamma^{\mathrm{SU}(2)}_J}(\mu_j,\mu)\right] j^{\mathrm{SU}(2)}_{\mathrm{int}}(\partial_\eta,\mu_j)\frac{e^{-\gamma_E\eta}}{\Gamma(\eta)}\frac{1}{p^2}\left(\frac{p^2}{\mu_j^2}\right)^{\eta} \,, \\ J^{\mathrm{U}(1)}_{\mathrm{int}}(p^2,\mu) &= \exp\left[2\,A_{\gamma^{\mathrm{U}(1)}_J}(\mu_j,\mu)\right] J^{\mathrm{U}(1)}_{\mathrm{int}}(p^2,\mu_j) \,, \end{aligned} \tag{6.114}$$

where $J^{\mathrm{U}(1)}_{\mathrm{int}}(p^2,\mu_j)$ in the second line of (6.114) is given by the fixed order expression in the second line of (6.102).

6.4 Soft function

The soft functions have a virtuality of $\mu_s \sim m_W$, where μ_s is the soft scale. This means that the soft function needs to be computed in the EW broken theory, which implies that we need to specify which DM multiplet we are considering. For wino DM the multiplet is an SU(2) triplet with isospin $j = 1$ and hypercharge $Y = 0$, while for Higgsino DM the multiplet is an $\mathrm{SU}(2)\otimes\mathrm{U}(1)_Y$ doublet with isospin $j = 1/2$ and hypercharge $Y = 1/2$. Although the discussion of the soft function resummation follows the same arguments for both models, the anomalous dimensions and evolution factors are different. We thus discuss the soft functions separately for each model.

In general, the soft functions are given by products of soft Wilson lines, which arise from the decoupling transformation that decouples soft SU(2) and $\mathrm{U}(1)_Y$ gauge bosons from initial and final states in the $2 \to 2$ scattering amplitude. Technical details about the computation of the necessary integrals and the complete soft function expressions, which are quite lengthy, are moved to the Appendix G. To guide the discussion of the soft function resummation in the intermediate resolution cases, in this Section we provide the results for the index combination for which the soft function is most general and exhibits the most complicated structure. The soft function computations were done by Alessandro Broggio and CH for the wino DM narrow resolution case, by Alessandro Broggio, CH and Kai Urban for the wino DM intermediate resolution case and by CH and Martin Vollmann for both Higgsino DM resolution cases.

6.4.1 Intermediate resolution soft function - Wino DM

In the case of wino DM, we focus on the index combination $i = j = 2$ and $I = J = (+-)$, for which the soft function takes the form

$$W^{22}_{(+-)(+-)}(\omega,\mu,\nu) = \delta(\omega) + \frac{\hat{\alpha}_2(\mu)}{4\pi}\left[\delta(\omega)\left(-8\ln\frac{m_W}{\mu} - 16\ln\frac{m_W}{\mu}\ln\frac{m_W}{\nu}\right)\right.$$
$$\left.\left[\frac{1}{\omega}\right]_*^{[m_W]}\left(-6\ln\left(\frac{m_W^2+\omega^2}{m_W^2}\right) - 2\frac{\omega^2}{m_W^2+\omega^2} + 8\ln\frac{\mu^2}{m_W^2}\right)\right]. \quad (6.115)$$

All intermediate resolution wino DM soft function expressions for all operator and two-particle-state index combinations are collected in Appendix G.4.1. As in the case of the unobserved jet function discussed in Section 6.3.2, it is convenient to perform the resummation in Laplace space. The necessary forward and inverse Laplace transforms are respectively defined as

$$w(s) = \mathcal{L}\{W(\omega)\} = \int_0^\infty d\omega\, e^{-\omega s}\, W(\omega)\,, \quad (6.116)$$

$$W(\omega) = \mathcal{L}^{-1}\{w(s)\} = \frac{1}{2\pi i}\int_{c-i\infty}^{c+i\infty} ds\, e^{s\omega}\, w(s)\,, \quad (6.117)$$

where $s = 1/(e^{\gamma_E}\kappa)$. Inspecting $W^{22}_{(+-)(+-)}$ in (6.115), which exhibits all ω-structures that we will encounter, we find that the following explicit forward Laplace transforms are relevant

$$\mathcal{L}\{\delta(\omega)\} = 1\,,$$
$$\mathcal{L}\left\{\left[\frac{1}{\omega}\right]_*^{[m_W]}\right\} = \ln\frac{\kappa}{m_W}\,,$$

$$\mathcal{L}\left\{\frac{1}{\omega}\ln\left(\frac{m_W^2+\omega^2}{m_W^2}\right)\right\} = \mathrm{si}^2\left(m_W s\right) + \mathrm{ci}^2\left(m_W s\right) \equiv \tilde{G}(s)\,,$$
$$\mathcal{L}\left\{\frac{\omega}{m_W^2+\omega^2}\right\} = \cos(m_W s)\,\mathrm{ci}(m_W s) - \sin(m_W s)\,\mathrm{si}(m_W s) \equiv \tilde{Q}(s)\,, \tag{6.118}$$

where the functions ci and si are defined as

$$\mathrm{si}(x) \equiv -\int_x^\infty dt\,\frac{\sin(t)}{t}, \quad \text{and} \quad \mathrm{ci}(x) \equiv -\int_x^\infty dt\,\frac{\cos(t)}{t}\,. \tag{6.119}$$

For reasons of brevity, it is most convenient to introduce the following vector notation for the Laplace transformed soft functions

$$\vec{w}_{IJ} = \left(w_{IJ}^{11}, w_{IJ}^{12}, w_{IJ}^{21}, w_{IJ}^{22}\right)^T\,. \tag{6.120}$$

Since the soft function has the same virtuality as the photon jet function, it is clear that it needs to be computed in $\mathrm{SCET_{II}}$ and thus suffers from rapidity divergences, which potentially need to be resummed. Let us thus first discuss rapidity resummation. The corresponding RRG equations take the form

$$\frac{d}{d\ln\nu}\vec{w}_{IJ}(s,\mu,\nu) = \mathbf{\Gamma}_W^\nu\,\vec{w}_{IJ}(s,\mu,\nu)\,, \tag{6.121}$$

where the fixed-order one-loop rapidity anomalous dimension is given by

$$\mathbf{\Gamma}_W^\nu = \frac{\hat{\alpha}_2}{4\pi}\,4\gamma_{\mathrm{cusp}}^{(0)}\,\ln\frac{m_W}{\mu}\,\mathbf{1}_4\,. \tag{6.122}$$

We can see from (6.122) that $\mathbf{\Gamma}_W^\nu$ has a vanishing non-cusp anomalous dimension at one-loop order. It is important to make sure that the correct path of resummation is taken in the $\mu-\nu$ plane and that the anomalous dimensions are included at the right loop order. This was already extensively discussed for the photon jet function in Section 6.2. We thus use(6.52), (6.53) and (6.121) to compute the wino DM rapidity-resummed soft function and find

$$\vec{w}_{IJ}(s,\mu,\nu) = \exp\left[\mathbf{\Gamma}_W^\nu(\mu)\ln\frac{\nu}{\nu_s}\right]\vec{w}_{IJ}(s,\mu,\nu_s)\,, \tag{6.123}$$

where $\mathbf{\Gamma}_W^\nu(\mu)$ is now the integrated rapidity anomalous dimension. Note that (6.123) is diagonal in both the two-particle state indices I,J and the operator indices, which are made explicit by the vector notation (6.120). In the intermediate energy resolution case, only the photon jet functions and the soft functions depend on the rapidity scale. For the computation of the cross section, we choose to resum the photon jet function in ν from the hard rapidity scale $\nu_h \sim 2m_\chi$ to the soft rapidity scale $\nu_s \sim m_W$. As a consequence we can set $\nu = \nu_s$ for the soft function, after which the rapidity evolution factor (6.123) becomes unity.

In the case of wino DM, the virtuality RG equation is more complicated. This is because while being diagonal in the two-particle indices I and J, the virtuality anomalous dimension of the Laplace transformed wino soft function has a non-diagonal contribution in the operator space. Specifically, the RGE is given by

$$\frac{d}{d\ln\mu}\vec{w}_{IJ}(s,\mu,\nu) = \mathbf{\Gamma}_W^\mu\,\vec{w}_{IJ}(s,\mu,\nu)\,, \tag{6.124}$$

where $\mathbf{\Gamma}_W^\mu$ is given by

$$\mathbf{\Gamma}_W^\mu = 4\,\gamma_{\text{cusp}} \ln\frac{\kappa}{\nu}\,\mathbf{1}_4 + \begin{pmatrix} 0 & 0 & 0 & 0 \\ -2\gamma_W & 3\gamma_W & 0 & 0 \\ -2\gamma_W^* & 0 & 3\gamma_W^* & 0 \\ 0 & -2\gamma_W^* & -2\gamma_W & 3\gamma_W + 3\gamma_W^* \end{pmatrix} . \tag{6.125}$$

Similar to the case of the photon jet functions, the soft function anomalous dimensions (6.122) and (6.125) may be computed from (6.121) and (6.124), respectively. For NLL' resummation, we need the one-loop contribution for the non-cusp anomalous dimension γ_W, which we find to be

$$\gamma_W^{(0)} = (2 + 2\pi i) c_2(j) . \tag{6.126}$$

Using (6.125) and (6.126) we can solve the RGE (6.124) to obtain

$$\vec{w}_{IJ}(s,\mu,\nu) = \boldsymbol{R}^{-1}\,\boldsymbol{U}_W(\mu,\mu_s)\,\boldsymbol{R}\,\vec{w}_{IJ}(s,\mu_s,\partial_\eta)\left(\frac{\kappa}{\nu}\right)^\eta , \tag{6.127}$$

with the following diagonal evolution matrix $\boldsymbol{U}_W$

$$\boldsymbol{U}_W = \begin{pmatrix} 1 & 0 & 0 & 0 \\ 0 & \exp\left[3A_{\gamma_W}\right] & 0 & 0 \\ 0 & 0 & \exp\left[3A_{\gamma_W^*}\right] & 0 \\ 0 & 0 & 0 & \exp\left[3(A_{\gamma_W} + A_{\gamma_W^*})\right] \end{pmatrix} , \tag{6.128}$$

and the diagonalization matrix $\boldsymbol{R}$ and its inverse $\boldsymbol{R}^{-1}$ are given by

$$\boldsymbol{R} = \begin{pmatrix} \frac{2}{3} & 0 & 0 & 0 \\ -\frac{2}{3} & 1 & 0 & 0 \\ -\frac{2}{3} & 0 & 1 & 0 \\ \frac{2}{3} & -1 & -1 & \frac{3}{2} \end{pmatrix} , \quad \boldsymbol{R}^{-1} = \begin{pmatrix} \frac{3}{2} & 0 & 0 & 0 \\ 1 & 1 & 0 & 0 \\ 1 & 0 & 1 & 0 \\ \frac{2}{3} & \frac{2}{3} & \frac{2}{3} & \frac{2}{3} \end{pmatrix} . \tag{6.129}$$

The intregals A_{γ_W} in the exponents in (6.128) and the variable η in (6.127) where defined in (6.111) and (6.112), respectively. Having computed the resummed soft function in Laplace space (6.127), it remains to return to momentum space via the inverse Laplace transform. The entire dependence on the transform parameter κ is contained in $\vec{w}_{IJ}(s,\mu_s,\partial_\eta)\left(\frac{\kappa}{\nu}\right)^\eta$ and we define $\hat{\vec{W}}_{IJ}(\omega,\mu_s,\nu)$ to be the inverse Laplace transform

$$\hat{\vec{W}}_{IJ}(\omega,\mu_s,\nu) = \mathcal{L}^{-1}\left[\vec{w}_{IJ}(s,\mu_s,\partial_\eta)\left(\frac{\kappa}{\nu}\right)^\eta\right] . \tag{6.130}$$

The relevant inverse Laplace transforms that need to be computed are the following

$$\mathcal{L}^{-1}\left[\left(\frac{\kappa}{\nu}\right)^\eta\right] = \frac{e^{-\gamma_E\eta}}{\Gamma(\eta)}\left(\frac{\omega}{\nu}\right)^\eta\frac{1}{\omega} , \tag{6.131}$$

$$\begin{aligned} F(\omega) &\equiv \mathcal{L}^{-1}\left[\left(\frac{\kappa}{\nu}\right)^\eta \tilde{G}\big(e^{-\gamma_E}/\kappa\big)\right] \\ &= \left(\frac{e^{-\gamma_E}}{\nu}\right)^\eta \frac{\omega^{1+\eta}}{\Gamma(2+\eta)m_W^2}\,{}_4F_3\left(1,1,1,\frac{3}{2};1+\frac{\eta}{2},\frac{3}{2}+\frac{\eta}{2},2;-\frac{\omega^2}{m_W^2}\right) , \\ P(\omega) &\equiv \mathcal{L}^{-1}\left[\left(\frac{\kappa}{\nu}\right)^\eta \tilde{Q}\big(e^{-\gamma_E}/\kappa\big)\right] \\ &= \left(\frac{e^{-\gamma_E}}{\nu}\right)^\eta \frac{\omega^{1+\eta}}{m_W^2\Gamma(2+\eta)}\,{}_3F_2\left(1,1,\frac{3}{2};1+\frac{\eta}{2},\frac{3}{2}+\frac{\eta}{2};-\frac{\omega^2}{m_W^2}\right) . \end{aligned} \tag{6.132}$$

As before, we use the index combination $i = j = 2$ and $I = J = (+-)$ to provide an example, for which we find

$$\hat{W}^{22}_{(+-)(+-)}(\omega, \mu_s, \nu) = \left[1 + \frac{\hat{\alpha}_2}{4\pi}\left(\left(-16\ln\frac{m_W}{\mu_s}\,\partial_\eta\right) - 8\ln\frac{m_W}{\mu_s}\right)\right]\frac{e^{-\gamma_E\eta}}{\Gamma(\eta)}\frac{1}{\omega}\left(\frac{\omega}{\nu}\right)^\eta + \frac{\hat{\alpha}_2}{4\pi}\left[-6F(\omega) - 2P(\omega)\right]. \tag{6.133}$$

The results for all resummed wino DM momentum space soft functions $\hat{W}^{ij}_{IJ}$ for all index combinations are provided in Appendix G.5.1. Combining the results from (6.127), (6.130) and (6.132) we arrive at the final expression for the virtuality resummed wino DM soft function in momentum space

$$\vec{W}^{ij}_{IJ}(\omega, \mu, \nu) = \boldsymbol{R}^{-1}\,\boldsymbol{U}_W(\mu, \mu_s)\,\boldsymbol{R}\,\hat{\vec{W}}^{ij}_{IJ}(\omega, \mu_s, \nu)\,. \tag{6.134}$$

We point out again that for the computation of the final cross section, we chose to run the photon jet function Z^{33}_γ in the rapidity scale from $\nu_h \to \nu_s$, which renders the soft function rapidity evolution factor (6.121) unity and it hence does not show up explicitly in (6.134).

6.4.2 Narrow resolution soft function - Wino DM

As explained before, the narrow resolution soft function differs from its intermediate resolution counterpart due to the fact that the former does not feature real radiation. This is because in the narrow case, the higher resolution $E^\gamma_{\text{res}} \sim m_W^2/m_\chi$ implies that real soft radiation of gauge bosons with masses around the electroweak scale can be resolved, while this is not possible in the intermediate case which has $E^\gamma_{\text{res}} \sim m_W$. The soft coefficients for the wino DM model are given by

$$\begin{aligned}
D^{\text{W},1}_{(00),\,33}(\mu, \nu) =& 1 + \frac{\hat{g}_2^2(\mu)}{16\pi^2}\left(8\ln^2\frac{m_W}{\mu} - 8i\pi\ln\frac{m_W}{\mu} - \frac{\pi^2}{3} - 16\ln\frac{m_W}{\mu}\ln\frac{m_W}{\nu}\right),\\
D^{\text{W},2}_{(00),\,33}(\mu, \nu) =& \frac{\hat{g}_2^2(\mu)}{16\pi^2}\,(8 - 8i\pi)\ln\frac{m_W}{\mu},\\
D^{\text{W},1}_{(+-),\,33}(\mu, \nu) =& D^{\text{W},1}_{(00),\,33}(\mu, \nu),\\
D^{\text{W},2}_{(+-),\,33}(\mu, \nu) =& D^{\text{W},1}_{(00),\,33}(\mu, \nu) - \frac{1}{2}D^{\text{W},2}_{(00),\,33}(\mu, \nu).
\end{aligned} \tag{6.135}$$

6.4.3 Intermediate resolution soft function - Higgsino DM

For resumming the intermedaite resolution Higgsino DM soft function, we proceed in a similar manner as for its wino DM counterpart. Naively, one might expect the Higgsino DM soft function to be more complicated since we need to deal with both SU(2) and $\text{U}(1)_Y$ soft gauge bosons. We will see however, that it turns out to be easier than in the wino DM case. All Higgsino DM soft function expressions in momentum space are collected in Appendix G.4.2. Using the forward Laplace transforms (6.118), we compute the Laplace transformed soft functions for which we again introduce the vector notation

$$\begin{aligned}
\vec{w}^{\,\text{SU}(2)}_{IJ}(s, \mu, \nu) &= \left(w^{\text{SU}(2),11}_{IJ,33}, w^{\text{SU}(2),14}_{IJ,34}, w^{\text{SU}(2),41}_{IJ,43}, w^{\text{SU}(2),44}_{IJ,44}\right)^T,\\
\vec{w}^{\,\text{U}(1)}_{IJ}(s, \mu, \nu) &= \left(w^{\text{U}(1),44}_{IJ,33}, w^{\text{U}(1),46}_{IJ,34}, w^{\text{U}(1),64}_{IJ,43}, w^{\text{U}(1),66}_{IJ,44}\right)^T,
\end{aligned} \tag{6.136}$$

where the superscripts SU(2) and U(1) expresses which soft gauge boson is radiated. As before we start by solving the RRG equations

$$\begin{aligned}\frac{d}{d\ln\nu}\vec{w}_{IJ}^{\mathrm{SU}(2)}(s,\mu,\nu) &= \mathbf{\Gamma}_W^{\mathrm{SU}(2),\nu}\vec{w}_{IJ}^{\mathrm{SU}(2)}(s,\mu,\nu)\,,\\ \frac{d}{d\ln\nu}\vec{w}_{IJ}^{\mathrm{U}(1)}(s,\mu,\nu) &= \mathbf{\Gamma}_W^{\mathrm{U}(1),\nu}\vec{w}_{IJ}^{\mathrm{U}(1)}(s,\mu,\nu)\,.\end{aligned} \tag{6.137}$$

We find that both the SU(2) and $\mathrm{U}(1)_Y$ one-loop rapidity anomalous dimensions are diagonal in both the operator indices i,j and the two-particle-state indices I,J. They take the form

$$\mathbf{\Gamma}_W^{\mathrm{SU}(2),\nu} = \mathbf{\Gamma}_W^{\mathrm{U}(1),\nu} = \frac{\hat{\alpha}_2(\mu)}{4\pi}2\gamma_{\mathrm{cusp}}^{(0)}\ln\frac{m_W}{\mu}\,\mathrm{diag}\,[2,1,1,0]\,. \tag{6.138}$$

Since the rapidity anomalous dimensions (6.138) are diagonal, solving the RRG equations (6.137) is straightforward. Neither $\mathbf{\Gamma}_W^{\mathrm{SU}(2),\nu}$ nor $\mathbf{\Gamma}_W^{\mathrm{U}(1),\nu}$ depends on the rapidity scale ν, which allows us to find the analytic solutions

$$\begin{aligned}\vec{w}_{IJ}^{\mathrm{SU}(2)}(s,\mu,\nu) &= \exp\left[\mathbf{\Gamma}_W^{\mathrm{SU}(2),\nu}\ln\frac{\nu}{\nu_s}\right]\vec{w}_{IJ}^{\mathrm{SU}(2)}(s,\mu,\nu)\,,\\ \vec{w}_{IJ}^{\mathrm{U}(1)}(s,\mu,\nu) &= \exp\left[\mathbf{\Gamma}_W^{\mathrm{U}(1),\nu}\ln\frac{\nu}{\nu_s}\right]\vec{w}_{IJ}^{\mathrm{U}(1)}(s,\mu,\nu)\,.\end{aligned} \tag{6.139}$$

Like in the wino DM model, also for Higgsino DM we have to choose whether we resum the rapidity logarithms of the photon jet function or those of the soft function. As before, we resum the photon jet function and evolve the rapidity scale from $\nu_h \sim 2m_\chi$ to $\nu_s \sim m_W$. This means that we can set $\nu = \nu_s$ in (6.139), which renders the Higgsino DM rapidity evolution factors unity.

The RG equations for the Higgsino DM soft functions are given by

$$\begin{aligned}\frac{d}{d\ln\mu}\vec{w}_{IJ}^{\mathrm{SU}(2)}(s,\mu,\nu) &= \mathbf{\Gamma}_W^{\mathrm{SU}(2),\mu}\vec{w}_{IJ}^{\mathrm{SU}(2)}(s,\mu,\nu)\,,\\ \frac{d}{d\ln\mu}\vec{w}_{IJ}^{\mathrm{U}(1)}(s,\mu,\nu) &= \mathbf{\Gamma}_W^{\mathrm{U}(1),\mu}\vec{w}_{IJ}^{\mathrm{U}(1)}(s,\mu,\nu)\,,\end{aligned} \tag{6.140}$$

with the anomalous dimensions

$$\begin{aligned}\mathbf{\Gamma}_W^{\mathrm{SU}(2),\mu} =& 4\gamma_{\mathrm{cusp}}\ln\frac{\kappa}{\nu}\,\mathbf{1}_4 + 2\gamma_{\mathrm{cusp}}\left(\ln\frac{m_W}{\mu} - \ln\frac{m_W}{\nu}\right)\mathrm{diag}\,[0,1,1,2]\\ &+ \mathrm{diag}\,[0,\gamma_H,\gamma_H^*,2\mathrm{Re}\,\gamma_H]\,,\\ \mathbf{\Gamma}_W^{\mathrm{U}(1),\mu} =& 2\gamma_{\mathrm{cusp}}\left(\ln\frac{m_W}{\nu} - \ln\frac{m_W}{\mu}\right)\mathrm{diag}\,[2,1,1,0]\\ &+ \mathrm{diag}\,[2\mathrm{Re}\,\gamma_H,\mathrm{Re}\,\gamma_H,\mathrm{Re}\,\gamma_H^*,0]\,.\end{aligned} \tag{6.141}$$

For NLL' accuracy we need the one-loop expression for the non-cusp anomalous dimension γ_H, which we can compute from the RG equations (6.140) and find it to be

$$\gamma_H^{(0)} = 4 + 8i\pi\,. \tag{6.142}$$

Making use of the relations (6.141) and (6.142) we can solve the RG equations (6.140) and find to following expressions for the Laplace space resummed Higgsino DM soft functions

$$\vec{w}_{IJ}^{\mathrm{SU}(2)}(s,\mu,\nu) = \mathbf{U}_W^{\mathrm{SU}(2),\mu}(\mu,\mu_s,\nu)\,\vec{w}_{IJ}^{\mathrm{SU}(2)}(s,\mu_s,\partial_\eta)\left(\frac{\kappa}{\nu}\right)^\eta\,,$$

$$\vec{w}_{IJ}^{\mathrm{U}(1)}(s,\mu,\nu) = \mathbf{U}_W^{\mathrm{U}(1),\mu}(\mu,\mu_s,\nu)\,\vec{w}_{IJ}^{\mathrm{U}(1)}(s,\mu_s,\nu)\,, \tag{6.143}$$

where the evolution matrices $\mathbf{U}_W^{\mathrm{SU}(2),\mu}$ and $\mathbf{U}_W^{\mathrm{U}(1),\mu}$ are given by

$$\begin{aligned}\mathbf{U}_W^{\mathrm{SU}(2),\mu}(\mu,\mu_s,\nu) &= \exp\left[\int_{\ln\mu_s}^{\ln\mu} d\ln\mu'\,\mathbf{\Gamma}_{W,\gamma_W}^{\mathrm{SU}(2),\mu}\right]\,,\\ \mathbf{U}_W^{\mathrm{U}(1),\mu}(\mu,\mu_s,\nu) &= \exp\left[\int_{\ln\mu_s}^{\ln\mu} d\ln\mu'\,\mathbf{\Gamma}_W^{\mathrm{U}(1),\mu}\right]\,.\end{aligned} \tag{6.144}$$

Again, the parameter η in (6.127) was defined in (6.112). After having computed the virtuality evolution factors, it is time to perform the inverse Laplace transforms to obtain the resummed soft functions in momentum space. For this, we make use of the relations (6.132) to find the final form of the virtuality-resummed Higgsino DM soft functions in momentum space

$$\begin{aligned}\vec{W}_{IJ}^{\mathrm{SU}(2)}(\omega,\mu,\nu) &= \mathbf{U}_W^{\mathrm{SU}(2),\mu}(\mu,\mu_s,\nu)\;\hat{\vec{W}}_{IJ}^{\mathrm{SU}(2)}(\omega,\mu_s,\nu)\,,\\ \vec{W}_{IJ}^{\mathrm{U}(1)}(\omega,\mu,\nu) &= \mathbf{U}_W^{\mathrm{U}(1),\mu}(\mu,\mu_s,\nu)\;\vec{W}_{IJ}^{\mathrm{U}(1)}(\omega,\mu_s,\nu)\,.\end{aligned} \tag{6.145}$$

The functions $\hat{\vec{W}}_{IJ}^{\mathrm{SU}(2)}$ for all index combinations I,J are collected in Appendix G.5.2 and the functions $\vec{W}_{IJ}^{\mathrm{U}(1)}$ are given in Appendix G.4.2. As in the corresponding expression for the wino DM soft function (6.134), the apparent lack of the rapidity evolution factor is caused by the resummation path we chose.

6.4.4 Narrow resolution soft function - Higgsino DM

The narrow resolution soft function coefficients for the Higgsino DM model are given by

$$\begin{aligned}D_{(00),33}^{\mathrm{H},1} &= 1 + \frac{\hat{g}_2^2(\mu)}{16\pi^2}\left[-\frac{\pi^2}{3} + 8i\pi\ln\frac{m_W}{\mu} - 16\ln\frac{m_W}{\mu}\ln\frac{m_W}{\nu} + 8\ln^2\frac{m_W}{\mu}\right]\,,\\ D_{(+-),33}^{\mathrm{H},1} &= D_{(00),33}^{\mathrm{H},1}\,,\\ D_{(00),34}^{\mathrm{H},4} &= -\frac{1}{2} - \frac{1}{2}\frac{\hat{g}_2^2(\mu)}{16\pi^2}\left[-\frac{\pi^2}{6} - 4\ln\frac{m_W}{\mu} - 8\ln\frac{m_W}{\mu}\ln\frac{m_W}{\nu} + 4\ln^2\frac{m_W}{\mu}\right]\,,\\ D_{(+-),34}^{\mathrm{H},4} &= -D_{(00),34}^{\mathrm{H},4}\,,\quad D_{(00),43}^{\mathrm{H},4} = D_{(00),34}^{\mathrm{H},4}\,,\quad D_{(+-),43}^{\mathrm{H},4} = D_{(+-),34}^{\mathrm{H},4}\,,\\ D_{(00),44}^{\mathrm{H},6} &= 1\,,\quad D_{(+-),44}^{\mathrm{H},6} = 1\,.\end{aligned} \tag{6.146}$$

6.5 RG and RRG invariance

After having computed all the necessary functions to evaluate the wino and Higgsino DM cross sections, we now check whether the the results presented so far are consistent. At NLL' accuracy, the physical photon energy spectrum has to be independent of the virtuality, μ, and rapidity, ν, scales, at one-loop order. This scale independence manifests itself via the two consistency equations

$$\frac{d}{d\ln\mu}\frac{d(\sigma v_{\mathrm{rel}})}{dE_\gamma} = 0\,, \tag{6.147}$$

$$\frac{d}{d\ln\nu}\frac{d(\sigma v_{\mathrm{rel}})}{dE_\gamma} = 0\,. \tag{6.148}$$

The cross sections in (6.147) and (6.148) are representative for both the wino and Higgsino DM cross sections. Note that in the analysis presented here we can disregard the Sommerfeld effect, because here it is taken at leading order and is thus scale independent. Consequently the factor S_{IJ} can be divided out when evaluating (6.147) and (6.148). We will confirm the scale independence for wino and Higgsino DM, for both the intermediate and narrow resolution cases.

6.5.1 Intermediate resolution RG and RRG invariance - Wino DM

We saw that for the unobserved jet and the soft functions it was convenient to compute their resummation using a Laplace transformation, which turns convolution into multiplication. Checking the scale independence will hence also be easiest if it is done in Laplace space, for which we have to take the Laplace transforms of the factorized cross section (3.28). We take the Laplace transform with respect to the variable $e_\gamma \equiv 2\,(m_\chi - E_\gamma)$. The Laplace variable will be called t. The convolution of the unobserved jet function and the soft function then turns into a simple multiplication as follows

$$\begin{aligned}\mathcal{L}\left[\int_0^\infty d\omega\, J_{\text{int}}(2m_\chi(e_\gamma-\omega))\, W(\omega)\right] &= \int_0^\infty de_\gamma\, e^{-te_\gamma} \int_0^\infty d\omega\, J_{\text{int}}(2m_\chi(e_\gamma-\omega))\, W(\omega) \\ &= \int_0^\infty \frac{dp^2}{2m_\chi}\, e^{-tp^2/2m_\chi} J_{\text{int}}(p^2) \int_0^\infty d\omega\, e^{-t\omega} W(\omega) \\ &= \frac{1}{2m_\chi}\, j_{\text{int}}\left(\ln\frac{2m_\chi}{te^{\gamma_E}\mu^2}\right)\, w(t)\,, \end{aligned} \tag{6.149}$$

where we omitted indices and scales in the function arguments for reasons of brevity. Introducing the substitution $p^2 = 2m_\chi\,(e_\gamma - \omega)$ allows us to move from the first to the second line. This substitution would in principle introduce a negative lower bound for the p^2-integration, but the fact that p^2 is strictly positive allows us to set the lower bound to zero. Comparing the second line in (6.149) with the definitions of the Laplace transforms in (6.103) and (6.116) we immediately arrive at the last line in (6.149). Because the Wilson coefficients and the photon jet function do not depend on e_γ or ω, they are not affected by the Laplace transform and we can rewrite (6.147) for the wino DM intermediate resolution cross section, which results in

$$\frac{d}{d\ln\mu}\left[\vec{H}(\mu)\cdot\vec{w}(t,\mu,\nu) Z_\gamma(\mu,\nu) j_{\text{int}}\left(\ln\frac{2m_\chi}{te^{\gamma_E}\mu^2},\mu\right)\right] = 0\,. \tag{6.150}$$

After performing the differentiation and remembering the definitions (6.33), (6.45), (6.105) and (6.124) of the anomalous dimensions, we find

$$\boldsymbol{\Gamma}_H^{\text{wino}} + \boldsymbol{\Gamma}_W^\mu + \gamma^\mu_{Z_\gamma^{33}}\mathbf{1}_4 + \gamma^\mu_{J^{\text{SU}(2)}}\mathbf{1}_4 = 0\,. \tag{6.151}$$

The anomalous dimensions in (6.151) are given in matrix form, where the matrix entries are determined by values of the operator indices i and j. The hard function and both jet functions are independent of the two-particle state indices I, J and in Section 6.4.1 we saw that the virtuality RG equation for the Laplace-transformed wino DM soft function is diagonal in I, J. Equation (6.151) thus holds for all combinations of I and J. In order to verify (6.151), we simply use the explicit expressions for the anomalous dimensions given in (6.34), (6.46), (6.106) and (6.125). Since the cusp anomalous dimensions are diagonal in both the operator and the two-particle state indices, it is easiest to confirm the consistency

equation for this case, which reads

$$\left(4\gamma_{\text{cusp}}\ln\frac{4m_\chi^2}{\mu^2}+4\gamma_{\text{cusp}}\ln\frac{1}{te^{\gamma_E}\nu}+4\gamma_{\text{cusp}}\ln\frac{\nu}{2m_\chi}-4\gamma_{\text{cusp}}\ln\frac{2m_\chi}{te^{\gamma_E}\mu^2}\right)\mathbf{1}_4=0\,. \quad (6.152)$$

It can be checked that the consistency equation is also fulfilled for the non-cusp parts of the anomalous dimensions, although it should be noted that the cancellation is non-trivial due to non-vanishing off-diagonal non-cusp terms appearing in $\mathbf{\Gamma}_H^{\text{wino}}$ and $\mathbf{\Gamma}_W^{\mu}$.

After having confirmed the virtuality scale independence of the intermediate resolution wino DM cross section, we now move on to also check for rapidity scale independence (6.148). The steps taken are exactly the same as in the virtuality case, but instead of differentiating with respect to μ, as we did in (6.150), we now differentiate with respect to ν. Note also, that only the photon jet and the soft functions depend on the rapidity scale, which simplifies the analysis. Making use of the RRG equations (6.49) and (6.121) we arrive at the intermediate resolution wino DM rapidity consistency equation

$$\gamma^{\nu}_{Z_\gamma^{33}}\mathbf{1}_4+\mathbf{\Gamma}_W^{\nu}=0\,, \quad (6.153)$$

which is easy to confirm by plugging in the explicit expressions for $\gamma^{\nu}_{Z_\gamma}$ and $\mathbf{\Gamma}_W^{\nu}$ from (6.50) and (6.122), respectively.

We have now shown that the virtuality (6.151) and rapidity (6.153) consistency equations are fulfilled, proving the complete one-loop scale independence of the intermediate resolution wino DM cross section. This serves as a strong cross check of the correctness of our results.

6.5.2 Narrow resolution RG and RRG invariance - Wino DM

In order to prove the scale independence in the narrow resolution case, we first have to compute the RRG and RG equations for the wino DM soft coefficients $D_{I,33}^{\text{W},i}$ $(i=1,2)$ and for the narrow resolution unobserved jet function J_{nrw}^{33}. These results were not calculated previously since these functions do not need to be resummed for the evaluation of the cross section. The RG and RRG equations for the soft coefficients are given by

$$\frac{d}{d\ln\mu}D_{I,33}^{\text{W},i}(\mu,\nu)=\gamma^{\mu}_{D^{\text{W}},ij}D_{I,33}^{\text{W},j}(\mu,\nu)\,, \quad (6.154)$$

$$\frac{d}{d\ln\nu}D_{I,33}^{\text{W},i}(\mu,\nu)=\gamma^{\nu}_{D^{\text{W}}}D_{I,33}^{\text{W},i}(\mu,\nu)\,. \quad (6.155)$$

The one-loop anomalous dimensions can be directly computed from (6.154) and (6.155), by making use of the soft coefficient expressions provided in (6.135). We find $\gamma^{\mu}_{D^{\text{W}},ij}$ and $\gamma^{\nu}_{D^{\text{W}}}$ to take the form

$$\gamma^{\mu\,(0)}_{D^{\text{W}}}=\begin{pmatrix}16\ln\frac{\mu}{\nu}+8\pi i & 0\\ c_2(j)(-4+4\pi i) & 16\ln\frac{\mu}{\nu}+(12-4\pi i)\end{pmatrix}\,, \quad (6.156)$$

$$\gamma^{\nu\,(0)}_{D^{\text{W}}}=16\ln\frac{m_W}{\mu}\mathbf{1}_2\,. \quad (6.157)$$

Similarly, the RG and RRG equations for the unobserved jet function J_{nrw}^{33} are

$$\frac{d}{d\ln\mu}J_{\text{nrw}}^{33}\left(p^2,\mu,\nu\right)=\gamma^{\mu}_{J_{\text{nrw}}^{33}}J_{\text{nrw}}^{33}\left(p^2,\mu,\nu\right)\,, \quad (6.158)$$

$$\frac{d}{d\ln\nu} J^{33}_{\text{nrw}}\left(p^2,\mu,\nu\right) = \gamma^{\nu}_{J^{33}_{\text{nrw}}} J^{33}_{\text{nrw}}\left(p^2,\mu,\nu\right) \,. \tag{6.159}$$

The anomalous dimensions appearing in (6.158) and (6.159) are determined by differentiating (6.66) with respect to μ and ν, respectively. At one-loop, they take the following form

$$\gamma^{\mu\,(0)}_{J^{33}_{\text{nrw}}} = 16\ln\frac{\nu}{2m_\chi} + \frac{19}{3} \tag{6.160}$$

$$\gamma^{\nu\,(0)}_{J^{33}_{\text{nrw}}} = 16\ln\frac{\mu}{m_W}, \,. \tag{6.161}$$

In order to confirm the scale independence of the narrow resolution wino DM cross section, we plug (3.31) into (6.147) and (6.148). Following the discussion that was outlined in the previous Section, we arrive at the following consistency equations

$$\gamma^{\nu}_{Z^{33}_\gamma}\mathbf{1}_2 + \gamma^{\nu}_{J^{33}_{\text{nrw}}}\mathbf{1}_2 + \gamma^{\nu}_{D^{\text{W}}} + \gamma^{\nu *}_{D^{\text{W}}} = 0\,, \tag{6.162}$$

$$\mathbf{\Gamma}^{\text{wino}}_C + \mathbf{\Gamma}^{\text{wino}\,*}_C + \boldsymbol{\gamma}^{\mu}_{D^{\text{W}}} + \boldsymbol{\gamma}^{\mu *}_{D^{\text{W}}} + \gamma^{\mu}_{Z^{33}_\gamma}\mathbf{1}_2 + \gamma^{\mu}_{J^{33}_{\text{nrw}}}\mathbf{1}_2 = 0\,, \tag{6.163}$$

where the matrix $\mathbf{\Gamma}^{\text{wino}}_C$ is given by

$$\mathbf{\Gamma}^{\text{wino}}_C = \begin{pmatrix} \Gamma_{11} & 0 \\ \Gamma_{21} & \Gamma_{22} \end{pmatrix}\,, \tag{6.164}$$

and the entries are provided in (6.35). Eq. (6.163) can be confirmed to be correct by using the anomalous dimensions for the Wilson coefficients (6.164), the photon jet function (6.46) and (6.50), the unobserved jet function (6.160) and (6.161) and the soft coefficients (6.156) and (6.157).

6.5.3 Intermediate resolution RG and RRG invariance - Higgsino DM

The derivation of the consistency equation for the intermediate resolution Higgsino DM cross section is completely analogous to the analysis presented for the intermediate resolution wino DM cross section in Section 6.5.1. However, the Higgsino cross section (3.30) is more involved than its wino counterpart since one has to take into account more functions and index combinations, which leads to more complicated consistency equations. In order to be able to write down the Higgsino DM consistency equations in a similarly compact form as was done for wino DM, we first need to introduce the vector of photon jet functions

$$\vec{Z}_\gamma = \left(Z^{33}_\gamma, Z^{34}_\gamma, Z^{43}_\gamma, Z^{44}_\gamma\right)^T \,. \tag{6.165}$$

Then, we split the analogue of (6.150) for Higgsino DM into an SU(2) and a $\text{U}(1)_Y$ part as follows

$$\frac{d}{d\ln\mu}\left[\sum_i H_{\text{SU}(2),\,i}(\mu) w^{\text{SU}(2)}_i(t,\mu,\nu) Z_{\gamma,\,i}(\mu,\nu) j^{\text{SU}(2)}_{\text{int}}\left(\ln\frac{2m_\chi}{te^{\gamma_E}\mu^2},\mu\right)\right] = 0\,, \tag{6.166}$$

$$\frac{d}{d\ln\mu}\left[\sum_i H_{\text{U}(1),\,i}(\mu) w^{\text{U}(1)}_i(t,\mu,\nu) Z_{\gamma,\,i}(\mu,\nu) j^{\text{U}(1)}_{\text{int}}\left(\ln\frac{2m_\chi}{te^{\gamma_E}\mu^2},\mu\right)\right] = 0\,. \tag{6.167}$$

The derivatives in (6.166) and (6.167) can readily be evaluated by remembering the definitions of the RG equations, we leads to the following conditions for the anomalous dimensions

$$\mathbf{\Gamma}^{\text{SU}(2)}_H + \mathbf{\Gamma}^{\text{SU}(2),\mu}_W + \text{diag}\left[\gamma^{\mu}_{Z^{33}_\gamma}, \gamma^{\mu}_{Z^{34}_\gamma}, \gamma^{\mu}_{Z^{43}_\gamma}, \gamma_{Z^{44}_\gamma}\right] + \gamma^{\mu}_{J^{\text{SU}(2)}}\mathbf{1}_4 = 0\,, \tag{6.168}$$

$$\mathbf{\Gamma}_H^{\mathrm{U}(1)} + \mathbf{\Gamma}_W^{\mathrm{U}(1),\mu} + \mathrm{diag}\left[\gamma^\mu_{Z_\gamma^{33}}, \gamma^\mu_{Z_\gamma^{34}}, \gamma^\mu_{Z_\gamma^{43}}, \gamma_{Z_\gamma^{44}}\right] + \gamma^\mu_{J^{\mathrm{U}(1)}} \mathbf{1}_4 = 0\,. \tag{6.169}$$

The correctness of the virtuality consistency equations (6.168) and (6.169) can straightforwardly be confirmed by using the values of the anomalous dimensions given in (6.39) for $\mathbf{\Gamma}_H^{\mathrm{SU}(2)}$ and $\mathbf{\Gamma}_H^{\mathrm{U}(1)}$, in (6.106) for $\gamma^\mu_{J^{\mathrm{SU}(2)}}$ and $\gamma^\mu_{J^{\mathrm{U}(1)}}$, in (6.46) and (6.61) for the photon jet function anomalous dimensions and in (6.141) for $\mathbf{\Gamma}_W^{\mathrm{SU}(2),\mu}$ and $\mathbf{\Gamma}_W^{\mathrm{U}(1),\mu}$. The equations (6.168) and (6.169) are given in operator space matrix notation. Since we previously found that all anomalous dimensions are also diagonal in the space of two-particle states, it is clear that the conditions (6.168) and (6.169) hold for all values of I and J.

We now move on to confirming the rapidity scale independence of the intermediate resolution Higgsino DM cross section, i.e. we confirm (6.148) for Higgsino DM. As mentioned before, the procedure is the same as for checking the virtuality scale independence. Making use of the RRG equations (6.49), (6.63) and (6.137) we find the intermediate resolution Higgsino DM rapidity consistency equations

$$\mathrm{diag}\left[\gamma^\nu_{Z_\gamma^{33}}, \gamma^\nu_{Z_\gamma^{34}}, \gamma^\nu_{Z_\gamma^{43}}, 0\right] + \mathbf{\Gamma}_W^{\mathrm{G},\nu} = 0\,, \tag{6.170}$$

where the superscript G on $\mathbf{\Gamma}_W^{\mathrm{G},\nu}$ stands for either SU(2) or U(1). Eq. (6.170) can easily be confirmed by using the anomalous dimensions given in (6.50), (6.64) and (6.138).

6.5.4 Narrow resolution RG and RRG invariance - Higgsino DM

If we want to confirm the scale independence of the narrow resolution Higgsino DM cross section, we first have to solve the RG and RRG equations for the soft coefficients $D^{\mathrm{H},i}_{I,VW}$, $i = 1, 4, 6$ and the narrow resolution jet functions J^{XV}_{nrw}. Let us start with the soft coefficients, for which the RG and RRG equations are given by

$$\frac{d}{d\ln\mu} D^{\mathrm{H},i}_{I,VW}(\mu,\nu) = \gamma^\mu_{D^{\mathrm{H}},ij} D^{\mathrm{H},j}_{I,VW}(\mu,\nu)\,, \tag{6.171}$$

$$\frac{d}{d\ln\nu} D^{\mathrm{H},i}_{I,VW}(\mu,\nu) = \gamma^\nu_{D^{\mathrm{H}}} D^{\mathrm{H},i}_{I,VW}(\mu,\nu)\,. \tag{6.172}$$

Using the soft coefficients from (6.146), we find the anomalous dimensions to be

$$\gamma^{\mu\,(0)}_{D^{\mathrm{H}}} = \mathrm{diag}\left[16\ln\frac{\mu}{\nu} - 8i\pi, 8\ln\frac{\mu}{\nu} + 4, 8\ln\frac{\mu}{\nu} + 4, 0\right]\,, \tag{6.173}$$

$$\gamma^{\nu\,(0)}_{D^{\mathrm{H}}} = \mathrm{diag}\left[16\ln\frac{m_W}{\mu}, 8\ln\frac{m_W}{\mu}, 8\ln\frac{m_W}{\mu}, 0\right]\,. \tag{6.174}$$

The RG and RRG equations for the narrow resolution unobserved jet function index combination $X = V = 3$ have already been solve in (6.158) and (6.159), respectively. The corresponding equations for the index combination $X = 3$, $V = 4$ read

$$\frac{d}{d\ln\mu} J^{34}_{\mathrm{nrw}}\left(p^2,\mu,\nu\right) = \gamma^\mu_{J^{34}_{\mathrm{nrw}}} J^{34}_{\mathrm{nrw}}\left(p^2,\mu,\nu\right)\,, \tag{6.175}$$

$$\frac{d}{d\ln\nu} J^{33}_{\mathrm{nrw}}\left(p^2,\mu,\nu\right) = \gamma^\nu_{J^{34}_{\mathrm{nrw}}} J^{34}_{\mathrm{nrw}}\left(p^2,\mu,\nu\right)\,, \tag{6.176}$$

where the anomalous dimensions are given by

$$\gamma^\mu_{J^{34}_{\mathrm{nrw}}} = \frac{\hat{\alpha_2}}{4\pi}\left(8\ln\frac{\nu}{2m_\chi} + \frac{19}{6}\right) + \frac{\hat{\alpha_1}}{4\pi}\left(-\frac{41}{6}\right) + \mathcal{O}(\hat{\alpha}^2_{1,2}) \tag{6.177}$$

$$\gamma^{\nu}_{J^{34}_{\text{nrw}}} = \frac{\hat{\alpha}_2}{4\pi}\left(-8\ln\frac{\mu}{m_W}\right) + \mathcal{O}(\hat{\alpha}_2^2)\,. \tag{6.178}$$

Note that since $J^{34}_{\text{nrw}} = J^{43}_{\text{nrw}}$, we don't need to compute the index combination $X = 4, V = 3$ separately. Lastly, the index combination $X = V = 4$ does not depend on the rapidity scale, which means that we only need to solve the RGE

$$\frac{d}{d\ln\mu} J^{44}_{\text{nrw}}\left(p^2,\mu\right) = \gamma_{J^{44}_{\text{nrw}}} J^{44}_{\text{nrw}}\left(p^2,\mu\right)\,, \tag{6.179}$$

where the anomalous dimension is given by

$$\gamma_{J^{44}_{\text{nrw}}} = \frac{\hat{\alpha}_1}{4\pi}\left(-\frac{41}{3}\right) + \mathcal{O}(\hat{\alpha}_1^2)\,. \tag{6.180}$$

In order to prove the scale independence of the Higgsino DM narrow resolution cross section, we differentiate (3.32) with respect to μ and ν. Following the discussion that has been outlined above, we first analyse the virtuality consistency equation for which we find

$$\begin{aligned}\boldsymbol{\Gamma}^{\text{Higgs.}}_{C} + \boldsymbol{\Gamma}^{\text{Higgs.}\,*}_{C} + \boldsymbol{\gamma}^{\mu}_{D^{\text{H}}} + \boldsymbol{\gamma}^{\mu *}_{D^{\text{H}}} + \text{diag}\left[\gamma^{\mu}_{Z^{33}_{\gamma}}, \gamma^{\mu}_{Z^{34}_{\gamma}}, \gamma^{\mu}_{Z^{43}_{\gamma}}, \gamma_{Z^{44}_{\gamma}}\right] \\ + \text{diag}\left[\gamma^{\mu}_{J^{33}_{\text{nrw}}}, \gamma^{\mu}_{J^{34}_{\text{nrw}}}, \gamma^{\mu}_{J^{43}_{\text{nrw}}}, \gamma_{J^{44}_{\text{nrw}}}\right] = 0\,,\end{aligned} \tag{6.181}$$

where

$$\boldsymbol{\Gamma}^{\text{Higgs.}}_{C} = \text{diag}\left[\tilde{\Gamma}_{11}, \tilde{\Gamma}_{44}, \tilde{\Gamma}_{44}, \tilde{\Gamma}_{66}\right]\,. \tag{6.182}$$

Using the explicit expressions for the anomalous dimensions provided in (6.42), (6.46), (6.61), (6.160), (6.177), (6.180) and (6.173), it is easy to confirm that (6.181) is satisfied.

For the narrow resolution Higgsino DM rapidity consistency equation, we find

$$\boldsymbol{\gamma}^{\nu}_{D^{\text{H}}} + \boldsymbol{\gamma}^{\nu *}_{D^{\text{H}}} + \text{diag}\left[\gamma^{\nu}_{Z^{33}_{\gamma}}, \gamma^{\nu}_{Z^{34}_{\gamma}}, \gamma^{\nu}_{Z^{43}_{\gamma}}, 0\right] + \text{diag}\left[\gamma^{\nu}_{J^{33}_{\text{nrw}}}, \gamma^{\nu}_{J^{34}_{\text{nrw}}}, \gamma^{\nu}_{J^{43}_{\text{nrw}}}, 0\right] = 0\,, \tag{6.183}$$

which can also be confirmed straightforwardly by using the rapidity anomalous dimensions in (6.50), (6.64), (6.161), (6.178) and (6.174). Note that the consistency equations (6.181) and (6.183) hold for all index values of I and J. We can hence conclude that also the narrow resolution Higgsino DM cross section is scale independent, as expected.

7 Results

It is now time to present the results for the DM annihilation into the semi-inclusive final state $\gamma + X$, for wino and Higgsino DM, which is given by (1.8). For the numerical results given in this section we use the couplings at the scale $m_Z = 91.1876\,\text{GeV}$ in the $\overline{\text{MS}}$ scheme as input: $\hat{\alpha}_2(m_Z) = 0.0350009$, $\hat{\alpha}_3(m_Z) = 0.1181$, $\hat{s}^2_W(m_Z) = \hat{g}_1^2/(\hat{g}_1^2 + \hat{g}_2^2)(m_Z) = 0.232497$,[1] $\hat{\lambda}_t(m_Z) = 0.952957$, $\lambda(m_Z) = 0.132944$. The $\overline{\text{MS}}$ gauge couplings are in turn computed via one-loop relations from $m_Z, m_W = 80.385\,\text{GeV}$, $\alpha_{\text{OS}}(m_Z) = 1/128.943$. Further, we compute the top Yukawa and Higgs self-coupling, which enter our calculation only implicitly through the two-loop evolution of the gauge couplings, via tree-level relations from $\overline{m}_t = 163.35\,\text{GeV}$ (corresponding to the top pole mass 173.2 GeV at four loops) and $m_H = 125.0\,\text{GeV}$. For Higgsino DM, the mass splittings are fixed to $\delta m = 355$ MeV and $\delta m_N = 20$ MeV and for wino DM, the mass splitting is fixed to $\delta m = 164.1$ MeV [104].

The numerical results in this Section were generated from private codes that were implemented in `Mathematica`. To ensure correctness, two versions of each code were implemented independently and subsequently compared via blind cross-checks. The codes for the Sommerfeld factors S_{IJ} were implemented independently and cross-checked by Martin Vollmann and Kai Urban. Since S_{IJ} is independent of E^γ_{res}, the same implementation was used for both resolution cases. The narrow resolution Sudakov annihilation rates Γ_{IJ} for both wino and Higgsino DM were implemented independently and cross checked by CH and Martin Vollmann. The same was done for the intermediate resolution Sudakov annihilation rates by CH and Kai Urban. The information given here was already presented in Sections 4 of [7,8]. The results for the intermediate resolution cross sections, for both wino and Higgsino DM, were computed using the more conventional second of the two resummation schemes discussed in Section 4. However, we implemented both schemes and found full numerical agreement at NNL' at the 0.1% level. For wino DM, this was investigated analytically and is discussed in Appendix A.

7.1 Energy spectrum - wino DM

The results for the intermediate resolution cross section $\langle\sigma v\rangle(E^\gamma_{\text{res}})$ for wino DM, plotted as a function of the DM mass, are shown in Figure 7.1. The upper panel shows the cross sections for different levels of accuracy. The (black) dotted line is the "tree" approximation, where we include the Sommerfeld factor S_{IJ} and use only tree-level results for the Sudakov annihilation rate Γ_{IJ} without any resummation. The (magenta) dot-dashed line gives the LL approximation, the (blue) dashed line gives the NLL approximation and the (red) solid line gives the NLL' approximation, which provides the highest accuracy. The plot includes the first two Sommerfeld resonances and the energy resolution was integrated up to $E^\gamma_{\text{res}} = m_W$ for this Figure.

[1] Note that the value for $\hat{s}^2_W(m_Z)$ in this thesis has been updated compared to the value given in [7–9]. We remark that all plots and numerical results presented in this thesis were computed with the updated value.

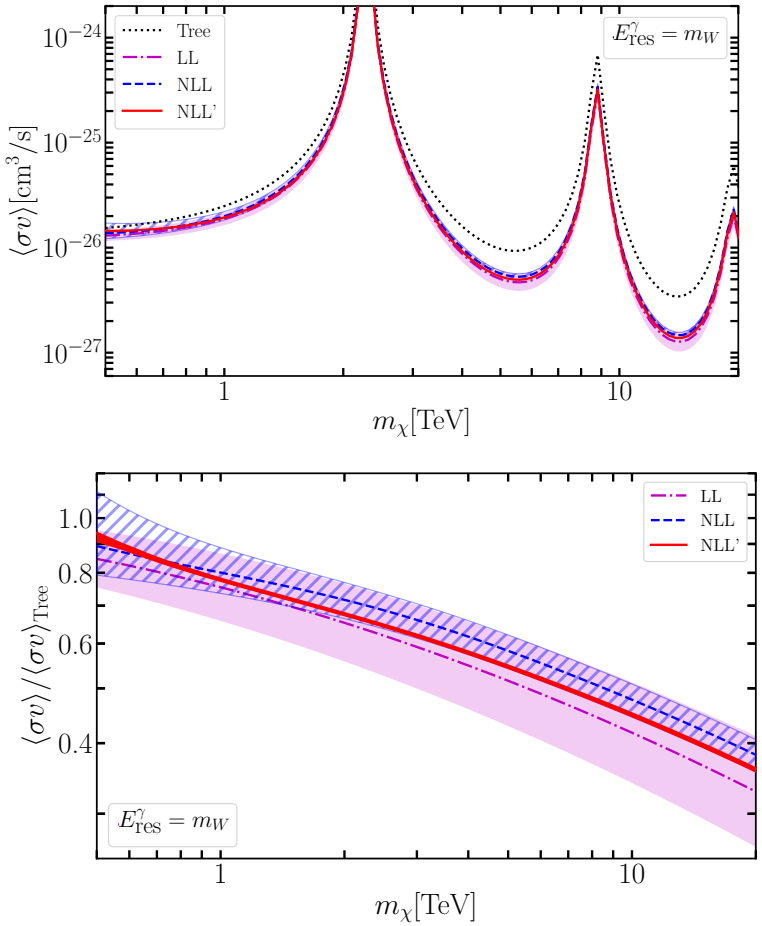

Figure 7.1: Integrated photon energy spectrum within $E^\gamma_{\rm res}$ from the endpoint m_χ in the tree (Sommerfeld only) and LL, NLL, NLL' resummed approximation. The energy resolution is set to $E^\gamma_{\rm res} = m_W$. The shaded/hatched bands show the scale variation of the respective approximation as described in the text. For the NLL' result the theoretical uncertainty is given by the thickness of the red line. This Figure was extracted from [7].

The lower panel shows the ratios of the LL, NLL and NLL' intermediate resolution wino DM cross sections normalized to the tree-level approximation. The purpose of this plot is to make more transparent the effect of resummation. We observe that resummation leads to a substantial reduction of the cross section, which is a general feature of Sudakov resummation. Particularly interesting is the $m_\chi \sim 3$ TeV mass range, where, as discussed in the introduction, wino DM is consistent with the observed relic density. Here, the annihilation rate is suppressed by $30 - 40\%$. These findings are consistent with previous computations of similar observables [66–68].

The shaded/hatched regions around the central lines in Figure 7.1 give an estimate of the theoretical uncertainty of the computations at the different levels of accuracy. The uncertainty bands are obtained from a parameter scan which is computed through a simultaneous variation of all scales. Specifically, the high virtuality and rapidity scales μ_h, ν_h are varied in the interval $2m_\chi[1/2, 2]$, the jet scale μ_j is varied in the interval $\sqrt{2m_\chi m_W}[1/2, 2]$ and the soft virtuality and rapidity scales μ_s, ν_s are varied in the interval $m_W[1/2, 2]$. For each mass value in Figure 7.1, the five scales are varied in their corresponding intervals over 21 logarithmically distributed values, with ten values lying above and ten values lying

below the central value. Then, for each mass point, the maximum and minimum values of the cross section in this five-dimensional parameter space are chosen to give an estimate of the scale uncertainty.

Using this very conservative approach for estimating the errors, we find that the scale uncertainty at NLL' accuracy is in fact negligible and is given by the width of the red solid line in Figure 7.1. Furthermore we observe, as expected, a negative correlation between the accuracy of the computation and the scale uncertainty. Specifically, the theoretical uncertainty reduces from 17% at LL, to 8% at NLL and to 1% at NLL' assuming $m_\chi =$ 2 TeV. The numerical benchmark values for the ratio of the cross sections with respect to the Sommerfeld-only result, for the mass values $m_\chi = 2$ TeV (10 TeV), are $0.641^{+0.115}_{-0.097}$ $(0.402^{+0.096}_{-0.077})$ at LL, $0.707^{+0.054}_{-0.054}$ $(0.463^{+0.032}_{-0.033})$ at NLL and $0.667^{+0.007}_{-0.006}$ $(0.435^{+0.005}_{-0.004})$ at NLL' accuracy, where the central values are computed using the central scales of the above intervals.

It is interesting to investigate the contributions of each two-particle channel combination $IJ = \{(00)(00), (00)(+-), (+-)(00), (+-)(+-)\}$ to the integrated photon energy spectrum $\langle\sigma v\rangle(E^\gamma_{\rm res})$. This will allows us to see how the different terms from S_{IJ} and Γ_{IJ} contribute to the final result. Hence, we separate the cross section as follows

$$\begin{aligned}\langle\sigma v\rangle = 2\times\big\{&\mathbf{S_{(00)(00)}}[\sigma v]_{(00)(00)} + 2\mathrm{Re}[\mathbf{S_{(00)(+-)}}[\sigma v]_{(00)(+-)}] \\ &+ \mathbf{S_{(+-)(+-)}}[\sigma v]_{(+-)(+-)}\big\}\,,\end{aligned} \tag{7.1}$$

where

$$[\sigma v]_{IJ}(E^\gamma_{\rm res}) = \int_{m_\chi - E^\gamma_{\rm res}}^{m_\chi} dE_\gamma\, \Gamma_{IJ}(E_\gamma)\,. \tag{7.2}$$

We find (Sommerfeld factors in bold and adopting $E^\gamma_{\rm res} = m_W$)

$$\begin{aligned}\langle\sigma v\rangle = 2\times\Bigg[&\underbrace{\mathbf{34.246}\times(1.1552)}_{\sim 3\%} + \underbrace{2\mathrm{Re}\left[\mathbf{42.100}\times(-0.8718+5.4288i)\right]}_{\sim -5\%} \\ &+ \underbrace{\mathbf{51.755}\times(29.242)}_{\sim 102\%}\Bigg]\times 10^{-28}\ \mathrm{cm}^3/\mathrm{s} = 2.9592\times 10^{-25}\ \mathrm{cm}^3/\mathrm{s}\,,\end{aligned} \tag{7.3}$$

for $m_\chi = 2$ TeV and

$$\begin{aligned}\langle\sigma v\rangle = 2\times\Bigg[&\underbrace{\mathbf{1.1345}\times(1.1159)}_{\sim 18\%} + \underbrace{2\mathrm{Re}\left[\mathbf{0.35103}\times(-0.8969+7.2167i)\right]}_{\sim -9\%} \\ &+ \underbrace{\mathbf{0.10861}\times(60.676)}_{\sim 91\%}\Bigg]\times 10^{-27}\ \mathrm{cm}^3/\mathrm{s} = 1.4453\times 10^{-26}\ \mathrm{cm}^3/\mathrm{s}\,.\end{aligned} \tag{7.4}$$

for the smaller DM mass value $m_\chi = 500$ GeV. By looking at the $m_\chi = 2$ TeV result (7.3) (the structure does not change for larger masses), we find the Sommerfeld factors to be large and to be roughly of the same order. At the same time $\Gamma_{(+-)(+-)}$ is larger than the contributions from the other channels by an order of magnitude, which means that the cross section is dominated by the $IJ = (+-)(+-)$ annihilation channel contribution, which starts at tree-level in the fixed-order approximation. For $m_\chi = 500$ TeV (7.4), the Sommerfeld factors are $\leq \mathcal{O}(1)$, with $S_{(00)(00)}$ giving the largest contribution. This means that for small DM masses, the Sommerfeld enhancement does somewhat compensate the loop suppression and the contributions from the different channels distributed more democratically.

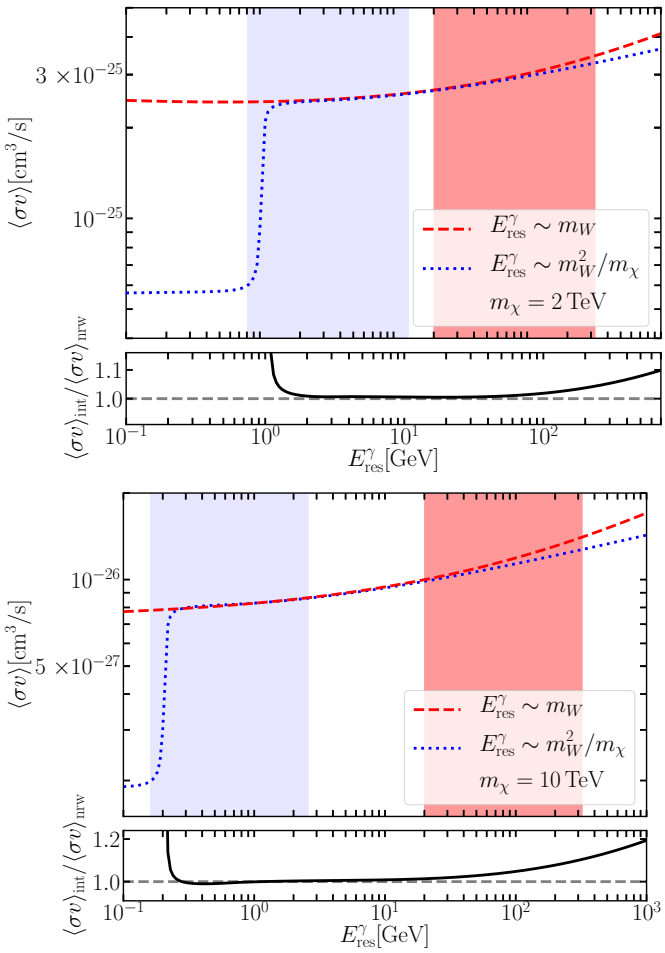

Figure 7.2: Annihilation cross sections plotted as function of $E^\gamma_{\rm res}$. The blue-dotted line shows the cross section for the narrow resolution computed in [9]. The red-dashed line shows the intermediate resolution cross section. The light-grey (blue) area represents the region of validity for the narrow resolution case and the dark-grey (red) area represents the region of validity for the intermediate resolution case. The ratio of the intermediate to narrow resolution annihilation cross section $\langle\sigma v\rangle_{\rm int}/\langle\sigma v\rangle_{\rm nrw}$ is added below each plot. The results are shown for DM masses of $m_\chi = 2\,\text{TeV}$ (upper plot) and $m_\chi = 10\,\text{TeV}$ (lower plot). This Figure was extracted from [7].

7.2 Matching energy resolutions - wino DM

In the previous Subsection, we presented the results for the wino DM cross section in the intermediate resolution regime, where the experimental energy resolution scales as $E^\gamma_{\rm res} \sim m_W$. In Section 1.4 we showed that the intermediate resolution regime would be most relevant for current and future indirect DM searches, for masses in the TeV range. Throughout this thesis however, we also provided results for the narrow energy resolution case $E^\gamma_{\rm res} \sim m_W^2/m_\chi$. This is closer to the line signal, where the DM particles annihilate into two photons or a photon and a Z boson. We now want to investigate whether we can combine the results for the narrow and intermediate energy resolutions in order to provide predictions for the range from $E^\gamma_{\rm res} \sim 0$ to $E^\gamma_{\rm res} \approx 4m_W$, with NLL' accuracy.

In Figure 7.2 we plot the narrow resolution (blue dotted line) and the intermediate resolution (red dashed line) cross sections, as functions of the energy resolution. For the upper panel, the DM mass was set to $m_\chi = 2$ TeV which is where wino DM is

consistent with the observed relic density, while the lower panel is used to investigate the matching for higher DM masses, in this case $m_\chi = 10$ TeV. The shaded vertical bands show the regions of validity for the two energy resolutions. The boundaries of the narrow resolution (blue/light-grey) region are defined by $m_W^2/m_\chi\,[1/4, 4]$ and the boundaries for the intermediate resolution (red/dark-grey) region are defined by $m_W\,[1/4, 4]$.

From Figure 7.2 we can see that the two calculations agree with high precision over a wide range of $E_{\rm res}^\gamma$, independently of the DM mass. The range of agreement not only covers the region between the two validity bands, but extends well into them for both resolutions. The narrow resolution cross section exhibits a steep increase at $E_{\rm res}^\gamma \simeq 4m_Z^2/m_\chi$, which is the resolution value above which the γZ contribution is included and can no longer be separated. This feature is absent for the intermediate resolution cross section, since the unobserved jet function in this case $J_{\rm int}^{33}$ is computed in the massless limit and is thus clearly insensitive to this effect. This shows that the intermediate resolution cross section is not valid for the lower values of $E_{\rm res}^\gamma$. The invariant mass p^2 of the narrow resolution unobserved jet function $J_{\rm nrw}^{33}$ also passes through the W^+W^-, ZH and $t\bar{t}$ thresholds, which however cannot be resolved with the choice of scale in Figure 7.2.

For both mass examples, the narrow resolution cross section provides an accurate result well into region of validity of the intermediate resolution cross section. Only when going to even higher values of $E_{\rm res}^\gamma$, we see that the two calculations start to show some discrepancy. This is sensible, since the narrow resolution case fails to capture the effect of real radiation of soft EW gauge bosons, which are explicitly not included in this case. The bottom parts of the two panels show the ratios $\langle\sigma v\rangle_{\rm int}/\langle\sigma v\rangle_{\rm nrw}$ as functions of $E_{\rm res}^\gamma$. From these we see that even at the highest resolution value $E_{\rm res}^\gamma = 1$ TeV the discrepancy is at most 20%. And although the distance between the regions of validity increases with increasing DM mass m_χ, the precision of the matching between the two calculations is not affected.

Note that so far, we did not explicitly discuss the results for $\langle\sigma v\rangle_{\rm nrw}$ as a function of the mass. Given the high degree with which the two computations match, we conclude that in Figure 7.1 $\langle\sigma v\rangle_{\rm nrw}$ would look indistinguishable from $\langle\sigma v\rangle_{\rm int}$, provided that $E_{\rm res}^\gamma$ is integrated to a value that lies somewhat above $m_Z^2/(4m_\chi)$ and below $4m_W^2/m_\chi$. An analogous parameter scan as the one that was described in the previous Section was also performed for $\langle\sigma v\rangle_{\rm nrw}$ and we find a similar behaviour of the scale uncertainties for the different levels of accuracy. (For explicit results, we refer to [9].)

Summarizing the above discussion, we find that our computations for the wino DM narrow and intermediate energy resolution regimes, as defined in (1.9), provide theoretical predictions with NLL' accuracy for the photon energy spectrum in DM annihilation in the entire energy resolution range from $E_{\rm res}^\gamma \sim 0$ to $E_{\rm res}^\gamma \approx 4m_W$. It would be interesting to try to match our results with the corresponding ones for the wide energy resolution $E_{\rm res}^\gamma \gg m_W$, which were computed in [69]. While this would allow one to cover the entire range of $E_{\rm res}^\gamma$, we expect that the results of [69] are relevant only for DM masses in the range $m_\chi \geq 10$ TeV, assuming the anticipated energy resolution of the CTA experiment (see Figure 1.7).

7.3 Energy spectrum - Higgsino DM

In Figure 7.3, we present the results for the intermediate resolution cross section for Higgsino DM, plotted as a function of m_χ. The colour coding and the styles of the curves remain the same as for wino DM, i.e. the black/dotted line is the cross section using the Sommerfeld-only approximation, while the magenta/dot-dashed, the blue/dashed and the red/solid lines respectively give the results for the LL, NLL and NLL' cross sections.

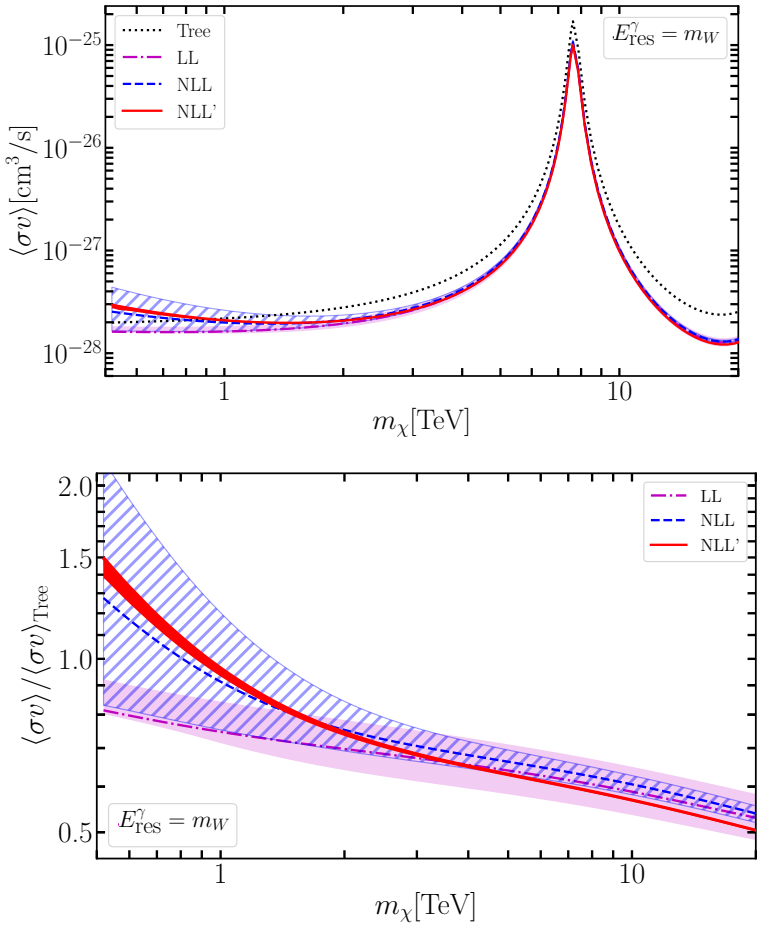

Figure 7.3: Integrated photon energy spectrum within $E^{\gamma}_{\rm res}$ from the endpoint m_χ in the tree (Sommerfeld only) and LL, NLL, NLL' resummed approximations. The energy resolution is set to $E^{\gamma}_{\rm res} = m_W$ and the mass splittings are $\delta m = 355$ MeV and $\delta m_N = 20$ MeV. The shaded/hatched bands show the scale variation of the respective approximation. For the NLL' result the theoretical uncertainty is given by the thickness of the red line. This Figure was extracted from [8].

While the upper panel simply shows the cross section at various accuracies and includes the first Sommerfeld resonance, the lower panel shows the LL, NLL and NLL' cross sections normalized by the tree-level result. Again, this is to make transparent the effect of resummation. While for masses larger than $m_\chi > 1$ TeV resummation of Sudakov logarithms leads to the expected reduction of the cross section, we see that for masses of $m_\chi = 1$ TeV and below, resummation actually enhances the annihilation rate. The reasons for this behaviour are twofold:

1. First, we check how much the different annihilation channels contribute to the final result at different DM masses. At large masses, the entries of the Sommerfeld matrix S_{IJ} have similar magnitude and the sum over I and J is dominated by the $IJ = (+-)(+-)$ channel. This is because only the Sudakov annihilation rate $\Gamma_{(+-)(+-)}$, which describes the annihilation $\chi^+\chi^- \to \gamma + X$, has a non-vanishing tree-level term making it dominant over the other channels. Furthermore, $\Gamma_{(+-)(+-)}$ also features a standard series of exponentiated negative double-logarithmic corrections, which causes the Sudakov suppression for $m_\chi \gtrsim 1$ TeV. If, on the other hand, $m_\chi \lesssim 1$ TeV, we find that the entries of the Sommerfeld matrix are such that $S_{(11)(11)} \approx 1$, while

the other entries are much smaller than one. This means that the various channels are not being mixed like for larger DM masses. The fact that $\Gamma_{(11)(11)}$ only starts at $\mathcal{O}(\alpha_{1,2}^3)$, means that all channels now contribute roughly equally to the final result. We find that since different index combinations of the soft function and photon jet function contribute with different signs, a partial cancellation occurs which results in an enhancement rather than a suppression.

2. Second, generally, depending on the numerical coefficients, it may happen that for small masses the leading logarithms are actually sub-dominant. We also find that for the neutral annihilation channels, the leading logarithms appear with a positive sign. This will be shown explicitly later in this Section in (7.5), where we discuss the behaviour of the uncertainty bands in Figure 7.3. Combining the sub-dominant behaviour of the leading logarithms for small DM masses with their positive sign in the neutral channels, means that this enhancement dominates over the negative interference terms from $\Gamma_{(11)(+-)}$, $\Gamma_{(22)(+-)}$ and the Sudakov suppression of $\Gamma_{(+-)(+-)}$.

We show the Higgsino DM annihilation cross section in Figure 7.3 with theoretical uncertainties. These are computed as for wino DM, i.e. the scales are simultaneously varied by a factor of two around their central values. Performing a parameter scan for each m_χ-value over the five-dimensional parameter space and taking the maximum and minimum values gives the error bands. Assuming a DM mass of $m_\chi = 1$ TeV, the theoretical uncertainties amount to $\pm 9\%$ at LL, $\pm 27\%$ at NLL, and only $\pm 2\%$ at NLL'. While for large DM masses the behaviour of the scale uncertainty is similar to the case of wino DM, in that going to higher accuracy results in a smaller scale dependence, we see that in the low-mass region the NLL-uncertainty exceeds the LL-uncertainty and is also large in absolute terms. For Higgsino DM, we thus find that only the inclusion of the one-loop corrections to the hard, jet and soft functions allows us to control the scale uncertainty and to make accurate predictions. The uncertainty of the NLL' result in Figure 7.3 is given by the width of the red solid line, which we find to be comparable to the case of wino DM. Normalizing by the tree-level results, we find the following numerical benchmark values for DM masses of $m_\chi = 1$ TeV (10 TeV): $0.730^{+0.102}_{-0.033}$ ($0.571^{+0.063}_{-0.053}$) at LL, $0.922^{+0.323}_{-0.178}$ ($0.590^{+0.022}_{-0.024}$) at NLL and $0.976^{+0.011}_{-0.034}$ ($0.555^{+0.004}_{-0.003}$) at NLL'.

In order to understand the surprising scale dependence in the low-mass region in the case of Higgsino DM that is displayed in Figure 7.3, we need to analytically investigate the logarithmic structure of the resummed Higgsino DM annihilation matrix. The neutral particles χ_1^0, χ_2^0 cannot undergo pair annihilation into $\gamma\gamma$ and γZ at tree-level. This implies, that the annihilation rates $\Gamma_{(00)(00)}$, $\Gamma_{(00)(+-)}$ and $\Gamma_{(+-)(00)}$ also vanish at tree-level.[2] While for wino DM these entries of the annihilation rate simply do not have a tree-level contribution, for Higgsino DM this is caused by a cancellation between the short-distance coefficients of the three operators $\mathcal{O}_{1,4,6}$. These operators are linearly independent and do not mix during resummation. This means that they have different anomalous dimensions and as a consequence, the cancellation between $\mathcal{O}_{1,4,6}$ does not happen for their evolution factors, i.e. there is no cancellation between the leading logarithms and despite the absence of a tree-level amplitude, there is a double logarithmic enhancement proportional to $L^2 = \ln^2(4m_\chi^2/m_W^2)$ in the one-loop amplitudes. Since the annihilation rate $\Gamma^{\text{NLL}}_{(00)(00)}$ is given at the squared amplitude level, it already features a leading logarithmic term proportional to L^4. In Appendix A, we will see that this is indeed not the case for wino DM, where the corresponding annihilation rate only contains an L^2 term.

[2] In the following discussion, (00) always refers to the combined neutral states (11) and (22).

When discussing the effect of resummation earlier in this Section, we noted that in the low-mass region all annihilation channels contribute roughly equally to the full cross section. This means that if the scale variations are large within one of these channels, this will affect the scale uncertainty of the final result, unless there are some accidental cancellations. Analytically expanding the neutral channel NLL resummed Sudakov annihilation rate, we find for the first non-vanishing contribution

$$\Gamma^{\mathrm{NLL}}_{(00),(00)} = \frac{\hat{\alpha}_2^4 \hat{s}_W^2}{64\pi m_\chi^2}\left[\frac{L^4}{4} + L^3 + \#\, L^2 + L\left(8\pi^2\, l_{\mu_h} - 8\pi^2\, l_{\mu_s} + \ldots\right)\right] + \ldots\,, \tag{7.5}$$

where $l_{\mu_s} \equiv \ln(\mu_s^2/m_W^2)$ and $l_{\mu_h} \equiv \ln(\mu_h^2/4m_\chi^2)$ are scale dependent logarithms. In (7.5) we only show the terms that are relevant for the current discussion. At NLL accuracy, the presence of the L^4 term means that coefficients of L^n, $0 \leq n \leq 2$, are not yet resummed and exhibit a scale dependence, which is what we see from (7.5). The terms responsible for the large scale variations at NLL are the ones proportional to $\pi^2 L$ in (7.5). These originate from the imaginary parts of the one-loop anomalous dimensions. At small masses, 0.5 TeV $\lesssim m_\chi \lesssim$ 1 TeV the scale variations from these terms dominate over the contributions from the leading logarithmic terms and cause the $\mathcal{O}(1)$ scale dependence seen in Figure 7.3. Including the one-loop corrections to the hard and soft functions into (7.5) will cancel the l_{μ_h} and l_{μ_s} terms, which finally puts us in control of the final result.

Note that the $\pi^2 L$ terms in (7.5) are already present at LL. Here however, we find that in the sum of the $IJ = (00),(00)$, $IJ = (00),(+-)$ and $IJ = (+-),(00)$ annihilation channels there is an accidental cancellation of large scale-dependent terms. In the end, this cancellation is responsible for the smallness of the LL error band compared with the NLL error band and its asymmetry, in the low-mass region. For large DM masses, the leading logarithmic terms in (7.5) will start to dominate, rendering the effect of the scale variations sub-dominant. Also, for $m_\chi \gtrsim 1$ TeV, the cross section is dominated by contributions from $\Gamma_{(+-)(+-)}$, which already has a small scale dependence at NLL.

7.4 Matching energy resolutions - Higgsino DM

In the previous Section, we discussed the results and characteristics of the intermediate resolution Higgsino DM cross section. As was done for wino DM in Section 7.2, we now want to investigate whether we can match our results from the narrow and intermediate energy resolutions. To do so, in Figure 7.4 we plot the Higgsino DM cross sections for the narrow (blue/dotted) and intermediate (red/dashed) resolution cases as a function of the energy resolution. We assume a DM mass of $m_\chi = 1$ TeV. As for the wino case, we indicate the regions of validity for the two resolution regimes, which are defined by $m_W^2/m_\chi[1/4, 4]$ for the narrow resolution and by $m_W[1/4, 4]$ for the intermediate resolution.

The general behaviour of the curves as well as the matching is comparable to the wino DM case. The sharp increase of the narrow resolution cross section at $E^\gamma_{\mathrm{res}} \simeq m_Z^2/(4m_\chi)$ is caused by the fact that the contribution from γZ can no longer be resolved. Again, in principle also the thresholds for W^+W^-, ZH and $t\bar{t}$ are shown, which are however invisible at the scale of Figure 7.4. Since the intermediate resolution unobserved jet functions were computed in the massless limit, these features are absent in the intermediate resolution cross section, which only becomes an accurate description for $E^\gamma_{\mathrm{res}} \gtrsim m_Z^2/(4m_\chi)$. Different from the wino DM case, the Higgsino DM intermediate resolution cross section starts to diverge quite severely from the intermediate resolution result for larger values of E^γ_{res}. Nevertheless, from the bottom part of Figure 7.4, which shows the ratio $\langle\sigma v\rangle_{\mathrm{int}}/\langle\sigma v\rangle_{\mathrm{nrw}}$, we see that there is still a wide E^γ_{res}-range where the results for the two regimes match

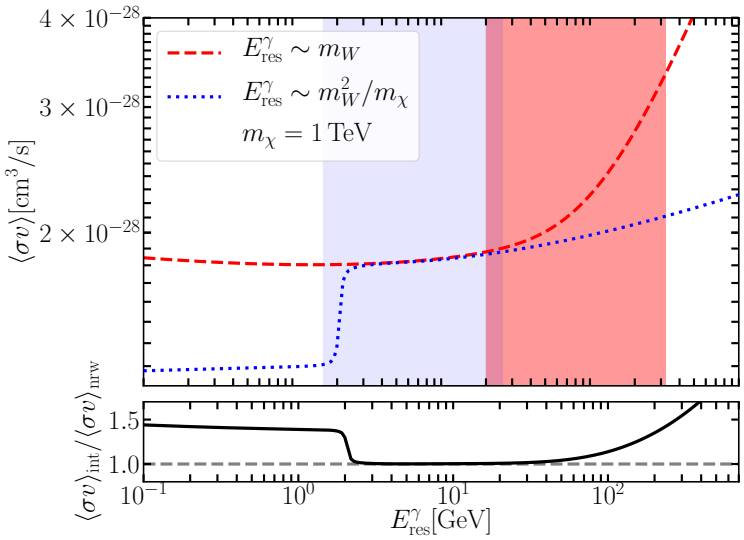

Figure 7.4: Annihilation cross sections plotted as function of $E^\gamma_{\rm res}$. The blue-dotted line refers to the narrow resolution. The red-dashed line shows the intermediate resolution cross section. The light-grey (blue) area represents the region of validity of the narrow resolution case and the dark-grey (red) area represents the region of validity of the intermediate resolution case. The ratio of the intermediate to narrow resolution annihilation cross section $\langle\sigma v\rangle_{\rm int}/\langle\sigma v\rangle_{\rm nrw}$ is added below. The results are shown for a DM mass of $m_\chi = 1\,$TeV. This Figure was extracted from [8].

very closely. In Appendix A an in depth investigation into the matching is performed for wino DM. A similar analysis can be done for Higgsino DM and we assume the results found in Appendix A are transferable.

Remember that the correct relic densities for wino and Higgsino DM are achieved for mass values of $m_\chi \sim 2$ TeV and $m_\chi \sim 1$ TeV, respectively. As already discussed at the end of Section 7.2, this means that for future experiments the intermediate resolution results will be most appropriate for wino DM. However, as can be seen from Figure 1.7, the narrow resolution regime becomes more relevant in the case of Higgsino DM. Independently of the resolution however, we emphasize that for Higgsino DM it is necessary to go to NLL' accuracy in order to have full control over the final result's uncertainty.

We are not going to discuss in depth the narrow resolution results. From Figure 7.4, we see that this is justified since the high degree of matching allows us to conclude that the results for $\langle\sigma v\rangle_{\rm nrw}$ as a function of m_χ would look indistinguishable from the intermediate resolution integrated photon energy spectrum (provided that the value of $E^\gamma_{\rm res}$ lies somewhat above $m_Z^2/(4m_\chi)$ and below $4m_W^2/m_\chi$). Having performed a parameter scan for the narrow resolution case, we find a similar behaviour as the one seen in Figure 7.3.

8 Conclusion

To date, the nature of DM remains one of the biggest mysteries in particle physics. Given the findings thus far, indirect detection experiments looking for multi-TeV DM in the center of the Milky Way are most promising for uncovering the nature of DM. These experiments which are already running or are currently being planned/built, will either allow one to constrain the parameter space of viable DM models or rule them out completely. To do so however, accurate predictions for these models need to be provided from the theoretical physics side. In this thesis, we investigated the semi-inclusive annihilation process $\chi\chi \to \gamma + X$ for wino and Higgsino DM. These two models extend the SM by an SU(2) (wino) multiplet and an SU(2)$\otimes$U(1)$_Y$ (Higgsino) multiplet and both models are well motivated due to their simplicity and their origin in SUSY. The computations were carried out up to NLL' accuracy, which gives the highest precision for these models to date.

The scaling of the energy resolution of the experiments has implications for what kind of radiation needs to be included in the computations. We find that the intermediate resolution regime, as defined in (1.9), is most appropriate for the next generation of experiments. This thesis provides the results for both narrow and intermediate energy resolutions and as can be seen from Figures 7.2 and 7.4, this allows us to accurately make predictions for the entire resolution range from $E^\gamma_{\text{res}} \sim 0$ to $E^\gamma_{\text{res}} \sim 4m_W$. The formalism presented here is kept as general as possible. In particular, the derivation of the factorization theorem in Section 3, holds for SU(2)$\otimes$U(1)$_Y$ multiplets with arbitrary multiplicity and hypercharge. Furthermore, the hard matching coefficients, the photon jet functions and the unobserved jet functions are universal and independent of the nature of the DM particles. Only for the computation of the soft functions, we assumed an SU(2) triplet (wino) and an SU(2)$\otimes$U(1)$_Y$ doublet with hypercharge $Y = 1/2$ (Higgsino).

The nature of the annihilation process, heavy non-relativistic particles annihilating to light energetic ones, implies several complications. Consequently multiple EFTs, non-relativistic and soft-collinear, need to be employed in order to be able to calculate reliable predictions. This thesis focused on the use of SCET for the resummation of large Sudakov logarithms that lead to a breakdown of the naive perturbative expansion in the coupling constants. We resummed large logarithms up to NLL', which resulted in predictions with theoretical uncertainties of 1% (wino) and 2% (Higgsino) in the interesting mass regions. These uncertainties were computed from a variation of the scales present in the computations. In particular, we found that for Higgsino DM it is vital to include the one-loop corrections to gain control over the uncertainties, because the NLL results showed unexpectedly large error bands in the interesting mass region.

Given the small uncertainties, it is expected that the largest theoretical uncertainty now arises from modifications of the Sommerfeld effect due to sub-leading effects in the non-relativistic theory, and, for smaller m_χ, from power-suppressed effects of order m_W/m_χ, which have been systematically neglected during this thesis. An investigation of the Sommerfeld effect at NLO for wino DM has been performed in [81], but has yet to be done for Higgsino DM. It would be interesting to include these effects into the work presented here.

A Fixed-order expansions - Wino DM

In Figures 7.2 and 7.4 we showed that for both wino and Higgsino DM, there is a wide range of $E_{\rm res}^\gamma$ where the narrow and intermediate energy resolution cross sections match to a high degree of accuracy. In this Appendix, we are going to perform an in depth investigation of this matching and ultimately will be able to show why it happens using analytic expressions. The analysis done here is specific to wino DM, but can be expected to also hold for Higgsino DM. Specifically, we are going to expand the Sudakov annihilation rate matrix Γ_{IJ} up to two-loop order, which will allow us to investigate the structure of large logarithms in both resolution cases. Comparing large logarithmic contributions from both resolution regimes, we will then be able to show why the photon energy spectra at large photon momentum agree remarkably well over a large $E_{\rm res}^\gamma$-interval. The arguments presented below follow Section 5 and Appendix E of [7] and the analytic expansions were done independently and cross checked by CH and Martin Vollmann.

Throughout this Appendix, we will focus on the first intermediate resolution resummation scheme of Section 4, where all scales are evolved to the soft scale. In this way, the evolution of the functions for both resolutions is treated on a more similar footing. Below, in Appendix A.3, we will show however that the findings hold independently of which resummation scheme is chosen.

A.1 Double-logarithmic approximation

Before considering the full expansion of the NLL' resummed cross sections, it will be instructive to consider the double-logarithmic approximation. This can be obtained by only keeping the tree-level term from each function, as well as the $\hat{\alpha}_2 \times \ln^2$ terms in the exponentials from the RG evolution factors. This example allows us to nicely demonstrate why it is necessary to perform a full NLL' calculation, if one wants to obtain accurate results. It also shows why it is necessary to analyse the full NLL' expression, when trying to explain the matching. The double-logarithmic approximations for the narrow and intermediate wino DM cross sections are given by

$$\langle\sigma v\rangle_{\rm nrw}(E_{\rm res}^\gamma) = \frac{2\pi\hat{\alpha}_2^2\hat{s}_W^2}{m_\chi^2}\left[\hat{s}_W^2+\hat{c}_W^2\Theta\left(E_{\rm res}^\gamma-\frac{m_Z^2}{4m_\chi}\right)\right] e^{-\frac{\hat{\alpha}_2}{\pi}\ln^2\frac{4m_\chi^2}{m_W^2}} S_{(+-)(+-)}\,, \quad \text{(A.1)}$$

$$\langle\sigma v\rangle_{\rm int}(E_{\rm res}^\gamma) = \frac{2\pi\hat{\alpha}_2^2\hat{s}_W^2}{m_\chi^2}\, e^{-\frac{3\hat{\alpha}_2}{4\pi}\ln^2\frac{4m_\chi^2}{m_W^2}} S_{(+-)(+-)}\,. \quad \text{(A.2)}$$

We can see that in the 'nrw'-case, the coefficient of the double logarithm is larger than in the 'int'-case. This is a general feature for more exclusive observables. The $\hat{\alpha}_2 \times \ln^2$ terms in (A.1) and (A.2) are easily traceable. For both resolutions, the hard function resummation contributes a factor of $-\frac{\hat{\alpha}_2}{4\pi} \times 4\ln^2\frac{4m_\chi^2}{m_W^2}$ and while the 'nrw'-case does not contain other double-logarithmic contributions, in the 'int'-case the hard-collinear SU(2) unobserved jet function, which is evolved from the jet to the soft scale $\mu_j \to \mu_s$, adds a positive factor $+\frac{\hat{\alpha}_2}{4\pi} \times \ln^2\frac{4m_\chi^2}{m_W^2}$. Hence, in the 'int'-case the suppression from the hard

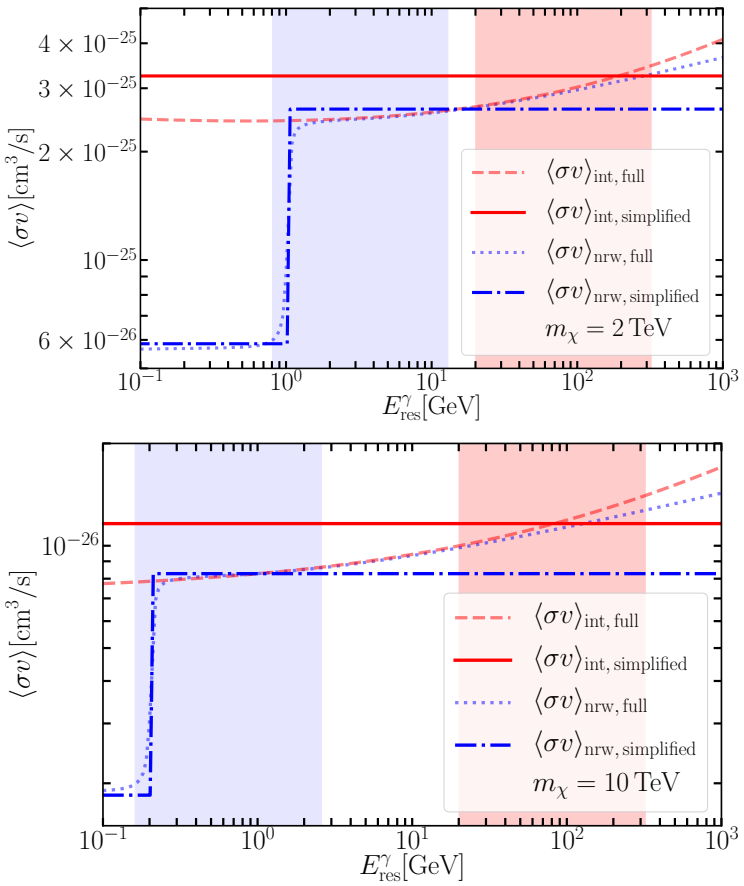

Figure A.1: Same as Figure 7.2 but in the double-logarithmic ("simplified") approximation. For comparison the complete ("full") NLL' results of Figure 7.2 are also included (dimmer dashed and dotted lines). Top: $m_\chi = 2$ TeV. Bottom: $m_\chi = 10$ TeV. This Figure was extracted from [7].

function resummation is partially canceled from the resummation of the unobserved jet function.

Figure A.1 shows the same matching that was already presented in Figure 7.2, but now includes the curves from the double-logarithmic approximations (A.1) and (A.2). The full results are shown with a dimmer shading. The blue/dotted and red/dashed curves are the full results for the narrow and intermediate cross sections, respectively, and the blue/dot-dashed and red/solid curves are the double-logarithmic approximations for the 'nrw'- and 'int'-cases, respectively. For the upper panel, a DM mass of $m_\chi = 2$ TeV is assumed, while for the lower panel $m_\chi = 10$ TeV. We again also include the regions of validity for both resolution regimes.

From Figure A.1 we can see that the double-logarithmic approximation for the 'nrw'-case correctly captures the opening of the γZ channel. Also, in their respective regions of validity (A.1) and (A.2) are close to the full NLL' resummed results. However, it is also clearly shown that the approximations fail to reproduce the precise shapes of the full results and, most importantly, they fail when it comes to matching the two resolution regimes. We thus turn to the full NLL' resummed results, in order to explain the matching of the narrow and intermediate resolution cross sections.

A.2 Expansion of the resummed annihilation rate

Since the Sommerfeld effect is the same in both resolution cases, we focus on the expansion of the resummed annihilation rate. The starting point of our analysis will be $[\sigma v]_{IJ}$, which was defined in (7.2), and can be written in the form

$$[\sigma v]_{IJ}(E_\gamma^{\text{res}}) = \frac{2\pi\hat{\alpha}_2^2(\mu)\hat{s}_W^2(\mu)}{\sqrt{2}^{n_{\text{id}}} m_\chi^2} \sum_{n=0}^{\infty}\sum_{m=0}^{2n} c_{IJ}^{(n,m)}(E_{\text{res}}^\gamma,\mu)\left(\frac{\hat{\alpha}_2(\mu)}{\pi}\right)^n \ln^m\frac{4m_\chi^2}{m_W^2} \tag{A.3}$$

where, by construction, the coefficients $c_{IJ}^{(n,m)}(E_{\text{res}}^\gamma,\mu)$ are $\mathcal{O}(1)$ numbers, and the large logarithms $\ln(4m_\chi^2/m_W^2)$ are made explicit. The coefficients of the large logarithms $c_{IJ}^{(n,m)}(E_{\text{res}}^\gamma,\mu)$ will take a different form depending on the resolution regime and the indices n and m denote the powers of the coupling constant and the large logarithms, respectively. Furthermore, the coefficients can depend on many different scales: μ from the renormalization of the coupling and the natural scales of the Wilson coefficients μ_h, the hard-collinear unobserved jet function μ_j, the (anti-) collinear jet functions μ_s, ν_h and the soft function μ_s, ν_s. These enter via the RG and RRG evolution factors, that have been derived in Section 6. In order to make sure that large logarithms and $\mathcal{O}(1)$ terms are well separated, we normalize scales by their natural values. This means that we will rewrite logarithms like $\ln(\mu_j^2/m_W^2)$ as $\ln(\mu_j^2/m_W^2) = \ln(\mu_j^2/(2m_\chi m_W)) + \frac{1}{2}\ln(4m_\chi^2/m_W^2)$, where the first term is now $\mathcal{O}(1)$ and contained in one of the $c_{IJ}^{(n,m)}$, while the second term is a large logarithm that is made explicit in (A.3). The complete list of coefficients is collected below in Appendices A.4.1 (narrow resolution) and A.4.2 (intermediate resolution). In Appendix A.4.3, we also provide more details about computation of the $c_{IJ}^{(n,m)}$. We expand $[\sigma v]_{IJ}$ up to the two-loop order, i.e. $n \leq 2$.

Before discussing the characteristics of the coefficients, let us take a moment and clarify some notation. This will also explain what exactly is actually meant when saying a *computation is done up to LL, NLL or NLL' accuracy* and will allow us to demonstrate which terms a computation to a certain order correctly reproduces. Schematically, a resummed annihilation cross section takes the form

$$\sigma v \quad \propto \quad (1 + C_1\hat{\alpha}_2 + \ldots)\exp\left[L f_0(\hat{\alpha}_2 L) + f_1(\hat{\alpha}_2 L) + \ldots\right], \tag{A.4}$$

where the exponent contains the RG and RRG evolution factors and the prefactor originates from the fixed-order computation. The $f_i(\hat{\alpha}_2 L)$ are functions of the $\mathcal{O}(1)$ quantity $\hat{\alpha}_2 L \equiv \hat{\alpha}_2 \ln(4m_\chi^2/m_W^2)$. An LL-computation will contain f_0, NLL will also include f_1 and NLL' will add the one-loop corrections C_1. Expanding (A.4) in $\hat{\alpha}_2$, we can see which large logarithms are correctly predicted by a certain calculation. LL will only provide the coefficient $c_{IJ}^{(n,2n)}$, NLL provides the coefficients $c_{IJ}^{(n,2n)}$ and $c_{IJ}^{(n,2n-1)}$, while NLL' will correctly provide the three coefficients $c_{IJ}^{(n,2n)}$, $c_{IJ}^{(n,2n-1)}$ and $c_{IJ}^{(n,2n-2)}$, for all n. Not that if a certain coefficient is fully reproduced by a computation, this coefficient must also be free of any of the scales present in the problem, since the dependence on the matching scales (e.g. μ_j) must cancel at every fixed order. This will provide us with another cross-check of our computation, as any physical observable must be scale independent (up to the order of the computation).

In Figure A.2 we show the full NLL' cross sections normalized by the Sommerfeld-only terms (same as Figure 7.1 but for narrow and intermediate resolution) and compare them to the fixed-order expansions up to one-loop (NLO) and two-loops (NNLO). From the NLO curves in Figure A.2, we can see the breakdown of EW perturbation theory which

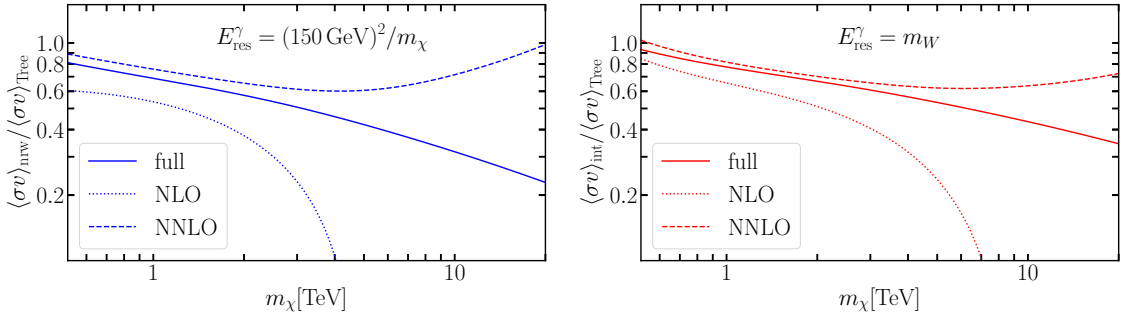

Figure A.2: Left: Ratios to the tree-level cross section of the various fixed-order cross sections at NLO (dotted) and NNLO (dashed) and of the fully resummed NLL' cross section (solid) for the narrow resolution $E^\gamma_{\rm res} = (150\,{\rm GeV})^2/m_\chi$. Right: The same ratios as in the left panel, but in the intermediate resolution regime $E^\gamma_{\rm res} = m_W$. As in Figure 7.1, in both cases the Sommerfeld factor S_{IJ} is included and the formulas are evaluated at the central scales. This Figure was extracted from [7].

nicely shows the need for resummation. And while the NNLO curve improves the accuracy of the computation, it still diverges significantly from the all-orders resummed result in the large-mass region.

In the following, we discuss the coefficients at tree-level $n = 0$, at one-loop $n = 1$ and at two-loops $n = 2$. The main focus will lie on the channel $IJ = (+-)(+-)$, since this is the only one that starts at tree-level and will thus have the most non-zero coefficients. However, in Appendices A.4.1 and A.4.2 the coefficients for all channels are listed. After presenting the coefficients, which are resolution specific, we will extrapolate them out of their region of validity. This means that for example a $E^\gamma_{\rm res}$-dependent narrow resolution coefficient is extrapolated to the intermediate resolution region $E^\gamma_{\rm res} \sim m_W$ or the transitional resolution region $E^\gamma_{\rm res} \sim (m_W/m_\chi)^{1/2} m_W$, which lies between the narrow and intermediate resolutions. Since this extrapolation will affect the structure of the large logarithms, i.e. formerly $\mathcal{O}(1)$ expressions might become large or vice versa, it will allow us to pin down the origin of the matching as a function of $E^\gamma_{\rm res}$.

A.2.1 Tree level

Since the channels $IJ = (00)(00)$ and $IJ = (00)(+-)$ do not have a tree-level contributions, their corresponding $n = 0$ coefficients vanish for both resolutions $c^{(0,0)}_{(00)(00)} = c^{(0,0)}_{(00)(+-)} = 0$. The tree-level coefficients $c^{(0,0)}_{(+-)(+-)}$ however are non-zero and can in fact be read off from the double-logarithmic approximations (A.1) and (A.2)

$$c^{{\rm nrw}(0,0)}_{(+-)(+-)} = \hat{s}^2_W + \hat{c}^2_W \Theta\left(E^\gamma_{\rm res} - \frac{m_Z^2}{4m_\chi}\right) , \tag{A.5}$$

$$c^{{\rm int}(0,0)}_{(+-)(+-)} = 1 . \tag{A.6}$$

Eq. (A.5) nicely shows the sensitivity of the 'nrw'-case to the opening of the γZ channel. The 'int'-case (A.6) on the other hand is ignorant to this feature, which is exactly what we observed from the matching plot in Figure 7.2. If $E^\gamma_{\rm res} > m_Z^2/(4m_\chi)$, it is easy to see that $c^{{\rm nrw}(0,0)}_{(+-)(+-)} = c^{{\rm int}(0,0)}_{(+-)(+-)}$.

A.2.2 One loop

Expanding the channel $IJ = (+-)(+-)$ of the annihilation rate (A.3) up to $n = 1$ explicitly gives

$$[\sigma v]^{1-\text{loop}}_{(+-)(+-)} = \frac{2\pi\hat{\alpha}_2^2\hat{s}_W^2}{m_\chi^2}\,\frac{\hat{\alpha}_2}{\pi}\left[c^{(1,2)}_{(+-)(+-)}L^2 + c^{(1,1)}_{(+-)(+-)}L + c^{(1,0)}_{(+-)(+-)}\right]. \tag{A.7}$$

In order to make the following discussion more transparent, it will prove helpful to introduce some abbreviations

$$L \equiv \ln\frac{4m_\chi^2}{m_W^2}, \quad x_\gamma \equiv \frac{2E^\gamma_{\text{res}}}{m_W}$$
$$l_R \equiv \ln(x_\gamma)\,, \quad \kappa_R = \kappa_R(x_\gamma) = \frac{1}{2}\ln\left(1+x_\gamma^2\right), \quad \lambda_R = \lambda_R(x_\gamma) = -\frac{1}{2}\text{Li}_2(-x_\gamma^2)\,.$$

The variable L represents the large logarithms and the E^γ_{res}-dependent l_R is of $\mathcal{O}(1)$ in the intermediate resolution but turns into a large logarithms if $E^\gamma_{\text{res}} \sim m_W^2/m_\chi$. In order to cancel the implicit scale dependence of the running couplings $\hat{\alpha}_2(\mu)$, $\hat{s}_W(\mu)$ we introduce the explicit factor $l_\mu \equiv \ln(\mu^2/m_W^2)$ to cancel the scale dependence from the couplings. Since all functions are evolved to the soft scale, μ is parametrically of order m_W which makes l_μ an $\mathcal{O}(1)$ quantity. Additionally, we introduce

$$\begin{aligned} z_\gamma \equiv\ & \frac{4\pi}{\hat{s}_W^2(\mu)\hat{\alpha}_2(\mu)} Z^{33}_{\gamma,\,1\text{-loop}}(\mu,\nu)\Big|_{\mu=m_W} \\ =\ & \left(-\frac{400}{27}+\frac{2}{3}+\frac{16}{9}\ln\frac{m_t^2}{m_W^2}\right)\hat{s}_W^2 + \left(\frac{80}{9}\hat{s}_W^2\ln\frac{m_Z^2}{m_W^2} - \frac{4\pi\Delta\alpha}{\hat{\alpha}_2}\right), \end{aligned} \tag{A.8}$$

as well as the resolution-dependent function

$$j(E^{\text{res}}_\gamma) \equiv \frac{4\pi}{\hat{\alpha}_2(\mu)}\int_0^{4m_\chi E^{\text{res}}_\gamma} \mathrm{d}p^2\, J^{33,\,1-\text{loop}}_{\text{nrw}}(p^2,\mu,\nu)\Big|_{\mu=m_W}. \tag{A.9}$$

The one-loop expressions for the photon jet function $Z^{33}_{\gamma,\,1\text{-loop}}$ and the unobserved collinear jet function $J^{33,\,1-\text{loop}}_{\text{nrw}}$ can be extracted from (6.44) and (6.66), respectively. Since the narrow resolution unobserved collinear jet function is a very complicated expression involving massive SM particles, we constructed $j(E^{\text{res}}_\gamma)$ in such a way that it is μ- and ν-independent while including the dependence on the masses of the SM particles.

With the notation we have just introduced, we can write (A.7) for the narrow and intermediate resolution cases as follows

$$[\sigma v]^{\text{nrw}\ 1-\text{loop}}_{(+-)(+-)} = \frac{2\pi\hat{\alpha}_2^2\hat{s}_W^2}{m_\chi^2}\,\frac{\hat{\alpha}_2}{\pi}\left[-L^2+L+c^{\text{nrw}(1,0)}_{(+-)(+-)}\right], \tag{A.10}$$

$$[\sigma v]^{\text{int}\ 1-\text{loop}}_{(+-)(+-)} = \frac{2\pi\hat{\alpha}_2^2\hat{s}_W^2}{m_\chi^2}\,\frac{\hat{\alpha}_2}{\pi}\left[-\frac{3}{4}L^2+\left(l_R+\frac{29}{48}\right)L+c^{\text{int}(1,0)}_{(+-)(+-)}\right], \tag{A.11}$$

where

$$c^{\text{nrw}(1,0)}_{(+-)(+-)} = \frac{1}{4}\left(\frac{19}{6}-\frac{11}{3}\hat{s}_W^2\right)l_\mu - 6 + \frac{3\pi^2}{4} + \frac{1}{4}\left[j(E^{\text{res}}_\gamma)+z_\gamma\right], \tag{A.12}$$

$$c^{\text{int}(1,0)}_{(+-)(+-)} = \frac{1}{4}\left(\frac{19}{6}-\frac{11}{3}\hat{s}_W^2\right)l_\mu - \frac{73}{18} + \frac{5\pi^2}{12} + \frac{1}{4}z_\gamma$$

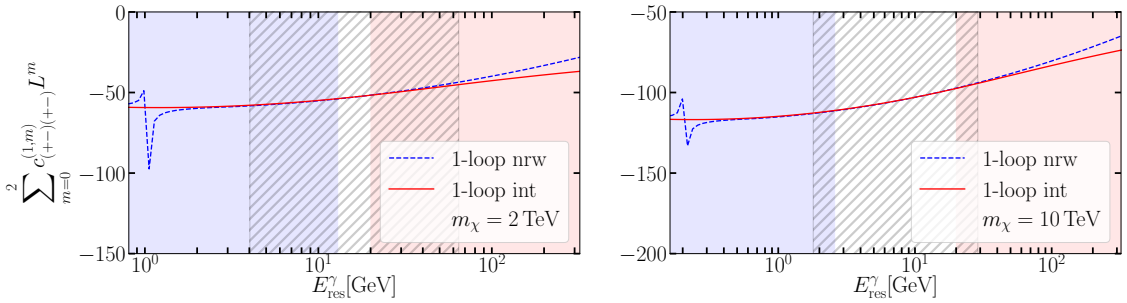

Figure A.3: One-loop coefficient of the series (A.3) (including all logarithms) for the 'nrw' (solid) and 'int' (dashed) factorization formulas. Left: m_χ =2 TeV. Right: m_χ =10 TeV. This Figure was extracted from [7].

$$+l_R^2 - \frac{19}{24} l_R - \frac{3}{2}\lambda_R - \frac{1}{2}\kappa_R \,. \tag{A.13}$$

Our NLL' calculation should correctly predict all terms at one-loop, which means that all coefficients should be scale-independent. The apparent scale dependence from l_μ in the $c^{(1,0)}_{(+-)(+-)}$ coefficients above, will be compensated by the running couplings $\hat{\alpha}_2(\mu)$ and $\hat{s}^2_W(\mu)$ in the corresponding LO terms. As expected, we thus find all coefficients to be scale independent at one-loop.

In order to better understand the matching between (A.10) and (A.11), we will extrapolate the 'nrw'-case coefficients to $E^\gamma_{\text{res}} \sim m_W$. It is easy to see that the only dependence on E^γ_{res} for $[\sigma v]^{\text{nrw 1-loop}}_{(+-)(+-)}$ comes from $j(E^{\text{res}}_\gamma)$. By expanding the explicit expressions for the one-loop Wilson line and self-energy contributions given in Section 6.3.1, we find

$$j(E^\gamma_{\text{res}}) \to 4\ln^2\frac{4m_\chi E^\gamma_{\text{res}}}{m_W^2} - \frac{19}{6}\ln\frac{4m_\chi E^\gamma_{\text{res}}}{m_W^2} + \frac{70}{9} - \frac{4\pi^2}{3} \quad \text{for} \quad 4m_\chi E^\gamma_{\text{res}} \gg m_W^2 \,. \tag{A.14}$$

In the intermediate resolution regime, $j(E^\gamma_{\text{res}})$ is then given by

$$\frac{1}{4} j(E^\gamma_{\text{res}}) \to +\frac{1}{4}L^2 + \left(l_R - \frac{19}{48}\right) L + l_R^2 - \frac{19}{24} l_R + \frac{35}{18} - \frac{\pi^2}{3} \,, \tag{A.15}$$

where we used $\ln(4m_\chi E^\gamma_{\text{res}}/m_W^2) = \frac{1}{2}L + l_R$. Plugging (A.15) into (A.12), it is easy to check that

$$[\sigma v]^{\text{nrw 1-loop}}_{(+-)(+-)} = [\sigma v]^{\text{int 1-loop}}_{(+-)(+-)} + [\sigma v]^{\text{tree}}_{(+-)(+-)} \frac{\hat{\alpha}_2}{\pi}\left[\frac{3}{2}\lambda_R\left(\frac{2E^\gamma_{\text{res}}}{m_W}\right) + \frac{1}{2}\kappa_R\left(\frac{2E^\gamma_{\text{res}}}{m_W}\right)\right] \,. \tag{A.16}$$

From (A.16) we can see that using the asymptotic behaviour of $j(E^\gamma_{\text{res}})$ shown in (A.15), allows us to show that the large logarithms contained $[\sigma v]^{\text{nrw 1-loop}}_{(+-)(+-)}$ and $[\sigma v]^{\text{int 1-loop}}_{(+-)(+-)}$ match exactly and the difference is only a non-logarithmic term which is numerically small. It amounts to $\mathcal{O}(1\%)$ of the tree-level cross sections and is independent of m_χ. We mentioned earlier that an NLL' computation should fully reproduce the one-loop result and one might thus wonder why (A.16) does not show exact agreement between the two resolutions. The terms λ_R and κ_R in the intermediate resolution coefficient (A.11) are power-suppressed effects of order m_W/m_χ for the narrow resolution. Since we consistently neglect these type of power corrections, they do not show up in (A.10).

Figure A.3 shows the dimensionless quantities $\sum_{m=0}^{2} c^{(1,m)}_{(+-)(+-)} L^m$ for both resolutions as functions of E^γ_{res}. In this matching plot we visualize how well the 1-loop coefficients match.

The color coding is the same as in the previous matching plots (Figures 7.2 and A.1), but now we include a hatched region which shows the transition region between the narrow and intermediate regions of validity. While the absolute values of the coefficients is large, they differ by no more than 3% in the hatched transition region. Given the analysis above, it is straightforward to confirm that a similar degree of matching is found if I or $J = (00)$.

A.2.3 Two loop

Having assessed the matching of the resolutions at one-loop, we now move on to two-loops. For $n = 2$, (A.3) is given by

$$[\sigma v]^{2-\text{loop}}_{(+-)(+-)} = \frac{2\pi\hat{\alpha}_2^2\hat{s}_W^2}{m_\chi^2}\frac{\hat{\alpha}_2^2}{\pi^2}\left[c^{(2,4)}_{(+-)(+-)}L^4 + c^{(2,3)}_{(+-)(+-)}L^3 + c^{(2,2)}_{(+-)(+-)}L^2 + c^{(2,1)}_{(+-)(+-)}L + c^{(2,0)}_{(+-)(+-)}\right]. \tag{A.17}$$

As explained earlier, with our NLL' computation we are able to determine the coefficients $c^{(2,4)}_{(+-)(+-)}$, $c^{(2,3)}_{(+-)(+-)}$ and $c^{(2,2)}_{(+-)(+-)}$, while the expressions given below for the coefficients $c^{(2,1)}_{(+-)(+-)}$ and $c^{(2,0)}_{(+-)(+-)}$ remain incomplete. The coefficients in (A.17) for the narrow resolution are given by

$$c^{\text{nrw}(2,4)}_{(+-)(+-)} = \frac{1}{2!}(-1)^2\,, \tag{A.18}$$

$$c^{\text{nrw}(2,3)}_{(+-)(+-)} = -\frac{53}{72}\,, \tag{A.19}$$

$$c^{\text{nrw}(2,2)}_{(+-)(+-)} = \frac{1}{4}(-1)\left[\frac{19}{3} - \frac{11}{3}\hat{s}_W^2\right]l_\mu + \frac{671}{144} - \frac{13\pi^2}{12} - \frac{z_\gamma + j(E^\gamma_{\text{res}})}{4}\,, \tag{A.20}$$

while for the intermediate resolution they read

$$c^{\text{int}(2,4)}_{(+-)(+-)} = \frac{1}{2!}\left(-\frac{3}{4}\right)^2 = \frac{9}{32}\,, \tag{A.21}$$

$$c^{\text{int}(2,3)}_{(+-)(+-)} = -\frac{2}{9} - \frac{3}{4}l_R\,, \tag{A.22}$$

$$c^{\text{int}(2,2)}_{(+-)(+-)} = \frac{1}{4}\left(-\frac{3}{4}\right)\left[\frac{19}{3} - \frac{11}{3}\hat{s}_W^2\right]l_\mu + \frac{4489}{2304} - \frac{37\pi^2}{48} - \frac{3}{16}z_\gamma + \frac{9}{8}\lambda_R + \frac{3}{8}\kappa_R + l_R - \frac{1}{4}l_R^2\,. \tag{A.23}$$

The incomplete coefficients $c^{(2,1)}_{(+-)(+-)}$ and $c^{(2,0)}_{(+-)(+-)}$ are rather lengthy and are given in Appendix A.4. The dependence on the energy resolution is captured by the variables $j(E^\gamma_{\text{res}})$, λ_R, κ_R and l_R and we can see that, as expected, the two-loop coefficients presented above are independent of the matching scales. Again, the logarithm l_μ is necessary to cancel the scale dependence of the running couplings and should not be confused with a left over scale-dependence.

Before visually assessing the matching of the two-loop coefficients, we are going to investigate the structure of the large logarithms which allows us to estimate what to expect. In order to do so, we collect in Table A.1 the asymptotic behaviour of the resolution-dependent variables, as a function of E^γ_{res}. As in the previous Section, we assume three different scalings for E^γ_{res}: the narrow regime $E^\gamma_{\text{res}} \sim m_W^2/m_\chi$, the transition regime $E^\gamma_{\text{res}} \sim m_W\sqrt{m_W/m_\chi}$ and the intermediate regime $E^\gamma_{\text{res}} \sim m_W$. Depending on the scaling of the

	$E^\gamma_{\rm res} \sim m_W^2/m_\chi$	$E^\gamma_{\rm res} \sim m_W\sqrt{m_W/m_\chi}$	$E^\gamma_{\rm res} \sim m_W$
$j(E^\gamma_{\rm res})$	$j = \mathcal{O}(1)$	$\frac{1}{4}L^2 + \mathcal{O}(L)$	$L^2 + \mathcal{O}(L)$
$l_R(E^\gamma_{\rm res})$	$-\frac{1}{2}L + \mathcal{O}(1)$	$-\frac{1}{4}L + \mathcal{O}(1)$	$l_R = \mathcal{O}(1)$
$\lambda_R(E^\gamma_{\rm res})$, $\kappa_R(E^\gamma_{\rm res})$	0	0	λ_R, $\kappa_R = \mathcal{O}(1)$

Table A.1: Leading-logarithmic dependence of the $E^\gamma_{\rm res}$-dependent functions appearing in the fixed-order expansions when evaluated at the three $E^\gamma_{\rm res}$-scales relevant to Figure A.4. Vanishing entries are to be understood as power-suppressed.

$\sum c^{(2,m)}_{(+-)(+-)} L^m$	$E^\gamma_{\rm res} \sim m_W^2/m_\chi$	$E^\gamma_{\rm res} \sim m_W\sqrt{m_W/m_\chi}$	$E^\gamma_{\rm res} \sim m_W$
'nrw'	$\frac{16}{32}L^4 + \mathcal{O}(L^3)$	$\frac{7}{16}L^4 + \mathcal{O}(L^3)$	$\frac{8}{32}L^4 + \mathcal{O}(L^3)$
'int'	$\frac{15}{32}L^4 + \mathcal{O}(L^3)$	$\frac{7}{16}L^4 + \mathcal{O}(L^3)$	$\frac{9}{32}L^4 + \mathcal{O}(L^3)$
'nrw'-'int'	$\frac{1}{32}L^4 + \mathcal{O}(L^3)$	$\mathcal{O}(L^3)$	$-\frac{1}{32}L^4 + \mathcal{O}(L^3)$

Table A.2: Leading-logarithmic terms of the two-loop coefficients in (A.3) for the 'nrw' and 'int' factorization formulas, and the difference of the two, at the scales relevant to Figure A.4.

resolution, the $E^\gamma_{\rm res}$-dependent variables might contribute large logarithms, be of $\mathcal{O}(1)$ or vanish altogether.

Using the insights from Table A.1, we can assess the leading logarithmic structure of $[\sigma v]^{2-\rm loop}_{(+-)(+-)}$. The results for this are provided in Table A.2. The last row of Table A.2 is particularly interesting, which shows how the leading logarithms for both resolutions differ depending on the scaling of $E^\gamma_{\rm res}$. We can see that in the transition region, $E^\gamma_{\rm res} \sim m_W\sqrt{m_W/m_\chi}$, the leading logarithms agree exactly and even in the 'nrw'- or 'int'-regions, the difference is small (as seen from the numerically small prefactor). We should thus expect a high degree of matching between the two-loop coefficients, which is confirmed by Figure A.4, where we plot the dimensionless quantities $\sum_{m=0}^4 c^{(2,m)}_{(+-)(+-)} L^m$ for both resolutions as functions of $E^\gamma_{\rm res}$. To plot Figure A.4, the coefficients $c^{(2,m)}_{(+-)(+-)}$, for all m, were included and the matching scales were set to their natural values which means that scale dependent logarithms are set to zero. We can see that the behaviour predicted from the large logarithms in Table A.2 is correctly reproduced in the plot. In the transition region, the curves match very closely which is expected since they share the same leading logarithmic structure. In the 'nrw'-resolution regime, the narrow resolution curve is larger which confirms the $+\frac{1}{32}L^4$ entry of the Table (last row, second column of Table A.2) and in the 'int'-regime, the intermediate resolution curve is larger which confirms the $-\frac{1}{32}L^4$ entry of the Table (last row, last column of Table A.2).

Summarizing the above discussion, we can conclude that the cross sections for the two resolutions match so well over a wide range of $E^\gamma_{\rm res}$, because of the smallness of the difference in the leading logarithms. At NNLO for example, we can extrapolate the narrow resolution two-loop coefficient to $E^\gamma_{\rm res} \sim m_W$ using Tables A.1 and A.2. The difference of the coefficients up to NNLO for the two resolutions is then given by

$$\begin{aligned}\frac{[\sigma v]^{\rm nrw}_{(+-)(+-)} - [\sigma v]^{\rm int}_{(+-)(+-)}}{[\sigma v]^{\rm tree}_{(+-)(+-)}} =& \frac{\hat\alpha_2}{\pi}\left[\frac{3}{2}\lambda_R + \frac{1}{2}\kappa_R\right] \\ &+ \frac{\hat\alpha_2^2}{\pi^2}\left[-\frac{L^4}{32} + \left(\frac{19}{144} - l_R\right)L^3 + \mathcal{O}(L^2)\right]. \end{aligned} \tag{A.24}$$

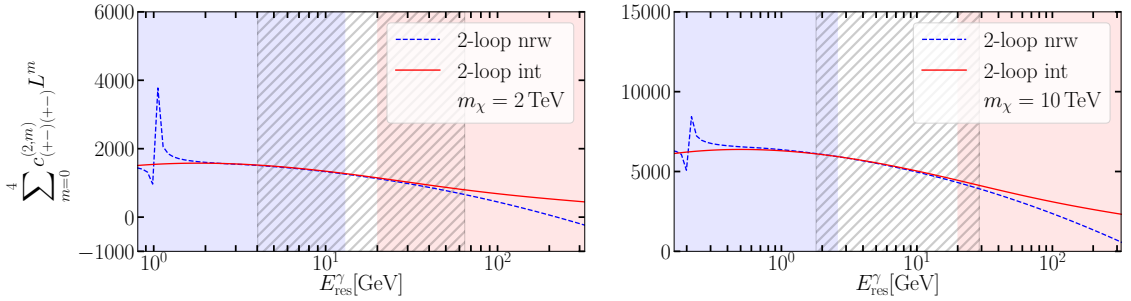

Figure A.4: Two-loop coefficient of the series (A.3) (including all logarithms and evaluated on the central scales) for the 'nrw' (solid) and 'int' (dashed) factorization formulas. Left: m_χ =2 TeV. Right: m_χ =10 TeV. This Figure was extracted from [7].

At the end of the previous Section, we discussed why the one-loop remainder $[\frac{3}{2}\lambda_R + \frac{1}{2}\kappa_R]$ in (A.24) is not problematic. Also, for $E^\gamma_{\rm res} \sim m_W$ the variables λ_R, κ_R are both $\mathcal{O}(1)$ and so the one-loop difference between the resolutions is small. At two-loops, the partial cancellation between the leading logarithms leads to the small coefficient $1/32 \ll 1$ of the leading logarithm of the difference between the two resolutions. The largest contribution to the difference between the resolutions, unless L is extremely large (which happens for large values of m_χ), then originates from the sub-leading logarithm L^3 which is also included in (A.24).

A.3 Intermediate resolution resummation schemes compared

We mentioned in the introduction to this Section that we chose to use the first resummation scheme for the intermediate resolution cross section (see Section 4 for definition), since it is more comparable to the resummation in the narrow resolution case. It would be interesting to see how the analysis presented above changes when using the second resummation scheme. To do so, we compared the intermediate resolution coefficients from both resummation schemes and found the following differences in the different channels

$$\begin{aligned}
\frac{[\sigma v]^{\text{Res.Sc.I}}_{(00)(00)} - [\sigma v]^{\text{Res.Sc.II}}_{(00)(00)}}{[\sigma v]^{\text{tree}}_{(00)(00)}} &= \frac{\hat{\alpha}_2^2}{\pi^2}\, 4 l_R\, (\varphi_{\lambda_R} - \varphi_{\kappa_R})\,, \\
\frac{[\sigma v]^{\text{Res.Sc.I}}_{(00)(+-)} - [\sigma v]^{\text{Res.Sc.II}}_{(00)(+-)}}{[\sigma v]^{\text{tree}}_{(00)(+-)}} &= \frac{\hat{\alpha}_2^2}{\pi^2}\, 2 l_R\, (\varphi_{\lambda_R} + \varphi_{\kappa_R})\,, \\
\frac{[\sigma v]^{\text{Res.Sc.I}}_{(+-)(+-)} - [\sigma v]^{\text{Res.Sc.II}}_{(+-)(+-)}}{[\sigma v]^{\text{tree}}_{(+-)(+-)}} &= -\frac{\hat{\alpha}_2^2}{\pi^2}\, l_R\, (3\varphi_{\lambda_R} + \varphi_{\kappa_R})\,,
\end{aligned} \tag{A.25}$$

where φ_{f_R} is defined in (A.30). We find that numerically these differences cannot be larger than $\mathcal{O}(0.1\%)$ of the tree-level cross section. Hence, if we had used the second resummation scheme throughout this Appendix, we would have reached the same conclusion. Interestingly, since NLL'only determines the coefficients up to $c_{IJ}^{n,2n-2}$, it would have been possible to also find a discrepancy in $c_{IJ}^{(2,1)}$, which however does not seem to be the case.

A.4 Complete NNLO expansions

In this Appendix, we list all coefficients relevant to the understanding of the logarithmic structure of the wino DM NLL' resummation up to NNLO, i.e. we provide the $c_{IJ}^{(n,m)}$ with $0 \leq n \leq 2$ and $0 \leq m \leq 2n$ for all $I, J \in \{(00), (+-)\}$. Additionally, this Appendix provides more details on the computation of the resummed cross section, as well as the fixed-order expansions. We introduce the following abbreviations (partially already given earlier in this Appendix but repeated here for completeness):

$$L \equiv \ln \frac{4m_\chi^2}{m_W^2}\,, \quad l_{\mu_h} \equiv \ln \frac{\mu_h^2}{4m_\chi^2}\,, \quad l_{\mu_j} \equiv \ln \frac{\mu_j^2}{2m_\chi m_W}\,, \quad l_{\mu_s} \equiv \ln \frac{\mu_s^2}{m_W^2}\,, \tag{A.26}$$

$$l_\mu \equiv \ln \frac{\mu^2}{m_W^2}\,, \quad l_{\nu_h} \equiv \ln \frac{\nu_h^2}{4m_\chi^2}\,, \quad l_{\nu_s} \equiv \ln \frac{\nu_s^2}{m_W^2}\,, \quad l_R \equiv \ln x_\gamma\,, \tag{A.27}$$

$$\kappa_R = \kappa_R(x_\gamma) \equiv \frac{1}{2}\ln(1+x_\gamma^2)\,, \tag{A.28}$$

$$\lambda_R = \lambda_R(x_\gamma) \equiv -\frac{1}{2}\mathrm{Li}_2(-x_\gamma^2)\,, \tag{A.29}$$

$$\varphi_{f_R} = \varphi_{f_R}(x_\gamma) \equiv \int_0^{x_\gamma} \frac{\mathrm{d}y}{y}[f_R(x_\gamma - y) - f_R(x_\gamma)]\,, \tag{A.30}$$

$$\vartheta_{f_R} = \vartheta_{f_R}(x_\gamma) \equiv \int_0^{x_\gamma} \mathrm{d}y \frac{\ln(y)}{y}[f_R(x_\gamma - y) - f_R(x_\gamma)]\,, \tag{A.31}$$

where

$$x_\gamma \equiv \frac{2E_{\mathrm{res}}^\gamma}{m_W}\,. \tag{A.32}$$

A.4.1 Narrow resolution coefficients

$\boldsymbol{I, J = (00), (00)}$ The fixed-order annihilation cross section starts at the two-loop order, and the two-loop coefficient exhibits at most two logarithms. Hence $c_{(00)(00)}^{\mathrm{nrw}(n,m)} = 0$ for $n \leq 2$, except for

$$\begin{aligned} c_{(00)(00)}^{\mathrm{nrw}(2,2)} &= 1 + \pi^2 \\ c_{(00)(00)}^{\mathrm{nrw}(2,1)} &= 4 - \frac{\pi^2}{2} \\ c_{(00)(00)}^{\mathrm{nrw}(2,0)} &= 4 - \pi^2 + \frac{\pi^4}{16} \end{aligned} \tag{A.33}$$

$\boldsymbol{I, J = (+-), (00)}$ The fixed-order annihilation cross section starts at the one-loop order. Hence $c_{(+-)(00)}^{\mathrm{nrw}(0,0)} = 0$, and

$$\begin{aligned} c_{(+-)(00)}^{\mathrm{nrw}(1,2)} &= 0 \\ c_{(+-)(00)}^{\mathrm{nrw}(1,1)} &= -1 - i\pi \\ c_{(+-)(00)}^{\mathrm{nrw}(1,0)} &= -2 + \frac{\pi^2}{4} \\ c_{(+-)(00)}^{\mathrm{nrw}(2,4)} &= 0 \\ c_{(+-)(00)}^{\mathrm{nrw}(2,3)} &= 1 + i\pi \end{aligned}$$

$$
\begin{aligned}
c^{\mathrm{nrw}(2,2)}_{(+-)(00)} &= \frac{55}{48} - \frac{53i\pi}{48} \\
c^{\mathrm{nrw}(2,1)}_{(+-)(00)} &= \left[\left(\frac{11}{12} + \frac{11i\pi}{12}\right)\hat{s}_W^2 - \frac{19}{12} - \frac{19i\pi}{12}\right] l_\mu + \frac{55}{12} + \frac{55i\pi}{18} - \frac{55\pi^2}{96} - \frac{11i\pi^3}{24} \\
&\quad - \left(\frac{1}{4} + \frac{i\pi}{4}\right)(z_\gamma + j(E^\gamma_{\mathrm{res}})) \\
c^{\mathrm{nrw}(2,0)}_{(+-)(00)} &= \left(\frac{1}{2} + \frac{i\pi}{2}\right) l^3_{\mu_h} + \left(-\frac{31}{48} + \frac{5i\pi}{48} + \frac{3\pi^2}{8}\right) l^2_{\mu_h} + \left(\frac{31}{12} + \frac{19i\pi}{18} - \frac{13\pi^2}{32} - \frac{7i\pi^3}{24}\right) l_{\mu_h} \\
&\quad + \left(\frac{1}{2} + \frac{i\pi}{2}\right) l^3_{\mu_s} + \left[(-1 - i\pi) l_{\nu_s} + \frac{\pi^2}{4} + \frac{43i\pi}{48} + \frac{55}{48}\right] l^2_{\mu_s} \\
&\quad + \left(\frac{35i\pi}{18} - \frac{\pi^2}{12} - \frac{i\pi^3}{4}\right) l_{\mu_s} + \left[\left(\frac{11}{6} - \frac{11\pi^2}{48}\right)\hat{s}_W^2 + \frac{19\pi^2}{48} - \frac{19}{6}\right] l_\mu \\
&\quad + \frac{7\pi^4}{96} - \frac{4\pi^2}{3} + 6 + \left(\frac{\pi^2}{16} - \frac{1}{2}\right)(z_\gamma + j(E^\gamma_{\mathrm{res}}))
\end{aligned} \tag{A.34}
$$

The coefficients for the index combination $I, J = (00), (+-)$ are obtained by taking the complex conjugate of the coefficients given in this section, i.e. $c^{(n,m)}_{(00)(+-)} = (c^{(n,m)}_{(+-)(00)})^*$.

$\boldsymbol{I, J = (+-), (+-)}$

$$
\begin{aligned}
c^{\mathrm{nrw}(0,0)}_{(+-)(+-)} &= \hat{s}_W^2 + \hat{c}_W^2 \Theta\left(E^\gamma_{\mathrm{res}} - \frac{m_Z^2}{4m_\chi}\right) \\
c^{\mathrm{nrw}(1,2)}_{(+-)(+-)} &= -1 \\
c^{\mathrm{nrw}(1,1)}_{(+-)(+-)} &= 1 \\
c^{\mathrm{nrw}(1,0)}_{(+-)(+-)} &= \left(\frac{19}{24} - \frac{11}{12}\hat{s}_W^2\right) l_\mu - 6 + \frac{3\pi^2}{4} + \frac{1}{4}(z_\gamma + j(E^\gamma_{\mathrm{res}})) \\
c^{\mathrm{nrw}(2,4)}_{(+-)(+-)} &= \frac{1}{2} \\
c^{\mathrm{nrw}(2,3)}_{(+-)(+-)} &= -\frac{53}{72} \\
c^{\mathrm{nrw}(2,2)}_{(+-)(+-)} &= \left(-\frac{19}{12} + \frac{11\hat{s}_W^2}{12}\right) l_\mu - \frac{13\pi^2}{12} + \frac{671}{144} - \frac{1}{4}(z_\gamma + j(E^\gamma_{\mathrm{res}})) \\
c^{\mathrm{nrw}(2,1)}_{(+-)(+-)} &= \frac{19}{24} l^2_{\mu_s} + \left(\frac{35}{9} - \frac{\pi^2}{3}\right) l_{\mu_s} + \left(\frac{19}{12} - \frac{11}{12}\hat{s}_W^2\right) l_\mu \\
&\quad + \frac{3}{4} - \frac{65\pi^2}{288} - \frac{\beta_{1,\mathrm{SU}(2)}}{8} + \frac{1}{4}(z_\gamma + j(E^\gamma_{\mathrm{res}})) \\
c^{\mathrm{nrw}(2,0)}_{(+-)(+-)} &= -\frac{1}{4} l^4_{\mu_h} - \frac{17}{72} l^3_{\mu_h} + \left(\frac{25\pi^2}{24} - \frac{203}{144}\right) l^2_{\mu_h} + \left(-\frac{\beta_{1,\mathrm{SU}(2)}}{8} - \frac{149\pi^2}{288} + \frac{15}{4}\right) l_{\mu_h} \\
&\quad - \frac{1}{4} l^4_{\mu_s} + \left(l_{\nu_s} - \frac{55}{72}\right) l^3_{\mu_s} + l^2_{\mu_s}\left[- l^2_{\nu_h} + \left(\frac{11\hat{s}_W^2}{12} - \frac{19}{24}\right) l_{\nu_h} - l^2_{\nu_s} + l_{\nu_s} \right. \\
&\quad \left. - \frac{121\hat{s}_W^4}{144} + \pi^2 - \frac{2141}{576}\right] + l_{\mu_s}\left[\left(-\frac{j(E^\gamma_{\mathrm{res}})}{4} - \frac{z_\gamma}{4}\right) l_{\nu_h} - \frac{\pi^2}{6} l_{\nu_s} \right. \\
&\quad + \frac{31\pi^2}{144} + \left(\frac{1}{16} - \frac{\hat{s}_W^2}{16}\right)\beta_{1,\mathrm{SU}(2)} - \frac{\hat{s}_W^4}{16\hat{c}_W^2}\beta_{1,Y} \\
&\quad \left. + \left(\frac{11\hat{s}_W^2}{48} - \frac{19}{96}\right) z_\gamma - \frac{19 j(E^\gamma_{\mathrm{res}})}{48}\right] + l^2_\mu\left(\frac{121\hat{s}_W^4}{144} - \frac{209\hat{s}_W^2}{288} + \frac{361}{576}\right)
\end{aligned}
$$

$$
\begin{aligned}
&+ l_\mu \Bigg[\left(\frac{11}{2} - \frac{11\pi^2}{16} \right) \hat{s}_W^2 + \frac{19\pi^2}{16} - \frac{19}{2} + \left(\frac{\hat{s}_W^2}{16} + \frac{1}{16} \right) \beta_{1,\mathrm{SU}(2)} + \frac{\hat{s}_W^4}{16\hat{c}_W^2} \beta_{1,Y} \\
&+ \left(\frac{19}{48} - \frac{11\hat{s}_W^2}{48} \right) (z_\gamma + j(E_{\mathrm{res}}^\gamma)) \Bigg] + \left(-\frac{3}{2} + \frac{3\pi^2}{16} + \frac{z_\gamma}{16} \right) j(E_{\mathrm{res}}^\gamma) \\
&+ 9 - \frac{7\pi^2}{4} + \frac{37\pi^4}{576} + \left(-\frac{3}{2} + \frac{3\pi^2}{16} \right) z_\gamma
\end{aligned} \tag{A.35}
$$

A.4.2 Intermediate resolution coefficients

$I, J = (00), (00)$

$$
\begin{aligned}
c_{(00)(00)}^{\mathrm{int}(0,0)} &= 0 \\
c_{(00)(00)}^{\mathrm{int}(1,2)} &= c_{(00)(00)}^{\mathrm{int}(1,1)} = 0 \\
c_{(00)(00)}^{\mathrm{int}(1,0)} &= 2\lambda_R - 2\kappa_R \\
c_{(00)(00)}^{\mathrm{int}(2,4)} &= c_{(00)(00)}^{\mathrm{int}(2,3)} = 0 \\
c_{(00)(00)}^{\mathrm{int}(2,2)} &= 1 + \pi^2 - \frac{3\lambda_R}{2} + \frac{3\kappa_R}{2} \\
c_{(00)(00)}^{\mathrm{int}(2,1)} &= 2l_R (\lambda_R - \kappa_R) + 4 - \frac{\pi^2}{2} + \frac{29}{24}\lambda_R - \frac{125}{24}\kappa_R + 2(\varphi_{\lambda_R} - \varphi_{\kappa_R}) \\
c_{(00)(00)}^{\mathrm{int}(2,0)} &= \left(-1 - \pi^2\right) l_{\mu_s}^2 + l_{\mu_s} \Bigg(2l_{\nu_s}(\lambda_R - \kappa_R) - 4l_R(\lambda_R - \kappa_R) - \frac{43\lambda_R}{12} + \frac{91\kappa_R}{12} \\
&\quad - 4(\varphi_{\lambda_R} - \varphi_{\kappa_R}) \Bigg) + l_\mu (\lambda_R - \kappa_R) \left(\frac{19}{6} - \frac{11}{6}\hat{s}_W^2 \right) + 2l_R^2 (\lambda_R - \kappa_R) \\
&\quad + l_R \left(-\frac{19}{12}(\lambda_R - \kappa_R) + 4(\varphi_{\lambda_R} - \varphi_{\kappa_R}) \right) + 4 - \pi^2 + \frac{\pi^4}{16} + \frac{z_\gamma}{2}(\lambda_R - \kappa_R) \\
&\quad + \left(-\frac{73}{9} + \frac{5\pi^2}{6} \right) \lambda_R + \left(\frac{1}{9} + \frac{\pi^2}{6} \right) \kappa_R - \frac{19}{12}(\varphi_{\lambda_R} - \varphi_{\kappa_R}) + 4(\vartheta_{\lambda_R} - \vartheta_{\kappa_R})
\end{aligned} \tag{A.36}
$$

$I, J = (+-), (00)$

$$
\begin{aligned}
c_{(+-)(00)}^{\mathrm{int}(0,0)} &= 0 \\
c_{(+-)(00)}^{\mathrm{int}(1,2)} &= 0 \\
c_{(+-)(00)}^{\mathrm{int}(1,1)} &= -1 - i\pi \\
c_{(+-)(00)}^{\mathrm{int}(1,0)} &= -2 + \frac{\pi^2}{4} + \lambda_R + \kappa_R \\
c_{(+-)(00)}^{\mathrm{int}(2,4)} &= 0 \\
c_{(+-)(00)}^{\mathrm{int}(2,3)} &= \frac{3}{4} + \frac{3i\pi}{4} \\
c_{(+-)(00)}^{\mathrm{int}(2,2)} &= (-1 - i\pi) l_R + \frac{25}{24} - \frac{17i\pi}{24} + \frac{\pi^2}{16} - \frac{3}{4}(\lambda_R + \kappa_R) \\
c_{(+-)(00)}^{\mathrm{int}(2,1)} &= l_\mu \left[-\frac{19}{12} - \frac{19i\pi}{12} + \left(\frac{11}{12} + \frac{11i\pi}{12} \right) \hat{s}_W^2 \right] - (1 + i\pi) l_R^2 \\
&\quad + \left(-\frac{29}{24} + \frac{19i\pi}{24} + \frac{\pi^2}{4} + \lambda_R + \kappa_R \right) l_R + \frac{247}{72} + \frac{10i\pi}{9} - \frac{65\pi^2}{192} - \frac{i\pi^3}{8}
\end{aligned}
$$

$$
\begin{aligned}
&- \left(\frac{1}{4}+\frac{i\pi}{4}\right) z_\gamma + \left(\frac{77}{48}+3i\pi\right)\lambda_R + \frac{125}{48}\kappa_R + \varphi_{\lambda_R} + \varphi_{\kappa_R} \\
c^{\mathrm{int}(2,0)}_{(+-)(00)} &= \left(\frac{1}{2}+\frac{i\pi}{2}\right) l^3_{\mu_h} + \left(-\frac{31}{48}+\frac{5i\pi}{48}+\frac{3\pi^2}{8}\right) l^2_{\mu_h} + \left(\frac{31}{12}+\frac{19i\pi}{18}-\frac{13\pi^2}{32}-\frac{7i\pi^3}{24}\right) l_{\mu_h} \\
&+ \left[-(1+i\pi)\, l_{\nu_s} + (2+2i\pi)\, l_R + \frac{79}{48}+\frac{91i\pi}{48}-\frac{\pi^2}{4}\right] l^2_{\mu_s} \\
&+ \Bigg[l_{\nu_s}(\lambda_R+\kappa_R) - 2l_R(\lambda_R+\kappa_R) + \frac{35i\pi}{18} - \frac{i\pi^3}{6} + \left(-\frac{67}{24}-3i\pi\right)\lambda_R \\
&- \frac{91}{24}\kappa_R - 2(\varphi_{\lambda_R}+\varphi_{\kappa_R})\Bigg] l_{\mu_s} + \Bigg[-\frac{19}{6} + \frac{19\pi^2}{48} + \left(\frac{11}{6}-\frac{11\pi^2}{48}\right)\hat{s}^2_W \\
&+ \left(\frac{19}{12}-\frac{11}{12}\hat{s}^2_W\right)(\lambda_R+\kappa_R)\Bigg] l_\mu + \left(-2+\frac{\pi^2}{4}+\lambda_R+\kappa_R\right) l^2_R \\
&+ \left(\frac{19}{12}-\frac{19\pi^2}{96}-\frac{19}{24}(\lambda_R+\kappa_R)+2(\varphi_{\lambda_R}+\varphi_{\kappa_R})\right) l_R + \frac{19}{9}-\frac{13\pi^2}{72}-\frac{\pi^4}{96} \\
&+ \left(-\frac{1}{2}+\frac{\pi^2}{16}\right) z_\gamma + \frac{z_\gamma}{4}(\lambda_R+\kappa_R) + \left(-\frac{37}{18}+\frac{\pi^2}{6}\right)\lambda_R + \left(-\frac{1}{18}-\frac{\pi^2}{12}\right)\kappa_R \\
&- \frac{19}{24}(\varphi_{\lambda_R}+\varphi_{\kappa_R}) + 2(\vartheta_{\lambda_R}+\vartheta_{\kappa_R})
\end{aligned}
\tag{A.37}
$$

The coefficients for the index combination $I,J = (00),(+-)$ are obtained by taking the complex conjugate of the coefficients given in this section, i.e. $c^{(n,m)}_{(00)(+-)} = (c^{(n,m)}_{(+-)(00)})^*$.

$I, J = (+-),(+-)$

$$
\begin{aligned}
c^{\mathrm{int}(0,0)}_{(+-)(+-)} &= 1 \\
c^{\mathrm{int}(1,2)}_{(+-)(+-)} &= -\frac{3}{4} \\
c^{\mathrm{int}(1,1)}_{(+-)(+-)} &= l_R + \frac{29}{48} \\
c^{\mathrm{int}(1,0)}_{(+-)(+-)} &= \left(\frac{19}{24}-\frac{11}{12}\hat{s}^2_W\right) l_\mu + l^2_R - \frac{19}{24} l_R - \frac{73}{18} + \frac{5\pi^2}{12} + \frac{z_\gamma}{4} - \frac{3}{2}\lambda_R - \frac{1}{2}\kappa_R \\
c^{\mathrm{int}(2,4)}_{(+-)(+-)} &= \frac{9}{32} \\
c^{\mathrm{int}(2,3)}_{(+-)(+-)} &= -\frac{3}{4} l_R - \frac{2}{9} \\
c^{\mathrm{int}(2,2)}_{(+-)(+-)} &= \left(-\frac{19}{16}+\frac{11}{16}\hat{s}^2_W\right) l_\mu - \frac{1}{4} l^2_R + l_R + \frac{4489}{2304} - \frac{37\pi^2}{48} - \frac{3}{16} z_\gamma + \frac{9}{8}\lambda_R + \frac{3}{8}\kappa_R \\
c^{\mathrm{int}(2,1)}_{(+-)(+-)} &= \frac{19}{48} l^2_{\mu_s} + \left[\left(\frac{19}{12}-\frac{11}{12}\hat{s}^2_W\right) l_R + \frac{551}{576} - \frac{319}{576}\hat{s}^2_W\right] l_\mu + l^3_R - \frac{7}{12} l^2_R \\
&+ \left(-\frac{437}{192} - \frac{\pi^2}{12} + \frac{1}{4} z_\gamma - \frac{3}{2}\lambda_R - \frac{1}{2}\kappa_R\right) l_R + \frac{1525}{432} - \frac{\beta_{1,\mathrm{SU}(2)}}{8} - \frac{227\pi^2}{576} \\
&+ 2\zeta(3) + \frac{29}{192} z_\gamma - \frac{29}{32}\lambda_R - \frac{125}{96}\kappa_R - \frac{3}{2}\varphi_{\lambda_R} - \frac{1}{2}\varphi_{\kappa_R} \\
c^{\mathrm{int}(2,0)}_{(+-)(+-)} &= -\frac{1}{4} l^4_{\mu_h} - \frac{17}{72} l^3_{\mu_h} + \left(-\frac{203}{144}+\frac{25\pi^2}{24}\right) l^2_{\mu_h} + \left(\frac{15}{4}-\frac{149\pi^2}{288}-\frac{\beta_{1,\mathrm{SU}(2)}}{8}\right) l_{\mu_h} \\
&- \frac{1}{2} l^4_{\mu_j} + \left(2l_R - \frac{19}{18}\right) l^3_{\mu_j} + \left(-3l^2_R + \frac{19}{6} l_R - \frac{289}{64} + \pi^2\right) l^2_{\mu_j}
\end{aligned}
$$

$$
\begin{aligned}
&+ l_{\mu_j}\left[2l_R^3 - \frac{19}{6}l_R^2 + \left(\frac{289}{32} - 2\pi^2\right)l_R - \frac{665}{216} + \frac{19\pi^2}{18} + 4\zeta(3)\right] \\
&+ l_{\mu_s}^2\Bigg[-\frac{1}{2}l_{\nu_h}^2 + \frac{11}{12}\hat{s}_W^2 l_{\nu_h} - \frac{1}{2}l_{\nu_s}^2 + (2l_R+1)\,l_{\nu_s} - 2l_R^2 - \frac{67}{24}l_R - \frac{67}{48} \\
&+ \frac{5\pi^2}{6} - \frac{121}{144}\hat{s}_W^4\Bigg] + l_{\mu_s}\Bigg[\left(-\frac{35}{18} + \frac{\pi^2}{6} - \frac{1}{4}z_\gamma\right)l_{\nu_h} + \left(\frac{35}{18} - \frac{\pi^2}{6} - \frac{3}{2}\lambda_R - \frac{1}{2}\varphi_{\kappa_R}\right)l_{\nu_s} \\
&+ \left(-\frac{35}{9} + \frac{\pi^2}{3} + 3\lambda_R + \varphi_{\kappa_R}\right)l_R - \frac{1}{16}\frac{\hat{s}_W^4}{\hat{c}_W^2}\beta_{1,Y} + \frac{1}{16}(1-\hat{s}_W^2)\beta_{1,\mathrm{SU}(2)} \\
&+ \left(-\frac{19}{96} + \frac{11}{48}\hat{s}_W^2\right)z_\gamma + \frac{43}{16}\lambda_R + \frac{91}{48}\kappa_R + 3\varphi_{\lambda_R} + \varphi_{\kappa_R}\Bigg] \\
&+ l_\mu^2\left(\frac{361}{576} - \frac{209}{288}\hat{s}_W^2 + \frac{121}{144}\hat{s}_W^4\right) + l_\mu\Bigg[\left(\frac{19}{12} - \frac{11}{12}\hat{s}_W^2\right)l_R^2 \\
&+ \left(-\frac{361}{288} + \frac{209}{288}\hat{s}_W^2\right)l_R - \frac{1387}{216} + \frac{1}{16}\beta_{1,\mathrm{SU}(2)} + \frac{95\pi^2}{144} \\
&+ \left(\frac{803}{216} + \frac{1}{16}\beta_{1,\mathrm{SU}(2)} - \frac{55\pi^2}{144}\right)\hat{s}_W^2 + \frac{1}{16}\frac{\hat{s}_W^4}{\hat{c}_W^2}\beta_{1,Y} + \left(\frac{19}{48} - \frac{11}{48}\hat{s}_W^2\right)z_\gamma \\
&+ \left(-\frac{19}{8} + \frac{11}{8}\hat{s}_W^2\right)\left(\lambda_R + \frac{1}{3}\kappa_R\right)\Bigg] + l_R^2\left(-6 + \frac{11\pi^2}{12} + \frac{1}{4}z_\gamma - \frac{3}{2}\lambda_R - \frac{1}{2}\kappa_R\right) \\
&+ l_R\left(+\frac{19}{4} - \frac{209\pi^2}{288} - \frac{19}{96}z_\gamma + \frac{19}{16}\left(\lambda_R + \frac{1}{3}\kappa_R\right) - 3\varphi_{\lambda_R} - \varphi_{\kappa_R}\right) - \frac{8}{3} + \frac{439\pi^2}{216} \\
&- \frac{143\pi^4}{576} + \left(-\frac{73}{72} + \frac{5\pi^2}{48}\right)z_\gamma - \frac{3}{8}z_\gamma\left(\lambda_R + \frac{1}{3}\kappa_R\right) + \left(\frac{73}{12} - \frac{5\pi^2}{8}\right)\lambda_R \\
&+ \left(\frac{1}{36} + \frac{\pi^2}{24}\right)\kappa_R + \frac{19}{16}\left(\varphi_{\lambda_R} + \frac{1}{3}\varphi_{\kappa_R}\right) - 3\left(\vartheta_{\lambda_R} + \frac{1}{3}\vartheta_{\kappa_R}\right)
\end{aligned}
\tag{A.38}
$$

A.4.3 Further input

In this part of the Appendix we collect useful expressions and relations that were used to obtain the coefficients listed above.

Running couplings at two loops The running of the SU(2) gauge coupling $\hat{\alpha}_2$ at the one-loop level is determined from the beta function $\beta_{\mathrm{SU}(2)}^{1-\mathrm{loop}}(\hat{\alpha}_2) = -\beta_{0,\mathrm{SU}(2)}\frac{\hat{\alpha}_2^2}{2\pi}$ and the running of the weak mixing angle $\sin^2\theta_W(\mu) \equiv \hat{s}_W^2(\mu)$ can be extracted from the running of the SU(2) and U(1)$_Y$ gauge couplings via the definition

$$
\hat{s}_W^2(\mu) = \frac{\hat{\alpha}_1(\mu)}{\hat{\alpha}_1(\mu) + \hat{\alpha}_2(\mu)}\ . \tag{A.39}
$$

Note that in principle, at the two-loop order, other SM couplings appear in the beta function which will then affect the running of the EW gauge couplings. This is irrelevant in our case however, since a term like $\hat{\alpha}_2(\mu)\hat{\alpha}_3(\mu)$ for example would only start to be important from NNNLO onwards. This means that at NNLO, which is the highest order we are considering, the running of the couplings is determined by

$$
\hat{\alpha}_2(\mu) = \hat{\alpha}_2(\mu_0) + \frac{\hat{\alpha}_2^2(\mu_0)}{4\pi}\beta_{0,\mathrm{SU}(2)}\ln\frac{\mu_0^2}{\mu^2} + \frac{\hat{\alpha}_2^3(\mu_0)}{16\pi^2}\left(\beta_{1,\mathrm{SU}(2)}\ln\frac{\mu_0^2}{\mu^2} + \beta_{0,\mathrm{SU}(2)}^2\ln^2\frac{\mu_0^2}{\mu^2}\right) + \dots\ , \tag{A.40}
$$

where, in the SM,

$$\beta_{0,\mathrm{SU}(2)} = \frac{19}{6}\,, \quad \beta_{1,\mathrm{SU}(2)} = -\frac{35}{6} - \frac{3}{2}\frac{\hat{s}_W^2}{\hat{c}_W^2} - 12\frac{\hat{\alpha}_3}{\hat{\alpha}_2} + \frac{3}{2}\frac{y_t^2}{4\pi\hat{\alpha}_2}\,, \tag{A.41}$$

$$\beta_{0,Y} = -\frac{41}{6}\,, \quad \beta_{1,Y} = -\frac{199}{18} - \frac{9}{2}\frac{\hat{c}_W^2}{\hat{s}_W^2} - \frac{44}{3}\frac{\hat{\alpha}_3}{\hat{\alpha}_1} + \frac{17}{6}\frac{y_t^2}{4\pi\hat{\alpha}_1}\,. \tag{A.42}$$

For the expansion up to two-loops, the ratios of coupling constants in $\beta_{1,\mathrm{SU}(2)}$ and $\beta_{1,Y}$ are treated as constants. The two-loop running of weak mixing angle is determined by

$$\begin{aligned}\hat{s}_W^2(\mu) &= \hat{s}_W^2(\mu_0) + \frac{\hat{\alpha}_2(\mu_0)\hat{s}_W^2(\mu_0)}{4\pi}\left[-\beta_{0,\mathrm{SU}(2)} + (\beta_{0,\mathrm{SU}(2)} + \beta_{0,Y})\hat{s}_W^2(\mu_0)\right]\ln\frac{\mu_0^2}{\mu^2} \\ &\quad + \frac{\hat{\alpha}_2^2(\mu_0)\hat{s}_W^2(\mu_0)}{16\pi^2}\left[\frac{1}{\hat{c}_W^2(\mu_0)}\left(\hat{s}_W^4(\mu_0)\beta_{1,Y} - \hat{c}_W^4(\mu_0)\beta_{1,\mathrm{SU}(2)}\right)\ln\frac{\mu_0^2}{\mu^2} + \right. \\ &\quad \left. + (\beta_{0,\mathrm{SU}(2)} + \beta_{0,Y})\hat{s}_W^2\left(\hat{s}_W^2(\mu_0)\beta_{0,Y} - \hat{c}_W^2(\mu_0)\beta_{0,\mathrm{SU}(2)}\right)\ln^2\frac{\mu_0^2}{\mu^2}\right] + \ldots\end{aligned} \tag{A.43}$$

Identities for the star distributions To obtain the fixed-order expansions of the resummed cross section, it is helpful to use the following relations. We also made use of them when checking the pole and scale cancellations of the individual cross sections:

$$\left[\frac{1}{x}\right]_*^{[a]} = \left[\frac{1}{x}\right]_*^{[b]} - \log\frac{a}{b}\,\delta(x)\,, \tag{A.44}$$

$$\left[\frac{\ln\frac{x}{a}}{x}\right]_*^{[a]} = \left[\frac{\ln\frac{x}{b}}{x}\right]_*^{[b]} + \ln\frac{b}{a}\left[\frac{1}{x}\right]_*^{[\sqrt{bc}]} + \frac{1}{2}\ln\frac{b}{a}\ln\frac{c}{a}\,\delta(x)\,. \tag{A.45}$$

Convolutions One of the more challenging parts of expanding the intermediate resolution resummed cross sections is the treatment of the convolution of the unobserved jet and soft function. The equation provided here were not only helpful for finding the coefficients $c_{IJ}^{(n,m)}$, but also for implementing the codes to generate the results shown in Section 7. Defining

$$f(\omega)\otimes g(p^2) \equiv \int_0^{\frac{p^2}{2m_\chi}} d\omega\, f(\omega)\, g(p^2 - 2m_\chi\omega)\big|_{p^2=4m_\chi E_{\mathrm{res}}^\gamma}, \tag{A.46}$$

we have

$$\int_0^{E_{\mathrm{res}}^\gamma} dE_\gamma\,\delta(\omega)\otimes\delta(p^2) = \frac{1}{4m_\chi}\,, \tag{A.47}$$

$$\int_0^{E_{\mathrm{res}}^\gamma} dE_\gamma\left[\frac{1}{\omega}\ln\left(1+\frac{\omega^2}{m_W^2}\right)\otimes\delta(p^2)\right] = \frac{1}{4m_\chi}\lambda_R(x_\gamma)\,, \tag{A.48}$$

$$\int_0^{E_{\mathrm{res}}^\gamma} dE_\gamma\left[\frac{1}{\omega}\right]_*^{[\nu_s]}\otimes\delta(p^2) = \frac{1}{4m_\chi}\ln\left(\frac{m_W}{\nu_s}x_\gamma\right)\,, \tag{A.49}$$

$$\int_0^{E_{\mathrm{res}}^\gamma} dE_\gamma\left[\frac{\ln\frac{\omega}{\nu_s}}{\omega}\right]_*^{[\nu_s]}\otimes\delta(p^2) = \frac{1}{8m_\chi}\ln^2\left(\frac{m_W}{\nu_s}x_\gamma\right)\,, \tag{A.50}$$

$$\int_0^{E_{\mathrm{res}}^\gamma} dE_\gamma\,\delta(\omega)\otimes\left[\frac{1}{p^2}\right]_*^{[\mu_j^2]} = \frac{1}{4m_\chi}\ln\left(\frac{2m_\chi m_W}{\mu_j^2}x_\gamma\right)\,, \tag{A.51}$$

$$\int_0^{E_{\rm res}^\gamma} dE_\gamma \left\{ \frac{1}{\omega} \ln\left(1+\frac{\omega^2}{m_W^2}\right) \otimes \left[\frac{1}{p^2}\right]_*^{[\mu_j^2]} \right\} = \frac{1}{4m_\chi} \left[\lambda_R(x_\gamma) \ln\left(\frac{2m_\chi m_W}{\mu_j^2} x_\gamma\right) + \right. \\ \left. + \varphi_R(x_\gamma) \right], \quad \text{(A.52)}$$

$$\int_0^{E_{\rm res}^\gamma} dE_\gamma \left[\frac{1}{\omega}\right]_*^{[\nu_s]} \otimes \left[\frac{1}{p^2}\right]_*^{[\mu_j^2]} = \frac{1}{4m_\chi} \left[\ln\left(\frac{m_W}{\nu_s} x_\gamma\right) \ln\left(\frac{2m_\chi m_W}{\mu_j^2} x_\gamma\right) - \frac{\pi^2}{6} \right], \quad \text{(A.53)}$$

$$\int_0^{E_{\rm res}^\gamma} dE_\gamma\, \delta(\omega) \otimes \left[\frac{\ln\frac{p^2}{\mu_j^2}}{p^2}\right]_*^{[\mu_j^2]} = \frac{1}{8m_\chi} \ln^2\left(\frac{2m_\chi m_W}{\mu_j^2} x_\gamma\right), \quad \text{(A.54)}$$

$$\int_0^{E_{\rm res}^\gamma} dE_\gamma \left\{ \frac{1}{\omega} \ln\left(1+\frac{\omega^2}{m_W^2}\right) \otimes \left[\frac{\ln\frac{p^2}{\mu_j^2}}{p^2}\right]_*^{[\mu_j^2]} \right\} = \frac{1}{4m_\chi} \left[\frac{1}{2} \lambda_R(x_\gamma) \ln^2\left(\frac{2m_\chi m_W}{\mu_j^2} x_\gamma\right) + \right. \\ \left. + \varphi_R(x_\gamma) \ln\frac{2m_\chi m_W}{\mu_j^2} + \vartheta_R(x_\gamma) \right], \quad \text{(A.55)}$$

$$\int_0^{E_{\rm res}^\gamma} dE_\gamma \left[\frac{1}{\omega}\right]_*^{[\nu_s]} \otimes \left[\frac{\ln\frac{p^2}{\mu_j^2}}{p^2}\right]_*^{[\mu_j^2]} = \frac{1}{4m_\chi} \left[\frac{1}{2} \ln\left(\frac{m_W}{\nu_s} x_\gamma\right) \ln^2\left(\frac{2m_\chi m_W}{\mu_j^2} x_\gamma\right) \right. \\ \left. - \frac{\pi^2}{6} \ln\left(\frac{2m_\chi m_W}{\mu_j^2} x_\gamma\right) + \zeta(3) \right], \quad \text{(A.56)}$$

$$\int_0^{E_{\rm res}^\gamma} dE_\gamma\, \delta(\omega) \otimes \left[\frac{\ln^2\frac{p^2}{\mu_j^2}}{p^2}\right]_*^{[\mu_j^2]} = \frac{1}{12m_\chi} \ln^3\left(\frac{2m_\chi m_W}{\mu_j^2} x_\gamma\right). \quad \text{(A.57)}$$

B Sommerfeld potential - Higgsino DM

In our numerical evaluations, the method-2 Sommerfeld matrix S_{IJ} (see [78]) is obtained by solving the Schrödinger equation with the spin-singlet potential

$$2\delta m_{IJ} + V_{IJ}^{S=0}(r) = \begin{pmatrix} 0 & -\frac{\alpha}{4\hat{s}_W^2\hat{c}_W^2}\frac{\mathrm{e}^{-m_Z r}}{r} & -\frac{\alpha_2}{2\sqrt{2}}\frac{\mathrm{e}^{-m_W r}}{r} \\ -\frac{\alpha}{4\hat{s}_W^2\hat{c}_W^2}\frac{\mathrm{e}^{-m_Z r}}{r} & 2\delta m_N & -\frac{\alpha_2}{2\sqrt{2}}\frac{\mathrm{e}^{-m_W r}}{r} \\ -\frac{\alpha_2}{2\sqrt{2}}\frac{\mathrm{e}^{-m_W r}}{r} & -\frac{\alpha_2}{2\sqrt{2}}\frac{\mathrm{e}^{-m_W r}}{r} & 2\delta m - \frac{\alpha}{r} - \frac{(1-2\hat{c}_W^2)^2\alpha}{4\hat{s}_W^2\hat{c}_W^2}\frac{\mathrm{e}^{-m_Z r}}{r} \end{pmatrix}. \tag{B.1}$$

The indices are ordered in the following way: (11), (22) and $(+-)$. We added the contribution of the mass-splitting matrix δm_{IJ}. As mentioned in the main text, there is no interaction between the above three two-particle states and the mixed (12) state.

C K matrices

For wino DM, the matrix $K^{\text{wino}}_{ab,I}$ can be read off from

$$\begin{pmatrix} \chi_1^T\epsilon\chi_1 \\ \chi_1^T\epsilon\chi_2 \\ \chi_1^T\epsilon\chi_3 \\ \chi_2^T\epsilon\chi_1 \\ \chi_2^T\epsilon\chi_2 \\ \chi_2^T\epsilon\chi_3 \\ \chi_3^T\epsilon\chi_1 \\ \chi_3^T\epsilon\chi_2 \\ \chi_3^T\epsilon\chi_3 \end{pmatrix}_{ab} = \begin{pmatrix} 0 & \frac{1}{2} & \frac{1}{2} & 0 & 0 & 0 & 0 & \frac{1}{2} & \frac{1}{2} \\ 0 & -\frac{i}{2} & \frac{i}{2} & 0 & 0 & 0 & 0 & \frac{i}{2} & -\frac{i}{2} \\ 0 & 0 & 0 & 0 & \frac{1}{\sqrt{2}} & 0 & \frac{1}{\sqrt{2}} & 0 & 0 \\ 0 & \frac{i}{2} & -\frac{i}{2} & 0 & 0 & 0 & 0 & \frac{i}{2} & -\frac{i}{2} \\ 0 & \frac{1}{2} & \frac{1}{2} & 0 & 0 & 0 & 0 & -\frac{1}{2} & -\frac{1}{2} \\ 0 & 0 & 0 & 0 & \frac{i}{\sqrt{2}} & 0 & -\frac{i}{\sqrt{2}} & 0 & 0 \\ 0 & 0 & 0 & \frac{1}{\sqrt{2}} & 0 & \frac{1}{\sqrt{2}} & 0 & 0 & 0 \\ 0 & 0 & 0 & \frac{i}{\sqrt{2}} & 0 & -\frac{i}{\sqrt{2}} & 0 & 0 & 0 \\ 1 & 0 & 0 & 0 & 0 & 0 & 0 & 0 & 0 \end{pmatrix} \begin{pmatrix} \chi^{0T}\epsilon\chi^0 \\ \chi^{+T}\epsilon\chi^- \\ \chi^{-T}\epsilon\chi^+ \\ \chi^{0T}\epsilon\chi^+ \\ \chi^{+T}\epsilon\chi^0 \\ \chi^{0T}\epsilon\chi^- \\ \chi^{-T}\epsilon\chi^0 \\ \chi^{+T}\epsilon\chi^+ \\ \chi^{-T}\epsilon\chi^- \end{pmatrix}_I . \quad \text{(C.1)}$$

For Higgsino DM on the other hand, the matrix $K^{\text{Higgs.}}_{ab,I}$ can be determined from

$$\begin{pmatrix} \eta_1^T\epsilon\eta_1 \\ \eta_1^T\epsilon\eta_2 \\ \eta_2^T\epsilon\eta_1 \\ \eta_2^T\epsilon\eta_2 \\ \eta_1^T\epsilon\zeta_1 \\ \zeta_1^T\epsilon\eta_1 \\ \eta_1^T\epsilon\zeta_2 \\ \zeta_2^T\epsilon\eta_1 \\ \eta_2^T\epsilon\zeta_1 \\ \zeta_1^T\epsilon\eta_2 \\ \eta_2^T\epsilon\zeta_2 \\ \zeta_2^T\epsilon\eta_2 \\ \zeta_1^T\epsilon\zeta_1 \\ \zeta_1^T\epsilon\zeta_2 \\ \zeta_2^T\epsilon\zeta_1 \\ \zeta_2^T\epsilon\zeta_2 \end{pmatrix} = K^{\text{Higgs.}}_{ab,I} \begin{pmatrix} \chi_1^{0T}\epsilon\chi_1^0 \\ \chi_1^{0T}\epsilon\chi_2^0 \\ \chi_2^{0T}\epsilon\chi_1^0 \\ \chi_2^{0T}\epsilon\chi_2^0 \\ \chi^{+T}\epsilon\chi^- \\ \chi^{-T}\epsilon\chi^+ \\ \chi_1^0\epsilon\chi^{+T} \\ \chi^{+T}\epsilon\chi_1^0 \\ \chi_2^0\epsilon\chi^{+T} \\ \chi^{+T}\epsilon\chi_2^0 \\ \chi_1^0\epsilon\chi^{-T} \\ \chi^{-T}\epsilon\chi_1^0 \\ \chi_2^0\epsilon\chi^{-T} \\ \chi^{-T}\epsilon\chi_2^0 \\ \chi^{+T}\epsilon\chi^+ \\ \chi^{-T}\epsilon\chi^- \end{pmatrix} , \quad \text{(C.2)}$$

in which case it is explicitly given by

$$K^{\text{Higgs.}}_{ab,I} =$$

$$\begin{pmatrix}
0 & 0 & 0 & 0 & 0 & 0 & 0 & 0 & 0 & 0 & 0 & 0 & 0 & 0 & 1 & 0 \\
0 & 0 & 0 & 0 & 0 & 0 & 0 & \frac{1}{\sqrt{2}} & 0 & \frac{i}{\sqrt{2}} & 0 & 0 & 0 & 0 & 0 & 0 \\
0 & 0 & 0 & 0 & 0 & 0 & \frac{1}{\sqrt{2}} & 0 & \frac{i}{\sqrt{2}} & 0 & 0 & 0 & 0 & 0 & 0 & 0 \\
\frac{1}{2} & \frac{i}{2} & \frac{i}{2} & -\frac{1}{2} & 0 & 0 & 0 & 0 & 0 & 0 & 0 & 0 & 0 & 0 & 0 & 0 \\
0 & 0 & 0 & 0 & 1 & 0 & 0 & 0 & 0 & 0 & 0 & 0 & 0 & 0 & 0 & 0 \\
0 & 0 & 0 & 0 & 0 & 1 & 0 & 0 & 0 & 0 & 0 & 0 & 0 & 0 & 0 & 0 \\
0 & 0 & 0 & 0 & 0 & 0 & 0 & \frac{1}{\sqrt{2}} & 0 & -\frac{i}{\sqrt{2}} & 0 & 0 & 0 & 0 & 0 & 0 \\
0 & 0 & 0 & 0 & 0 & 0 & \frac{1}{\sqrt{2}} & 0 & -\frac{i}{\sqrt{2}} & 0 & 0 & 0 & 0 & 0 & 0 & 0 \\
0 & 0 & 0 & 0 & 0 & 0 & 0 & 0 & 0 & 0 & \frac{1}{\sqrt{2}} & 0 & \frac{i}{\sqrt{2}} & 0 & 0 & 0 \\
0 & 0 & 0 & 0 & 0 & 0 & 0 & 0 & 0 & 0 & 0 & \frac{1}{\sqrt{2}} & 0 & \frac{i}{\sqrt{2}} & 0 & 0 \\
\frac{1}{2} & -\frac{i}{2} & \frac{i}{2} & \frac{1}{2} & 0 & 0 & 0 & 0 & 0 & 0 & 0 & 0 & 0 & 0 & 0 & 0 \\
\frac{1}{2} & \frac{i}{2} & -\frac{i}{2} & \frac{1}{2} & 0 & 0 & 0 & 0 & 0 & 0 & 0 & 0 & 0 & 0 & 0 & 0 \\
0 & 0 & 0 & 0 & 0 & 0 & 0 & 0 & 0 & 0 & 0 & 0 & 0 & 0 & 0 & 1 \\
0 & 0 & 0 & 0 & 0 & 0 & 0 & 0 & 0 & 0 & 0 & \frac{1}{\sqrt{2}} & 0 & -\frac{i}{\sqrt{2}} & 0 & 0 \\
0 & 0 & 0 & 0 & 0 & 0 & 0 & 0 & 0 & 0 & \frac{1}{\sqrt{2}} & 0 & -\frac{i}{\sqrt{2}} & 0 & 0 & 0 \\
\frac{1}{2} & -\frac{i}{2} & -\frac{i}{2} & -\frac{1}{2} & 0 & 0 & 0 & 0 & 0 & 0 & 0 & 0 & 0 & 0 & 0 & 0
\end{pmatrix}. \tag{C.3}$$

It should be noted however that the bilinear terms of the form $\zeta_a \epsilon \zeta_a$ and $\eta_a \epsilon \eta_a$ can be ignored, since they are not relevant for the annihilation operators. Doing so would greater simplify the K-matrix for Higgsino DM.

D Effective theory Feynman rules - unbroken EW limit

In this Appendix we collect the Feynman rules that are needed to compute the effective theory diagrams in Figure 6.2. We give the SCET Feynman rules in the EW symmetric limit. They can be derived from the operator basis (2.53). In the process of computing the Feynman rules, one has to expand the gauge covariant building blocks that were defined in (2.44). When considering the 4-point and 5-point vertex rules given in Figure D.1, one notices terms proportional to n_- (n_+) and n_-n_- (n_+n_+), respectively. These terms originate from the partial derivative acting on the (anti-) collinear gauge fields and it is interesting to note that these terms vanish at the order at which we are considering the scattering process. This is because n_- (n_+) points along the longitudinal direction and when contracted with polarization vectors, which only have transverse components, these terms vanish. This is true when dealing with (almost) on-shell fields.

Using this argument, one might naively expect the 5-point vertex to vanish altogether. This is not the case however in the scattering process at hand. Here, the 5-point vertex is always accompanied by a 3-(anti-)collinear gauge boson vertex, see Figure 6.2. When analyzing how the various terms combine, one will see that the terms proportional to n_-n_- (n_+n_+) vanish, since one of the n_- (n_+) is always contracted with a polarization vector. For the terms proportional to $g_\perp^{\alpha\sigma} n_{+,-}^\mu$ this is not true, since, when multiplied with the 3-gauge boson vertex, the n_- (n_+) will in some cases be contracted with the momenta appearing in the 3-point vertex and not with a polarization vector, leading to the survival of these terms. Hence, only terms proportional to $g_\perp^{\alpha\sigma}$ (for the 4-point vertex) and $g_\perp^{\alpha\sigma} n_{+,-}^\mu$ (for the 5-point vertex), are relevant for the case we are interested in.

Note that although the argument employing the polarization vectors cannot be made for the case of the jet function computation (since there are no polarization vectors), the terms originating from the partial derivative acting on (anti-) collinear gauge fields still vanish. When evaluating the jet function, one notices that these terms contract in such a way that they are either proportional to $n_{+,-} \cdot n_{+,-}$, or proportional to $p \cdot p$. The former vanish because of how $n_{+,-}$ is defined and the latter are neglected since $p^2 \sim M_\chi^2 \lambda^2$ is subleading. Hence, also for the jet function computation, the terms proportional to $n_{+,-}$ (one-emission) and $n_{+,-}n_{+,-}$ (two-emission) vanish.

The Feynman rule for the 5-point vertex is specific to two collinear and one anti-collinear emission. To obtain the Feynman rule for one collinear and two anti-collinear emissions, one has to exchange $n_+ \leftrightarrow n_-$, $p_3 \leftrightarrow p_5$, $\alpha \leftrightarrow \beta$, $\mu \leftrightarrow \nu$ and $B \leftrightarrow D$, and remember that p_4 is now anti-collinear instead of collinear. Due to the abelian nature of the $\mathrm{U}(1)_Y$ gauge boson, the double emission in the (anti-) collinear direction can only happen for an SU(2) field. This constrains which operators are relevant for this type of diagram.

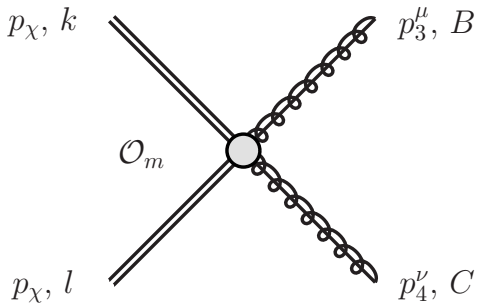

$$= i\left[\sigma^\sigma, \sigma^\rho\right]\,(n_- - n_+)\cdot\sigma\left(g_\perp^{\sigma\mu} - \tfrac{p_3^\sigma n_+^\mu}{n_+\cdot p_3}\right)\left(g_\perp^{\rho\nu} - \tfrac{p_4^\rho n_-^\nu}{n_-\cdot p_4}\right)\left(T_m^{BC}\right)_{kl}$$

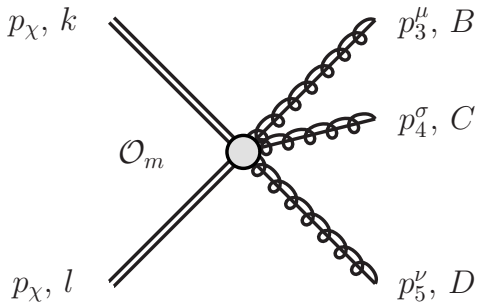

$$= -2\hat{g}_2\left[\sigma^\alpha, \sigma^\beta\right](n_- - n_+)\cdot\sigma\varepsilon^{ABC}(T_m^{AD})_{kl}$$

$$\times\Big[\left(g_\perp^{\alpha\sigma}\tfrac{n_+^\mu}{n_+\cdot p_3} - g^{\alpha\mu}\tfrac{n_+^\sigma}{n_+\cdot p_4}\right) + \tfrac{(p_3+p_4)^\alpha n_+^\mu n_+^\sigma}{2n_+\cdot(p_3+p_4)}\left(\tfrac{1}{n_+\cdot p_4} - \tfrac{1}{n_+\cdot p_3}\right)$$

$$+\tfrac{n_+^\mu n_+^\sigma}{2n_+\cdot p_3 n_+\cdot p_4}\left(p_3 - p_4\right)^\alpha\Big]\left[g_\perp^{\beta\nu} - \tfrac{p_5^\nu n_-^\nu}{n_-\cdot p_5}\right]$$

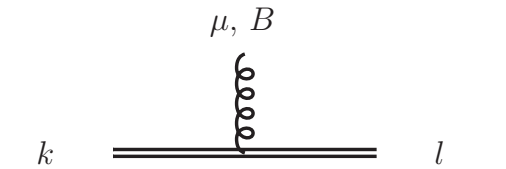

$$= i\hat{g}_2\left(T^B\right)_{lk}v^\mu \qquad \text{or} \qquad i\hat{g}_1 Y v^\mu$$

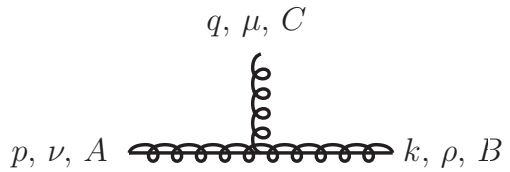

$$= \hat{g}_2\,\varepsilon^{ABC} n_+\cdot p\, n_-^\mu\, g_\perp^{\nu\rho}$$

Figure D.1: Effective field theory Feynman rules.

E Collinear integrals and rapidity regularization

In this Appendix we will provide details on the computation of the integrals that were encountered when calculating the narrow resolution unobserved jet function and photon jet functions. While doing so, we will also give more explanations about the rapidity regulator that needed to be employed while computing said integrals. We use the rapidity regulator introduced in [76], which is implemented via the following replacements in the eikonal Feynman rules originating from soft and (anti-) collinear Wilson lines

$$\begin{aligned}
\text{collinear emission}: \quad & \frac{n_+^\mu}{n_+k} \to \frac{n_+^\mu}{n_+k}\frac{\nu^\eta}{|n_+k|^\eta}\,, \\
\text{anti-collinear emission}: \quad & \frac{n_-^\mu}{n_-k} \to \frac{n_-^\mu}{n_-k}\frac{\nu^\eta}{|n_-k|^\eta}\,, \\
\text{soft emission from (anti-) collinear direction}: \quad & \frac{n_\pm^\mu}{n_\pm k} \to \frac{n_\pm^\mu}{n_\pm k}\frac{\nu^{\eta/2}}{|2k^3|^{\eta/2}}\,, \\
\text{soft emission from the heavy line}: \quad & \frac{v^\mu}{v\cdot k} \to \frac{v^\mu}{v\cdot k}\frac{\nu^{\eta/2}}{|2k^3|^{\eta/2}}\,.
\end{aligned} \tag{E.1}$$

Similarly to dimensional regularization, η is the rapidity regulator and ν is the rapidity scale that accompanies the regulator. In the (anti-) collinear limit, we find that the loop momentum behaves as follows $2k^3 \to n_+k$ ($2k^3 \to n_-k$), which shows that the η-regulators in (E.1) is consistent between soft and collinear integrals. In Section 6 we have seen that both the soft and the photon jet functions require rapidity regularization independently of the detector resolution, while the unobserved collinear jet function only needs an additional regulator in the narrow resolution case. We will now discuss integrals relevant for the jet functions and postpone computational details concerning the soft functions to Appendix G. This Appendix follows Appendix B.1 of [7] and the integrals that are shown were computed independently by Alessandro Broggio, CH, Kai Urban and Martin Vollmann.

The first integral we discuss is the collinear integral relevant for the computation of the first two diagrams in the upper row of Figure 6.6, which give the Wilson line contribution to the collinear jet function. For this, the off-shell scalar integral ($p^2 \neq 0$) is given by

$$I_c(p^2) = \int [dk] \frac{\nu^\eta}{[k^2 - m_W^2 + i0][(p+k)^2 - m_W^2 + i0][n_+k + i0]|n_+k|^\eta}\,, \tag{E.2}$$

where the integration measure is defined as

$$[dk] = \tilde{\mu}^{2\epsilon}\frac{d^dk}{(2\pi)^d} = \left(\frac{\mu^2 e^{\gamma_E}}{4\pi}\right)^\epsilon \frac{d^dk}{(2\pi)^d}\,, \tag{E.3}$$

with $d = 4-2\epsilon$ and γ_E the Euler-Mascheroni constant. Using contour integration one finds that $n_+k < 0$, which means that we can get rid of the absolute value in the denominator of (E.2) as follows $|n_+k| \to -n_+k$. Because I_c includes a linear propagator, it proves

convenient to introduce the Feynman parametrization

$$\frac{1}{abc^{1+\eta}} = \int_0^\infty dx_1 \int_0^\infty dx_2 \, \frac{(2+\eta)(1+\eta)}{(c+ax_1+bx_2)^{3+\eta}} \,. \tag{E.4}$$

The integration over the loop momentum can now be executed in the standard way, which results in

$$\begin{aligned} I_c(p^2) &= \left(\mu^2 e^{\gamma_E}\right)^\epsilon \frac{(-i)}{16\pi^2} \frac{\Gamma(1+\eta+\epsilon)}{\Gamma(1+\eta)} \\ &\times \int_0^\infty dx_1 \int_0^\infty dx_2 \, \frac{\nu^\eta}{(x_1+x_2)^{1-\eta-2\epsilon} \left[(x_1+x_2)^2 m_W^2 - x_2 x_1 p^2 + n_+ p x_2\right]^{1+\epsilon+\eta}} \,. \end{aligned} \tag{E.5}$$

Solving the Feynman parameter integrals proves somewhat more complicated. Subsituting $x_1 \to x_1' x_2$ allows us to integrate over x_2, remembering to include a factor x_2 from the Jacobian. We also assume to work in the region where $p^2 < 0$ such that for the moment we don't develop any imaginary parts in intermediate steps. The correct imaginary part will later be recovered by means of analytic continuation $p^2 \to p^2 + i0$. After the x_2 integration, the collinear integral takes the form

$$I_c(p^2) = \left(\mu^2 e^{\gamma_E}\right)^\epsilon \frac{(-i)}{16\pi^2} \left(\frac{\nu}{n_+ p}\right)^\eta \frac{\Gamma(\epsilon)}{n_+ p} \int_0^\infty dx_1' \, (1+x_1')^{-1+2\epsilon+\eta} \left[m_W^2 (1+x_1')^2 - p^2 x_1'\right]^{-\epsilon}. \tag{E.6}$$

We now introduce $r \equiv m_W^2/(-p^2)$ and rewrite part of the integrand as follows

$$\left[m_W^2 (1+x_1')^2 - p^2 x_1'\right]^{-\epsilon} = (-p^2)^{-\epsilon} \left[r \, (1+x_1')^2 + x_1'\right]^{-\epsilon} . \tag{E.7}$$

After subsequently performing the variable change $x_1' = (1-y)/y$, where the Jacobian for this transformation is y^{-2}, we can execute the last Feynman parameter integral over y which results in

$$\int_0^1 dy \, y^{-1-\eta} (r + y - y^2)^{-\epsilon} = -\frac{r^{-\epsilon}}{\eta} F_1\left(-\eta, \epsilon, \epsilon, 1-\eta; \frac{2}{1+\sqrt{1+4r}}, \frac{2}{1-\sqrt{1+4r}} \right), \tag{E.8}$$

where F_1 is the Appell-F_1 hypergeometric function. This is the result for $I_c(p^2)$ to all orders in η and ϵ and the consistency of (E.5) and (E.8) was cross-checked by performing multiple numerical checks. The all-orders result (E.8) now needs to be expanded first in η and then in ϵ. The expansion in terms of the rapidity regulator for $\eta \to 0$ is done using the relation [105]

$$y^{-1-\eta} = -\frac{\delta(y)}{\eta} + \sum_{m=0}^\infty \frac{(-\eta)^m}{m!} \left[\frac{\ln^m(y)}{y}\right]_+ = -\frac{\delta(y)}{\eta} + \left[\frac{1}{y}\right]_+ + \dots \,. \tag{E.9}$$

The +-distribution in (E.9) is related to the star-distribution defined in (6.76), in that the star-distribution is like the +-distribution for a dimensionful variable [106]. It is defined as

$$\int_0^1 dx \left[\frac{\ln^n(x)}{x}\right]_+ f(x) = \int_0^1 dx \, \frac{\ln^n(x)}{x} \left(f(x) - f(0)\right) \,. \tag{E.10}$$

After taking in successive order the limits $\eta \to 0$ and $\epsilon \to 0$, we can perform the y integral (E.8) to arrive at

$$\int_0^1 dy\, y^{-1-\eta}(r+y-y^2)^{-\epsilon} = -\frac{r^{-\epsilon}}{\eta} + \epsilon\left[-\frac{\ln^2(-x)}{2}\right] + \mathcal{O}(\eta,\epsilon^2)\,, \tag{E.11}$$

where we find this compact result after introducing the Landau variable

$$x \equiv \frac{1-\beta}{1+\beta}\,, \qquad \beta = \sqrt{1-\frac{4m_W^2}{p^2}}\,, \tag{E.12}$$

and by employing relations between polylogarithms with different arguments at intermediate steps for simplification. The correctness of the expansions in $\eta \to 0$ and in $\epsilon \to 0$ used in the evaluation of (E.11) was checked numerically. The package `NumExp` [107] was used for the numerical expansion of the Appell-F_1 function, after which (E.8) could be used to cross-checked (E.11). Using (E.11) we can write the final result for the collinear integral (E.2) as follows

$$I_c(p^2) = \frac{i\,(n_+p)^{-1}}{16\pi^2}\left[\frac{1}{\epsilon\eta} - \frac{1}{\eta}\ln\frac{m_W^2}{\mu^2} - \frac{1}{\epsilon}\ln\frac{n_+p}{\nu} + \ln\frac{m_W^2}{\mu^2}\,\ln\frac{n_+p}{\nu} + \frac{\ln^2(-x)}{2}\right] + \mathcal{O}(\eta,\epsilon)\,. \tag{E.13}$$

This result was derived in the non-physical region $p^2 < 0$ and we now have to perform the analytic continuation to the physical regions $p^2 > 4m_W^2$ and $0 < p^2 < 4m_W^2$. To obtain the result in the region $p^2 > 4m_W^2$ from (E.13), the following substitution is required

$$\ln(-x) \to \ln(x) + i\pi\,, \tag{E.14}$$

while in the region $0 < p^2 < 4m_W^2$ the result does not develop an imaginary part. It can be extracted from (E.13) via the substitution

$$\ln(-x) \to i\big(-2\arctan(\bar\beta) + \pi\big)\,, \tag{E.15}$$

where we define

$$\bar\beta = \sqrt{\frac{4m_W^2}{p^2} - 1}\,. \tag{E.16}$$

The result for the collinear integral with general p^2 in (E.13) is useful for several reasons. First of all, it is needed for the computation of the unobserved jet function in the narrow resolution case. Furthermore, it can be used to cross-check the result for the corresponding integral relevant for the intermediate resolution unobserved jet function and to confirm that the collinear function is not mass-dependent at the one-loop order. To see this, we remind ourselves that the external momentum p in the intermediate resolution case has hard-collinear scaling $p^\mu \sim m_\chi(\lambda, 1, \sqrt{\lambda})$. Consequently, we have the scaling $p^2 \sim \lambda m_\chi^2$ which is much bigger than $m_W^2 \sim \lambda^2 m_\chi^2$. This means that we have the scale hierarchy $p^2 \gg m_W^2$ and we can try to expand (E.13) in a straightforward manner to obtain

$$\begin{aligned} I_c(p^2) = \frac{i\,(n_+p)^{-1}}{16\pi^2}\Bigg[&\frac{1}{\epsilon\eta} - \frac{1}{\eta}\ln\frac{m_W^2}{\mu^2} - \frac{1}{\epsilon}\ln\frac{n_+p}{\nu} + \ln\frac{m_W^2}{\mu^2}\,\ln\frac{n_+p}{\nu} \\ &+ \frac{1}{2}\ln^2\left(-\frac{m_W^2}{p^2}\right)\Bigg] + \mathcal{O}(\eta,\epsilon) + \mathcal{O}\left(\frac{m_W^2}{p^2}\right). \end{aligned} \tag{E.17}$$

Naively one might expect the collinear integral to be independent of the gauge boson mass after the expansion, such that it can be used for the intermediate resolution jet function that was given in Section 6.3.2. However, this is clearly not the case. To understand this we note that by assuming a hard-collinear scaling for p, the original collinear integral (E.2) is now a two-scale object. The two scales are determined by p (hard-collinear) and m_W (soft) and we can use the strategy of regions approach to evaluate (E.2) in the soft and hard-collinear limits. The soft contribution is determined by expanding the propagator

$$\left[(p+k)^2 - m_W^2\right] = p^2 + n_+p\, n_-k + \mathcal{O}(\lambda^2)\,. \tag{E.18}$$

The collinear integral after the soft-region expansion is then given by

$$I_{c\text{-}s}(p^2) = \int [dk] \frac{\nu^\eta}{[k^2 - m_W^2 + i\varepsilon][p^2 + n_+p\, n_-k + i\varepsilon][n_+k + i\varepsilon]|n_+k|^\eta}\,. \tag{E.19}$$

Following the same reasoning that was used for the calculation of I_c, we can evaluate $I_{c\text{-}s}$ and find

$$\begin{aligned} I_{c\text{-}s}(p^2) = \frac{i\,(n_+p)^{-1}}{16\pi^2}\bigg[&-\frac{1}{\epsilon^2} + \frac{1}{\epsilon\eta} + \frac{\pi^2}{12} + \frac{1}{\epsilon}\ln\frac{m_W^2}{\mu^2} + \frac{1}{\epsilon}\ln\left(\frac{-p^2\nu}{m_W^2 n_+p}\right) - \frac{1}{\eta}\ln\frac{m_W^2}{\mu^2} \\ &- \frac{1}{2}\ln^2\frac{m_W^2}{\mu^2} - \ln\frac{m_W^2}{\mu^2}\,\ln\left(\frac{-p^2\nu}{m_W^2 n_+p}\right)\bigg] + \mathcal{O}(\eta,\epsilon)\,. \end{aligned} \tag{E.20}$$

The collinear integral expanded in the hard-collinear region on the other hand can be obtained by simply dropping the gauge boson masses at leading power. The result of the hard-collinear expanded collinear integral is given by

$$I_{c\text{-}hc}(p^2) = \frac{i\,(n_+p)^{-1}}{16\pi^2}\left[\frac{1}{\epsilon^2} + \frac{1}{\epsilon}\ln\left(-\frac{\mu^2}{p^2}\right) + \frac{1}{2}\ln^2\left(-\frac{\mu^2}{p^2}\right) - \frac{\pi^2}{12}\right] + \mathcal{O}(\epsilon)\,. \tag{E.21}$$

As expected, we see that only the soft contribution $I_{c\text{-}s}$ requires an additional regulator. Adding the results for $I_{c\text{-}s}$ (E.20) and $I_{c\text{-}hc}$ (E.21), we are able to recuperate the expanded collinear integral (E.17), which serves as a cross-check that the method of regions expansion was done correctly.

The result for $I_{c\text{-}s}$ in (E.20) allows us to confirm that there are no mass-dependent contributions to the collinear function in the intermediate resolution case. The soft contribution to the jet function Wilson line diagram is obtained by multiplying (E.19) with the appropriate tree level factors. After taking the imaginary part, we find that the virtual part (with only a single particle cut) vanishes since it is given by a scale-less integral. The real contribution (where the cut goes through two particles) on the other hand is non-vanishing. This real contribution can be checked to be equal to the appropriate soft function integral (G.16) after convoluting it with the tree-level jet function. This means that the real emissions of the intermediate resolution soft functions correctly reproduce the soft region of the jet function integral in the small mass limit $p^2 \gg m_W^2$. As a result, we see that there are no mass-dependent contributions to the intermediate resolution unobserved jet function, which only receives mass-independent contributions from the hard-collinear region.

Lastly we discuss the anti-collinear integral relevant for the Wilson line diagram contribution to the photon jet functions. As we saw in Section 6.2, the photon jet functions Z_γ^{33}, Z_γ^{34} and Z_γ^{43} are computed with the rapidity regulator and for all photon jet functions, only virtual diagrams contribute. The integral needed to evaluate diagrams (a) and (b) of Figure 6.5 is the rapidity and dimensionally regulated on-shell anti-collinear scalar integral

$$I_{\bar{c}}(0) = \int [dk] \frac{\nu^\eta}{[k^2 - m_W^2 + i0][k^2 + 2p\cdot k - m_W^2 + i0][n_-k + i0]|n_-k|^\eta}\,. \tag{E.22}$$

$I_{\bar{c}}(0)$ can be derive from the collinear integral $I_{\bar{c}}(0)$ in (E.2) by setting $p^2 \to 0$ and by substituting $n_+k \to n_-k$. To simplify the integration it will turn out to be convenient to parametrize the integration measure as follows

$$d^dk = \frac{1}{2}\, dn_-k\, dn_+k\, d^{d-2}k_\perp\,, \tag{E.23}$$

and rewrite the integrand as

$$\frac{\nu^\eta}{n_-k[n_+k - \frac{k_T^2+m_W^2-i0}{n_-k}](n_-k+2m_\chi)[n_+k - \frac{k_T^2+m_W^2-i0}{n_-k+2m_\chi}][n_-k+i0]|n_-k|^\eta}. \tag{E.24}$$

From this expression it is possible to see that there is only one configuration in which the n_+k integral is non-vanishing and this corresponds to the case in which we close the integration contour in the upper half plane and pick up the pole $(k_T^2 + m_W^2 - i0)/n_-k$ for $-2m_\chi < n_-k < 0$. It was checked that this is the only relevant range for n_-k since the integral vanishes for $n_-k < -2m_\chi$ or $n_-k > 0$. The n_-k and $k_\perp$ integrations can then be straightforwardly evaluated to give the final result of the anti-collinear integral

$$I_{\bar{c}}(0) = \frac{i}{32\pi^2 m_\chi}\left(\frac{\mu}{m_W}\right)^{2\epsilon}\left(\frac{\nu}{2m_\chi}\right)^\eta \frac{e^{\gamma_E\epsilon}\,\Gamma(\epsilon)}{\eta}\,. \tag{E.25}$$

F Details unobserved jet function - narrow resolution

In this Appendix we provide the SM gauge boson self-energies and their derivatives. These are used for the massive self-energy contributions to the narrow resolution unobserved jet functions that were discussed in Section 6.3.1. In particular, these expressions are needed to implement the codes that generate the numerical results provided in Section 7. The required self-energies are given in Feynman gauge and have been extracted from [102]. They are repeated here for convenience and read

$$\begin{aligned}\Sigma_T^{\gamma\gamma}(p^2) = -\frac{\hat{g}_2^2\hat{s}_W^2}{16\pi^2}\Bigg\{\frac{2}{3}\sum_{f,i}N_C^f 2Q_f^2\Big[-(p^2+2m_{f,i}^2)B_0(p^2,m_{f,i},m_{f,i}) \\ + 2m_{f,i}^2 B_0(0,m_{f,i},m_{f,i}) + \frac{1}{3}p^2\Big] \\ + \Big\{\Big[3p^2+4m_W^2\Big]B_0(p^2,m_W,m_W) - 4m_W^2 B_0(0,m_W,m_W)\Big\}\Bigg\},\end{aligned} \tag{F.1}$$

$$\begin{aligned}\left.\frac{\partial\,\Sigma_T^{\gamma\gamma}(p^2)}{\partial p^2}\right|_{p^2\to 0} = -\frac{\hat{g}_2^2\hat{s}_W^2}{16\pi^2}\Bigg\{\frac{2}{3}\sum_{f,i}N_C^f 2Q_f^2\Big[-B_0(p^2,m_{f,i},m_{f,i}) \\ - (p^2+2m_{f,i}^2)\frac{\partial\,B_0(p^2,m_{f,i},m_{f,i})}{\partial p^2} + \frac{1}{3}\Big] \\ + \Big\{3B_0(p^2,m_W,m_W) + (3p^2+4m_W^2)\frac{\partial\,B_0(p^2,m_W,m_W)}{\partial p^2}\Big\}\Bigg\}\Bigg|_{p^2\to 0},\end{aligned} \tag{F.2}$$

$$\begin{aligned}\Sigma_T^{\gamma Z}(p^2) = -\frac{\hat{g}_2^2\hat{s}_W^2}{16\pi^2}\Bigg\{\frac{2}{3}\sum_{f,i}N_C^f(-Q_f)\Big(\hat{g}_f^+ + \hat{g}_f^-\Big)\Big[-(p^2+2m_{f,i}^2)B_0(p^2,m_{f,i},m_{f,i}) \\ + 2m_{f,i}^2 B_0(0,m_{f,i},m_{f,i}) + \frac{1}{3}p^2\Big] \\ + \frac{1}{3\hat{s}_W\hat{c}_W}\Bigg\{\Big[\left(9\hat{c}_W^2+\frac{1}{2}\right)p^2 + (12\hat{c}_W^2+4)m_W^2\Big]B_0(p^2,m_W,m_W) \\ - (12\hat{c}_W^2-2)m_W^2 B_0(0,m_W,m_W) + \frac{1}{3}p^2\Bigg\}\Bigg\},\end{aligned} \tag{F.3}$$

$$\begin{aligned}\Sigma_T^{ZZ}(p^2) = -\frac{\hat{g}_2^2\hat{s}_W^2}{16\pi^2}\Bigg\{\frac{2}{3}\sum_{f,i}N_C^f\Bigg\{\Big((\hat{g}_f^+)^2 + (\hat{g}_f^-)^2\Big)\Big[-(p^2+2m_{f,i}^2)B_0(p^2,m_{f,i},m_{f,i}) \\ + 2m_{f,i}^2 B_0(0,m_{f,i},m_{f,i}) + \frac{1}{3}p^2\Big] + \frac{3}{4\hat{s}_W^2\hat{c}_W^2}m_{f,i}^2 B_0(p^2,m_{f,i},m_{f,i})\Bigg\}\end{aligned}$$

$$
\begin{aligned}
&+\frac{1}{6\hat{s}_W^2\hat{c}_W^2}\Big\{\Big[\Big(18\hat{c}_W^4+2\hat{c}_W^2-\frac{1}{2}\Big)p^2+(24\hat{c}_W^4+16\hat{c}_W^2-10)m_W^2\Big]B_0(p^2,m_W,m_W)\\
&-(24\hat{c}_W^4-8\hat{c}_W^2+2)m_W^2B_0(0,m_W,m_W)+(4\hat{c}_W^2-1)\frac{1}{3}p^2\Big\}\\
&+\frac{1}{12\hat{s}_W^2\hat{c}_W^2}\Big\{\Big(2m_H^2-10m_Z^2-p^2\Big)B_0(p^2,m_Z,m_H)\\
&-2m_Z^2B_0(0,m_Z,m_Z)-2m_H^2B_0(0,m_H,m_H)\\
&-\frac{(m_Z^2-m_H^2)^2}{p^2}\Big(B_0(p^2,m_Z,m_H)-B_0(0,m_Z,m_H)\Big)-\frac{2}{3}p^2\Big\}\Big\},
\end{aligned}
\tag{F.4}
$$

$$
\begin{aligned}
\frac{\partial\,\Sigma_T^{ZZ}(p^2)}{\partial p^2}\Big|_{p^2=m_Z^2} \;=\;& -\frac{\hat{g}_2^2\hat{s}_W^2}{16\pi^2}\Big\{\frac{2}{3}\sum_{f,i}N_C^f\Big\{\Big((\hat{g}_f^+)^2+(\hat{g}_f^-)^2\Big)\Big[-B_0(p^2,m_{f,i},m_{f,i})\\
&-(m_Z^2+2m_{f,i}^2)\frac{\partial B_0(p^2,m_{f,i},m_{f,i})}{\partial p^2}+\frac{1}{3}\Big]+\frac{3}{4\hat{s}_W^2\hat{c}_W^2}m_{f,i}^2\frac{\partial B_0(p^2,m_{f,i},m_{f,i})}{\partial p^2}\Big\}\\
&+\frac{1}{6\hat{s}_W^2\hat{c}_W^2}\Big\{\Big(18\hat{c}_W^4+2\hat{c}_W^2-\frac{1}{2}\Big)B_0(p^2,m_W,m_W)\\
&+\Big[\Big(18\hat{c}_W^4+2\hat{c}_W^2-\frac{1}{2}\Big)m_Z^2+(24\hat{c}_W^4+16\hat{c}_W^2-10)m_W^2\Big]\frac{\partial B_0(p^2,m_W,m_W)}{\partial p^2}\\
&+(4\hat{c}_W^2-1)\frac{1}{3}\Big\}\\
&+\frac{1}{12\hat{s}_W^2\hat{c}_W^2}\Big\{-B_0(p^2,m_Z,m_H)+\Big(2m_H^2-11m_Z^2\Big)\frac{\partial B_0(p^2,m_Z,m_H)}{\partial p^2}\\
&+\frac{(p^2-m_H^2)^2}{m_Z^4}\Big(B_0(p^2,m_Z,m_H)-B_0(0,m_Z,m_H)\Big)\\
&-\frac{(m_Z^2-m_H^2)^2}{m_Z^2}\Big(\frac{\partial B_0(p^2,m_Z,m_H)}{\partial p^2}\Big)-\frac{2}{3}\Big\}\Big\}\Big|_{p^2=m_Z^2}.
\end{aligned}
\tag{F.5}
$$

The parameter $m_{f,i}$ denotes the masses of fermions, where i specifies the generation and f specifies the fermion within a generation. Furthermore, N_C^f indicates the number of fermion colors, which means that $N_C^f=1$ in the case of leptons and $N_C^f=3$ in the case of quarks. The EW couplings are written in terms of the charge Q_f and the third SU(2) generator $I_{W,f}^3$, as follows

$$
\hat{g}_f^+=\frac{\hat{s}_W}{\hat{c}_W}Q_f,\qquad\qquad \hat{g}_f^-=\frac{\hat{s}_W^2Q_f-I_{W,f}^3}{\hat{s}_W\hat{c}_W}\,.
\tag{F.6}
$$

The functions B_0 in (F.1) to (F.5) above are scalar integrals given in Passarino-Veltman notation. To evaluate the self-energies, one needs the explicit expressions for these integrals and their derivatives, $\partial B_0/\partial p^2$, which we provide in the following. While the integrals (and their derivatives) given below still contain poles, these have been subtracted in the self-energies. Lastly, we also assume $p^2>0$, since the imaginary parts are made explicit. The B_0 and $\partial B_0/\partial p^2$ functions are given by

$$
B_0(0,m,m)=\frac{1}{\epsilon}-2\ln\frac{m}{\mu}\,,
\tag{F.7}
$$

$$B_0(0,0,m) = \frac{1}{\epsilon} + 1 - 2\ln\frac{m}{\mu}\,, \tag{F.8}$$

$$B_0(0,m_1,m_2) = \frac{1}{\epsilon} + 1 + \frac{m_1^2+m_2^2}{m_1^2-m_2^2}\ln\frac{m_2}{m_1} + \ln\frac{\mu^2}{m_1 m_2}\,, \tag{F.9}$$

$$B_0(p^2,0,0) = \frac{1}{\epsilon} + 2 + \ln\frac{\mu^2}{p^2} + i\pi\,, \tag{F.10}$$

$$\frac{\partial B_0(p^2,0,0)}{\partial p^2} = -\frac{1}{p^2}\,, \tag{F.11}$$

$$\begin{aligned} B_0(p^2,m,m) = \Bigg\{ &\theta(4m^2-p^2)\left[\frac{1}{\epsilon} + 2 - 2\ln\frac{m}{\mu} - 2\bar{\beta}\arctan\frac{1}{\bar{\beta}}\right] \\ &+ \theta(p^2-4m^2)\left[\frac{1}{\epsilon} + 2 - 2\ln\frac{m}{\mu} + \beta\ln(x) + i\beta\pi\right]\Bigg\}\,, \end{aligned} \tag{F.12}$$

$$\begin{aligned} \frac{\partial B_0(p^2,m,m)}{\partial p^2} = \Bigg\{ &\theta(4m^2-p^2)\frac{1}{p^2}\left[\frac{1+\bar{\beta}^2}{\bar{\beta}}\arctan\frac{1}{\bar{\beta}} - 1\right] \\ &+ \theta(p^2-4m^2)\left[-\frac{1}{p^2} + \frac{2m_W^2}{p^4\beta}\left(\ln(x) + i\pi\right)\right]\Bigg\}\,, \end{aligned} \tag{F.13}$$

$$\left.\frac{\partial B_0(p^2,m,m)}{\partial p^2}\right|_{p^2=0} = \frac{1}{6m^2}\,, \tag{F.14}$$

$$\begin{aligned} B_0(p^2,0,m) = \Bigg[\frac{1}{\epsilon} + 2 - 2\ln\frac{m}{\mu} - \left(1-\frac{m^2}{p^2}\right)\Bigg[&\theta(m^2-p^2)\ln\left(1-\frac{p^2}{m^2}\right) \\ &+ \theta(m^2-p^2)\left(\ln\left(\frac{p^2}{m^2}-1\right) - i\pi\right)\Bigg]\Bigg]\,, \end{aligned} \tag{F.15}$$

$$\begin{aligned} B_0(p^2,M,m) = \Bigg[\frac{1}{\epsilon} + 2 - \frac{M^2-m^2}{p^2}\ln\frac{M}{m} + \ln\frac{\mu^2}{mM} \\ + \frac{\sqrt{|\kappa(p^2,m^2,M^2)|}}{p^2}F(p^2,M,m)\Bigg]\,, \end{aligned} \tag{F.16}$$

$$\begin{aligned} \left.\frac{\partial B_0(p^2,m_H,m_Z)}{\partial p^2}\right|_{p^2=m_Z^2} = \Bigg[&-\frac{1}{m_Z^2} - \frac{m_H^2-m_Z^2}{m_Z^4}\ln\left(\frac{m_Z}{m_H}\right) \\ &- \frac{(m_H^2-3m_Z^2)\arctan\left[\sqrt{\frac{4m_Z^2}{m_H^2}-1}\right]}{m_Z^4\sqrt{\frac{4m_Z^2}{m_H^2}-1}}\Bigg]\,, \end{aligned} \tag{F.17}$$

where for $M > m$

$$F(p^2,M,m) = \begin{cases} \ln\frac{\sqrt{(M+m)^2-p^2}+\sqrt{(M-m)^2-p^2}}{\sqrt{(M+m)^2-p^2}-\sqrt{(M-m)^2-p^2}} & p^2 < (m-M)^2 \\ -2\arctan\sqrt{\frac{p^2-(M-m)^2}{(M+m)^2-p^2}} & (M-m)^2 < p^2 < (m+M)^2 \\ \ln\frac{\sqrt{p^2-(M-m)^2}-\sqrt{p^2-(M+m)^2}}{\sqrt{p^2-(M-m)^2}+\sqrt{p^2-(M+m)^2}} + i\pi & p^2 > (m+M)^2 \end{cases}$$

and

$$\kappa(x,y,z) = x^2+y^2+z^2-2xy-2xz-2yz \tag{F.18}$$

is the Källen function. The parameters β and x were defined in (E.12) and $\bar{\beta}$ in (E.16).

G Details intermediate resolution soft functions

In this Appendix we present details for the calculation of the intermediate resolution soft functions at one-loop, for both wino and Higgsino DM. The structure follows Appendix C of [7] and the results were independently calculated by Alessandro Broggio, CH and Kai Urban. First, we give the relevant virtual and real scalar integrals that arise during the computation of the soft functions. Then, we illustrate how the structure of the rapidity divergences changes when going from the intermediate to the narrow resolution regime. Lastly, we collect the explicit expressions for the soft functions for all relevant index combinations which were omitted in the main text.

The general definition for integrated the intermediate resolution soft function was given in (3.19). It turns out to be helpful to shift the position of the Wilson line to 0 and to execute the n_+y-integration when calculating the integrals and the soft coefficients. This results in

$$W^{ij}_{IJ,VWXY}(\omega) \;=\; \sum\!\!\!\!\!\!\int_{X_s} \delta\left(\omega - n_- p_{X_s}\right) \langle 0|\, \bar{\mathbf{T}}[[\mathcal{S}^\dagger]^j_{J,XY}(y_-)]\, \mathbf{T}[\mathcal{S}^i_{I,VW}(0)]\, |0\rangle\,. \tag{G.1}$$

A diagrammatic representation of the one-loop soft function is depicted in Figure G.1. The contributing diagrams are found by connecting two distinct (red) dots on the external legs with a single soft gauge boson. Due to the abelian nature of the $\mathrm{U}(1)_Y$ gauge boson, it cannot connect to the np or n_- external legs. This constrains the type of diagrams that are relevant for the different Higgsino DM operators. The integrals we discuss now are named according to which external legs the emitted soft gauge boson attaches to. For example, if the soft gauge boson connects a heavy DM (v) and an anti-collinear (n_+) external leg, we name it the vn_+ *virtual* ($I^{\text{virt.}}_{vn_+}$) or *real* ($I^{\text{real}}_{vn_+}$) *integral*, depending on whether the soft gauge boson passes through the cut or not.

G.1 Virtual soft integrals

Virtual integrals arise from diagrams, where a soft gauge boson connects any two distinct red dots in Figure G.1, but does not traverse the cut. The integration measure is the same as for the collinear integrals in Appendix E and is given by

$$[dk] = \tilde{\mu}^{2\epsilon} \frac{d^d k}{(2\pi)^d} = \left(\frac{\mu^2 e^{\gamma_E}}{4\pi}\right)^{\epsilon} \frac{d^d k}{(2\pi)^d}\,. \tag{G.2}$$

Remember that $d = 4 - 2\epsilon$ and γ_E is the Euler-Mascheroni constant. For some integrals it will turn out to be useful to split the integration into the components k^0, k^3 and $k_\perp$ as follows

$$d^d k = \frac{1}{2} dk^0 dk^3 d^{d-2} k_\perp\,. \tag{G.3}$$

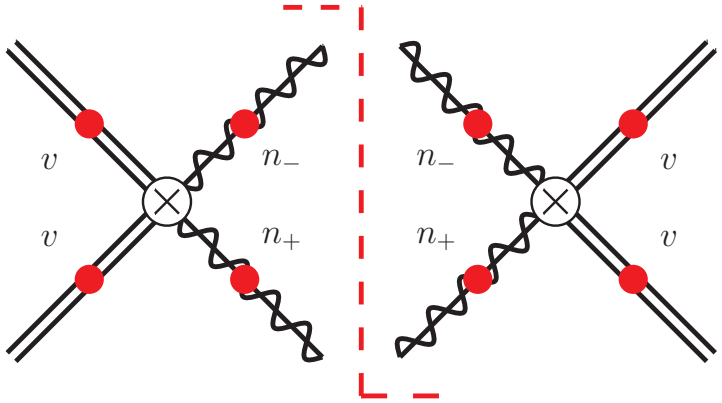

Figure G.1: Diagrammatic representation of the one-loop soft function. This Figure was extracted from [7].

The n_+n_- virtual integral

We define the virtual integral where the soft gauge boson connects the collinear and anti-collinear external lines on the same side of the cut as

$$I^{\text{virt.}}_{n_+n_-} = -i\hat{g}_2^2\delta(\omega)(n_+\cdot n_-)\int[dk]\frac{\nu^\eta}{[k^2-m_W^2+i0][n_-k+i0][n_+k-i0]|2k^3|^\eta}\,. \tag{G.4}$$

The integral (G.4) is most easily solved by first using the method of contour integration to perform the k^0-integral, which means that we first rewrite $I^{\text{virt.}}_{n_+n_-}$ in terms of k^0, k^3 and $k_\perp$

$$\begin{aligned} I^{\text{virt.}}_{n_+n_-} = -2i\hat{g}_2^2\delta(\omega)\tilde{\mu}^{2\epsilon}\int\frac{dk^0dk^3d^{d-2}k_\perp}{(2\pi)^d}\frac{\nu^\eta}{|2k^3|^\eta} \\ \times\frac{1}{[(k^0)^2-E_k^2+i0][k^0-k^3+i0][k^0+k^3-i0]}\,, \end{aligned} \tag{G.5}$$

where $E_k^2=(k^3)^2+k_T^2+m_W^2$ and $k_T^2=-k_\perp^2>0$. In order to perform the k^0-integration, we have to locate the poles in the propagators. These take different positions depending on whether k^3 is positive or negative. If $k^3>0$, we find that there are four poles in the k^0 complex plane located at $\pm(E_k-i0)$, k^3-i0 and $-k^3+i0$. We choose to close the integration contour in the lower half plane, with which we pick up a factor of $-2\pi i$ along with the residues associated to the poles $-(E_k-i0)$ and $-k^2+i0$. If on the other hand k^3 is negative $k^3<0$ there are again four poles, two on either side of the real k^3-axis. However the poles k^3-i0 and $-k^3+i0$ moved from the positive to the negative k^0 domain and vice versa, respectively, compared with the case where $k^3>0$. After closing the contour and picking up the corresponding residues, we arrive at

$$\begin{aligned} I^{\text{virt.}}_{n_+n_-} = 2i\hat{g}_2^2\delta(\omega)\tilde{\mu}^{2\epsilon}\int\frac{d^{d-2}k_\perp}{(2\pi)^d}\Bigg\{\int_0^\infty dk^3\frac{\nu^\eta}{(2k^3)^\eta}\frac{2\pi i}{k_T^2+m_W^2}\left[\frac{1}{2E_k}-\frac{1}{2k^3-i0}\right] \\ +\int_{-\infty}^0 dk^3\frac{\nu^\eta}{(-2k^3)^\eta}\frac{2\pi i}{k_T^2+m_W^2}\left[\frac{1}{2E_k}-\frac{1}{2k^3-i0}\right]\Bigg\}\,. \end{aligned} \tag{G.6}$$

We can simplify (G.6) by noting that the two E_k-terms in the square brackets are in fact the same. This can be shown straightforwardly by making the substitution $k^3\to-k^3$

in the second line of (G.6). The k^3 and $k_\perp$ integrations for the E_k-terms can then be executed using the standard procedure, which results in

$$-\frac{\hat{g}_2^2}{4\pi^2}\delta(\omega)\left(\frac{\mu}{m_W}\right)^{2\epsilon} e^{\gamma_E\epsilon}\left(\frac{\nu}{m_W}\right)^{\eta}\frac{\Gamma\left(\frac{1}{2}-\frac{\eta}{2}\right)\Gamma\left(\epsilon+\frac{\eta}{2}\right)}{2^\eta\,\pi^{\frac{1}{2}}\,\eta}\,. \tag{G.7}$$

We are now left with the integration of the terms associated with $1/(2k^3-i0)$. The integral over k^3 can be done as follows

$$\begin{aligned}\int dk^3\frac{(-2\pi i)\nu^\eta}{[2k^3-i0]|2k^3|^\eta} =& \int_0^\infty dk^3\frac{(-2\pi i)\nu^\eta}{(2k^3)^\eta}\left[\frac{1}{2k^3-i0}+\frac{1}{-2k^3-i0}\right]\\ =&(-i\pi)\nu^\eta\pi\csc(\pi\eta)\left((-i0)^{-\eta}-(i0)^{-\eta}\right)\\ =&(2\pi^2)\nu^\eta\csc(\pi\eta)\,0^{-\eta}\sin(\eta\,\pi/2)\\ =&\pi^2+\mathcal{O}(\eta)\,.\end{aligned} \tag{G.8}$$

We note that at order $\mathcal{O}(\eta^0)$, the result is independent of the small imaginary part $i0$. Finally, after executing the $k_\perp$ integration and summing over the two contributions (from the upper and lower line of (G.6)) we arrive at the final result for $I^{\text{virt.}}_{n_+n_-}$

$$\begin{aligned}I^{\text{virt.}}_{n_+n_-} =& -\frac{\hat{g}_2^2\delta(\omega)}{4\pi^2}\left(\frac{\mu}{m_W}\right)^{2\epsilon}\left(\frac{\nu}{m_W}\right)^{\eta}e^{\gamma_E\epsilon}\left[\frac{\Gamma\left(\frac{1}{2}-\frac{\eta}{2}\right)\Gamma\left(\epsilon+\frac{\eta}{2}\right)}{2^\eta\,\pi^{\frac{1}{2}}\,\eta}-\frac{\Gamma\left(\epsilon+\frac{\eta}{2}\right)}{\Gamma\left(1+\frac{\eta}{2}\right)}\left(\frac{i\,\pi}{2}+\mathcal{O}(\eta)\right)\right]\\ =&-\frac{\hat{\alpha}_2}{2\pi}\delta(\omega)\left[-\frac{1}{\epsilon^2}+\frac{2}{\epsilon\eta}-\frac{i\pi}{\epsilon}+\frac{2}{\epsilon}\ln\frac{m_W}{\mu}-\frac{2}{\epsilon}\ln\frac{m_W}{\nu}-\frac{4}{\eta}\ln\frac{m_W}{\mu}\right.\\ &\left.+\frac{\pi^2}{12}+2\pi i\ln\frac{m_W}{\mu}-2\ln^2\frac{m_W}{\mu}+4\ln\frac{m_W}{\mu}\ln\frac{m_W}{\nu}\right].\end{aligned} \tag{G.9}$$

The vn_+ and vn_- virtual integrals

Next, we compute the integral which arises from diagrams where either one of the external lines of the DM particles in Figure G.1 is connected to a collinear or anti-collinear external line via a soft gauge boson, which again does not traverse the cut. Since the virtual part of the soft function is symmetric under the exchange $n_+ \leftrightarrow n_-$, the integrals for the Wilson line combinations vn_+ and vn_- give the same result. Explicitly, the vn_+-integral is given by

$$I^{\text{virt.}}_{vn_+} = -i\hat{g}_2^2\delta(\omega)(v\cdot n_+)\int[dk]\frac{\nu^\eta}{[k^2-m_W^2+i0][n_+k-i0][v\cdot k-i0]|2k^3|^\eta}\,. \tag{G.10}$$

We apply the same strategy that was used to compute $I^{\text{virt.}}_{n_+n_-}$ in the previous paragraph. As before we can see that the integral has four poles in the k^0 complex plane. However $I^{\text{virt.}}_{vn_+}$ turns out to be simpler than $I^{\text{virt.}}_{n_+n_-}$, since for $I^{\text{virt.}}_{vn_+}$ three of the poles are in the upper half plane and only one, $(E_k - i0)$, is in the lower half plane. This is true independently of whether $k^3 > 0$ or $k^3 < 0$. Thus closing the integration contour in the lower half plane we only pick up the residue from a single pole. After summing over contributions from $k^3 > 0$ and $k^3 < 0$ and after integrating over $k_\perp$, we obtain

$$\begin{aligned}I^{\text{virt}}_{vn_+} =& -\frac{\hat{g}_2^2}{8\pi^2}\delta(\omega)\left(\frac{\mu}{m_W}\right)^{2\epsilon}\left(\frac{\nu}{m_W}\right)^{\eta}e^{\gamma_E\epsilon}\frac{\Gamma\left(\frac{1}{2}-\frac{\eta}{2}\right)\Gamma\left(\epsilon+\frac{\eta}{2}\right)}{2^\eta\,\pi^{\frac{1}{2}}\,\eta}\\ =&-\frac{\hat{\alpha}_2}{4\pi}\delta(\omega)\left[-\frac{1}{\epsilon^2}+\frac{2}{\epsilon\eta}+\frac{2}{\epsilon}\ln\frac{m_W}{\mu}-\frac{2}{\epsilon}\ln\frac{m_W}{\nu}-\frac{4}{\eta}\ln\frac{m_W}{\mu}\right.\end{aligned}$$

$$+\frac{\pi^2}{12}+4\ln\frac{m_W}{\mu}\ln\frac{m_W}{\nu}-2\ln^2\frac{m_W}{\mu}\Bigg]\,. \tag{G.11}$$

The integral $I^{\text{virt.}}_{vn_-}$ can be obtained from $I^{\text{virt.}}_{vn_+}$ by making the substitution $n_+ \to n_-$ in (G.10). We do not discuss $I^{\text{virt.}}_{vn_-}$ explicitly since, as discussed at the beginning of the paragraph, it can be checked that $I^{\text{virt.}}_{vn_-} = I^{\text{virt.}}_{vn_+}$.

The vv virtual integral

The last virtual integral that needs to be evaluated comes from the diagram where two heavy DM external lines on the same side of the cut are connected via a soft gauge boson in Figure G.1. The starting expression is given by

$$I^{\text{virt.}}_{vv} = -i\hat{g}_2^2\delta(\omega)(v\cdot v)\int[dk]\frac{1}{[k^2-m_W^2+i0][k^0+i0][k^0-i0]}\,. \tag{G.12}$$

We again integrate first over k^0. The poles are located at $\pm(E_k - i0)$ and $\pm i0$. Naively, one would also pick up the pinched poles at $k^0 = \pm i0$, which would be wrong however since these correspond to the potential region and are consequently already included in the one-loop contribution to the Sommerfeld factor. The remainder of the integral can be done without effort and we find that the final result is independent of rapidity divergences

$$I^{\text{virt.}}_{vv} = -\frac{\hat{\alpha}_2}{2\pi}\delta(\omega)\left[\frac{1}{\epsilon}+\ln\frac{\mu^2}{m_W^2}\right]\,. \tag{G.13}$$

This concludes our discussion of the virtual soft function integrals. Please note that the results for $I^{\text{virt.}}_{vn_+}$, $I^{\text{virt.}}_{vn_-}$ and $I^{\text{virt.}}_{n_+n_-}$ were already calculated in [69]. While we find agreement for $I^{\text{virt.}}_{vn_+}$ and $I^{\text{virt.}}_{vn_-}$, the result for $I^{\text{virt.}}_{n_+n_-}$ in our case has an additional term associated with the imaginary parts of (G.9).

G.2 Real soft integrals

The real soft integrals at one-loop arise from diagrams where the soft gauge boson, which connects two distinct red dots in Figure G.1, crosses the cut exactly once. The real integrals can be extracted from the virtual ones discussed in Appendix G.1, by applying the Cutkosky cut rules to the propagators associated with the soft gauge boson

$$\frac{1}{k^2-m_W^2+i\varepsilon} \to -2\pi i\,\delta(k^2-m_W^2)\,\theta(k^0)\,. \tag{G.14}$$

In order to evaluate the real emission integrals, it turns out to be convenient to express the phase-space measure in terms of light-cone coordinates

$$\begin{aligned}\int d^dk\,\theta(k^0)\delta(k^2-m_W^2) &= \frac{1}{2}\int_0^\infty dn_+k\int_0^\infty dn_-k\int d^{d-2}k_\perp\delta(n_+k\,n_-k+k_\perp^2-m_W^2)\\ &= \frac{\Omega_{d-2}}{2}\int_0^\infty dn_+k\int_0^\infty dn_-k\int_0^\infty dk_T\,k_T^{d-3}\delta(n_+k\,n_-k-k_T^2-m_W^2)\,,\end{aligned} \tag{G.15}$$

where the delta- and theta-functions enforce n_+k, $n_-k \geq 0$. Note that the limit $\omega \to 0$ is still regulated using the rapidity regulator, which for the real integrals introduces star-distributions [106] that have been defined in (6.76).

The n_+n_- real integral

The n_+n_- real emission contribution originates from diagrams where the soft gauge boson connects a collinear and an anti-collinear external line and passes the cut. Applying the rule (G.14) to (G.4), we find the expression for the real emission n_+n_- integral to be

$$I^{\text{real}}_{n_+n_-} = (n_+ \cdot n_-)\, \hat{g}_2^2 \int [dk] \frac{\left(-2\pi\delta\left(k^2 - m_W^2\right)\theta(k^0)\right)}{(n_+k)(n_-k)} \delta(\omega - n_-k) \frac{\nu^\eta}{|2k^3|^\eta}\,. \tag{G.16}$$

Using the delta function $\delta(\omega - n_-k)$ we can easily integrate over n_-k, which results in

$$I^{\text{real}}_{n_+n_-} = -\frac{\hat{\alpha}_2 e^{\gamma_E \epsilon}}{2\pi^{2-\epsilon}}\, \mu^{2\epsilon} \nu^\eta \int dn_+k d^{d-2}k_T \frac{\delta(\omega n_+k - k_T^2 - m_W^2)\theta(\omega + n_+k)}{\omega n_+k\, |n_+k - \omega|^\eta}\,. \tag{G.17}$$

Next, we integrate over n_+k. The step function $\theta(\omega + n_+k)$ ensures that $n_+k > -\omega$, but $\omega \geq 0$. Furthermore $k_T^2 + m_W^2 > 0$ such that the delta function is only relevant for positive n_+k. We conclude that the step function does not impose any more restrictions and can thus be discarded. After the n_+k integration, we obtain

$$I^{\text{real}}_{n_+n_-} = -\frac{\hat{\alpha}_2 e^{\gamma_E \epsilon}}{\pi\Gamma(1-\epsilon)}\, \mu^{2\epsilon} \omega^{\eta-1} \nu^\eta \int_0^\infty dk_T\, \frac{k_T^{1-2\epsilon}}{k_T^2 + m_W^2} \frac{1}{\left|k_T^2 + m_W^2 - \omega^2\right|^\eta}\,, \tag{G.18}$$

where a factor of ω^η was included into the absolute value, which can easily be done since $\omega \geq 0$. To properly treat the absolute value, we have to consider distinct cases depending on how ω scales with respect to m_W and k. If $\omega < m_W$ we can drop the absolute value since $k_T, m_W > 0$ and so $k_T^2 + m_W^2 - \omega^2 > 0$. However, if $\omega > m_W$, then we need to further distinguish the cases where $k_T^2 < m_W - \omega$ and $k_T^2 > m_W - \omega$. In the former case we trade the absolute value for an overall factor of $(-1)^\eta$ and integrate k_T from 0 to $\sqrt{\omega^2 - m_W^2}$, in the latter case the absolute value can simply be dropped and the k_T integration goes from $\sqrt{\omega^2 - m_W^2}$ to ∞. Before evaluating the integral, we first simplify the expression by introducing the substitution $k'_T = k_T/m_W$ and defining $\omega' = \omega/m_W$, which results in

$$I^{\text{real}}_{n_+n_-} = -\frac{\hat{\alpha}_2}{\pi} \left(\frac{\mu^2 e^{\gamma_E}}{m_W^2}\right)^\epsilon \left(\frac{\nu\omega}{m_W^2}\right)^\eta \frac{1}{\omega\Gamma(1-\epsilon)} \int_0^\infty dk'_T \frac{k_T'^{1-2\epsilon}}{\left(k_T'^2 + 1\right)\left|k_T'^2 + 1 - \omega'^2\right|^\eta}\,, \tag{G.19}$$

where the integration is now over dimensionless quantities.

Starting with the case $\omega' < 1$, we find that (written in terms of dimensionless quantities ω' and k'_T) $k_T'^2 + 1 - \omega'^2 > 0$ such that we can omit the absolute value without further alterations. Performing the integration results in

$$\begin{aligned} I^{\text{real}}_{n_+n_-} = -\frac{\hat{\alpha}_2}{2\pi} \left(\frac{\mu^2 e^{\gamma_E}}{m_W^2}\right)^\epsilon \left(\frac{\nu\omega}{m_W^2}\right)^\eta \frac{1}{\omega\Gamma(1-\epsilon)} \Bigg\{ &\left(\omega'\right)^{-2\eta} \Gamma(\epsilon+\eta)\Gamma(1-\epsilon-\eta) \\ &+ \left(1-\omega'^2\right)^{1-\epsilon-\eta} \frac{\Gamma(1-\epsilon)\Gamma(\epsilon+\eta-1)}{\Gamma(\eta)}\, {}_2F_1\left(1, 1-\epsilon, 2-\epsilon-\eta, 1-\omega'^2\right) \Bigg\} \end{aligned} \tag{G.20}$$

with ${}_2F_1$ being the hypergeometric function. The result for $I^{\text{real}}_{n_+n_-}$ as it is written in (G.20) is valid to all orders in η and ϵ. We find that for the dimensionless terms inside the curly brackets, we can safely take the limits $\omega, \eta \to 0$ which means that these terms do not give rise to rapidity divergences and are not of distributional type. For the prefactor on the

other hand, it is not safe to take this limit and we need to make use of the expansion that was defined in (6.101)

$$\frac{1}{\omega}\left(\frac{\omega}{m_W}\right)^{\eta} = \frac{\delta(\omega)}{\eta} + \left[\frac{1}{\omega}\right]_*^{[m_W]} + \mathcal{O}(\eta)\,. \tag{G.21}$$

After expanding the prefactor in (G.20) according to (G.21), we expand the term in the curly brackets. The $1/\eta$-factor associated with the delta function in (G.21) forces us to expand the expressions in the curly brackets up to η^1 such that in the end we obtain a η^0-term. At the same time, the delta function allows us to set $\omega' \to 0$ with which we can simplify the hypergeometric ${}_2F_1$ function. If the terms in the curly brackets are multiplied with the star-distribution from (G.21) however, we only need to expand them up to η^0. We find that the η^0-term from the curly brackets is ω-independent. Therefore, the integral $I^{\text{real}}_{n_+n_-}$ up to order $\mathcal{O}(\eta,\epsilon)$ is given by

$$\begin{aligned} I^{\text{real}}_{n_+n_-} &= -\frac{\hat{\alpha}_2}{2\pi}\left(\frac{\mu^2 e^{\gamma_E}}{m_W^2}\right)^{\epsilon}\left(\frac{\nu\,\omega}{m_W^2}\right)^{\eta}\frac{\Gamma(\epsilon+\eta)}{\omega\Gamma(1+\eta)} + \mathcal{O}(\eta,\epsilon) \\ &= -\frac{\hat{\alpha}_2}{2\pi}\left[\delta(\omega)\left(-\frac{1}{\epsilon^2}+\frac{1}{\epsilon\,\eta}+\frac{1}{\eta}\ln\frac{\mu^2}{m_W^2}+\frac{1}{\epsilon}\left(-\ln\frac{\mu^2}{m_W^2}+\ln\frac{\nu}{m_W}\right)\right.\right. \\ &\quad \left.\left.+\frac{\pi^2}{12}-\frac{1}{2}\ln^2\frac{\mu^2}{m_W^2}+\frac{1}{2}\ln\frac{\mu^2}{m_W^2}\ln\frac{\nu^2}{m_W^2}\right)-\left[\frac{1}{\omega}\right]_*^{[m_W]}\left(\frac{1}{\epsilon}+\ln\frac{\mu^2}{m_W^2}\right)\right]. \end{aligned} \tag{G.22}$$

The result in (G.22) was computed assuming the scaling $\omega' < 1$. Next, we consider the case where $\omega' > 1$. We find that (G.22) also holds for this second scaling. To see this, we split the integration over k'_T according to the argument presented prior to (G.19)

$$\begin{aligned} \int_0^\infty dk'_T \frac{k_T'^{1-2\epsilon}}{\left(k_T'^2+1\right)\left|k_T'^2+1-\omega'^2\right|^{\eta}} &= \int_0^{\sqrt{\omega'^2-1}} dk'_T \frac{k_T'^{1-2\epsilon}}{\left(k_T'^2+1\right)\left(k_T'^2+1-\omega'^2\right)^{\eta}} \\ &\quad + \int_{\sqrt{\omega'^2-1}}^\infty dk'_T \frac{k_T'^{1-2\epsilon}}{\left(k_T'^2+1\right)\left(-k_T'^2-1+\omega'^2\right)^{\eta}}\,. \end{aligned} \tag{G.23}$$

The individual terms yield

$$\begin{aligned} &\int_0^{\sqrt{\omega'^2-1}} dk'_T \frac{k_T'^{1-2\epsilon}}{\left(k_T'^2+1\right)\left(k_T'^2+1-\omega'^2\right)^{\eta}} \\ &\quad = \frac{\left(\omega'^2-1\right)^{1-\epsilon-\eta}}{2}\frac{\Gamma(1-\epsilon)\Gamma(1-\eta)}{\Gamma(2-\epsilon-\eta)}\,{}_2F_1(1,1-\epsilon,2-\epsilon-\eta,1-\omega'^2)\,, \\ &\int_{\sqrt{\omega'^2-1}}^\infty dk'_T \frac{k_T'^{1-2\epsilon}}{\left(k_T'^2+1\right)\left(-k_T'^2-1+\omega'^2\right)^{\eta}} \\ &\quad = \frac{\left(\omega'^2-1\right)^{-\epsilon}\left(1-\omega'^2\right)^{-\eta}}{2}\frac{\Gamma(1-\eta)\Gamma(\epsilon+\eta)}{\Gamma(1+\epsilon)}\,{}_2F_1\left(1,\epsilon+\eta,1+\epsilon,\frac{1}{1-\omega'^2}\right) \end{aligned} \tag{G.24}$$

The rest of the discussion is analogous to the case $\omega' < 1$ and to order $\mathcal{O}(\eta,\epsilon)$ we find the same result as in that case (G.22). This is an important finding since it considerably simplifies the convolution of the soft function with the collinear unobserved jet function.

The vn_+ real integral

This integral appears when computing diagrams where the soft gauge boson connects one

heavy DM external line with an n_+-external line and passes through the cut in Figure G.1. It is given by

$$I^{\text{real}}_{vn_+} = (v\cdot n_+)\hat{g}_2^2 \int [dk] \frac{\left(-2\pi\delta(k^2-m_W^2)\theta(k^0)\right)}{(v\cdot k)(n_+k)} \delta(\omega - n_-k) \frac{\nu^\eta}{|2k^3|^\eta}\,. \tag{G.25}$$

As was done in the previous paragraph for $I^{\text{real}}_{n_+n_-}$, we can evaluate the integrals over n_+k and n_-k by making use of the delta functions, which results in

$$I^{\text{real}}_{vn_+} = -\frac{\hat{\alpha}_2}{\pi}\frac{\mu^{2\epsilon}e^{\epsilon\gamma_E}}{\Gamma(1-\epsilon)}\nu^\eta\omega^{\eta+1}\int_0^\infty dk_T \frac{k_T^{1-2\epsilon}}{k_T^2+m_W^2}\frac{1}{\omega^2+k_T^2+m_W^2}\frac{1}{\left|\omega^2-k_T^2-m_W^2\right|^\eta}\,. \tag{G.26}$$

We remark the fact that the prefactor in (G.26) is now given by $\omega^{\eta+1}$. This considerably simplifies the computation of $I^{\text{real}}_{vn_+}$ compared with the computation of $I^{\text{real}}_{n_+n_-}$. This is because $\omega^{\eta+1}$ is finite in the limit $\eta,\omega\to 0$. Hence, we can set $\eta\to 0$ now which turns (G.26) into a standard integral that can be solved straightforwardly. In the end, we find

$$\begin{aligned} I^{\text{real}}_{vn_+} &= -\frac{\hat{\alpha}_2 e^{\epsilon\gamma_E}}{2\pi\omega}\mu^{2\epsilon}\Gamma(\epsilon)\left(m_W^{-2\epsilon}-(m_W^2+\omega^2)^{-\epsilon}\right)+\mathcal{O}(\eta) \\ &= -\frac{\hat{\alpha}_2}{2\pi}\frac{1}{\omega}\ln\left(\frac{m_W^2+\omega^2}{m_W^2}\right)+\mathcal{O}(\eta,\epsilon)\,, \end{aligned} \tag{G.27}$$

which is free of both rapidity and virtuality divergences.

The vn_- real integral

This integral appears when computing diagrams where the soft gauge boson connects one heavy DM external line with an n_--external line and passes through the cut in Figure G.1. It is given by

$$I^{\text{real}}_{vn_-} = (v\cdot n_-)\hat{g}_2^2 \int [dk] \frac{\left(-2\pi\delta(k^2-m_W^2)\theta(k^0)\right)}{(v\cdot k)(n_-k)} \delta(\omega - n_-k) \frac{\nu^\eta}{|2k^3|^\eta}\,. \tag{G.28}$$

The integral $I^{\text{real}}_{vn_-}$ in (G.28) is most easily computed by making use of the results for $I^{\text{real}}_{n_+n_-}$ and $I^{\text{real}}_{vn_+}$ in (G.22) and (G.27), respectively, as well as the relation

$$\frac{(n_+\cdot n_-)}{(n_+k)(n_-k)} - \frac{(v\cdot n_+)}{(v\cdot k)(n_+k)} = \frac{(v\cdot n_-)}{(n_-k)(v\cdot k)}\,, \tag{G.29}$$

which allows us to establish the following connection between $I^{\text{real}}_{n_+n_-}$, $I^{\text{real}}_{vn_+}$ and $I^{\text{real}}_{vn_-}$

$$I^{\text{real}}_{vn_-} = I^{\text{real}}_{n_+n_-} - I^{\text{real}}_{vn_+}\,. \tag{G.30}$$

The vv real integral

The last real integral that is relevant for the computation of the intermediate resolution soft functions comes from diagrams where two heavy DM external lines on different sides of the cut are connected via a soft gauge boson in Figure G.1. We apply (G.14) to (G.12) to find the starting expression

$$I^{\text{real}}_{vv} = (v\cdot v)\,\hat{g}_2^2 \int [dk] \frac{1}{(v\cdot k)^2}(-2\pi\delta(k^2-m_W^2)\theta(k^0))\delta(\omega-n_-k)\frac{\nu^\eta}{|2k^3|^\eta} \tag{G.31}$$

To solve (G.31) we apply the same steps as for $I^{\text{real}}_{vn_+}$ and first solve the n_+k and n_-k integrations with the help of the delta functions. We obtain

$$I^{\text{real}}_{vv} = -\frac{2\hat{\alpha}_2}{\pi}\frac{\mu^{2\epsilon}e^{\epsilon\gamma_E}\nu^\eta}{\Gamma(1-\epsilon)}\omega^{\eta+1}\int_0^\infty dk_T \frac{k_T^{1-2\epsilon}}{\left(\omega^2+k_T^2+m_W^2\right)^2}\frac{1}{\left|\omega^2-k_T^2-m_W^2\right|^\eta}\,. \tag{G.32}$$

Again, we can set $\eta \to 0$ and find the following expression for the final results for I^{real}_{vv}

$$\begin{aligned} I^{\text{real}}_{vv} &= -\frac{2\hat{\alpha}_2}{\pi}\frac{\mu^{2\epsilon}e^{\epsilon\gamma_E}}{\Gamma(1-\epsilon)}\,\omega\int_0^\infty dk_T \frac{k_T^{1-2\epsilon}}{\left(\omega^2+k_T^2+m_W^2\right)^2} + \mathcal{O}(\eta) \\ &= -\frac{\hat{\alpha}_2}{\pi}\epsilon\,\Gamma(\epsilon)\mu^{2\epsilon}e^{\epsilon\gamma_E}\omega\left(\frac{1}{m_W^2+\omega^2}\right)^{1+\epsilon} + \mathcal{O}(\eta) \\ &= -\frac{\hat{\alpha}_2}{\pi}\frac{\omega}{m_W^2+\omega^2} + \mathcal{O}(\eta,\epsilon)\,. \end{aligned} \tag{G.33}$$

Please note that the real integrals $I^{\text{real}}_{n_+n_-}$, $I^{\text{real}}_{vn_+}$ and $I^{\text{real}}_{vn_-}$ were previously computed in [69] and we find full agreement with the results presented there.

G.3 Cut two loop diagrams Wino DM

Having computed in Appendices G.1 and G.2 respectively the virtual and real integrals relevant for the calculation of the soft functions, we can now use them to determine the total discontinuity of a given two-loop diagram, after summing over all cuts. Together with the discussion presented towards the end of Appendix E, about the rapidity divergences in the soft expansion of the collinear integral I_{c-s}, this will allow us to demonstrate how the structure of the rapidity divergences changes in the soft and unobserved jet functions, when moving from the narrow to the intermediate resolution regime or vice versa. The total discontinuity is given by

$$\sum_{\text{cuts}} = \text{Disc}(i\mathcal{M}) = -2\,\text{Im}\,\mathcal{M}\,, \tag{G.34}$$

where $\mathcal{M}$ is representative for one type of matrix element. An example for the sum of all possible cuts for one type of diagram is given in Figure G.2, where we show the four possible ways to cut the n_+n_--diagram. Similar procedures are applied to the other diagram types. Note that for this discussion, it suffices to consider the results for the virtual and real integrals while neglecting the Dirac structures that usually accompany a Feynman diagram. Not taking into account Dirac structures will not affect the structure of the rapidity divergences.

The sum over all cuts for n_+n_--diagrams is given by

$$\begin{aligned} \text{Disc}(i\mathcal{M}_{n_+n_-}) &= 2\,\text{Re}\left(I^{\text{real}}_{n_+n_-} - I^{\text{virt.}}_{n_+n_-}\right) \\ &= \frac{\hat{\alpha}_2}{\pi}\left[\delta(\omega)\left(\frac{1}{\epsilon\eta} - \frac{2}{\eta}\ln\frac{m_W}{\mu} - \frac{1}{\epsilon}\ln\frac{m_W}{\nu} + 2\ln\frac{m_W}{\mu}\ln\frac{m_W}{\nu}\right)\right. \\ &\qquad \left. + \left[\frac{1}{\omega}\right]_*^{[m_W]}\left(-\frac{1}{\epsilon} + 2\ln\frac{m_W}{\mu}\right)\right]\,, \end{aligned} \tag{G.35}$$

where the relative minus sign between $I^{\text{real}}_{n_+n_-}$ and $I^{\text{virt.}}_{n_+n_-}$ is owed to the way the scalar integrals were defined in Appendices G.1 and G.2. For the same reason, a relative minus

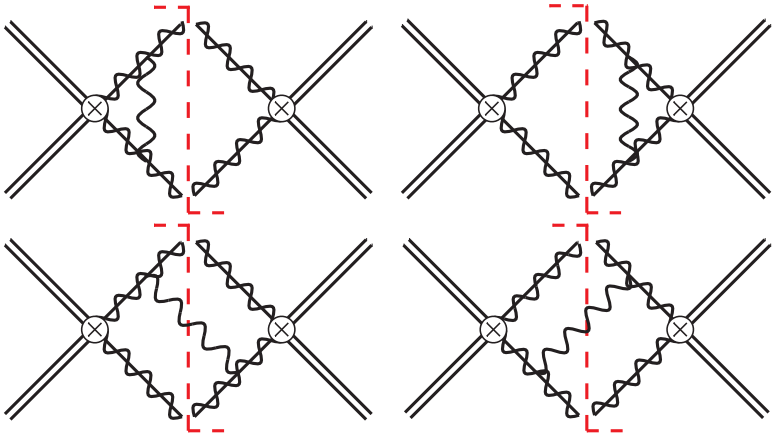

Figure G.2: The four possible cuts through the n_+n_--two-loop diagram. This Figure was extracted from [7].

sign appears for vn_--diagrams which are discussed below. By looking at the individual expressions for $I^{\text{real}}_{n_+n_-}$ and $I^{\text{virt.}}_{n_+n_-}$ given in (G.22) and (G.9), respectively, we can see that including real emissions into the soft function cancels half of the rapidity divergences of the virtual contributions.

For vn_--diagrams we content ourselves with considering one specific example. For this type of amplitude different diagrams differ by overall signs and/or prefactors, such that considering one explicit implementation suffices to make a general statement about vn_--diagrams

$$\begin{aligned}\text{Disc}(i\mathcal{M}_{vn_-}) &= I^{\text{virt.}}_{vn_-} - I^{\text{real}}_{vn_-} \\ &= \frac{\hat{\alpha}_2}{4\pi}\left[\delta(\omega)\left(-\frac{1}{\epsilon^2}+\frac{2}{\epsilon}\ln\frac{m_W}{\mu}+\frac{\pi^2}{12}-2\ln^2\frac{m_W}{\mu}\right)\right. \\ &\qquad \left.+\left[\frac{1}{\omega}\right]_*^{[m_W]}\left(\frac{2}{\epsilon}-2\ln\left(\frac{m_W^2+\omega^2}{m_W^2}\right)-2\ln\frac{m_W^2}{\mu^2}\right)\right]. \end{aligned} \tag{G.36}$$

While both real and virtual vn_--diagrams suffer from rapidity divergences, we can see that the inclusion of real emissions cancels those. For vn_+-diagrams, where we also only consider one possible implementation, we find

$$\begin{aligned}\text{Disc}(i\mathcal{M}_{vn_+}) &= I^{\text{virt.}}_{vn_+} + I^{\text{real}}_{vn_+} \\ &= -\frac{\hat{\alpha}_2}{4\pi}\left[\delta(\omega)\left(-\frac{1}{\epsilon^2}+\frac{2}{\epsilon\eta}-\frac{4}{\eta}\ln\frac{m_W}{\mu}+\frac{2}{\epsilon}\ln\frac{m_W}{\mu}-\frac{2}{\epsilon}\ln\frac{m_W}{\nu}\right.\right. \\ &\qquad \left.\left.+\frac{\pi^2}{12}-2\ln^2\frac{m_W}{\mu}+4\ln\frac{m_W}{\mu}\ln\frac{m_W}{\nu}\right)\right. \\ &\qquad \left.+\left[\frac{1}{\omega}\right]_*^{[m_W]}2\ln\left(\frac{m_W^2+\omega^2}{m_W^2}\right)\right]. \end{aligned} \tag{G.37}$$

From (G.27) we can see that $I^{\text{real}}_{vn_+}$ is in fact finite which means that the divergent structure of $I^{\text{virt.}}_{vn_+}$ does not change.

Summarizing the above analysis, we find that including real emissions into the soft function when increasing the energy resolution leads to the following relation concerning

the rapidity divergences

$$\sum_{\text{virt.}} |_{\eta-\text{div.}} + \sum_{\text{real}} |_{\eta-\text{div.}} = \frac{1}{2} \sum_{\text{virt.}} |_{\eta-\text{div.}} \,, \tag{G.38}$$

which means that roughly speaking the intermediate resolution soft function only has half of the η-divergences compared to the narrow resolution soft function. This was somewhat to be expected. If $E^{\gamma}_{\text{res}} \sim m_W^2/m_\chi$, the rapidity divergences of the soft function needs to cancel both the rapidity divergences of the photon jet function *and* of the unobserved jet function. When increasing the resolution to $E^{\gamma}_{\text{res}} \sim m_W$ however, we saw that the now hard-collinear unobserved jet function is free of η-divergences, while the photon jet function remains unchanged. This essentially means that in the intermediate resolution case we only require half of the η-divergences in the soft function compared to the narrow resolution case which, as we have seen, is exactly what happens when we include real emissions. It is easy to confirm that the above discussion applies equally for wino and Higgsino DM.

G.4 Soft functions in momentum space

In this Appendix we collect the expressions for the intermediate resolution soft functions for both wino and Higgsino DM, which have been omitted in the main text for reasons of brevity.

G.4.1 Wino DM

For the operator combination $ij = 11$ we find

$$\begin{aligned} W^{11}_{(00)(00)}(\omega,\mu,\nu) &= W^{11}_{(00)(+-)}(\omega,\mu,\nu) = W^{11}_{(+-)(00)}(\omega,\mu,\nu) = W^{11}_{(+-)(+-)}(\omega,\mu,\nu) \\ &= \delta(\omega) + \frac{\hat{\alpha}_2}{4\pi}\left[\delta(\omega)(-16)\ln\frac{m_W}{\mu}\ln\frac{m_W}{\nu} + \left[\frac{1}{\omega}\right]_*^{[m_W]}(-16)\ln\frac{m_W}{\mu}\right]. \end{aligned} \tag{G.39}$$

The operator combinations $ij = \{12, 21\}$ are given by

$$\begin{aligned} W^{12}_{(00)(00)}(\omega,\mu,\nu) &= W^{21*}_{(00)(00)}(\omega,\mu,\nu) \\ &= \frac{\hat{\alpha}_2}{4\pi}\left[\delta(\omega)\,(8+8\pi i)\ln\frac{m_W}{\mu} + \left[\frac{1}{\omega}\right]_*^{[m_W]} 8\ln\left(\frac{m_W^2+\omega^2}{m_W^2}\right)\right], \\ W^{12}_{(00)(+-)}(\omega,\mu,\nu) &= W^{21*}_{(+-)(00)}(\omega,\mu,\nu) \\ &= \delta(\omega) + \frac{\hat{\alpha}_2}{4\pi}\left[\delta(\omega)\left((4+4\pi i)\ln\frac{\mu}{m_W} - 16\ln\frac{m_W}{\mu}\ln\frac{m_W}{\nu}\right)\right. \\ &\qquad \left. + \left[\frac{1}{\omega}\right]_*^{[m_W]}\left(-4\ln\left(\frac{m_W^2+\omega^2}{m_W^2}\right) + 8\ln\frac{\mu^2}{m_W^2}\right)\right], \\ W^{12}_{(+-)(00)}(\omega,\mu,\nu) &= W^{21*}_{(00)(+-)}(\omega,\mu,\nu) = W^{12}_{(00)(00)}(\omega,\mu,\nu)\,, \\ W^{12}_{(+-)(+-)}(\omega,\mu,\nu) &= W^{21*}_{(+-)(+-)}(\omega,\mu,\nu) \\ &= W^{12}_{(00)(+-)}(\omega,\mu,\nu) + \frac{\hat{\alpha}_2}{4\pi}\left[\frac{1}{\omega}\right]_*^{[m_W]}(-2)\ln\left(\frac{m_W^2+\omega^2}{m_W^2}\right). \end{aligned} \tag{G.40}$$

Finally, the operator combination $ij = 22$ is

$$
\begin{aligned}
W^{22}_{(00)(00)}(\omega,\mu,\nu) &= \frac{\hat{\alpha}_2}{4\pi}\left[\frac{1}{\omega}\right]_*^{[m_W]}\left(8\ln\left(\frac{m_W^2+\omega^2}{m_W^2}\right)-8\frac{\omega^2}{m_W^2+\omega^2}\right),\\
W^{22}_{(00)(+-)}(\omega,\mu,\nu) &= W^{22*}_{(+-),(00)}(\omega,\mu,\nu)\\
&= \frac{\hat{\alpha}_2}{4\pi}\left[\delta(\omega)\,(8-8\pi i)\ln\frac{m_W}{\mu}+\left[\frac{1}{\omega}\right]_*^{[m_W]}\left(4\ln\left(\frac{m_W^2+\omega^2}{m_W^2}\right)+4\frac{\omega^2}{m_W^2+\omega^2}\right)\right]\\
W^{22}_{(+-)(+-)}(\omega,\mu,\nu) &= \delta(\omega)+\frac{\hat{\alpha}_2}{4\pi}\left[\delta(\omega)\left(-8\ln\frac{m_W}{\mu}-16\ln\frac{m_W}{\mu}\ln\frac{m_W}{\nu}\right)\right.\\
&\quad\left.+\left[\frac{1}{\omega}\right]_*^{[m_W]}\left(-6\ln\left(\frac{m_W^2+\omega^2}{m_W^2}\right)-2\frac{\omega^2}{m_W^2+\omega^2}+8\ln\frac{\mu^2}{m_W^2}\right)\right]. \qquad \text{(G.41)}
\end{aligned}
$$

G.4.2 Higgsino DM

$$
\begin{aligned}
W^{\mathrm{SU}(2),\,11}_{IJ,\,33}(\omega,\mu,\nu) &= \delta(\omega)+\frac{\hat{g}_2^2(\mu)}{16\pi^2}\\
&\quad\times\left\{\delta(\omega)\left[-16\ln\frac{m_W}{\mu}\ln\frac{m_W}{\nu}\right]+\left[\frac{1}{\omega}\right]_*^{[m_W]}\left[-16\ln\frac{m_W}{\mu}\right]\right\}, \qquad \text{(G.42)}\\
W^{\mathrm{SU}(2),\,14}_{IJ,\,34}(\omega,\mu,\nu) &= \frac{n^{14}_{IJ}}{2}\delta(\omega)+\frac{n^{14}_{IJ}}{2}\frac{\hat{g}_2^2(\mu)}{16\pi^2}\left\{\delta(\omega)\left[\frac{\pi^2}{6}-(4+8i\pi)\ln\frac{m_W}{\mu}\right.\right.\\
&\quad\left.-8\ln\frac{m_W}{\mu}\ln\frac{m_W}{\nu}-4\ln^2\frac{m_W}{\mu}\right]\\
&\quad\left.-8\left[\frac{1}{\omega}\right]_*^{[m_W]}\left[\ln\left(\frac{m_W^2+\omega^2}{m_W^2}\right)+\ln\frac{m_W^2}{\mu^2}\right]\right\}, \qquad \text{(G.43)}\\
W^{\mathrm{SU}(2),\,41}_{IJ,\,43}(\omega,\mu,\nu) &= W^{\mathrm{SU}(2),\,14\,*}_{JI,34}(\omega,\mu,\nu)\,, \qquad \text{(G.44)}\\
W^{\mathrm{SU}(2),\,44}_{IJ,\,44}(\omega,\mu) &= \frac{n^{44}_{IJ}}{4}\delta(\omega)+\frac{n^{44}_{IJ}}{4}\frac{\hat{g}_2^2(\mu)}{16\pi^2}\left\{\delta(\omega)\left[\frac{\pi^2}{3}-8\ln\frac{m_W}{\mu}-8\ln^2\frac{m_W}{\mu}\right]\right.\\
&\quad\left.+8\left[\frac{1}{\omega}\right]_*^{[m_W]}\left[-\ln\left(\frac{m_W^2+\omega^2}{m_W^2}\right)-\ln\frac{m_W^2}{\mu^2}\right]-8\frac{w}{m_W^2+w^2}\right\}, \qquad \text{(G.45)}\\
W^{\mathrm{U}(1),\,44}_{IJ,\,33}(\omega,\mu,\nu) &= \frac{n^{44}_{IJ}}{4}\delta(\omega)+\frac{n^{44}_{IJ}}{4}\frac{\hat{g}_2^2(\mu)}{16\pi^2}\\
&\quad\times\left\{\delta(\omega)\left[-\frac{\pi^2}{3}-8\ln\frac{m_W}{\mu}-16\ln\frac{m_W}{\mu}\ln\frac{m_W}{\nu}+8\ln^2\frac{m_W}{\mu}\right]\right\}, \qquad \text{(G.46)}\\
W^{\mathrm{U}(1),\,46}_{IJ,\,34}(\omega,\mu,\nu) &= \frac{n^{46}_{IJ}}{2}\delta(\omega)+\frac{n^{46}_{IJ}}{2}\frac{\hat{g}_2^2(\mu)}{16\pi^2}\\
&\quad\times\left\{\delta(\omega)\left[-\frac{\pi^2}{6}-4\ln\frac{m_W}{\mu}-8\ln\frac{m_W}{\mu}\ln\frac{m_W}{\nu}+4\ln^2\frac{m_W}{\mu}\right]\right\}, \qquad \text{(G.47)}\\
W^{\mathrm{U}(1),\,64}_{IJ,\,43}(\omega,\mu,\nu) &= W^{\mathrm{U}(1),\,46\,*}_{JI,\,34}(\omega,\mu,\nu) \qquad \text{(G.48)}\\
W^{\mathrm{U}(1),\,66}_{IJ,\,44}(\omega) &= \delta(\omega)\,, \qquad \text{(G.49)}
\end{aligned}
$$

where we introduced

$$
n^{ij}_{IJ} = (-1)^{\delta_{I(00)}\delta_{i4}}(-1)^{\delta_{J(00)}\delta_{j4}} \quad \text{with} \quad (00)=(11)\text{ or }(22), \qquad \text{(G.50)}
$$

to allow for a more compact notation.

G.5 Expressions for the resummed soft coefficients

G.5.1 Wino DM

For the operator combination $ij = 11$, the $\hat{W}$ coefficients are given by

$$\begin{aligned}\hat{W}^{11}_{(00)(00)}(\omega,\mu_s,\nu) &= \hat{W}^{11}_{(00)(+-)}(\omega,\mu_s,\nu) = \hat{W}^{11}_{(+-)(00)}(\omega,\mu_s,\nu) = \hat{W}^{11}_{(+-)(+-)}(\omega,\mu_s,\nu)\\ &= \left(1+\frac{\hat{\alpha}_2}{4\pi}(-16)\ln\frac{m_W}{\mu_s}\,\partial_\eta\right)\frac{e^{-\gamma_E\eta}}{\Gamma(\eta)}\frac{1}{\omega}\left(\frac{\omega}{\nu}\right)^\eta . \end{aligned} \tag{G.51}$$

We note that here η is defined as in (6.112) and should not be confused with the rapidity regulator. For the operator combination $ij = 12$, the results read

$$\begin{aligned}\hat{W}^{12}_{(00)(00)}(\omega,\mu_s,\nu) &= \hat{W}^{12}_{(+-)(00)}(\omega,\mu_s,\nu)\\ &= \frac{\hat{\alpha}_2}{4\pi}\left[(8+8\pi i)\ln\frac{m_W}{\mu_s}\right]\frac{e^{-\gamma_E\eta}}{\Gamma(\eta)}\frac{1}{\omega}\left(\frac{\omega}{\nu}\right)^\eta + \frac{\hat{\alpha}_2}{4\pi}\left[8F(\omega)\right] ,\\ \hat{W}^{12}_{(00)(+-)}(\omega,\mu_s,\nu) &= \left[1+\frac{\hat{\alpha}_2}{4\pi}\left(\left(-16\ln\frac{m_W}{\mu_s}\,\partial_\eta\right)-(4+4\pi i)\ln\frac{m_W}{\mu_s}\right)\right]\frac{e^{-\gamma_E\eta}}{\Gamma(\eta)}\frac{1}{\omega}\left(\frac{\omega}{\nu}\right)^\eta\\ &\quad+\frac{\hat{\alpha}_2}{4\pi}\left[-4F(\omega)\right] ,\\ \hat{W}^{12}_{(+-)(+-)}(\omega,\mu_s,\nu) &= \hat{W}^{12}_{(00)(+-)}(\omega,\mu_s,\nu)+\frac{\hat{\alpha}_2}{4\pi}\left[-2F(\omega)\right] , \end{aligned} \tag{G.52}$$

and for $ij = 21$,

$$\begin{aligned}\hat{W}^{21}_{(00)(00)}(\omega,\mu_s,\nu) &= \hat{W}^{12*}_{(00)(00)}(\omega,\mu_s,\nu)\\ \hat{W}^{21}_{(00)(+-)}(\omega,\mu_s,\nu) &= \hat{W}^{12*}_{(+-)(00)}(\omega,\mu_s,\nu)\\ \hat{W}^{21}_{(+-)(00)}(\omega,\mu_s,\nu) &= \hat{W}^{12*}_{(00)(+-)}(\omega,\mu_s,\nu)\\ \hat{W}^{21}_{(+-)(+-)}(\omega,\mu_s,\nu) &= \hat{W}^{12*}_{(+-)(+-)}(\omega,\mu_s,\nu) \end{aligned} \tag{G.53}$$

Finally, for the operator combination $ij = 22$, we have the inverse Laplace-transformed soft coefficients

$$\begin{aligned}\hat{W}^{22}_{(00)(00)}(\omega,\mu_s,\nu) &= \frac{\hat{\alpha}_2}{4\pi}\left[8F(\omega)-8P(\omega)\right] ,\\ \hat{W}^{22}_{(00)(+-)}(\omega,\mu_s,\nu) &= \hat{W}^{22*}_{(+-)(00)}(\omega,\mu_s,\nu)\\ &= \left[\frac{\hat{\alpha}_2}{4\pi}(8-8\pi i)\ln\frac{m_W}{\mu_s}\right]\frac{e^{-\gamma_E\eta}}{\Gamma(\eta)}\frac{1}{\omega}\left(\frac{\omega}{\nu}\right)^\eta+\frac{\hat{\alpha}_2}{4\pi}\left[4F(\omega)+4P(\omega)\right] ,\\ \hat{W}^{22}_{(+-)(+-)}(\omega,\mu_s,\nu) &= \left[1+\frac{\hat{\alpha}_2}{4\pi}\left(\left(-16\ln\frac{m_W}{\mu_s}\,\partial_\eta\right)-8\ln\frac{m_W}{\mu_s}\right)\right]\frac{e^{-\gamma_E\eta}}{\Gamma(\eta)}\frac{1}{\omega}\left(\frac{\omega}{\nu}\right)^\eta\\ &\quad+\frac{\hat{\alpha}_2}{4\pi}\left[-6F(\omega)-2P(\omega)\right] . \end{aligned} \tag{G.54}$$

G.5.2 Higgsino DM

$$\hat{W}^{\mathrm{SU}(2),\,11}_{IJ,\,33} = n^{11}_{IJ}\left[1+\frac{\hat{g}_2^2}{16\pi^2}\left(-16\ln\frac{m_W}{\mu}\partial_\eta\right)\right]\frac{e^{-\gamma_E\eta}}{\Gamma(\eta)}\frac{1}{\omega}\left(\frac{\omega}{\nu}\right)^\eta , \tag{G.55}$$

$$\hat{W}^{\mathrm{SU}(2),14}_{IJ,34} = \frac{n^{14}_{IJ}}{2}\Bigg[1+\frac{\hat{g}_2^2}{16\pi^2}\Bigg(+\frac{\pi^2}{6}-4\ln\frac{m_W}{\mu}-8i\pi\ln\frac{m_W}{\mu}+8\ln\frac{m_W}{\mu}\ln\frac{m_W}{\nu} \\ -16\ln\frac{m_W}{\mu}\partial_\eta-4\ln^2\frac{m_W}{\mu}\Bigg)\Bigg]\frac{e^{-\gamma_E\eta}}{\Gamma(\eta)}\frac{1}{\omega}\left(\frac{\omega}{\nu}\right)^\eta+\frac{n^{14}_{IJ}}{2}\frac{\hat{g}_2^2}{16\pi^2}\left(-8F(\omega)\right)\,, \tag{G.56}$$

$$\hat{W}^{\mathrm{SU}(2),41}_{IJ,43} = \hat{W}^{\mathrm{SU}(2),14\,*}_{JI,34}\,, \tag{G.57}$$

$$\hat{W}^{\mathrm{SU}(2),44}_{IJ,44} = \frac{n^{44}_{IJ}}{4}\Bigg[1+\frac{\hat{g}_2^2}{16\pi^2}\Bigg(+\frac{\pi^2}{3}-8\ln\frac{m_W}{\mu}-8\ln^2\frac{m_W}{\mu}+16\ln\frac{m_W}{\mu}\ln\frac{m_W}{\nu} \\ -16\ln\frac{m_W}{\mu}\partial_\eta\Bigg)\Bigg]\frac{e^{-\gamma_E\eta}}{\Gamma(\eta)}\frac{1}{\omega}\left(\frac{\omega}{\nu}\right)^\eta+\frac{n^{44}_{IJ}}{4}\frac{\hat{g}_2^2}{16\pi^2}\left(-8F(\omega)-8P(\omega)\right)\,, \tag{G.58}$$

where n^{ij}_{IJ} was defined in (G.50). Note that we did not include the resummed expressions for $\hat{W}^{\mathrm{U}(1),ij}_{IJ,WY}$, since these are independent of the Laplace parameter and the inverse Laplace transform simply leads to the originial expressions $W^{\mathrm{U}(1),ij}_{IJ,WY}$. This fact was already used in the derivation of the resummed Higgsino soft functions given in (6.145).

Bibliography

[1] T. S. van Albada, J. N. Bahcall, K. Begeman, and R. Sancisi. The Distribution of Dark Matter in the Spiral Galaxy NGC-3198. *Astrophys. J.*, 295:305–313, 1985. doi:10.1086/163375.

[2] D. Clowe, M. Bradac, A. H. Gonzalez, M. Markevitch, S. W. Randall, C. Jones, and D. Zaritsky. A direct empirical proof of the existence of dark matter. *Astrophys. J.*, 648:L109–L113, 2006. arXiv:astro-ph/0608407, doi:10.1086/508162.

[3] J. L. Feng. Dark Matter Candidates from Particle Physics and Methods of Detection. *Ann. Rev. Astron. Astrophys.*, 48:495–545, 2010. arXiv:1003.0904, doi:10.1146/annurev-astro-082708-101659.

[4] Review of particle physics. *Phys. Rev. D*, 98:030001 and 2019 update, Aug 2018. URL: https://link.aps.org/doi/10.1103/PhysRevD.98.030001, doi:10.1103/PhysRevD.98.030001.

[5] L. Roszkowski, E. M. Sessolo, and S. Trojanowski. WIMP dark matter candidates and searches—current status and future prospects. *Rept. Prog. Phys.*, 81(6):066201, 2018. arXiv:1707.06277, doi:10.1088/1361-6633/aab913.

[6] K. Bernlöhr et al. Monte Carlo design studies for the Cherenkov Telescope Array. *Astropart. Phys.*, 43:171–188, 2013. arXiv:1210.3503, doi:10.1016/j.astropartphys.2012.10.002.

[7] M. Beneke, A. Broggio, C. Hasner, K. Urban, and M. Vollmann. Resummed photon spectrum from dark matter annihilation for intermediate and narrow energy resolution. *JHEP*, 08:103, 2019. arXiv:1903.08702, doi:10.1007/JHEP08(2019)103.

[8] M. Beneke, C. Hasner, K. Urban, and M. Vollmann. Precise yield of high-energy photons from Higgsino dark matter annihilation. *JHEP*, 03:030, 2020. arXiv:1912.02034, doi:10.1007/JHEP03(2020)030.

[9] M. Beneke, A. Broggio, C. Hasner, and M. Vollmann. Energetic γ-rays from TeV scale dark matter annihilation resummed. *Phys. Lett.*, B786:347–354, 2018. arXiv:1805.07367, doi:10.1016/j.physletb.2018.10.008.

[10] F. Zwicky. Die Rotverschiebung von extragalaktischen Nebeln. *Helv. Phys. Acta*, 6:110–127, 1933. [Gen. Rel. Grav.41,207(2009)]. doi:10.1007/s10714-008-0707-4.

[11] V. C. Rubin and W. K. Ford, Jr. Rotation of the Andromeda Nebula from a Spectroscopic Survey of Emission Regions. *Astrophys. J.*, 159:379–403, 1970. doi:10.1086/150317.

[12] V. C. Rubin, N. Thonnard, and W. K. Ford, Jr. Rotational properties of 21 SC galaxies with a large range of luminosities and radii, from NGC 4605 /R = 4kpc/ to UGC 2885 /R = 122 kpc/. *Astrophys. J.*, 238:471, 1980. doi:10.1086/158003.

[13] A. Refregier. Weak gravitational lensing by large scale structure. *Ann. Rev. Astron. Astrophys.*, 41:645–668, 2003. arXiv:astro-ph/0307212, doi:10.1146/annurev.astro.41.111302.102207.

[14] J. A. Tyson, G. P. Kochanski, and I. P. Dell'Antonio. Detailed mass map of CL0024+1654 from strong lensing. *Astrophys. J.*, 498:L107, 1998. arXiv:astro-ph/9801193, doi:10.1086/311314.

[15] A. D. Lewis, D. A. Buote, and J. T. Stocke. Chandra observations of Abell 2029: The Dark matter profile at ¡ 0.01 R(VIR) in an unusually relaxed cluster. *Astrophys. J.*, 586:135–142, 2003. arXiv:astro-ph/0209205, doi:10.1086/367556.

[16] S. W. Allen, A. C. Fabian, R. W. Schmidt, and H. Ebeling. Cosmological constraints from the local x-ray luminosity function of the most x-ray luminous galaxy clusters. *Mon. Not. Roy. Astron. Soc.*, 342:287, 2003. arXiv:astro-ph/0208394, doi:10.1046/j.1365-8711.2003.06550.x.

[17] A. G. Riess et al. Observational evidence from supernovae for an accelerating universe and a cosmological constant. *Astron. J.*, 116:1009–1038, 1998. arXiv:astro-ph/9805201, doi:10.1086/300499.

[18] S. Perlmutter et al. Measurements of Ω and Λ from 42 high redshift supernovae. *Astrophys. J.*, 517:565–586, 1999. arXiv:astro-ph/9812133, doi:10.1086/307221.

[19] E. Komatsu et al. Seven-Year Wilkinson Microwave Anisotropy Probe (WMAP) Observations: Cosmological Interpretation. *Astrophys. J. Suppl.*, 192:18, 2011. arXiv:1001.4538, doi:10.1088/0067-0049/192/2/18.

[20] M. Milgrom. A Modification of the Newtonian dynamics as a possible alternative to the hidden mass hypothesis. *Astrophys. J.*, 270:365–370, 1983. doi:10.1086/161130.

[21] G. W. Angus, B. Famaey, and D. A. Buote. X-ray Group and cluster mass profiles in MOND: Unexplained mass on the group scale. *Mon. Not. Roy. Astron. Soc.*, 387:1470, 2008. arXiv:0709.0108, doi:10.1111/j.1365-2966.2008.13353.x.

[22] S. Bharadwaj and S. Kar. Modeling galaxy halos using dark matter with pressure. *Phys. Rev.*, D68:023516, 2003. arXiv:astro-ph/0304504, doi:10.1103/PhysRevD.68.023516.

[23] H. Velten and D. Schwarz. Dissipation of dark matter. *Phys. Rev.*, D86:083501, 2012. arXiv:1206.0986, doi:10.1103/PhysRevD.86.083501.

[24] S. W. Randall, M. Markevitch, D. Clowe, A. H. Gonzalez, and M. Bradac. Constraints on the Self-Interaction Cross-Section of Dark Matter from Numerical Simulations of the Merging Galaxy Cluster 1E 0657-56. *Astrophys. J.*, 679:1173–1180, 2008. arXiv:0704.0261, doi:10.1086/587859.

[25] C. S. Frenk and S. D. M. White. Dark matter and cosmic structure. *Annalen Phys.*, 524:507–534, 2012. arXiv:1210.0544, doi:10.1002/andp.201200212.

[26] K. Abazajian. Linear cosmological structure limits on warm dark matter. *Phys. Rev.*, D73:063513, 2006. arXiv:astro-ph/0512631, doi:10.1103/PhysRevD.73.063513.

[27] R. de Putter et al. New Neutrino Mass Bounds from Sloan Digital Sky Survey III Data Release 8 Photometric Luminous Galaxies. *Astrophys. J.*, 761:12, 2012. arXiv:1201.1909, doi:10.1088/0004-637X/761/1/12.

[28] V. N. Lukash, E. V. Mikheeva, and A. M. Malinovsky. Formation of the large-scale structure of the Universe. *Phys. Usp.*, 54:983–1005, 2011. arXiv:1209.0371, doi:10.3367/UFNe.0181.201110a.1017.

[29] S. Tremaine and J. E. Gunn. Dynamical Role of Light Neutral Leptons in Cosmology. *Phys. Rev. Lett.*, 42:407–410, 1979. [,66(1979)]. doi:10.1103/PhysRevLett.42.407.

[30] S. D. M. White, C. S. Frenk, and M. Davis. Clustering in a Neutrino Dominated Universe. *Astrophys. J.*, 274:L1–L5, 1983. [,80(1984)]. doi:10.1086/161425.

[31] B. Moore, S. Ghigna, F. Governato, G. Lake, T. R. Quinn, J. Stadel, and P. Tozzi. Dark matter substructure within galactic halos. *Astrophys. J.*, 524:L19–L22, 1999. arXiv:astro-ph/9907411, doi:10.1086/312287.

[32] A. A. Klypin, A. V. Kravtsov, O. Valenzuela, and F. Prada. Where are the missing Galactic satellites? *Astrophys. J.*, 522:82–92, 1999. arXiv:astro-ph/9901240, doi:10.1086/307643.

[33] H.-Y. Chiu. Symmetry between particle and anti-particle populations in the universe. *Phys. Rev. Lett.*, 17:712, 1966. doi:10.1103/PhysRevLett.17.712.

[34] G. Steigman. Cosmology Confronts Particle Physics. *Ann. Rev. Nucl. Part. Sci.*, 29:313–338, 1979. doi:10.1146/annurev.ns.29.120179.001525.

[35] R. J. Scherrer and M. S. Turner. On the Relic, Cosmic Abundance of Stable Weakly Interacting Massive Particles. *Phys. Rev.*, D33:1585, 1986. [Erratum: Phys. Rev.D34,3263(1986)]. doi:10.1103/PhysRevD.33.1585,10.1103/PhysRevD.34.3263.

[36] H. Baer, K.-Y. Choi, J. E. Kim, and L. Roszkowski. Dark matter production in the early Universe: beyond the thermal WIMP paradigm. *Phys. Rept.*, 555:1–60, 2015. arXiv:1407.0017, doi:10.1016/j.physrep.2014.10.002.

[37] M. Cirelli, N. Fornengo, and A. Strumia. Minimal dark matter. *Nucl. Phys.*, B753:178–194, 2006. arXiv:hep-ph/0512090, doi:10.1016/j.nuclphysb.2006.07.012.

[38] S. D. Thomas and J. D. Wells. Phenomenology of Massive Vectorlike Doublet Leptons. *Phys. Rev. Lett.*, 81:34–37, 1998. arXiv:hep-ph/9804359, doi:10.1103/PhysRevLett.81.34.

[39] M. W. Goodman and E. Witten. Detectability of Certain Dark Matter Candidates. *Phys. Rev.*, D31:3059, 1985. [,325(1984)]. doi:10.1103/PhysRevD.31.3059.

[40] A. H. G. Peter, V. Gluscevic, A. M. Green, B. J. Kavanagh, and S. K. Lee. WIMP physics with ensembles of direct-detection experiments. *Phys. Dark Univ.*, 5-6:45–74, 2014. arXiv:1310.7039, doi:10.1016/j.dark.2014.10.006.

[41] T. Marrodán Undagoitia and L. Rauch. Dark matter direct-detection experiments. *J. Phys.*, G43(1):013001, 2016. arXiv:1509.08767, doi:10.1088/0954-3899/43/1/013001.

[42] R. Bernabei et al. The DAMA/LIBRA apparatus. *Nucl. Instrum. Meth.*, A592:297–315, 2008. arXiv:0804.2738, doi:10.1016/j.nima.2008.04.082.

[43] E. Aprile et al. Dark Matter Search Results from a One Ton-Year Exposure of XENON1T. *Phys. Rev. Lett.*, 121(11):111302, 2018. arXiv:1805.12562, doi:10.1103/PhysRevLett.121.111302.

[44] A. Tan et al. Dark Matter Results from First 98.7 Days of Data from the PandaX-II Experiment. *Phys. Rev. Lett.*, 117(12):121303, 2016. arXiv:1607.07400, doi:10.1103/PhysRevLett.117.121303.

[45] S. P. Ahlen, F. T. Avignone, R. L. Brodzinski, A. K. Drukier, G. Gelmini, and D. N. Spergel. Limits on Cold Dark Matter Candidates from an Ultralow Background Germanium Spectrometer. *Phys. Lett.*, B195:603–608, 1987. doi:10.1016/0370-2693(87)91581-4.

[46] C. E. Aalseth et al. CoGeNT: A Search for Low-Mass Dark Matter using p-type Point Contact Germanium Detectors. *Phys. Rev.*, D88:012002, 2013. arXiv:1208.5737, doi:10.1103/PhysRevD.88.012002.

[47] Q. Yue et al. Limits on light WIMPs from the CDEX-1 experiment with a p-type point-contact germanium detector at the China Jingping Underground Laboratory. *Phys. Rev.*, D90:091701, 2014. arXiv:1404.4946, doi:10.1103/PhysRevD.90.091701.

[48] G. K. Giovanetti et al. A Dark Matter Search with MALBEK. *Phys. Procedia*, 61:77–84, 2015. arXiv:1407.2238, doi:10.1016/j.phpro.2014.12.014.

[49] R. Agnese et al. Maximum Likelihood Analysis of Low Energy CDMS II Germanium Data. *Phys. Rev.*, D91:052021, 2015. arXiv:1410.1003, doi:10.1103/PhysRevD.91.052021.

[50] R. Agnese et al. Search for Low-Mass Weakly Interacting Massive Particles Using Voltage-Assisted Calorimetric Ionization Detection in the SuperCDMS Experiment. *Phys. Rev. Lett.*, 112(4):041302, 2014. arXiv:1309.3259, doi:10.1103/PhysRevLett.112.041302.

[51] J. Conrad, J. Cohen-Tanugi, and L. E. Strigari. WIMP searches with gamma rays in the Fermi era: challenges, methods and results. *J. Exp. Theor. Phys.*, 121(6):1104–1135, 2015. [Zh. Eksp. Teor. Fiz.148,no.6,1257(2015)]. arXiv:1503.06348, doi:10.1134/S1063776115130099.

[52] J. M. Gaskins. A review of indirect searches for particle dark matter. *Contemp. Phys.*, 57(4):496–525, 2016. arXiv:1604.00014, doi:10.1080/00107514.2016.1175160.

[53] M. Cirelli, G. Corcella, A. Hektor, G. Hutsi, M. Kadastik, P. Panci, M. Raidal, F. Sala, and A. Strumia. PPPC 4 DM ID: A Poor Particle Physicist Cookbook for Dark Matter Indirect Detection. *JCAP*, 1103:051, 2011. [Erratum: JCAP1210,E01(2012)]. arXiv:1012.4515, doi:10.1088/1475-7516/2012/10/E01,10.1088/1475-7516/2011/03/051.

[54] L. Bergstrom, P. Ullio, and J. H. Buckley. Observability of gamma-rays from dark matter neutralino annihilations in the Milky Way halo. *Astropart. Phys.*, 9:137–162, 1998. arXiv:astro-ph/9712318, doi:10.1016/S0927-6505(98)00015-2.

[55] D. J. Thompson et al. Calibration of the Energetic Gamma-Ray Experiment Telescope (EGRET) for the Compton Gamma-Ray Observatory. *Astrophys. J. Suppl.*, 86:629–656, 1993. doi:10.1086/191793.

[56] W. B. Atwood et al. The Large Area Telescope on the Fermi Gamma-ray Space Telescope Mission. *Astrophys. J.*, 697:1071–1102, 2009. arXiv:0902.1089, doi:10.1088/0004-637X/697/2/1071.

[57] J. Aleksic et al. Performance of the MAGIC stereo system obtained with Crab Nebula data. *Astropart. Phys.*, 35:435–448, 2012. arXiv:1108.1477, doi:10.1016/j.astropartphys.2011.11.007.

[58] J. Holder et al. Status of the VERITAS Observatory. *AIP Conf. Proc.*, 1085(1):657–660, 2009. arXiv:0810.0474, doi:10.1063/1.3076760.

[59] F. Aharonian et al. Observations of the Crab Nebula with H.E.S.S. *Astron. Astrophys.*, 457:899–915, 2006. arXiv:astro-ph/0607333, doi:10.1051/0004-6361:20065351.

[60] M. Actis et al. Design concepts for the Cherenkov Telescope Array CTA: An advanced facility for ground-based high-energy gamma-ray astronomy. *Exper. Astron.*, 32:193–316, 2011. arXiv:1008.3703, doi:10.1007/s10686-011-9247-0.

[61] J. Hisano, S. Matsumoto, and M. M. Nojiri. Explosive dark matter annihilation. *Phys. Rev. Lett.*, 92:031303, 2004. arXiv:hep-ph/0307216, doi:10.1103/PhysRevLett.92.031303.

[62] J. Hisano, S. Matsumoto, M. M. Nojiri, and O. Saito. Non-perturbative effect on dark matter annihilation and gamma ray signature from galactic center. *Phys. Rev.*, D71:063528, 2005. arXiv:hep-ph/0412403, doi:10.1103/PhysRevD.71.063528.

[63] N. Arkani-Hamed, D. P. Finkbeiner, T. R. Slatyer, and N. Weiner. A Theory of Dark Matter. *Phys. Rev.*, D79:015014, 2009. arXiv:0810.0713, doi:10.1103/PhysRevD.79.015014.

[64] M. Beneke, C. Hellmann, and P. Ruiz-Femenia. Heavy neutralino relic abundance with Sommerfeld enhancements - a study of pMSSM scenarios. *JHEP*, 03:162, 2015. arXiv:1411.6930, doi:10.1007/JHEP03(2015)162.

[65] M. Baumgart, I. Z. Rothstein, and V. Vaidya. Calculating the Annihilation Rate of Weakly Interacting Massive Particles. *Phys. Rev. Lett.*, 114:211301, 2015. arXiv:1409.4415, doi:10.1103/PhysRevLett.114.211301.

[66] G. Ovanesyan, T. R. Slatyer, and I. W. Stewart. Heavy Dark Matter Annihilation from Effective Field Theory. *Phys. Rev. Lett.*, 114(21):211302, 2015. arXiv:1409.8294, doi:10.1103/PhysRevLett.114.211302.

[67] M. Bauer, T. Cohen, R. J. Hill, and M. P. Solon. Soft Collinear Effective Theory for Heavy WIMP Annihilation. *JHEP*, 01:099, 2015. arXiv:1409.7392, doi:10.1007/JHEP01(2015)099.

[68] G. Ovanesyan, N. L. Rodd, T. R. Slatyer, and I. W. Stewart. One-loop correction to heavy dark matter annihilation. *Phys. Rev.*, D95(5):055001, 2017. [Erratum: Phys. Rev.D100,no.11,119901(2019)]. arXiv:1612.04814, doi:10.1103/PhysRevD.100.119901,10.1103/PhysRevD.95.055001.

[69] M. Baumgart, T. Cohen, I. Moult, N. L. Rodd, T. R. Slatyer, M. P. Solon, I. W. Stewart, and V. Vaidya. Resummed Photon Spectra for WIMP Annihilation. *JHEP*, 03:117, 2018. arXiv:1712.07656, doi:10.1007/JHEP03(2018)117.

[70] M. Beneke and V. A. Smirnov. Asymptotic expansion of Feynman integrals near threshold. *Nucl. Phys.*, B522:321–344, 1998. arXiv:hep-ph/9711391, doi:10.1016/S0550-3213(98)00138-2.

[71] V. Smirnov. Applied asymptotic expansions in momenta and masses. *Applied Asymptotic Expansions in Momenta and Masses, Edited by Vladimir A. Smirnov, Springer Tracts in Modern Physics, vol. 177*, 177, 01 2001. doi:10.1007/3-540-44574-9_1.

[72] T. Becher and M. Neubert. Drell-Yan Production at Small q_T, Transverse Parton Distributions and the Collinear Anomaly. *Eur. Phys. J.*, C71:1665, 2011. arXiv:1007.4005, doi:10.1140/epjc/s10052-011-1665-7.

[73] J.-y. Chiu, F. Golf, R. Kelley, and A. V. Manohar. Electroweak Sudakov corrections using effective field theory. *Phys. Rev. Lett.*, 100:021802, 2008. arXiv:0709.2377, doi:10.1103/PhysRevLett.100.021802.

[74] J.-y. Chiu, F. Golf, R. Kelley, and A. V. Manohar. Electroweak Corrections in High Energy Processes using Effective Field Theory. *Phys. Rev.*, D77:053004, 2008. arXiv:0712.0396, doi:10.1103/PhysRevD.77.053004.

[75] J.-y. Chiu, A. Jain, D. Neill, and I. Z. Rothstein. The Rapidity Renormalization Group. *Phys. Rev. Lett.*, 108:151601, 2012. arXiv:1104.0881, doi:10.1103/PhysRevLett.108.151601.

[76] J.-Y. Chiu, A. Jain, D. Neill, and I. Z. Rothstein. A Formalism for the Systematic Treatment of Rapidity Logarithms in Quantum Field Theory. *JHEP*, 05:084, 2012. arXiv:1202.0814, doi:10.1007/JHEP05(2012)084.

[77] M. Baumgart, T. Cohen, E. Moulin, I. Moult, L. Rinchiuso, N. L. Rodd, T. R. Slatyer, I. W. Stewart, and V. Vaidya. Precision Photon Spectra for Wino Annihilation. *JHEP*, 01:036, 2019. arXiv:1808.08956, doi:10.1007/JHEP01(2019)036.

[78] M. Beneke, C. Hellmann, and P. Ruiz-Femenia. Non-relativistic pair annihilation of nearly mass degenerate neutralinos and charginos III. Computation of the Sommerfeld enhancements. *JHEP*, 05:115, 2015. arXiv:1411.6924, doi:10.1007/JHEP05(2015)115.

[79] M. Beneke, C. Hellmann, and P. Ruiz-Femenia. Non-relativistic pair annihilation of nearly mass degenerate neutralinos and charginos I. General framework and S-wave annihilation. *JHEP*, 03:148, 2013. [Erratum: JHEP10,224(2013)]. arXiv:1210.7928, doi:10.1007/JHEP10(2013)224,10.1007/JHEP03(2013)148.

[80] G. T. Bodwin, E. Braaten, and G. P. Lepage. Rigorous QCD analysis of inclusive annihilation and production of heavy quarkonium. *Phys. Rev.*, D51:1125–1171, 1995. [Erratum: Phys. Rev.D55,5853(1997)]. arXiv:hep-ph/9407339, doi:10.1103/PhysRevD.55.5853,10.1103/PhysRevD.51.1125.

[81] M. Beneke, R. Szafron, and K. Urban. Wino potential and Sommerfeld effect at NLO. *Phys. Lett.*, B800:135112, 2020. arXiv:1909.04584, doi:10.1016/j.physletb.2019.135112.

[82] C. Hellmann and P. Ruiz-Femenía. Non-relativistic pair annihilation of nearly mass degenerate neutralinos and charginos II. P-wave and next-to-next-to-leading order S-wave coefficients. *JHEP*, 08:084, 2013. arXiv:1303.0200, doi:10.1007/JHEP08(2013)084.

[83] C. W. Bauer, S. Fleming, and M. E. Luke. Summing Sudakov logarithms in B —¿ X(s gamma) in effective field theory. *Phys. Rev.*, D63:014006, 2000. arXiv:hep-ph/0005275, doi:10.1103/PhysRevD.63.014006.

[84] C. W. Bauer, S. Fleming, D. Pirjol, and I. W. Stewart. An Effective field theory for collinear and soft gluons: Heavy to light decays. *Phys. Rev.*, D63:114020, 2001. arXiv:hep-ph/0011336, doi:10.1103/PhysRevD.63.114020.

[85] C. W. Bauer and I. W. Stewart. Invariant operators in collinear effective theory. *Phys. Lett.*, B516:134–142, 2001. arXiv:hep-ph/0107001, doi:10.1016/S0370-2693(01)00902-9.

[86] C. W. Bauer, D. Pirjol, and I. W. Stewart. Soft collinear factorization in effective field theory. *Phys. Rev.*, D65:054022, 2002. arXiv:hep-ph/0109045, doi:10.1103/PhysRevD.65.054022.

[87] M. Beneke, A. P. Chapovsky, M. Diehl, and T. Feldmann. Soft collinear effective theory and heavy to light currents beyond leading power. *Nucl. Phys.*, B643:431–476, 2002. arXiv:hep-ph/0206152, doi:10.1016/S0550-3213(02)00687-9.

[88] T. Becher, A. Broggio, and A. Ferroglia. Introduction to Soft-Collinear Effective Theory. *Lect. Notes Phys.*, 896:pp.1–206, 2015. arXiv:1410.1892, doi:10.1007/978-3-319-14848-9.

[89] M. Beneke, M. Garny, R. Szafron, and J. Wang. Anomalous dimension of subleading-power N-jet operators. *JHEP*, 03:001, 2018. arXiv:1712.04416, doi:10.1007/JHEP03(2018)001.

[90] A. Alloul, N. D. Christensen, C. Degrande, C. Duhr, and B. Fuks. FeynRules 2.0 - A complete toolbox for tree-level phenomenology. *Comput. Phys. Commun.*, 185:2250–2300, 2014. arXiv:1310.1921, doi:10.1016/j.cpc.2014.04.012.

[91] T. Hahn. Generating Feynman diagrams and amplitudes with FeynArts 3. *Comput. Phys. Commun.*, 140:418–431, 2001. arXiv:hep-ph/0012260, doi:10.1016/S0010-4655(01)00290-9.

[92] T. Hahn and M. Perez-Victoria. Automatized one loop calculations in four-dimensions and D-dimensions. *Comput. Phys. Commun.*, 118:153–165, 1999. arXiv:hep-ph/9807565, doi:10.1016/S0010-4655(98)00173-8.

[93] H. H. Patel. Package-X: A Mathematica package for the analytic calculation of one-loop integrals. *Comput. Phys. Commun.*, 197:276–290, 2015. arXiv:1503.01469, doi:10.1016/j.cpc.2015.08.017.

[94] J. Kuipers, T. Ueda, J. A. M. Vermaseren, and J. Vollinga. FORM version 4.0. *Comput. Phys. Commun.*, 184:1453–1467, 2013. arXiv:1203.6543, doi:10.1016/j.cpc.2012.12.028.

[95] T. van Ritbergen, A. Schellekens, and J. Vermaseren. Group theory factors for Feynman diagrams. *Int. J. Mod. Phys. A*, 14:41–96, 1999. arXiv:hep-ph/9802376, doi:10.1142/S0217751X99000038.

[96] A. von Manteuffel and C. Studerus. Reduze 2 - Distributed Feynman Integral Reduction. 2012. arXiv:1201.4330.

[97] W. Beenakker, R. Kleiss, and G. Lustermans. No Landau-Yang in QCD. 2015. arXiv:1508.07115.

[98] M. Cacciari, L. Del Debbio, J. R. Espinosa, A. D. Polosa, and M. Testa. A note on the fate of the Landau–Yang theorem in non-Abelian gauge theories. *Phys. Lett.*, B753:476–481, 2016. arXiv:1509.07853, doi:10.1016/j.physletb.2015.12.053.

[99] A. Ferroglia, M. Neubert, B. D. Pecjak, and L. L. Yang. Two-loop divergences of massive scattering amplitudes in non-abelian gauge theories. *JHEP*, 11:062, 2009. arXiv:0908.3676, doi:10.1088/1126-6708/2009/11/062.

[100] M. Beneke, P. Falgari, and C. Schwinn. Soft radiation in heavy-particle pair production: All-order colour structure and two-loop anomalous dimension. *Nucl. Phys.*, B828:69–101, 2010. arXiv:0907.1443, doi:10.1016/j.nuclphysb.2009.11.004.

[101] G. P. Korchemsky and A. V. Radyushkin. Renormalization of the Wilson Loops Beyond the Leading Order. *Nucl. Phys.*, B283:342–364, 1987. doi:10.1016/0550-3213(87)90277-X.

[102] A. Denner. Techniques for calculation of electroweak radiative corrections at the one loop level and results for W physics at LEP-200. *Fortsch. Phys.*, 41:307–420, 1993. arXiv:0709.1075, doi:10.1002/prop.2190410402.

[103] T. Becher and G. Bell. The gluon jet function at two-loop order. *Phys. Lett.*, B695:252–258, 2011. arXiv:1008.1936, doi:10.1016/j.physletb.2010.11.036.

[104] M. Ibe, S. Matsumoto, and R. Sato. Mass Splitting between Charged and Neutral Winos at Two-Loop Level. *Phys. Lett. B*, 721:252–260, 2013. arXiv:1212.5989, doi:10.1016/j.physletb.2013.03.015.

[105] T. Becher and M. D. Schwartz. Direct photon production with effective field theory. *JHEP*, 02:040, 2010. arXiv:0911.0681, doi:10.1007/JHEP02(2010)040.

[106] F. De Fazio and M. Neubert. B —¿ X(u) lepton anti-neutrino lepton decay distributions to order alpha(s). *JHEP*, 06:017, 1999. arXiv:hep-ph/9905351, doi:10.1088/1126-6708/1999/06/017.

[107] Z.-W. Huang and J. Liu. NumExp: Numerical epsilon expansion of hypergeometric functions. *Comput. Phys. Commun.*, 184:1973–1980, 2013. arXiv:1209.3971, doi:10.1016/j.cpc.2013.03.016.